Acoustical Physics, Vol. 48, No. 3, 2002, pp. 247–253. Translated from Akusticheskiĭ Zhurnal, Vol. 48, No. 3, 2002, pp. 293–299.
Original Russian Text Copyright © 2002 by Abakumova.

Sound Field Characteristics in the Eastern Part of the Sea of Okhotsk

N. K. Abakumova

Andreev Acoustics Institute, Russian Academy of Sciences, ul. Shvernika 4, Moscow, 117036 Russia

e-mail: bvp@akin.ru

Received March 7, 2001

Abstract—The problem of how the parameters of the underwater sound channel affect the sound field calculated in the ray and parabolic-equation approximations is studied. To that end, the calculations are compared with the experimental data obtained in the eastern part of the Sea of Okhotsk with the use of cw sound sources. The decay laws are analyzed for the sound field of a point source in a waveguide with varying parameters. The calculated and experimental characteristics of the sound field are compared for the frequency range 100–3000 Hz. © *2002 MAIK "Nauka/Interperiodica".*

Studies of sound propagation in a shallow sea and coastal sea regions are the subject of many publications, because each region of this type has its individual features governed by the instability of the hydrological parameters and by the influence of the sea boundaries (the surface and the bottom). Depending on the specific sound field profile $c(z)$, the bottom or surface can predominate. With a positive gradient of the sound speed, a surface sound channel is formed, and the sound field is strongly influenced by the wavy surface. With a negative gradient, the acoustic properties of the sea floor prevail.

Here, we report some results obtained by processing the experimental data that were collected earlier in the eastern part of the Sea of Okhotsk.

To compare the experimental data with calculations, we used computer codes based on the ray [1] and parabolic-equation [2] approximations; in addition, the computer program [3] based on the method of normal waves was used.

When the ray approximation is valid, it is very advantageous and easy to grasp. For some distances, the solution of the wave equation by the normal-wave method fails because of the poor convergence, and it is necessary to apply the ray approximation, parabolic equation, or other methods [1, 2, 4, 5]. However, the widely used numerical methods can lead to unsatisfactory results, if information on the waveguide parameters is insufficient [6–11].

In August 1981, experimental studies of the sound field were carried out in the Sea of Okhotsk. In the eastern part of this sea, cw sound sources were used with the frequencies 63, 127, 260, 510, 1250, and 3150 Hz. At each frequency, the signal was transmitted for 10 min, which was followed by a pause of 5 min. The sound field structure was studied at the distances 1, 5, 8, 20, 40, 80, 120, and 200 km from the source. At each distance, the interference pattern of the sound field was recorded within some range interval (about 100 m). The acoustic experiments were accompanied by measuring the sound speed profiles and the ambient sea noise. One of the oceanographic features of the eastern part of the Sea of Okhotsk is a 20-m subsurface layer where the sound speed can either be constant or have positive or negative gradients with a mean sound speed value of 1491 m/s. Lower, down to the 60-m depth, a rather sharp discontinuity layer is observed where the sound speed gradient is about 6.5×10^{-4} 1/m.

Table 1 summarizes the values of the relative sound speed gradient a in the discontinuity layer for several hydrological stations located at different distances along the path.

The following notations are used: r is the distance at which the sound speed profile was measured, $C_{\min}$ and C_{surf} are the sound speeds at the axis of the sound channel and at the water surface, respectively, and H_1 is the thickness of the discontinuity layer.

Figure 1 shows the sound speed profiles $C(z)$ at some points of the path (at $r = 0$, 25, and 50 km) and the bottom relief. The same figure also shows the ray pat-

Table 1

No.	r, km	$C_{\min}$, m/s	C_{surf}	$H_{\min}$, m	H_1	a, 1/m
1	0	1482.1	1488.5	100	80	2.5×10^{-4}
2	25	1452.0	1488.6	80	60	3.1×10^{-4}
3	50	1452.3	1490.3	70	45	3.7×10^{-4}

1063-7710/02/4803-0247$22.00 © 2002 MAIK "Nauka/Interperiodica"

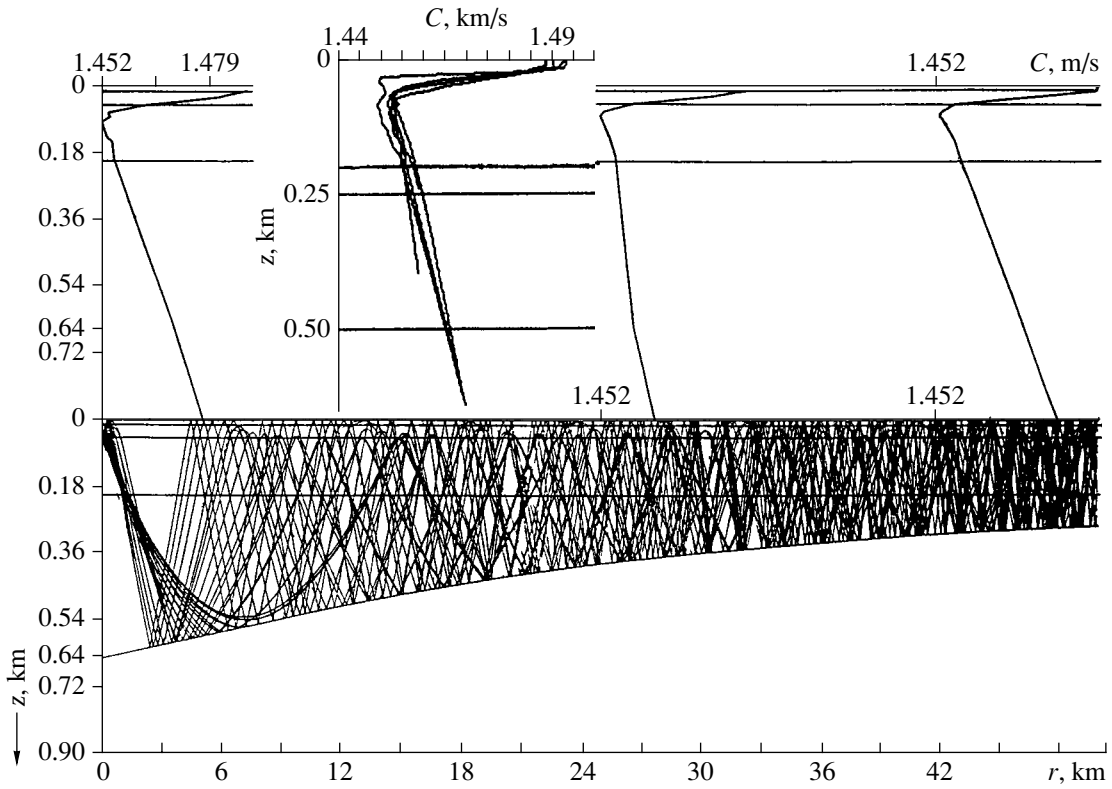

Fig. 1. Sea depth at the initial 200-km fraction of the path, vertical distributions of the sound speed at distances of 1, 20, and 40 km, and the profiles $C(z)$ measured on the path.

tern for the 50-km fraction of the path with a source depth of 50 m.

According to long-term observations in the Sea of Okhotsk, the sound speed values increase as the sea depth increases from 500 to 4000 m with gradients from $a_1 = 1.2 \times 10^{-5}$ 1/m to $a_2 = 2.04 \times 10^{-5}$ 1/m. In deeper water layers, the sound speed is fully determined by the hydrostatic pressure, and the gradient is equal to a_1. At the maximal depth H_{max} = 640 m observed on the path, the sound speed becomes equal to 1469 m/s, which is $\Delta C \sim$ 20–22 m/s lower than that at the surface. Thus, the refracted sound field is formed by the whole angular spectrum ($\chi \cong \pm 15°$) of the signal, which is determined by the difference in the sound speeds near the bottom and at the channel axis.

The signals were received at the 200-m depth with the source depth being equal to 50 m. Let us consider the horizontal sections of the sound field for the 200-m reception depth. Since the near-surface sound speed is higher than the near-bottom one, the sound signals mainly propagate with bottom reflections (Fig. 1). This fact leads to a high energy loss for the propagating signals.

In experimenting in shallow-water regions and subsequently interpreting the experimental data, one needs information on the structure and parameters of the bottom sediments to choose the geoacoustic model. The data required include the thickness values of the bottom layers, the sediment densities, and the velocities of longitudinal and transverse waves in the bottom. From the literature [11], it is known that, in the region of interest, the upper sediment layer is represented by sandy silt. Experiments with explosion-generated sound signals allowed the observation of ground waves in this region. The estimated velocity C_1 of the longitudinal waves proved to be 1550–1640 m/s. The near-bottom sound speed in water was 1469 m/s.

To compare the experimental data with calculations, we chose two models for the sea floor. By numerically experimenting, we found the waveguide parameters that allowed us to model the sound propagation in a region of varying sea depth and sound speed profile in accordance with the experimental data. We analyzed the loss in the sound field intensity due to changes in the hydrological parameters and sea depth along the path, as well as the loss in the bottom.

Let us consider the sound field decays calculated in the ray approximation for the bottom modeled as a liquid absorbing halfspace. For the simplest bottom model of this kind, the coefficient of bottom reflection is calculated according to the Fresnel formula and has no frequency dependence. However, the experimental range dependences of the sound field are different for differ-

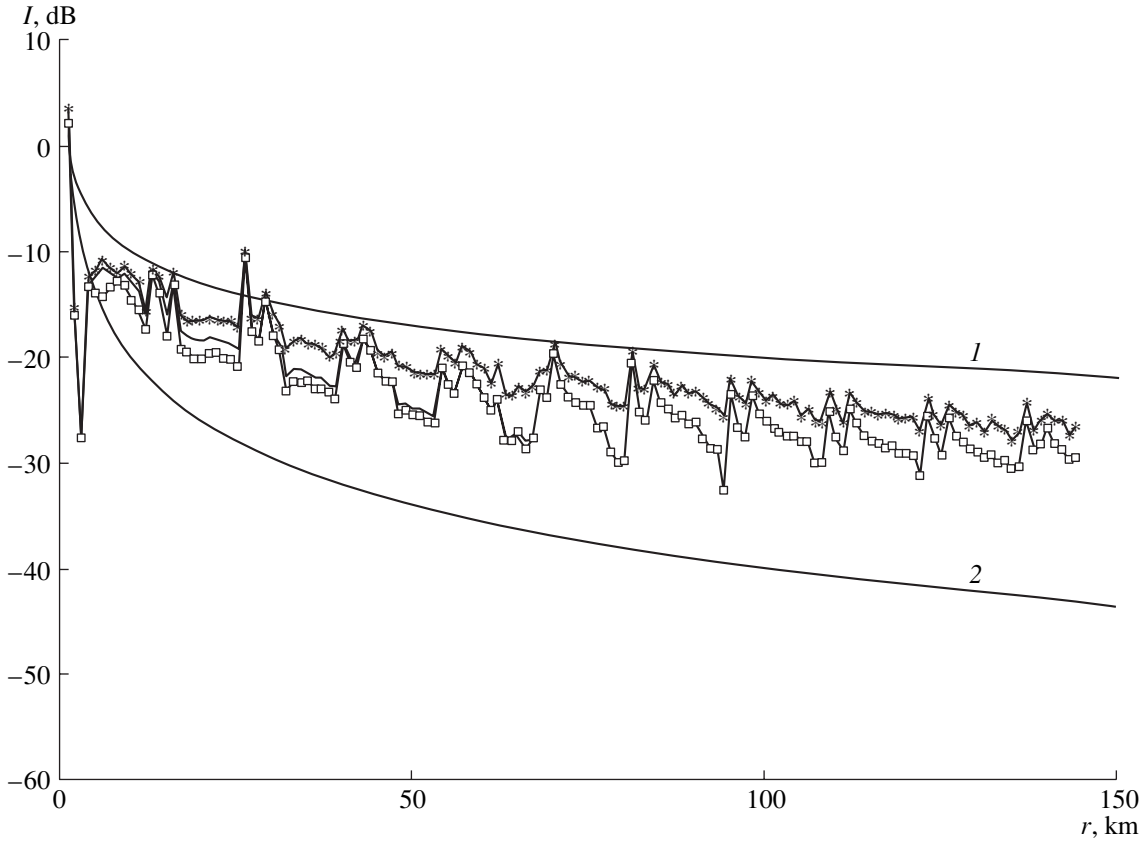

Fig. 2. Range dependences of the sound field intensity in the deep-water region of the Sea of Okhotsk with a flat bottom and the maximal sea depth $H = 640$ m. The hydrological parameters and the reflection coefficients vary along the path: (∗) $|V| = 1$; (—) sand; (□) silt; (*1*) cylindrical and (*2*) spherical decay laws.

ent frequencies. Neglect of the changes in the bottom parameters with depth may cause this difference. When the bottom is modeled as a liquid absorbing halfspace, the depth dependence of the bottom parameters is usually taken into account by using their values averaged over the effective layer that contributes to the sound field. The following parameters of the liquid bottom should be specified: the ratio m of the bottom-material density (ρ_b) to the water density (ρ_0), the ratio n of the sound speed (C_0) in water to that (C_b) in the bottom material, and the loss coefficient η [6].

Figure 2 illustrates the effect of the changes in the bottom parameters on the sound field decay $I(r)$ for the bottom modeled as a liquid absorbing halfspace. This figure presents the results of the ray-approximation calculations for the maximal sea depth $H = 640$ m, with the hydrological parameters varying along the path. The range dependences of the sound field intensity are calculated by the incoherent summation of the signals arriving along different rays. The horizons of transmission and reception are $z_1 = 50$ m and $z = 200$ m, respectively. The directivity diagram of the source has the angular width $\chi_1 = \pm 15°$, and the rms height of the surface waves is $\sigma = 0$ m. In processing the experimental data obtained at ranges longer than 200 km, we took into account the level of the ambient noise. In Fig. 2, the asterisks label the sound field decay calculated for a totally reflecting bottom ($|V| = 1$). The dependences $I(r)$ for sand ($m = 1.9$, $n = 0.9$, and $\eta = 0.02$) and silt ($m = 1.45$, $n = 0.98$, and $\eta = 0.001$) are shown by the solid curve and squares, respectively. Two smooth curves labeled *1* and *2* correspond to the cylindrical ($1/r$) and spherical ($1/r^2$) decay laws, respectively.

At distances of 0.5–5 km, the main contribution to the sound field comes from the singly bottom-reflected signals arriving along the water rays within a narrow ray bundle limited by the departure angles $\chi_1 = \pm 4.2°$ at the source. Starting from a distance of about 10 km, the sound field is mainly formed by multiply bottom-reflected signals that arrive along rays with departure angles $|\chi_1| < 10°$. At distances longer than 100 km, the rays that are reflected from the bottom and surface at high angles govern the sound field. For such rays, the reflection coefficients are nearly equal, and the type of the bottom material does not considerably affect the decay law $I(r)$. As the frequency increases, the thickness of the effective layer that contributes to the sound field decreases, and the reflection coefficient begins to

Table 2

Hz	*m*	*n*	η
63	1.4	0.9	10^{-2}
127	1.4	0.88	5×10^{-3}
250	1.4	0.9	5×10^{-3}
500	1.4	0.9	6×10^{-3}
1250	1.4	0.93	10^{-2}
3150	1.4	0.95	10^{-2}

depend on frequency. Table 2 summarizes the parameters of the bottom material that are selected for the frequencies used in the experiment so as to obtain the agreement between the calculations and the experiment.

The experimental range dependences of the sound field intensity are presented in Figs. 3a–3f. The interference pattern of the sound field is shown as vertical bars

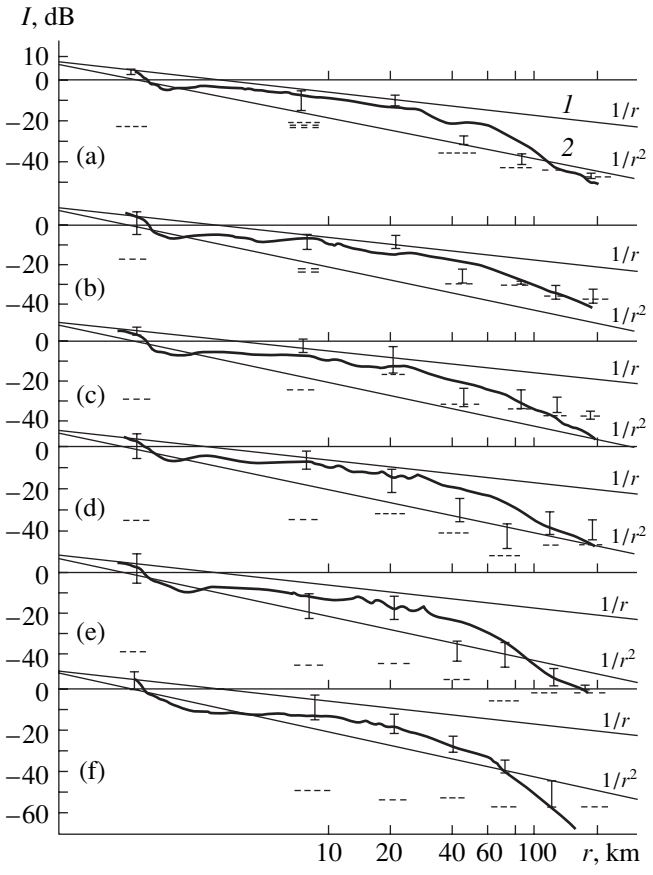

Fig. 3. Experimental and calculated range dependences of the sound field intensity for the sound speed profiles and bottom relief varying along the path. The ray-approximation computation for the frequencies 60–3000 Hz corresponds to the solid curves.

that are limited from above and below by the levels of the interference maxima and minima, respectively. Because of the high roughness of the curves, they are shown for a relatively short interval of distance. The cylindrical decay law with an exponential loss was used to approximate the experimental dependences. The solid curves represent the sound field levels calculated in the ray approximation for the frequencies 60–3150 Hz. The dashed lines indicate the noise levels at different reception points of the path (in experimenting at different distances, different "regimes of silence" were established on the receiving vessel).

In addition, starting from a distance of about 10 km, the experimental dependences $I(r)$ were approximated by cylindrical and exponential laws. The resulting coefficient β of the total loss ($\beta = \beta_0 + \beta_1$) shows the loss of the signal energy while it propagates in the shallow sea [9]. Here, β_0 is the loss coefficient caused by the sound absorption in water and β_1 is related to the loss due to the sound reflection from the bottom. As for the parameters of the bottom material for the model of the shallow-water waveguide, for which the effect of the bottom is significant, they were chosen individually for each frequency.

As a quantitative criterion for comparing the experimental and calculated data, we chose the standard deviation σ of the calculated value from the measured one. The numerical calculation showed that, for the coastal region of the Sea of Okhotsk with varying sea depth and sound speed profile, the bottom model in the form of a liquid absorbing halfspace does not lead to agreement with the experiment. The standard deviation of the calculation from the experiment was $\sigma = 1.8$ dB at the frequency $f = 1.25$ kHz, $\sigma = 7.5$ dB at $f = 510$ Hz, and $\sigma = 5.8$ dB at $f = 260$ Hz. To obtain agreement between the calculations and the experiment and smaller values of σ, one should use different sets of bottom parameters at different frequencies.

To adequately model the shallow-water waveguide for the whole frequency band at hand, we chose the model of a stratified bottom in the form of two layers characterized by the velocities C_1 and C_2 of longitudinal waves in them and an underlying halfspace with the sound speed C_b. We specified the value of C_1 to be lower than the near-bottom sound speed C_0 in water, and the values of C_2 and C_b to be both higher than C_0. We also fitted the thickness values H_1 and H_2 of the first and second bottom layers. The loss coefficients η_1, η_2, and η_0 in the first bottom layer, the second, and the liquid absorbing halfspace, respectively, were varied according to [6].

Figure 4 shows the frequency dependences of the loss coefficient obtained for the layered-bottom model for the 200-km path (the calculation is based on the parabolic-equation approximation). The dots (*1*) represent the experimental dependence of the loss coefficient for

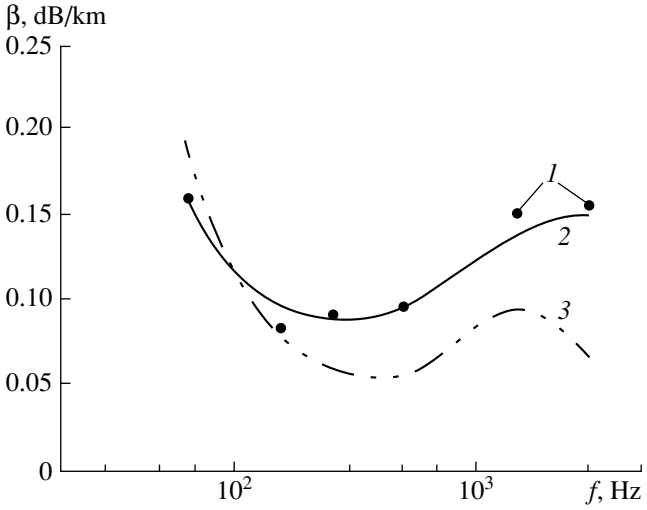

Fig. 4. Frequency dependences of the loss coefficient determined by the leak of acoustic energy into the sea floor. Dots (*1*) show the experimental dependence of the loss coefficient, and curves (*2*, *3*) are calculated in the parabolic-equation approximation for the model of a layered bottom.

the bottom-caused loss (β_1). Among all the sets of the bottom parameters summarized in Table 3, set no. 2 provides the most adequate representation of the experimental range dependence of the sound field. Curve *3* corresponds to set no. 3 of Table 3. It shows the frequency dependence of the bottom-caused loss coefficient calculated in the parabolic-equation approximation for the bottom model in the form of three layers. Note that this curve has a maximum at 1250 Hz. For the case at hand, the experimental frequency dependence of the loss coefficient is governed by the leak of acoustic energy into the sea floor. At high frequencies, the frequency dependence exhibits a saturation region, and the 1250-Hz maximum in curve *3* representing the calculated values of β_1 can presumably be related to the resonant properties of the partial waveguides in the layered bottom. The layered model is the only one for which bottom parameters can be found that lead to agreement with the experimental decay of the sound field. The calculated decay curves $I(r)$ are presented in Figs. 5–7 for the frequencies 63, 127, and 260 Hz. Here, curve *1* also corresponds to the cylindrical decay law.

Figures 5–7 illustrate the agreement between the calculated and experimental interference patterns for the entire frequency range. The experimental data are shown in the form of vertical bars. The standard deviations of the calculated values from the measured ones are about 3.1 dB at 63 Hz (σ = 1.35 dB); for the frequencies 260 and 127 Hz, σ = 4.1 and 1.2 dB, respectively. In the calculations, the following values of the parameters were specified: the thickness values for the bottom layers, H_{l1} = 10 m and H_{l2} = 30 m; the velocities of longitudinal waves in the sediments C_{l1} = 1410 m/s and C_{l2} = 1516 m/s; the loss coefficients η_{l1} = 0.05 and η_{l2} = 0.05; the densities of the sediment layers m_{l1} = 1.4 and m_{l2} = 1.5; and the parameters of the halfspace m_l = 1.8, C_l = 1640 m/s, and η_l = 0.001. These values allowed us to obtain comparable experimental and calculated data in the entire frequency band.

Table 3 summarizes the parameters of the layered bottom and the underlying halfspace. The subscripts "l" and "1" mean longitudinal waves and the ordinal number of the bottom layer, respectively, for the bottom model used in the parabolic-equation calculations. The best agreement between the calculations and the experiment was achieved for set no. 2 of Table 3 with the fol-

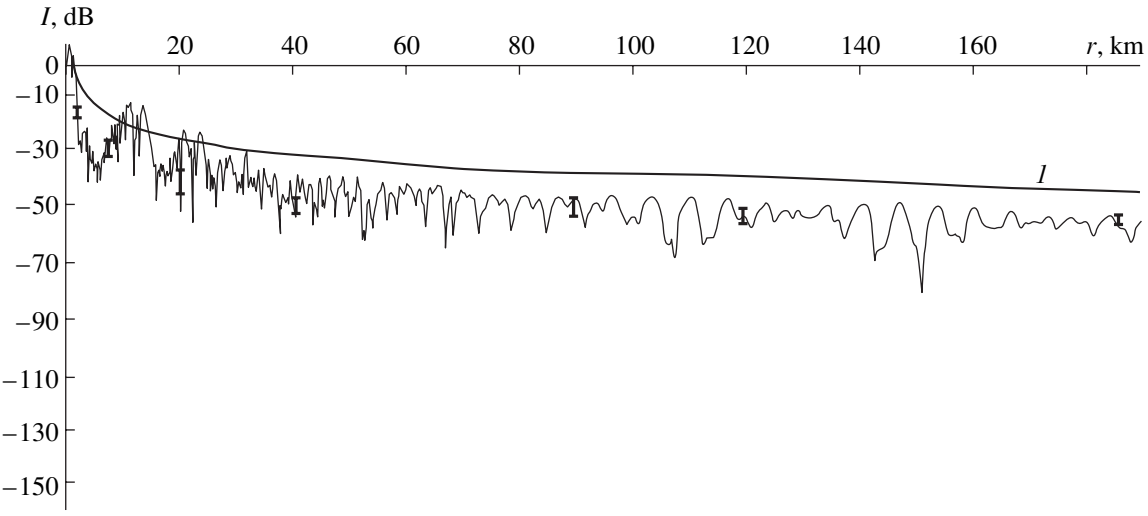

Fig. 5. Experimental and calculated decays of the sound field intensity for the frequency 260 Hz. Parabolic-equation calculations for varying sound speed profiles and bottom relief.

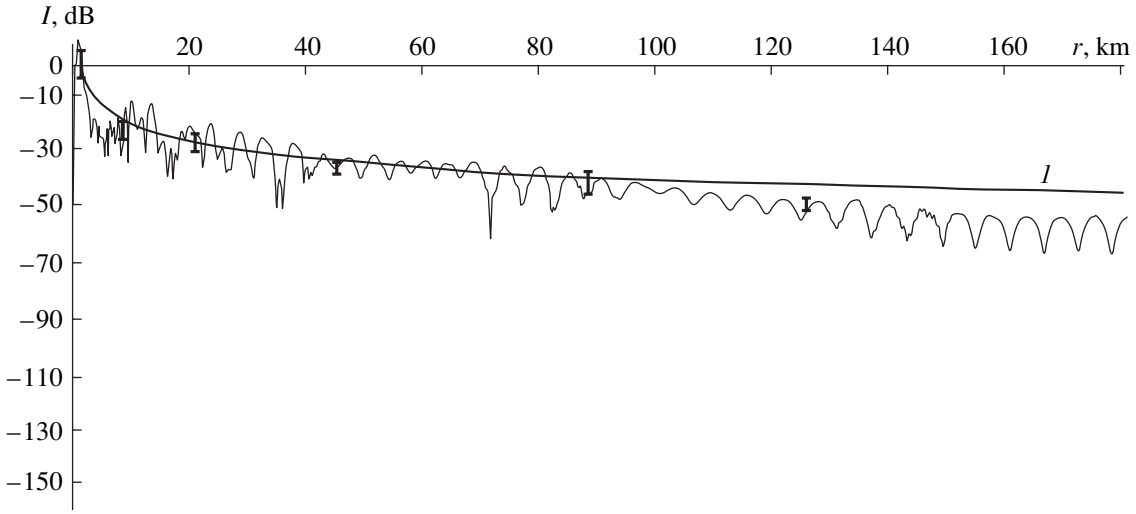

Fig. 6. Same as in Fig. 5 for the frequency 127 Hz, with the same parameters of the three-layer bottom.

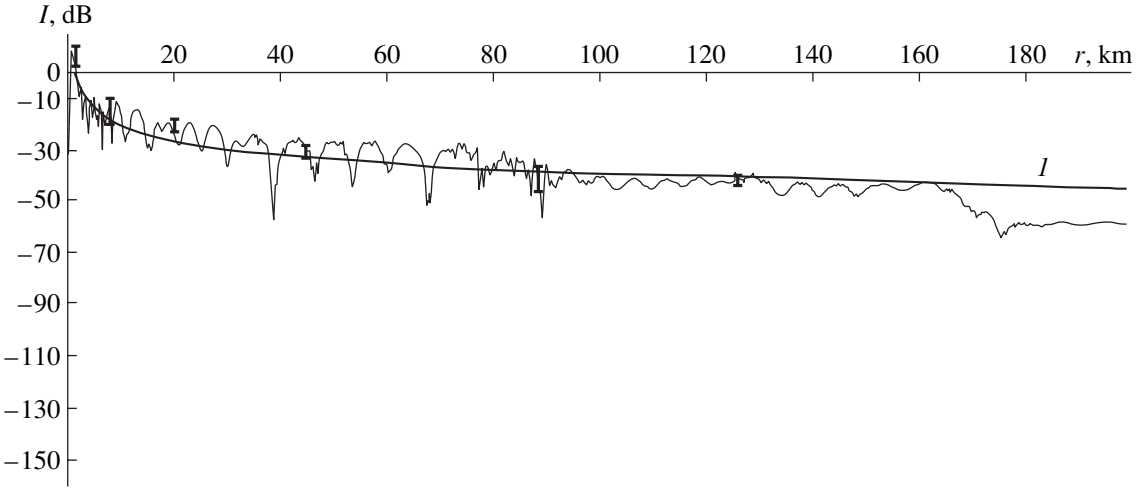

Fig. 7. Same as in Fig. 5 for the frequency 63 Hz, with the same parameters of the three-layer bottom.

lowing halfspace parameters: $m_l = 1.8$, $C_l = 1640$ m/s, and $\eta_l = 0.001$. The three-layer bottom model with certain relations between the velocities of longitudinal waves and the thicknesses of the layers allowed us to obtain a frequency dependence of the loss coefficient, which had a minimum and agreed well with the experiment in the whole frequency band under investigation.

Table 3

No.	First layer				Second layer				Halfspace		
	H_l	m_l	n_l	η_l	H_l	m_l	n_l	η_l	m_L	n_L	η_L
1	–	–	–	–	–	–	–	–	1.4	0.9	10^{-2}
2	10	1.4	1.04	0.05	30	1.5	0.97	0.05	1.8	0.9	10^{-3}
3	4	1.4	1.06	0.03	30	1.5	0.97	0.01	1.8	0.9	10^{-3}

ACKNOWLEDGMENTS

This work was supported by the Russian Foundation for Basic Research, project no. 00-02-17694.

REFERENCES

1. A. V. Vagin, *A Report of the Acoustics Institute, USSR Acad. Sci.* (Moscow, 1974).
2. K. V. Avilov, *A Report of the Acoustics Institute, USSR Acad. Sci.* (Moscow, 1985).
3. N. S. Ageeva and V. D. Krupin, Akust. Zh. **27**, 669 (1981) [Sov. Phys. Acoust. **27**, 372 (1981)].

4. N. K. Abakumova, in *Proceedings of 9th All-Union Acoustical Conference* (Nauka, Moscow, 1977), Sect. A, p. 5.
5. M. Ainslie and M. Packman Harrison, J. Acoust. Soc. Am. **103**, 1804 (1998).
6. N. K. Abakumova and O. P. Galkin, Vopr. Sudostr., Ser. Akust., No. 14, 90 (1980).
7. J. L. Spiesberger, J. Acoust. Soc. Am. **99**, 173 (1996).
8. N. K. Abakumova and O. P. Galkin, Akust. Zh. **45**, 581 (1999) [Acoust. Phys. **45**, 515 (1999)].
9. S. D. Richards, J. Acoust. Soc. Am. **103**, 205 (1998).
10. W. S. Hodgkiss, H. S. Song, W. A. Kuperman, *et al.*, J. Acoust. Soc. Am. **105**, 1597 (1999).
11. R. A. Vadov, Akust. Zh. **45**, 174 (1999) [Acoust. Phys. **45**, 143 (1999)].
12. A. V. Mikryukov and O. E. Popov, Akust. Zh. **46**, 102 (2000) [Acoust. Phys. **46**, 87 (2000)].

Translated by E. Kopyl

Acoustical Physics, Vol. 48, No. 3, 2002, pp. 254–262. Translated from Akusticheskiĭ Zhurnal, Vol. 48, No. 3, 2002, pp. 300–308.
Original Russian Text Copyright © 2002 by Bulatova, Gumerova, Shagapov.

Evolution of Acoustic Waves in Channels with Permeable-Wall Regions in an Inhomogeneous Porous Medium

Z. A. Bulatova*, G. A. Gumerova, and V. Sh. Shagapov***

** Sterlitamak State Pedagogical Institute, pr. Lenina 37, Sterlitamak, 453103 Russia*

e-mail: b_za@mail.ru

*** Institute of Power Resources Transportation Problems, Academy of Sciences of Bashkortostan, pr. Oktyabrya 144/3, Ufa, 450055 Russia*

Received July 14, 2000

Abstract—The evolution of acoustic waves that propagate in cylindrical channels containing permeable regions and surrounded with a porous medium is studied. The quantitative and qualitative features of the wave dynamics are determined in relation to the condition of the inhomogeneous porous medium. In particular, cases when the channel is surrounded with radial fractures or with a low-permeability mudcake are considered. © *2002 MAIK "Nauka/Interperiodica".*

To improve the permeability of the face zones of oil and gas pools, various physicochemical, hydrodynamic, and wave techniques are used for their treatment. One of the efficient methods of the online pre- and posttreatment testing of the bottom zones of wells seems to be the acoustic method based on the special features of the reflection and transmission of acoustic signals at the boundaries between borehole regions with different permeability of the walls.

Some aspects of the wave dynamics in fluid-filled boreholes with permeable walls are considered in [1]. The main features of the propagation and attenuation of acoustic waves in channels surrounded with porous and permeable media are presented in [2, 3]. The theoretical foundations of the acoustics of fluid-saturated porous media are described in [4, 5]. The propagation of nonlinear waves in saturated porous media is theoretically and experimentally studied in [6–8]. The evolutionary equations describing and explaining some experimental data are obtained. The mathematical models of the acoustics of fluid-saturated fractured porous media (media with a double porosity) are presented in [9–12]. Some features of the dynamics of linear waves excited by electromagnetic radiation in water-saturated porous media are investigated in [13].

In this paper, an acoustic remote-control method for the well-bottom zone is considered. According to this method, the primary signal is supposed to be generated at some distance from the region under investigation and transmitted along the waveguide, which can be the cased wall of a well. In this case, the echo signal reflected from the permeable region of the well provides some information about the permeability of this region.

Consider the evolution of small-amplitude pressure waves in a cylindrical channel in the permeable-wall region (Fig. 1). We assume that both the channel and the incompressible skeleton of the surrounding porous space are filled with the same compressible fluid (liquid or gas). Then, in the linear approximation, we have

$$p = C^2\rho,$$

where ρ and p are the perturbations of density and pressure and C is the speed of sound. In addition, we assume that the wavelength λ in the channel is much greater than the length L of the permeable region ($\lambda \gg L$). Owing to this assumption, the permeable region can be interpreted as a "reflecting surface" with the coordinate $z = 0$. To obtain the boundary conditions at this "reflecting surface," we use the mass conservation equation for the permeable region in the linearized approximation

$$\frac{1}{C^2}\frac{dp}{dt} = \rho_0\frac{w_- - w_+}{L} - \rho_0\frac{2u}{a}, \qquad (1)$$

where w_- and w_+ represent the axial velocity of the medium at the upper and lower boundaries (respectively) of the permeable region of the cylindrical channel (the velocity of the fluid disturbance in the channel has a discontinuity at the "reflecting surface" $z = 0$ because of the filtration of the fluid through the channel walls); u is the speed of filtration through the permeable walls; and a is the radius of the channel. The subscript "0" marking the parameter means that its value corresponds to the initial (unperturbed) state. When the permeable region borders upon a fluid-tight wall (e.g., the permeable region is close to the well bottom), w_+ in Eq. (1) should be set equal to zero.

Replacing the permeable region by the "reflecting surface," we assume this region to be homogeneous. The pressure field in the permeable region of the channel does not take into account the dependence on the axial coordinate (e.g., due to the end effects in the per-

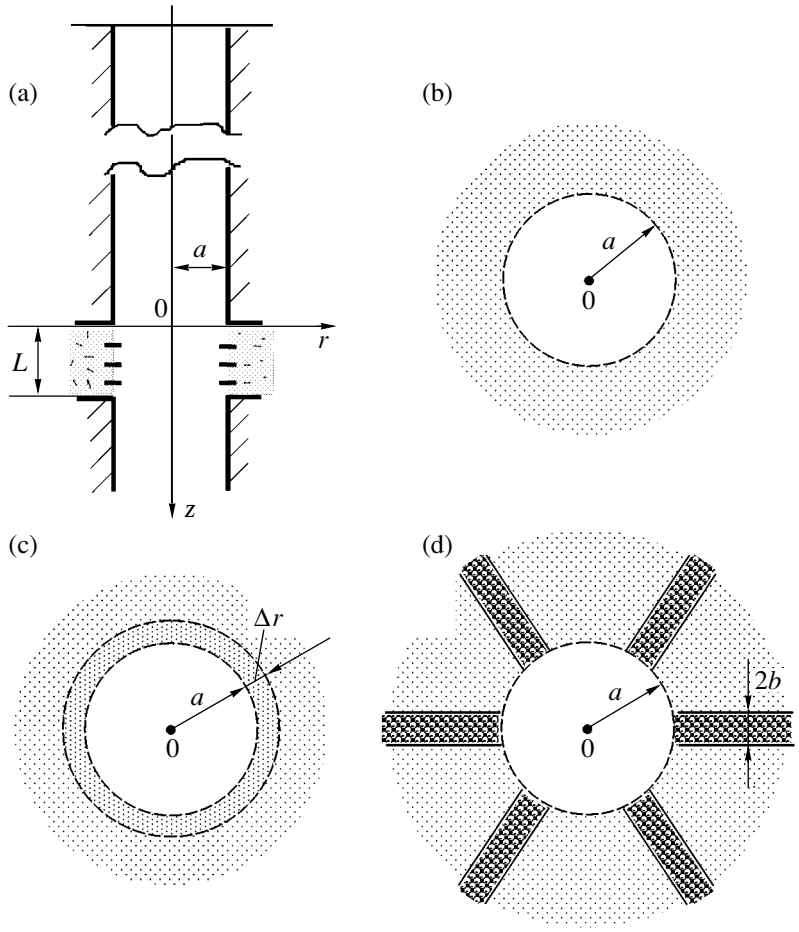

Fig. 1. (a) Schematic drawing of a channel with a permeable region and different possible structures of the surrounding porous medium: (b) a homogeneous medium, (c) a medium with a mudcake, and (d) a medium with fractures.

meable region of the channel). Therefore, to determine the pressure in the porous medium around the borehole, we use the equation of filtration in the one-dimensional radial approximation [14]. To minimize the influence of the above-mentioned two-dimensional effects, this way of taking into account the filtration processes can be used for rather short wave disturbances, whose characteristic penetration depth Δr_* in the surrounding porous medium is much smaller than the length of the permeable region ($\Delta r_* \ll L$). To assess the penetration depth of filtration waves, one can use the estimate

$$\Delta r_* = \sqrt{\chi^{(1)} t_*} \quad \left(\chi^{(1)} = \frac{C^2 \rho_0 k_c^{(1)}}{m^{(1)} \mu}\right),$$

where μ and C are the dynamic viscosity of the fluid and the speed of sound in it and $k_c^{(1)}$, $m^{(1)}$, and $\chi^{(1)}$ are the permeability, porosity, and diffusion constant of the fluid in the surrounding medium. In this case, for the time length t_* of a pulse, we obtain the condition $t_* \ll L^2/\chi^{(1)}$. Note that this condition covers a rather wide (from practical point of view) range of values for L, t_*, and $\chi^{(1)}$. In particular, at $\chi^{(1)} = 1$ m^2/s ($k^{(1)} = 10^{-12}$ m^2, $m^{(1)} = 0.1$, $C = 1500$ m/s, $\mu = 10^{-3}$ kg/m s, and $\rho_0 = 10^3$ kg/m^3), we obtain the condition $t_* \ll 1$ s even for rather short permeable regions with $L = 1$ m.

Hence, to determine the intensity of the fluid flow to the surrounding porous medium in the course of the wave propagation through the channel region with permeable walls, we use the equation of filtration in the one-dimensional radial approximation:

$$\frac{\partial p^{(1)}}{\partial t} = \chi^{(1)} \frac{1}{r} \frac{\partial}{\partial r}\left(r \frac{\partial p^{(1)}}{\partial r}\right), \quad u^{(1)} = -\frac{k_c^{(1)} \partial p^{(1)}}{\mu \partial r}, \quad (r > a). \qquad (2)$$

Here, $p^{(1)}$ and $u^{(1)}$ are the pressure disturbance and the speed of filtration in the porous medium around the channel. For generality, we assume that the inner surface of the permeable region of the channel is covered with a thin ($\Delta r \ll a$) mudcake of low permeability

(Fig. 1c). Then, the boundary conditions for Eqs. (2) at the channel wall ($r = a$) can be written as

$$u^{(1)} = u, \quad u = h(p - p^{(1)}) \quad (h = k_c^*/\mu\Delta r). \tag{3}$$

Here, h, k_c^*, and Δr are the flow friction, the characteristic permeability of the mudcake, and its thickness.

When the channel is surrounded with a porous medium of infinite thickness (the filtration processes accompanying the propagation of disturbances take place in the layers whose thickness is much smaller than that of the porous medium around the channel), the set of conditions (3) should be supplemented with the boundary condition

$$p^{(1)} = 0, \quad r \longrightarrow \infty. \tag{4}$$

The flow friction of the mudcake being neglected ($h \longrightarrow 0$), we can replace conditions (3) by

$$u^{(1)} = u, \quad p^{(1)} = p, \quad (r = a). \tag{5}$$

Outside the permeable region ($z < 0$ and $z > 0$), we assume that the pressure disturbance and the velocity satisfy the conditions of continuity and momentum conservation:

$$\frac{1}{C^2}\frac{\partial p}{\partial t} + \rho_0\frac{\partial w}{\partial z} = 0, \quad \rho_0\frac{\partial w}{\partial t} + \frac{\partial p}{\partial z} = -\frac{2\tau}{a}. \tag{6}$$

Here, τ is the shearing viscous stress at the inner surface of the channel wall, which can be determined by the expression [2]

$$\tau = \frac{\mu}{(\pi\nu)^{1/2}}\int_{-\infty}^{t}\frac{\partial w/\partial t'}{(t-t')^{1/2}}dt', \quad \left(\nu = \frac{\mu}{\rho_0}\right).$$

This expression is applicable when, in the course of wave disturbance propagation, the viscosity manifests itself only in a thin boundary layer close to the hard wall of the cylindrical channel. This, in its turn, requires that the pressure pulse length t_* satisfy the condition $\sqrt{t_*\nu} \ll a$.

Let the initial disturbance be a wave incident upon the "reflecting surface" from above ($z < 0$). When this wave interacts with the reflecting surface, the wave motion in the upper zone ($z < 0$) is determined by the superposition of two waves (the incident wave and the reflected one), and in the lower zone ($z > 0$), it is determined by one wave (the transmitted wave). At the reflecting surface, the relations that follow from the continuity conditions for the pressure and for the medium at the boundary are valid:

$$\begin{gathered} p^{(I)} + p^{(R)} = p^{(T)} = p, \\ w_- = w^{(I)} + w^{(R)}, \quad w_+ = w^{(T)} \quad (z = 0). \end{gathered} \tag{7}$$

Here, the superscripts I, R, and T indicate the values of the perturbed parameters in the incident, reflected, and transmitted waves. For the case of an impermeable right-hand wall ($w_+ = 0$), the term $p^{(T)}$ in Eq. (7) represents the pressure disturbance at this wall.

Consider the reflection and transmission of harmonic waves. The solution to the problem is sought in the form of a traveling harmonic wave (which is assumed to propagate along the channel axis). Then, for the waves in the channel ($z < 0$, $z > 0$), we can write

$$\begin{gathered} p^{(I)} = A_p^{(I)}\exp[i(Kz - \omega t)], \\ w^{(I)} = A_w^{(I)}\exp[i(Kz - \omega t)], \\ p^{(R)} = A_p^{(R)}\exp[i(-Kz - \omega t)], \\ w^{(R)} = A_w^{(R)}\exp[i(-Kz - \omega t)] \quad (z < 0), \\ p^{(T)} = A_p^{(T)}\exp[i(Kz - \omega t)], \\ w^{(T)} = A_w^{(T)}\exp[i(Kz - \omega t)] \quad (z > 0). \end{gathered} \tag{8}$$

In the absorption zone ($z = 0$), the following relations are valid:

$$\begin{gathered} p = A_p\exp(-i\omega t), \quad u = A_u\exp(-i\omega t), \\ p^{(1)} = A_p^{(1)}(r)\exp(-i\omega t), \quad u^{(1)} = A_u^{(1)}(r)\exp(-i\omega t). \end{gathered} \tag{9}$$

Here, K is the wave number, ω is the circular frequency, and i is the imaginary unit. The condition of the existence of solutions (8) to Eqs. (6) leads to the dispersion equation

$$K = \frac{\omega\sqrt{1 + 2y_{(\nu)}^{-1}}}{C}, \quad y_{(\nu)} = \sqrt{-i\omega a^2/\nu}. \tag{10}$$

Equations (6) yield the relations between the velocity and pressure amplitudes:

$$\begin{gathered} A_w^{(I)} = A_p^{(I)}\frac{\omega}{\rho_0 C^2 K}, \quad A_w^{(R)} = -A_p^{(R)}\frac{\omega}{\rho_0 C^2 K}, \\ A_w^{(T)} = A_p^{(T)}\frac{\omega}{\rho_0 C^2 K}. \end{gathered} \tag{11}$$

Taking into account Eqs. (9), we obtain from Eqs. (2) and (3):

$$\begin{gathered} y^2 A_p^{(1)}(R) = \frac{1}{R}\frac{d}{dR}\left(R\frac{dA_p^{(1)}(R)}{dR}\right), \\ A_u^{(1)}(R) = -\frac{k_c^{(1)}}{\mu r_0}\frac{dA_p^{(1)}(R)}{dR} \quad (R > 1), \\ A_u = h(A_p - A_p^{(1)}), \quad A_u^{(1)} = A_u \quad (R = 1), \\ \left(y = \sqrt{-\frac{i\omega a^2}{\chi^{(1)}}}, \quad R = r/a\right). \end{gathered} \tag{12}$$

Note that the parameter $|y| = a/a_\omega$ ($a_\omega = \sqrt{\chi^{(1)}/\omega}$) is determined by the ratio of the channel radius a to the depth of penetration a_ω of the filtration waves with the frequency ω into the porous medium [15].

The general solution to Eq. (12) has the form

$$A_p^{(1)}(R) = AI_0(yR) + BK_0(yR),$$
$$K_0(yR) = \int_0^\infty \exp(-yR\cosh(\xi))d\xi, \qquad (13)$$
$$I_0(yR) = J_0(iyR),$$

where $K_0(yR)$ and $J_0(yR)$ are zero-order Macdonald and Bessel functions and A and B are arbitrary constants.

To make solution (13) satisfy boundary condition (4), one should set $A = 0$. Then, on the basis of conditions (3), one obtains

$$B = \frac{A_p}{K_0(y) - \gamma y K_0'(y)} \quad \left(\gamma = \frac{k_c^*}{\mu a h}\right). \qquad (14)$$

From Eqs. (1) and (7), with allowance for Eqs. (13) and (14), we obtain the reflection ($N = A_p^{(R)}/A_p^{(I)}$) and transmission ($M = A_p^{(T)}/A_p^{(I)}$) coefficients:

$$N = \left(\frac{2C}{i\omega L - D} - 1\right)^{-1}, \quad M = N + 1,$$

$$D = -2\frac{m^{(1)}\omega_\chi^{(1)} L y(\ln K_0(y))'}{1 - \gamma y(\ln K_0(y))'} \qquad (15)$$

$$\left(\omega_\chi^{(1)} = \chi^{(1)}/a^2, \quad K_0'(x) = \frac{dK_0(x)}{dx}\right).$$

Here, the complex parameter D describes the filtration processes in the absorption zone.

When the permeable region is close to the well bottom ($w_+ = 0$), the reflection coefficient is

$$N = \left(\frac{2C}{C + i\omega L - D} - 1\right)^{-1}. \qquad (16)$$

Now, let the low-permeability mudcake be absent ($\gamma = 0$). Then, in the high-frequency range where the condition $|y| \gg 1$ ($\omega \gg \omega_\chi^{(1)}$) is fulfilled, expression (15) for D leads to

$$D = 2m^{(1)}\omega_\chi^{(1)} L y.$$

Note that, at $\omega \longrightarrow \infty$, Eqs. (15) and (16) lead to $N \longrightarrow -1$. Hence, the reflecting surface acts as a free boundary for high-frequency incident disturbances. However, one should take into account that these solutions are valid on condition that the wavelength is much greater than the length of the permeable region of the channel ($\lambda \gg L$). Using the estimate $\lambda = 2\pi C/\omega$ for the relation between the wavelength and the frequency, we obtain the condition $\omega \ll \omega_*$ ($\omega_* = 2\pi C/L$), which determines the applicability limit of this theory. For water-filled and methane-filled channels at $L = 10$ m, we obtain $\omega_* = 10^3$ and 10^2 s^{-1}, respectively. In this case, at $a = 5 \times 10^{-2}$ m, $k_c^{(1)} = 10^{-12}$ m^2, and $m^{(1)} = 0.2$, the value of the characteristic frequency at which the penetration depth of filtration waves is of the order of the channel radius is $\omega_\chi^{(1)} = 3 \times 10^3$ and 10 s^{-1} for the channels filled with water and methane, respectively.

In the low-frequency range, when $|y| \ll 1$ ($\omega \ll \omega_\chi$), we have the following asymptotic formula:

$$D = -2m^{(1)} L \omega_\chi/(\ln y).$$

In Fig. 2, the solid lines represent magnitudes $|M|$ and $|N|$ and arguments $\arg M$ and $\arg N$ of the reflectance and transmittance calculated by Eqs. (15) as functions of frequency, and also their hodographs in the channels ($a = 5 \times 10^{-2}$ m, $L = 2$ m, and $m^{(1)} = 0.2$) filled with water ($\nu = 10^{-6}$ m^2/s and $C = 1.53 \times 10^3$ m/s). Note that water is also taken as a fluid in all the following examples. Curves *1*, *2*, and *3* correspond to the permeability of the porous medium around the channel $k_c^{(1)} = 10^{-10}$, 10^{-12}, and 10^{-14} m^2, respectively. It can be seen from these curves that the real part of the reflectance is negative ($\arg(N) > \pi/2$) in the whole frequency range (the existence of a permeable region for the waves incident from the left ($z < 0$) makes the right-hand region ($z > 0$) acoustically softer). Furthermore, as the permeability of the surrounding porous medium increases, the magnitude of the reflectance also increases, whereas the magnitude of the transmittance decreases. In the frequency range shown in Fig. 2, in the case of a high-permeability porous medium ($k_c^{(1)} \geq 10^{-10}$ m^2), the dynamics of the wave reflection from the permeable region of the channel ($z = 0$) is similar to the reflection from a free surface ($N \longrightarrow -1$), and, accordingly, the transmittance tends to zero ($M \longrightarrow 0$). The dashed lines in Fig. 2 demonstrate the coefficients of reflection and transmission calculated by Eqs. (16) for cases when the permeable region is close to the well bottom ($w_+ = 0$).

Calculations were also performed for a thin mudcake ($\Delta r = 0.5 \times 10^{-2}$ m and $k_c^* = 10^{-14}$ m^2). The results show that even a tenfold increase in the permeability of the basic porous medium around the channel only slightly affects the value of the reflectance in the presence of a thin low-permeability mudcake. When the mudcake completely screens the basic porous medium around the channel, we obtain

$$D = \frac{2LC^2\rho_0 h}{a}.$$

Now, on the basis of expressions (15) and (16) for the reflectance and transmittance and dispersion relation (10), we consider the dynamics of pulses and analyze the evolution of finite-length waves propagating through the permeable region of a cylindrical channel. Let a signal of a finite length, $p = \tilde{p}^{(I)}(t)$, be sent through the boundary $z = -H$ into the region $z < 0$. Then,

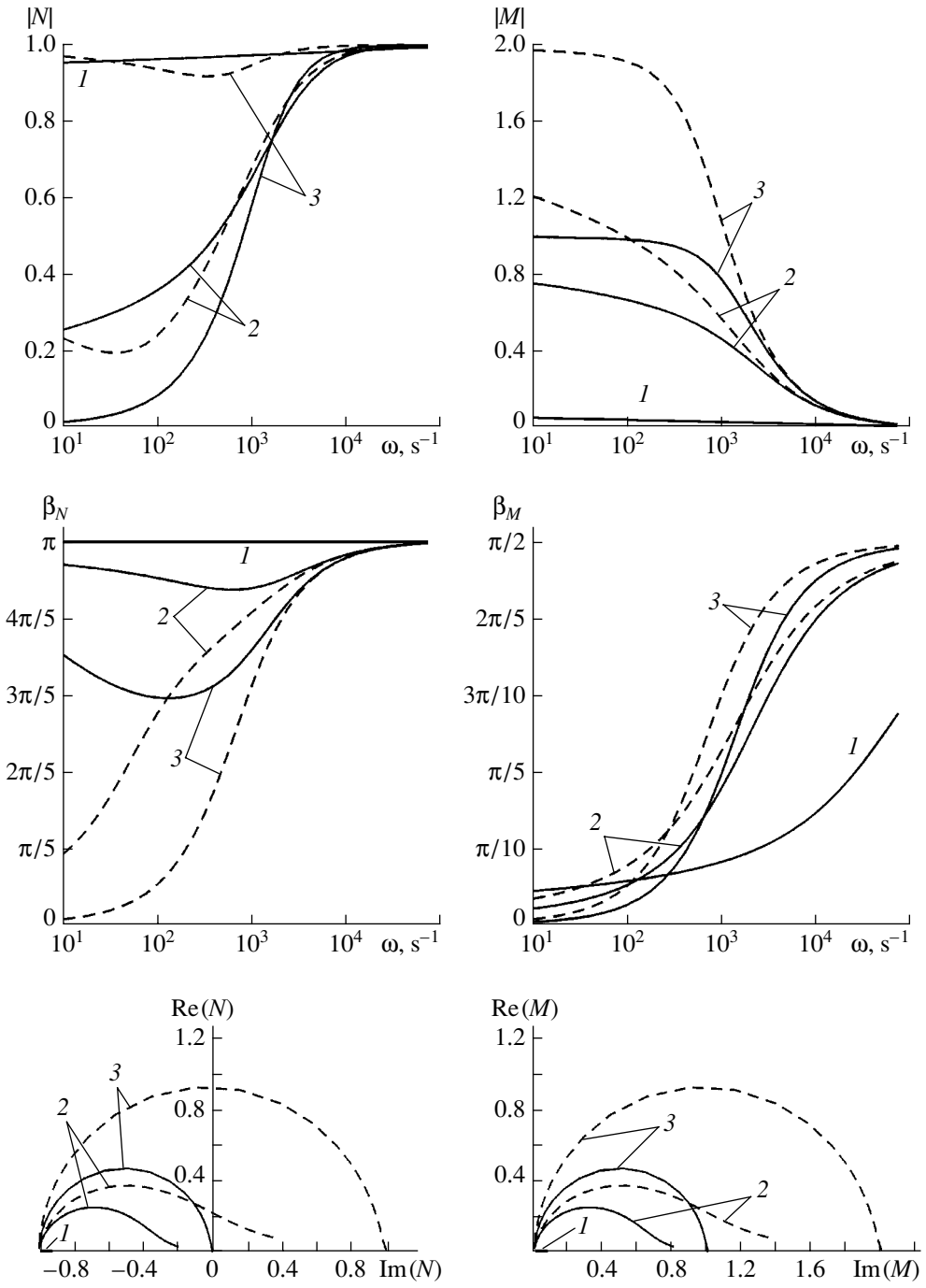

Fig. 2. Dispersion of the reflectance and transmittance as a function of the permeability of the homogeneous porous medium around the borehole.

using the Fourier transformation, for the pulse reaching the reflecting surface $z = 0$, we obtain

$$p^{(I)}(0, t) = \frac{1}{\pi}\int_{0}^{\infty}\int_{-\infty}^{\infty} \tilde{p}^{(I)}(t')\exp(iK(\omega)H) \times \exp[i\omega(t-t')]d\omega dt'.$$

Similar relations can be written for the pulse reflected from the boundary $z = 0$ and the pulse transmitted through it:

$$p^{(R)} = \frac{1}{\pi}\int_{0}^{\infty}\int_{-\infty}^{\infty} p^{(I)}(0, t')N(\omega)\exp[i\omega(t-t')]d\omega dt',$$

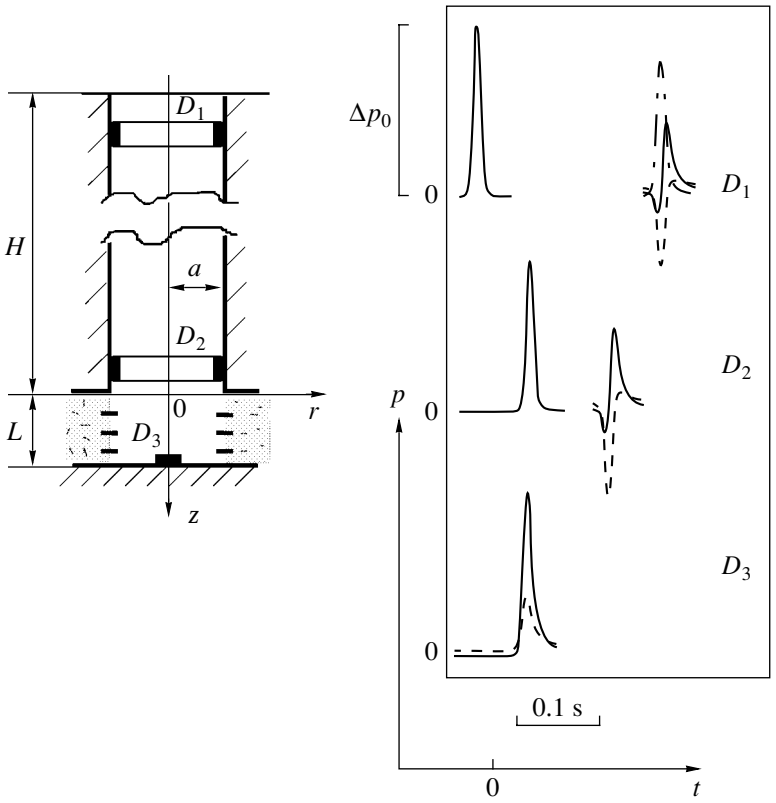

Fig. 3. Dynamics of the reflection of a pressure pulse from the bottom region of a channel surrounded with homogeneous and fractured porous media.

$$p^{(T)} = \frac{1}{\pi}\int_{0}^{\infty}\int_{-\infty}^{\infty} p^{(I)}(0, t')M(\omega)\exp[i\omega(t-t')]d\omega dt'.$$

As the primary wave signal, we take a bell-shaped pressure pulse with the amplitude Δp_0:

$$\tilde{p}^{(I)}(t) = \Delta p_0 \exp\left(-\left(\frac{t-t_0}{t_*/2}\right)^2\right).$$

Here, t_* determines the characteristic time length of the pulse.

Figure 3 shows the calculated oscillograms illustrating the evolution of a wave signal generated at a distance from the permeable region when the latter is close to the well bottom. Oscillograms 1, 2, and 3 correspond to the readings of the sensors D_1, D_2, and D_3 located at the distance H from the reflecting surface, near this surface, and at the bottom, respectively. The primary signal is a bell-shaped of pressure pulse of unit amplitude. The time length of the primary pulse is $t_* = 0.04$ s. As before, the cylindrical channel ($a = 5 \times 10^{-2}$ m) is assumed to be surrounded by a homogeneous porous medium ($m^{(1)} = 0.2$, $k^{(1)} = 10^{-13}$ m^2), the length of the permeable region being $L = 5$ m. The first peak in the oscillogram D_1 corresponds to the primary signal sent from the distance $H = 1000$ m to the permeable region. On its way to the permeable region, this pulse becomes somewhat attenuated due to the viscosity of the fluid in the channel (the first peak in the oscillogram D_2). The second peak in the oscillogram D_2 corresponds to the signal reflected from the permeable region (the reflecting surface). Then, the signal returns to the sensor D_1 (the second peak in the oscillogram D_1). The dot-and-dash line in this oscillogram corresponds to the reflected signal when the bottom region of the borehole is impermeable ($u = 0$). From the calculated oscillograms, it follows (e.g., from comparing the curves in the oscillogram D_1) that the signal reflected from the permeable region lying near the well bottom provides some information on the permeability of the porous medium near the bottom.

Consider the wave evolution at the boundary of the permeable region in the channel surrounded by an inhomogeneous porous medium. Let the porous medium around the cylindrical channel (Fig. 1d) have n radial fractures (slot-like channels with plane-parallel walls) filled with a porous medium that is more permeable than the main porous permeable medium. This situation takes place, for example, in the case of a hydraulic break of the face zone of a pool and the subsequent filling of the resulting fractures with propanate. Assume that the half-width b of the fractures is far less than the channel radius a ($b \ll a$). Then, the continuity equation

generalizing Eq. (1) by including the fluid filtration into fractures can be written as

$$\frac{1}{C^2}\frac{dp}{dt} = \rho_0\frac{w_- - w_+}{L} - \rho_0 u\frac{2(\pi a - nb)}{\pi a^2} - \rho_0\tilde{u}\frac{2nb}{\pi a^2}. \quad (17)$$

Here, $\tilde{u}$ is the speed of filtration of the fluid (liquid or gas) from the cylindrical channel into the fracture. To find this speed for harmonic waves in the main cylindrical channel, one should simultaneously consider the acoustic problem for radial fractures. To take into account the process of filtration into radial fractures, we introduce an additional coordinate axis in the radial direction along the fracture with the origin at the surface of the channel wall ($r = a$). Describing acoustic waves in a fracture, we assume that the fracture is a channel with plane-parallel walls that is surrounded by a porous medium of infinite thickness. The latter assumption means that the radial fractures are rather widely spaced, so the interaction of the filtration flows of neighboring fractures can be ignored. Moreover, we assume that a fracture has an infinite width (its height is far less than its width $b \ll L$) and the wavelength $\lambda^{(2)}$ in the fracture is greater than the fracture height ($\lambda^{(2)} > b$).

Taking into account that the permeability of the porous medium in the fracture is higher than that of the surrounding medium, we write the linearized system of equations describing the propagation of disturbances in the fracture in the form [3]

$$m\frac{\partial\rho^{(2)}}{\partial t} + \rho_0\frac{\partial u^{(2)}}{\partial x} = -\frac{\rho_0 v}{b},$$
$$\rho_0\frac{\partial u^{(2)}}{\partial t} = -m^{(2)}\frac{\partial p^{(2)}}{\partial x} - m^{(2)}\frac{\mu}{k_c^{(2)}}u^{(2)}, \quad |x'| < b, \quad (18)$$

$$m^{(1)}\frac{\partial\rho'}{\partial t} + \rho_0\frac{\partial v'}{\partial x'} = 0, \quad v' = -\frac{k_c^{(1)}}{\mu}\frac{\partial p'}{\partial x'}, \quad |x'| > b, \quad (19)$$

$$v' = v, \quad p' = p^{(2)}, \quad |x'| = b. \quad (20)$$

Here, x' is the value of the coordinate measured along the axis normal to the upper (lower) wall of the fracture; the subscript $i = 2$ in parentheses corresponds to the parameters inside the fracture ($|x'| < b$); p', ρ', and v' are the distributions of the pressure, density, and filtration speed in the porous medium around the fracture; $m^{(1)}$ and $k_c^{(1)}$ are the porosity and permeability, respectively, of the main porous medium around the permeable region of the borehole.

Equations (18)–(20) yield

$$\frac{1}{C^2}\frac{\partial^2 p^{(2)}}{\partial t^2} + \frac{1}{\chi^{(2)}}\frac{\partial p^{(2)}}{\partial t} = \frac{\partial^2 p^{(2)}}{\partial x^2} - \frac{\rho_0}{b}\left(\frac{\nu}{k_c^{(2)}}v + \frac{1}{m^{(2)}}\frac{\partial v}{\partial t}\right), \quad |x'| < b, \quad (21)$$

$$\frac{\partial p'}{\partial t} = \chi^{(1)}\frac{\partial^2 p'}{\partial x'^2} \quad \left(\chi^{(i)} = \frac{C^2\rho_0 k_c^{(i)}}{m^{(i)}\mu}; \quad i = 1, 2\right), \quad |x'| > b. \quad (22)$$

Equation (21), together with piezoconductivity equation (22) and with boundary conditions (20), yields the wave equation describing the dynamics of linear perturbations in fractures filled with a porous medium and surrounded with another porous medium. For an unambiguous description of the process in question, Eqs. (21) and (22) should be supplemented with the initial and boundary conditions

$$p' = 0, \quad t = t_0, \quad |x'| > b;$$
$$p' = p^{(2)}, \quad t > t_0, \quad |x'| = b. \quad (23)$$

According to the Duhamel principle, the solution to Eq. (21) under conditions (23) has the form [15]

$$p' = \int_{t_0}^{t}\frac{\partial U(x' - b, t - \tau)}{\partial t}p^{(2)}(x, \tau)d\tau. \quad (24)$$

Here, $U(x', t)$ is the solution of the similar boundary-value problem at $U(0, t) = 1$. From Eq. (19) with allowance for Eq. (24) at $|x'| = b$, we obtain

$$v' = -\frac{k_c^{(1)}}{\mu}\frac{\partial p'}{\partial x'} = -\frac{k_c^{(1)}}{\mu}\frac{\partial}{\partial x'}\int_{t_0}^{t}\frac{\partial U(x' - b, t - \tau)}{\partial t}p^{(2)}(x, \tau)d\tau$$

and

$$v = -\frac{k_c^{(1)}}{\mu}\left(\frac{\partial p'}{\partial x'}\right)_b = \frac{k_c^{(1)}}{\sqrt{\pi}\mu}\frac{\partial}{\partial t}\int_{t_0}^{t}\frac{p^{(2)}(x, \tau)}{\sqrt{\chi^{(1)}(t - \tau)}}d\tau. \quad (25)$$

Substituting Eq. (25) in Eq. (21) and taking for generality $t_0 = -\infty$, we obtain the wave equation

$$\frac{1}{C^2}\frac{\partial^2 p^{(2)}}{\partial t^2} + \frac{1}{\chi^{(2)}}\frac{\partial p^{(2)}}{\partial t} = \frac{\partial^2 p^{(2)}}{\partial x^2} - \frac{k_c^{(1)}}{b\sqrt{\pi}} \times\frac{\partial}{\partial t}\left(\frac{1}{k_c^{(2)}}\int_{-\infty}^{t}\frac{p^{(2)}(x, \tau)}{\sqrt{\chi^{(1)}(t - \tau)}}d\tau + \frac{1}{m^{(2)}v}\frac{\partial}{\partial t}\int_{-\infty}^{t}\frac{p^{(2)}(x, \tau)}{\sqrt{\chi^{(1)}(t - \tau)}}d\tau\right), \quad (26)$$

which describes the evolution of small disturbances in a fracture. The second term on the left-hand side of this equation is related to the viscous friction inside the fracture, and the second term on the right-hand side corresponds to the filtration processes in the porous medium around the fracture.

From the condition of the existence of a traveling-wave solution to Eq. (26),

$$p^{(2)} = A_p^{(2)}\exp[i(K^{(2)}(\omega)x - \omega t)],$$

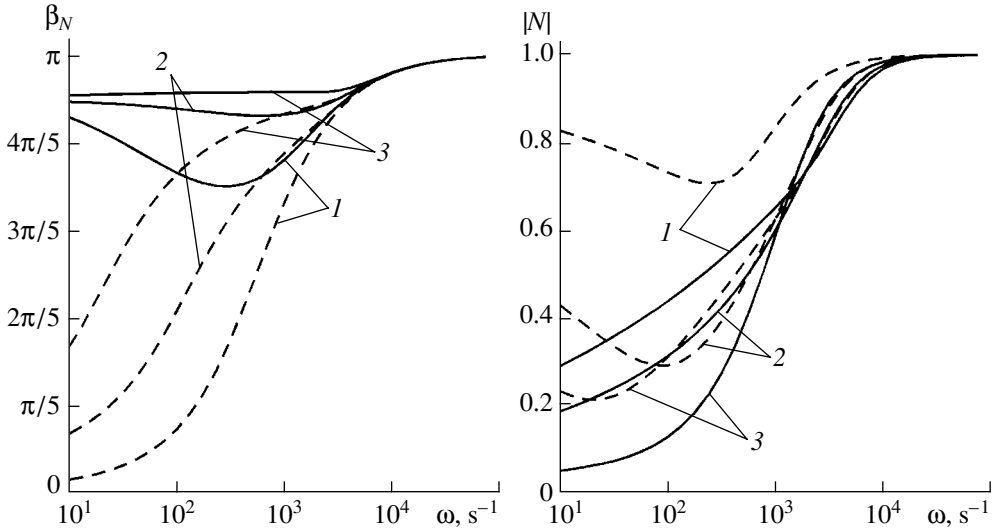

Fig. 4. Effect of fractures formed in the porous medium on the dispersion of the reflectance.

we obtain the dispersion relation

$$K^{(2)^2} = \frac{\omega^2}{C^2}\left(1 + i\frac{\omega_c^{(2)}}{\omega}\right)\left(1 + \frac{m^{(1)}}{m^{(2)}y^{(2)}}\right), \quad y^{(2)} = \sqrt{-i\frac{\omega b^2}{\chi^{(1)}}}$$

$$(\omega_c^{(2)} = C^2/\chi^{(2)}, \quad \omega_\chi^{(2)} = \chi^{(1)}/b^2),$$

where $\omega_\chi^{(2)}$ is the characteristic frequency at which the penetration depth of filtration waves is about half the height of the fracture.

Since at the fracture inlet ($x = 0$) the amplitudes of pressure and filtration speed should satisfy the conditions

$$A_p^{(2)} = A_p \text{ and } A_u^{(2)} = \tilde{A}_{\tilde{u}},$$

on the basis of the momentum equation from Eqs. (18), we can write

$$\tilde{A}_{\tilde{u}} = \frac{m^{(2)}iK^{(2)}(\omega)}{\rho_0 i\omega - m^{(2)}\mu/k_c^{(2)}}A_p. \tag{27}$$

Using the continuity equation (17) and taking into account Eqs. (11) and (27), one can obtain expressions similar to Eqs. (15) for the coefficients of reflection and transmission of harmonic disturbances with allowance made for the radial fractures in the permeable region of the channel. For the parameter D, we have

$$D = -2m^{(1)}\omega_\chi^{(1)}Ly(\ln K_0(y))'\left(1 - \frac{nb}{\pi a}\right)$$

$$+ 2Lm^{(2)}C\frac{nb}{\pi a^2}\sqrt{\frac{1 + m^{(1)}/(m^{(2)}y^{(2)})}{1 + i\omega_c^{(2)}/\omega}}.$$

Figure 4 illustrates the effect of radial fractures ($b = 2 \times 10^{-3}$ m, $m^{(2)} = 0.2$, $k_c^{(2)} = 10^{-10}$ m^2) on the values of the reflectance for the permeable region located near the well bottom ($a = 5 \times 10^{-2}$ m, $L = 2$ m, $m^{(1)} = 0.2$, $k_c^{(1)} = 10^{-13}$ m^2). Lines *1*, *2*, and *3* correspond to the number of radial fractures $n = 0$, 2, and 4, respectively.

In Fig. 3, the dashed curves show the calculated oscillograms for the following values of the system parameters: the borehole is a cylindrical channel with the radius $a = 5 \times 10^{-2}$ m; the surrounding porous medium ($k^{(1)} = 10^{-13}$ m^2, $m^{(1)} = 0.2$) has $n = 4$ radial fractures ($b = 2 \times 10^{-3}$ m, $m^{(2)} = 0.2$, $k_c^{(2)} = 10^{-10}$ m^2); and the length of the permeable region is $L = 5$ m. The primary signal is generated at the distance $H = 1000$ m from the permeable region. The length of the primary pulse is $t_* = 0.04$ s. The solid lines correspond to the absence of radial fractures ($n = 0$).

REFERENCES

1. J. E. White and H. H. Frost, J. Acoust. Soc. Am. **28**, 924 (1956).
2. V. Sh. Shagapov, N. M. Khlestkina, and D. Lhuillier, Transp. Porous Media **35** (3), 327 (1999).
3. G. A. Gumerova, Candidate's Dissertation in Physics and Mathematics (Tyumen, 1996).
4. M. A. Biot, J. Acoust. Soc. Am. **28**, 169 (1956).
5. M. A. Biot, J. Acoust. Soc. Am. **28**, 179 (1956).
6. A. G. Egorov, A. V. Kosterin, and É. V. Skvortsov, *Consolidation and Acoustic Waves in Saturated Porous Media* (Kazan. Gos. Univ., Kazan, 1990).
7. S. Sorek, A. Levy, G. Ben-dor, and D. Smeulders, Transp. Porous Media **34**, 63 (1999).
8. I. Ya. Edelman, Transp. Porous Media **34**, 117 (1999).

9. K. Tuncay and M. Y. Corapcioglu, Transp. Porous Media **23** (3), 237 (1996).
10. K. Tuncay and M. Y. Corapcioglu, Transp. Porous Media **23** (3), 259 (1996).
11. A. A. Gubaidullin and O. Yu. Kuchugurina, Transp. Porous Media **34**, 29 (1999).
12. A. A. Gubaĭdullin and O. Yu. Kuchugurina, Prikl. Mat. Mekh. **63** (5), 816 (1999).
13. A. A. Davydov and L. M. Lyamshev, Akust. Zh. **47**, 62 (2001) [Acoust. Phys. **47**, 50 (2001)].
14. G. I. Barenblatt, V. M. Entov, and V. M. Ryzhik, *Movement of Liquids and Gases in Natural Pools* (Nedra, Moscow, 1984).
15. A. N. Tikhonov and A. A. Samarskiĭ, *Mathematical Physics Equations*, 4th ed. (Nauka, Moscow, 1972; Pergamon, Oxford, 1964).

Translated by A. Kruglov

Acoustical Physics, Vol. 48, No. 3, 2002, pp. 263–267. Translated from Akusticheskiĭ Zhurnal, Vol. 48, No. 3, 2002, pp. 309–313.
Original Russian Text Copyright © 2002 by Vdovicheva, Matveev, Sazontov.

Experimental and Theoretical Study of the Vertical Coherence of the Sound Field in a Shallow Sea

N. K. Vdovicheva, A. L. Matveev, and A. G. Sazontov

Institute of Applied Physics, Russian Academy of Sciences, ul. Ul'yanova 46, Nizhni Novgorod, 603950 Russia

e-mail: sazontov@hydro.appl.sci-nnov.ru

Received December 19, 2000

Abstract—The combined effect of multiple scattering by random inhomogeneities of a waveguide and bottom-caused sound absorption is known to be a fundamental factor that governs the formation of the sound field in a shallow sea [1, 2]. A number of publications [2–6] present statistical analyses of the fluctuation phenomena that accompany the sound propagation in shallow sea regions. In these publications, most attention is paid to studying the evolution of the intensities of normal waves under the effect of scattering by the random field of internal waves. It is shown that in natural conditions, in addition to the inhomogeneities of the water column, one should take into account the irregular boundaries of the sound channel, which can also affect the correlation characteristics of the sound field. In this paper, we present experimental data on the vertical coherence of the sound field on a fixed path in the Barents Sea. We also compare the experimental data with theoretical calculations based on a model of sound scattering by the rough sea surface. © *2002 MAIK "Nauka/Interperiodica".*

The acoustic measurements were carried out in October 1990 in the Barents Sea. Two research vessels were used in the experiment, both of which were fixed to anchored buoys. From one of the vessels, a frame carrying sound projectors was deployed to a depth of about 148 m. The projectors transmitted cw signals at frequencies of 107 and 240 Hz. For signal reception, a vertical array was used that consisted of 12 elements equidistantly arranged with a step of 8.5 m. A near-bottom hydrophone was deployed at 155 m. The distance between the transmitting and receiving vessels was measured with the use of a radio range finder and equaled 13.82 km. The sea depths were about 170 and 150 m near the array and the source, respectively. The experimental layout is sketched in Fig. 1.

Figure 2 shows a typical seasonal profile of the sound speed in the sea region at hand. This profile exhibits a near isovelocity character down to a depth of about 40 m. Then, down to 60 m, a water layer follows that has a negative gradient; deeper, almost no changes are observed in $c(z)$ down to the bottom. According to the geoacoustical model proposed in [7], the sediments that occur in the studied region consist of clay silt, with a characteristic density of 1.8 g/cm^3 and a sound speed of 1.78 km/s. The attenuation coefficient for these sediments is 0.4 dB/λ.

In the data processing, 30-min samples of the signal were used. The processing procedure consisted in filtering in the 0.5-Hz frequency band, quadratic demodulation, and spectral and correlation analysis.

Let $x_k(t_l)$ be the complex amplitude of the signal received by the kth array element at the time point t_l. In Figs. 3a and 3b, the 30-min fragments of the records are shown (in relative units) for the signal amplitudes $|x_k(t)|$ at four depths of the receiving hydrophones. The signal frequencies are f_0 = 107 and 240 Hz in Figs. 3a and 3b, respectively.

Figure 4 shows a typical power spectrum $S_k(f)$ of the fluctuations, which was obtained with the carrier frequency f_0 = 240 Hz, at a fixed depth of 138 m. The frequency spectrum consists of a central peak (at the carrier frequency), which corresponds to the coherent component of the received signal, and two side peaks corresponding to the scattered component. (The spectral density is expressed in decibels relative to the level of the coherent component.) Note that the shape of the frequency spectrum is typical of a shallow-water experiment in which the sound scattering by the rough surface is significant.

The spatial correlation of the sound field is fully determined by the complex coefficient of cross-correla-

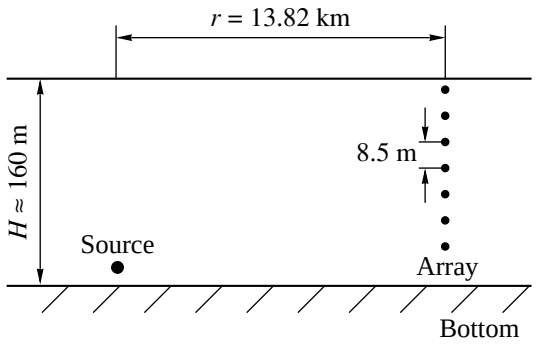

Fig. 1. Layout of the experiment.

1063-7710/02/4803-0263$22.00 © 2002 MAIK "Nauka/Interperiodica"

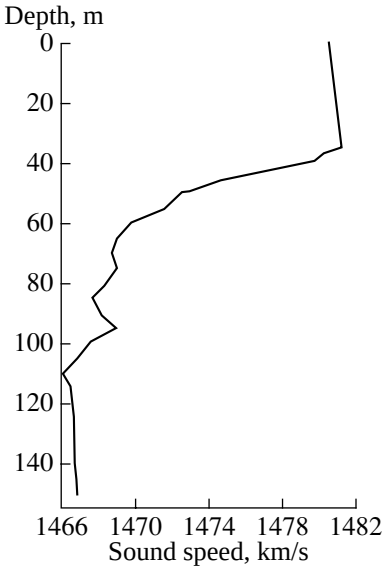

Fig. 2. Sound speed profile at the experimental site.

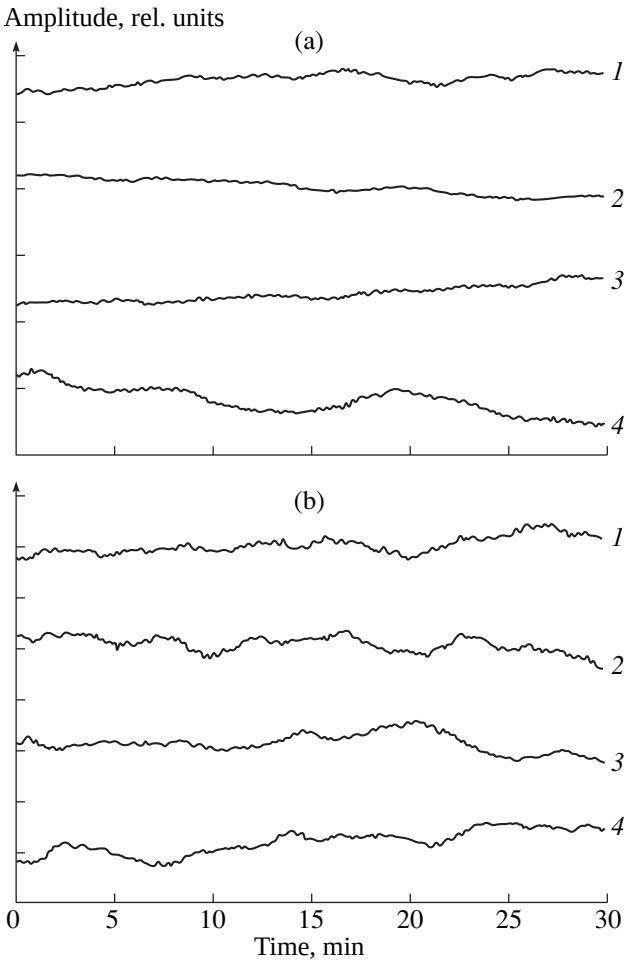

Fig. 3. Time dependences of the amplitudes of the received signals with the carrier frequencies f_0 = (a) 107 and (b) 240 Hz for different depths of reception: z = (*1*) 61.5; (*2*) 87; (*3*) 138; and (*4*) 155 m.

tion for the signals at the outputs of the kth and jth hydrophones:

$$C_{kj} = \frac{\sum_{l=1}^{L} x_k(t_l)x_j^*(t_l)}{\sqrt{\sum_{l=1}^{L}|x_k(t_l)|^2\sum_{l=1}^{L}|x_j(t_l)|^2}} \quad (1)$$

where $L = 2056$. The absolute values of correlation coefficient (1) are summarized in the table. According to these values, the vertical coherence of the sound field depends on the carrier frequency: the coherence decreases as f_0 increases.

To interpret the experimental data, we used the following statistical model. Let us consider a channel of depth H in which the acoustic refractive index $n(z)$ is a function of depth z:

$$n(z) = \begin{cases} n_0(z), & 0 \le z \le H \\ n_\infty[1 + i\alpha], & z > H. \end{cases}$$

The parameter α characterizes the absorption properties of the sediments and is related to the sound attenuation coefficient β (measured in decibels per wavelength) in the bottom as follows: $\beta[\text{dB}/\lambda] = \frac{40\pi}{\ln 10}\alpha$. We assume that the main phenomenon that causes the sound fluctuations is represented by the wind waves on the sea surface, which are described by the Pierson–Moskowitz isotropic spectral distribution [8]:

$$F_\eta(\kappa, \Omega) = \frac{8.1\times 10^{-3}}{4\pi}\kappa^{-4} \times \exp\left(-0.74\frac{g^2}{\kappa^2 v^4}\right)\delta(\Omega - \sqrt{g\kappa}), \quad (2)$$

where g is the acceleration of gravity and v is the wind speed.

Far from the source, the sound pressure $P(\mathbf{r}, z, t)$ (where $\mathbf{r}$ is the horizontal radius-vector, z is the vertical coordinate, and t is time) can be formally expressed as a superposition of a finite number M of propagating modes:

$$P(\mathbf{r}, z, t) = \sum_{n=1}^{M}\frac{1}{\sqrt{\kappa_n}}p_n(\mathbf{r}, t)\varphi_n(z). \quad (3)$$

Here, $\varphi_n(z)$ and κ_n^2 are the eigenfunctions and eigenvalues of the regular waveguide, respectively, which are the solutions to the following boundary problem:

$$\frac{d^2}{dz^2}\varphi_n(z) + [k^2 n_0^2(z) - \kappa_n^2]\varphi_n(z) = 0, \quad n = 1, 2, \ldots, M,$$

$$\varphi_n(0) = 0, \quad \varphi_n(z) + Q_n\frac{\varphi_n(z)}{dz}\bigg|_{z=H} = 0, \quad (4)$$

$$\rho_w\int_0^\infty dz\frac{1}{\rho(z)}\varphi_n(z)\varphi_m(z) = \delta_{nm}.$$

Matrix of the correlation coefficients $|C_{kj}|$

f_0 = 107 Hz								
Depth (m)	155	146.5	138	129.5	87	70	61.5	44.5
155	1.000							
146.5	0.892	1.000						
138	0.877	0.958	1.000					
129.5	0.831	0.896	0.956	1.000				
87	0.906	0.893	0.966	0.933	1.000			
70	0.898	0.934	0.981	0.934	0.986	1.000		
61.5	0.852	0.915	0.974	0.934	0.980	0.985	1.000	
44.5	0.883	0.877	0.946	0.909	0.984	0.975	0.982	1.000

f_0 = 240 Hz							
Depth (m)	155	146.5	138	129.5	70	61.5	44.5
155	1.000						
146.5	0.934	1.000					
138	0.918	0.914	1.000				
129.5	0.758	0.728	0.831	1.000			
70	0.783	0.838	0.861	0.661	1.000		
61.5	0.545	0.438	0.486	0.202	0.535	1.000	
44.5	0.687	0.821	0.646	0.434	0.730	0.830	1.000

In these expressions, k is the reference wave number; Q_n is the complex impedance of the absorbing liquid bottom, which is expressed as

$$Q_n = \frac{\rho_b}{\rho_w}\frac{1}{\sqrt{\kappa_n^2 - k^2 n_\infty^2}};$$

and $\rho(z)$ is the density of the medium, which, in our case, is a step function of the following form:

$$\rho(z) = \begin{cases} \rho_w, & 0 \le z \le H \\ \rho_b, & z > H. \end{cases}$$

The expansion coefficients $p_n(\mathbf{r}, t)$ are random functions of the coordinates and time because of the sound scattering by the wavy surface.

We are interested in the behavior of the coherence function of the sound field with varying vertical separation of the observation points:

$$\Gamma(\mathbf{r}, z_1, z_2) = \langle P(\mathbf{r}, z_1, t)P^*(\mathbf{r}, z_2, t)\rangle. \quad (5)$$

Here, the angular brackets denote averaging over the statistical ensemble. By substituting Eq. (3) into Eq. (5), we obtain

$$\Gamma(\mathbf{r}, z_1, z_2) = \sum_{n,m}\frac{1}{\sqrt{\kappa_n\kappa_m}}\Gamma_{nm}(\mathbf{r})\varphi_n(z_1)\varphi_m(z_2), \quad (6)$$
$$\Gamma_{nm}(\mathbf{r}) = \langle p_n(\mathbf{r})p_m^*(\mathbf{r})\rangle.$$

To calculate the quantities $\Gamma_{nm}(\mathbf{r})$ in the multimode waveguide with a randomly rough surface, we use the results obtained in [9–11]:

$$\Gamma_{nm}(\mathbf{r}) = \langle p_n(\mathbf{r})\rangle\langle p_m^*(\mathbf{r})\rangle + [\Gamma_{nn}(\mathbf{r}) - \langle p_n(\mathbf{r})\rangle\langle p_n^*(\mathbf{r})\rangle]\delta_{nm}. \quad (7)$$

Here, $\langle p_n(\mathbf{r})\rangle$ is the coherent component of the nth mode excited by a point source located at the depth z_0:

$$\langle p_n(\mathbf{r})\rangle = \frac{-i\varphi_n(z_0)}{\sqrt{8\pi r}}\exp\left[\left(i\kappa_n - \frac{1}{2}\sigma_n\right)r - i\frac{\pi}{4}\right], \quad (8)$$

where σ_n is the extinction coefficient and $\Gamma_{nn}(\mathbf{r})$ is the autocorrelation function. For a medium that is statisti-

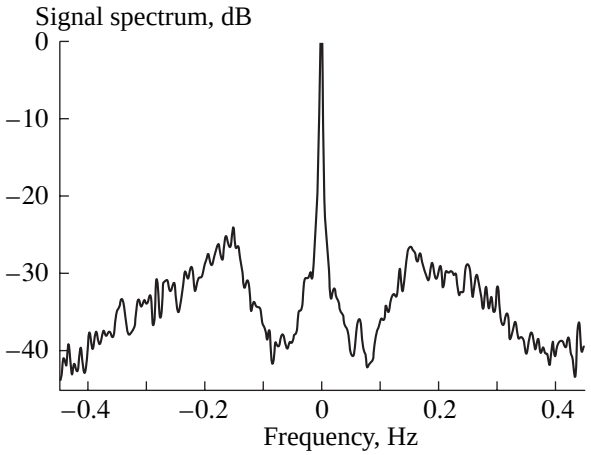

Fig. 4. Spectrum of the cw signal with carrier frequency f_0 = 240 Hz at a distance of 13.82 km.

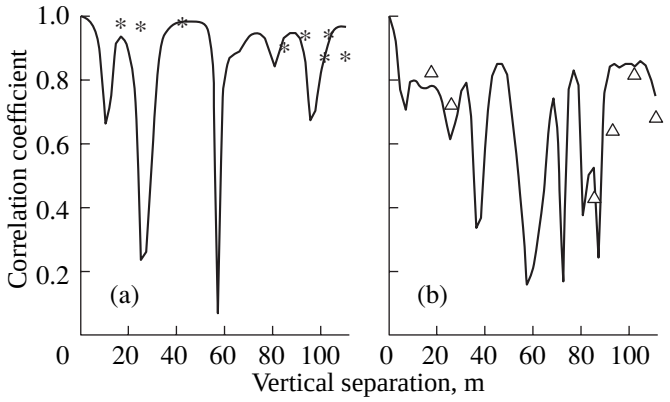

Fig. 5. Computed and experimental spatial correlation functions for the sound field in the Barents Sea: f_0 = (a) 107 and (b) 240 Hz.

cally isotropic in the horizontal plane, the quantity $\Gamma_{nn}(\mathbf{r})$ obeys the equation

$$\left(\frac{d}{dr} + \frac{1}{r} + \sigma_n^a\right)\Gamma_{nn}(r) = \sum_m a_{nm}[\Gamma_{mm}(r) - \Gamma_{nn}(r)] + \varphi_n^2(z_0)\frac{\delta(r)}{8\pi r}, \quad (9)$$

where

$$a_{nm} = \frac{\pi}{2}\frac{[\varphi_n'(0)\varphi_m'(0)]^2}{\kappa_n\kappa_m}\int_{-\infty}^{\infty}\int d\Omega d\varkappa_y F_\eta(\kappa_n - \kappa_m, \varkappa_y, \Omega),$$

and the prime denotes the differentiation with respect to depth z. Equation (9) is the well-known transfer equation for mode intensities, which describes the transformation of cylindrical normal waves as a result of scattering (see, e.g, [12, 13]). On the left-hand side of this equation, an additional term σ_n^a is introduced to take into account the sound absorption in the bottom. For the bottom model in use (see, e.g., [2]), this quantity is expressed as follows:

$$\sigma_n^a = \frac{\rho_w}{\rho_b}\frac{k^2 n_\infty^2 |\varphi_n(H)|^2}{2\kappa_n\sqrt{\kappa_n^2 - k^2 n_\infty^2}}\alpha.$$

Note that, for the Pierson–Moskowitz spectrum (2), the coupling matrix a_{nm} is calculated in [13], and it has the form

$$a_{nm} = \frac{8.1\times 10^{-3}\sqrt{2}\pi[\varphi_n'(0)\varphi_m'(0)]^2}{8\kappa_n\kappa_m k_0^3} f(x_{nm}).$$

Here, $k_0^2 = 0.74g^2/v^4$, $x_{nm} = 0.5k_0^2/(\kappa_n - \kappa_m)^2$, and $f(x) = x^{3/2}e^{-x}[I_0(x) - I_1(x)]$, where I_0 and I_1 are the modified Bessel functions of the zero and first orders, respectively.

One can easily verify that the solution to Eq. (9) can be written in the form

$$\Gamma_{nn}(r) = \frac{1}{4}\sum_{m=1}^{M} g_{nm}(r)\varphi_m^2(z_0),$$
$$g_{nm}(r) = \frac{1}{2\pi r}\sum_{l=1}^{M}\Psi_n^{(l)}\exp(-\lambda_l r)\Psi_m^{(l)}, \quad (10)$$

where $\Psi_n^{(l)}$ and λ_l are the eigenfunctions and eigenvalues of the matrix $h_{nm} = \delta_{nm}(\sigma_n^a + \sum_{m=1}^{M} a_{nm}) - a_{nm}$.

Note that the quantity σ_n appearing in Eq. (8) is the resulting coefficient of mode decay: $\sigma_n = \sigma_n^a + \sigma_n^s$, which is governed by both the scattering ($\sigma_n^s = \sum_{m=1}^{M} a_{nm}$) and absorption.

We used formulas (6)–(8) in combination with Eqs. (10) as a basis for a computer simulation program.

For the sound speed profile shown in Fig. 2 and the experimental layout at hand, Fig. 5 shows the computed correlation coefficients along the aperture of the vertical receiving array (the solid curves). The experimental points are also plotted in Fig. 5. The origin of the abscissa axis corresponds to the depth of the near-surface hydrophone (44.5 m). In the computations, the wind speed was specified as 10 m/s. The results of the computer simulation qualitatively agree with the experimental data.

ACKNOWLEDGMENTS

This work was supported by the Russian Foundation for Basic Research, project nos. 99-02-16401 and 00-15-96-741.

REFERENCES

1. *Bottom-Interacting Ocean Acoustics*, Ed. by W. Kuperman and F. Jensen (Plenum, New York, 1981; Mir, Moscow, 1984).
2. B. G. Katsnel'son and V. G. Petnikov, *Acoustics of a Shallow Sea* (Nauka, Moscow, 1997).
3. D. B. Creamer and B. J. Orchard, J. Acoust. Soc. Am. **95**, 2927 (1994).
4. D. B. Creamer, J. Acoust. Soc. Am. **99**, 2825 (1996).
5. D. Tielbürger, S. Finette, and S. Wolf, J. Acoust. Soc. Am. **101**, 789 (1997).
6. S. Finette, M. H. Orr, A. Turgut, *et al.*, J. Acoust. Soc. Am. **108**, 957 (2000).
7. B. G. Katsnel'son, L. G. Kulapin, A. A. Migulin, and V. G. Petnikov, Akust. Zh. **38**, 308 (1992) [Sov. Phys. Acoust. **38**, 164 (1992)].

8. W. J. Pierson and L. Moskowitz, J. Geophys. Res. **69** (24), 5181 (1964).
9. V. M. Kudryashov, in *Mathematical Problems of Geophysics* (Novosibirsk, 1973), Issue 4, pp. 256–272.
10. A. G. Nechaev, Akust. Zh. **33**, 535 (1987) [Sov. Phys. Acoust. **33**, 312 (1987)].
11. E. Yu. Gorodetskaya, A. I. Malekhanov, A. G. Sazontov, and N. K. Vdovicheva, in *Formation of Acoustic Fields in Oceanic Waveguides: Reconstruction of Inhomogeneities in Shallow Water*, Ed. by V. A. Zverev (Inst. of Applied Physics, Russ. Acad. Sci., Nizhni Novgorod, 1998), pp. 5–56.
12. F. G. Bass and I. M. Fuks, *Wave Scattering from Statistically Rough Surfaces* (Nauka, Moscow, 1972; Pergamon, Oxford, 1978).
13. A. Beilis and F. D. Tappert, J. Acoust. Soc. Am. **66**, 811 (1979).

Translated by E. Kopyl

Acoustical Physics, Vol. 48, No. 3, 2002, pp. 268–272. Translated from Akusticheskiĭ Zhurnal, Vol. 48, No. 3, 2002, pp. 314–318.
Original Russian Text Copyright © 2002 by Galechyan, Mkrtchyan.

Acoustic Wave Amplification in a Plasma of a Molecular Gaseous Discharge

G. A. Galechyan and A. R. Mkrtchyan

Institute of Applied Problems of Physics, National Academy of Sciences of Armenia, ul. Nersesyana 25, Yerevan, 375014 Armenia

e-mail: malpic@iapp.sci.am

Received March 6, 2001

Abstract—From the experimental investigation of sound propagation in a gaseous discharge, it is established that, in a stationary diffusive discharge in nitrogen, sound amplification takes place according to the linear theory, whereas a sharp transverse constriction of the discharge leads to a sharp, jump-like increase in the amplification factor because of the steep dependence of the relaxation constant of a vibrationally excited molecule on the gas temperature. This result agrees well with the nonlinear theory of sound amplification in a nonequilibrium molecular gas. It is shown that the introduction of oxygen in the nitrogen discharge leads to an increase in the sound amplification factor in the plasma, because the constant of the vibrational relaxation of an excited nitrogen molecule by oxygen is two orders of magnitude greater than the constant of relaxation of nitrogen by nitrogen. © *2002 MAIK "Nauka/Interperiodica".*

The mechanisms of sound amplification in a nonequilibrium plasma of inert gases are considered in [1–4]. The results of experimental investigations of this phenomenon are presented in [5, 6]. Theoretical studies of the possibilities of sound amplification in a plasma of a molecular gas with a high vibrational energy content are described in [7–11], where various mechanisms of sound amplification in a vibrational nonequilibrium medium are discussed.

In papers [7–9], the process of a linear amplification of sound in a nonequilibrium molecular gas is considered, and the relation between the amplification factor of low-intensity sound and the constant characterizing the relaxation rate of vibrationally excited molecules is established. This theory describes the initial stage of the development of sound in an amplifying vibrationally nonequilibrium gas. However, it does not take into account the nonlinear nature of the sound propagation that includes the processes of the mutual influence of sound and the amplifying medium. The effects of the mutual influence of sound and gas determine the behavior of a sound wave at high levels of amplification. The nonlinear theory of sound amplification in a vibrationally nonequilibrium gas is analyzed in paper [10]. We note that publications devoted to the experimental results of sound amplification in a molecular gas plasma are limited. We should mention the study [11] of the processes of sound amplification in discharges in nitrogen, air, and nitrogen-argon mixtures at low pressures.

In this paper, we describe the results of the measurements of the sound amplification factor in a discharge in nitrogen and nitrogen-oxygen mixtures in a diffusion discharge in the case of an abrupt constriction of the positive column and in discharges pinched and depinched by sound at a pressure of 78 torr. The investigations were performed at this pressure because a jump-like constriction of the discharge in nitrogen was observed at the pressure $P \geq 78$ torr.

The investigations were carried out by using the experimental setup shown in Fig. 1, which consisted of a quartz discharge tube whose inner diameter was 9.8 cm and length, 52 cm. The distance between the two grid electrodes was 27 cm. The sound in the discharge tube was produced by an electrodynamic source attached to one of the tube ends. For monitoring the sound parameters, a microphone was mounted at the opposite end of the tube, behind the anode. The flange to which the microphone was attached had a cavity whose diameter exceeded the inner diameter of the tube. An acoustic resonator of such design is similar to a cylindrical resonator with one open end. Theoretical calculations show [12] that the frequencies of this resonator can be computed by the formula

$$f = \frac{ck}{4(L + 0.8R)},$$

where c is the sound velocity; $k = 1, 3, 5, \ldots$; L is the length of the tube; and R is the tube radius. At resonance, an odd number of quarters of wavelength fits within the length $L + 0.8R$. Precisely these resonance frequencies were observed in the experiment in the mode of a standing sound wave.

The sound frequency was varied by a low-frequency generator of sinusoidal signals, and the amplitude was varied by an amplifier. The signal was passed from the microphone to an oscilloscope. The calibration was

1063-7710/02/4803-0268$22.00 © 2002 MAIK "Nauka/Interperiodica"

performed in real time by using a spectrum analyzer. The measurements were made with currents from 40 to 120 mA at the first resonant sound frequency f_1 = 170 Hz. The nitrogen used in the experiment contained up to 0.07% water vapor and no more than 0.4% oxygen.

The current–voltage characteristics of the discharge in the field of a sound wave at the nitrogen pressure P = 78 torr and in the range of currents from 40 to 120 mA are presented in [13]. From these data, it follows that, in a diffusive discharge, as the current grows above I_{d0} = 40 mA, the discharge voltage decreases, and at a current I_{d1}, an abrupt constriction of the plasma column is observed.

In a discharge in nitrogen in the absence of sound at P = 78 torr, the transition from a diffusive to a pinched state occurs at the current I_{d1} = 70 mA. The generation of sound results in a shift of I_{d1} toward greater currents. At the constriction of the discharge, a jump-like decrease in the column diameter takes place along with a decrease in the voltage across the electrodes by ~1 kV and an increase in the current up to I_{d2}. The measurements were made at fixed values of the sound amplitude J_0 (at the current I_{d0} = 40 mA). The value of the sound intensity J_0, depending on the amplitude, was set in the interval from 66 to 88 dB. The sound intensity was not maintained constant in the course of the current variation from 40 to 120 mA.

Figure 2 shows the sound amplification factor as a function of the discharge current at P = 78 torr and the sound frequency f_1 = 170 Hz. In the range of currents from I_{d0} = 40 mA to I_{d1} = 73 mA and at the sound intensity J_0 = 68 dB (curve *a*), a diffusive discharge was sustained in the tube. The growth of the current was accompanied by a smooth increase in the amplification factor, and at the current I_{d1}, this factor was equal to K_{i1} = 2.2 m^{-1}, its value being defined as $K_{i01} = (\ln A_1/A_0)/L$, where A_0 is the sound amplitude at the current I_{d0} = 40 mA, A_1 is the sound amplitude at I_{d1} = 73 mA, and L is the length of the plasma column. The constriction of the discharge is accompanied by a jump-like increase in the sound amplification factor up to K_{i2} = 5.2 m^{-1}. The value of the current at the end of the process of constriction is I_{d2} = 77 mA. At the constriction of discharge, the visible boundary of the column decreases from 5 to 0.5 cm (transforming into a brightly glowing pinch). The increase in the current in a pinched discharge from I_{d2} to I_{d3} = 120 mA leads to an increase in the sound amplitude and amplification factor up to K_{i3} = 5.9 m^{-1}.

The investigations show that at the constriction of discharge in the range of intensities J_0 from 66 to 72 dB, the increase in J_0 is accompanied by a jump-like growth of the amplification factor. At J_0 = 72 dB, the greatest increase in the sound amplification factor is observed, which can be seen from curve *b* in Fig. 2. In the process of constriction, the sound amplitude grows so fast (as the current increases from I_{d1} = 76 mA to I_{d2} = 80 mA) that the amplification factor becomes equal to K_{i2} = 6.6 m^{-1}. The growth of current in a pinched discharge from I_{d2} = 80 mA to I_{d3} = 120 mA is accompanied by a smooth growth of sound amplification, which reaches K_{i3} = 7.2 m^{-1}.

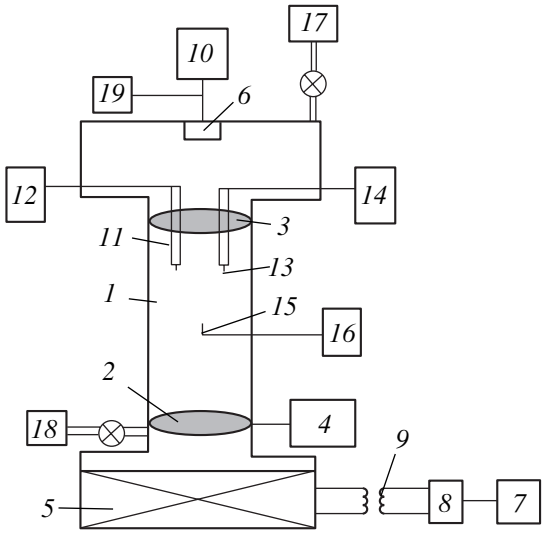

Fig. 1. Schematic view of the experimental setup: (*1*) the discharge tube, (*2*, *3*) grid electrodes, (*4*) a high-voltage source of direct current, (*5*) an electrodynamic source of acoustic vibrations, (*6*) a microphone, (*7*) a low-frequency generator of sinusoidal signals, (*8*) an amplifier, (*9*) an isolation transformer, (*10*) an oscilloscope, (*11*) electric probes for measuring the strength of the longitudinal electric field, (*12*) a device for measuring the electric field, (*13*) a single electric probe, (*14*) a power source for the electric probe, (*15*) a thermocouple, (*16*) the thermocouple measuring circuit, (*17*) the system for feeding gas into the discharge tube, (*18*) a vacuum pump, and (*19*) an acoustic vibration analyzer.

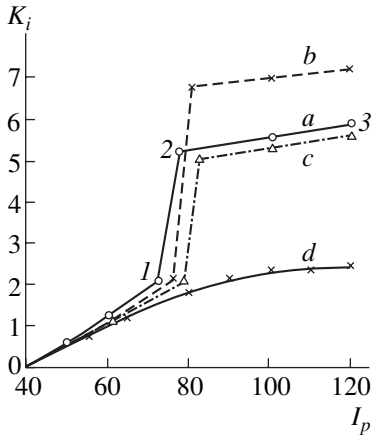

Fig. 2. Dependences of the amplification factor of the sound wave on the current in the discharge in nitrogen at a pressure of 78 torr, at the first resonance frequency f_1 = 170 Hz in a tube with inner diameter 9.8 cm. The sound intensity is J_0 = (*a*) 66 (with the current I_{d0} = 40 mA), (*b*) 72, (*c*) 76, and (*d*) 88 dB (a depinched discharge).

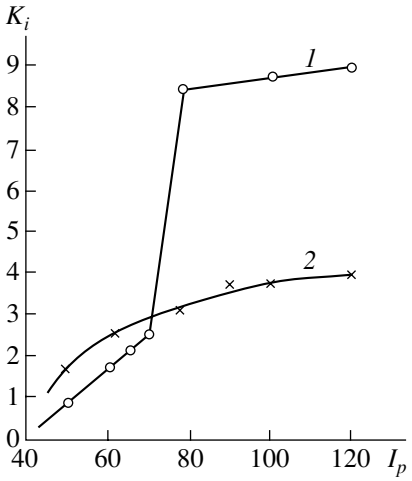

Fig. 3. Dependences of the amplification factor of the sound wave on the current in the discharge in a mixture of nitrogen and oxygen (10%) at a pressure of 78 torr. The sound intensity is J_0 = (*1*) 72 and (*2*) 88 dB.

At $J_0 > 72$ dB, the increase in the intensity is accompanied by the reduction of the effect of the jump-like growth of the sound amplitude. This is seen from curve *c* in Fig. 2 for J_0 = 76 dB. Under these conditions, the beginning of the constriction occurs at the current I_{d1} = 78 mA, and it ends at I_{d2} = 82 mA. The jump of the amplification factor leads to the value of K_{i2} = 5.0 m^{-1} at the end of the process of constriction. The amplification factor in a pinched discharge at the current I_{d1} = 120 mA is equal to K_{i3} = 5.6 m^{-1}. The increase in the sound intensity in a pinched discharge up to J_0 = 88 dB (curve *d* in Fig. 2) is accompanied by the depinching of the plasma column under the action of the vortex acoustic streaming arising in the tube [14]. The diameter of the visible boundary of the column increases by about a factor of 10. The sound amplification factor in this discharge increases with the current growth from I_{d0} = 40 mA, and at I_{d3} = 120 mA it becomes equal to K_{i3} = 2.5 m^{-1}.

Below, we consider the influence of the introduction of O_2 in the discharge in N_2 on the sound amplification factor in the plasma. The appearance of O_2 in the discharge in N_2 led to a shift of the resonance frequency (f_1 = 170 Hz) downward. For a 10% content of O_2 in the mixture, f_1 = 167 Hz; for a 20% content, f_1 = 165 Hz; and for a 40% content, f_1 = 162 Hz. The current–voltage characteristic of the discharge in the mixture N_2 + 10%O_2 is given in [13]. From this characteristic, one can see that a jump-like constriction of the column occurs at the current I_{d2} = 69 mA (at an intensity of 72 dB).

Figure 3 shows the dependences of the sound amplification factor on the current in a discharge in the mixture N_2 + 10%O_2. From curve *1* in Fig. 3, it is seen that, with an increase in the current in a diffusive discharge from I_{d0} = 40 mA to I_{d1} = 69 mA (just before the constriction), the sound amplification factor smoothly grows up to K_{i1} = 2.56 m^{-1}. In the process of constriction, when the current jumps to I_{d2} = 76 mA, the amplification factor increases to K_{i2} = 8.4 m^{-1}. A further increase in the current in a pinched discharge leads to the growth of the amplification factor, which becomes equal to K_{i3} = 9 m^{-1} when the current equals 120 mA.

At the sound intensity J_0 = 88 dB, the depinching of the discharge by a vortex motion occurs. As is seen from curve *2* of Fig. 3, in a depinched discharge, the increase in the current above 40 mA results in the growth of the sound amplification factor, and at I_{d3} = 120 mA, it equals to K_{i3} = 4 m^{-1}.

From the results presented above, it follows that, with the growth of the percentage of O_2 in the N_2 + O_2 mixtures, the jump of the sound amplification factor accompanying the constriction of the discharge becomes more conspicuous. Figure 4 shows the dependence of the jump of the sound amplification factor in the plasma at the constriction of the discharge on the percentage of O_2 in the N_2 + O_2 mixtures. One can see that, for the N_2 + 40%O_2 mixture, the jump of the amplification factor due to the constriction equals K_{i2} = 8 m^{-1}.

We now turn to the analysis of the experimental results obtained for the sound amplification in a plasma of molecular gases. The physical mechanism of sound amplification in a vibrationally nonequilibrium gas is as follows. The energy transfer between the internal and translational degrees of freedom occurs in different ways for different parts of the sound wave. The energy transfer to translational degrees of freedom in the half-period of sound that corresponds to the increase in temperature may exceed the inverse process in the half-period where the temperature is lower than the equilibrium one (the main factor affecting the rate of the energy transfer is the temperature, and when it increases, the energy transfer is enhanced) [9].

In a diffusive discharge, with an increase in the current from I_{d0} = 40 mA to I_{d1} (just before the constriction), the amplification factor grows. This result is connected with the fact that the increase in the current leads to an increase in the electron concentration, the gas temperature at the discharge axis, and the frequency of vibrational relaxation τ_{VT}. The phenomenon observed is consistent with the linear theory of the sound wave amplification in a diffusive glow discharge [7–9].

To consider the jump of the sound amplification factor at the discharge pinching, we list the conditions at which the constriction occurs. An increase in the current of the discharge is accompanied by an increase in the gas temperature. As a consequence, the relation between the deactivation of vibrationally excited molecules in the volume and at the wall changes in favor of the volume processes [15]. The transition from wall to volume deactivation may have the character of instability of a heat explosion type. The development of this instability takes place when the time of vibrational

relaxation of molecules is commensurable with the time of heat transfer to the tube wall. If this condition is satisfied, the vibrational relaxation accompanied by an intense heat release proceeds in an avalanche way, which results in the transition of the discharge to a pinched state in which practically all vibrationally excited molecules generated in the discharge are deactivated in the volume. Thus, a considerable part of the energy introduced in the discharge is transformed to heat [15].

The propagation of sound along the plasma column leads to the modulation of the temperature and density of gas in the discharge, which causes a modulation of the heat release due to the vibrational relaxation. This effect, in turn, leads to an increase in the initial modulation depth for the temperature and the density of gas and to a growth of the sound intensity. If, at the jumplike constriction of discharge and the growth of the temperature at the column axis, the relaxation time τ_{VT} is smaller than the period of the sound wave τ_S, the intensity of heat release will be modulated by the sound, which will result in the growth of the initial modulation depth for the temperature and density of gas and, hence, in the jump of the sound amplitude.

The measurement of the gas temperature at the axis of the diffusive column by a thermocouple showed that it did not exceed 860 K. The constriction of the discharge at a constant pressure leads to the existence of a constant temperature of 935 K at the column axis. In pure nitrogen, the vibrational relaxation constant at a temperature of 900 K is $k_{VT} = 10^{-16}$ cm^3/s [16], and the relaxation time is $\tau_{VT} = (k_{VT}N)^{-1} \cong 1.1 \times 10^{-2}$ s. Then, the period of acoustic vibrations is $\tau_S = 6 \times 10^{-3}$ s, and, consequently, $\tau_{VT} > \tau_S$. Since the nitrogen used in the experiment contains 0.07% water vapor, the actual situation is different. At a temperature of 900 K, the constant of vibrational relaxation of nitrogen molecules by molecules of water is $k_{VT} = 10^{-13}$ cm^3 [17]. The mean relaxation time of vibrationally excited molecules in the mixture of nitrogen with 0.07% water vapor at a pressure of 78 torr is $\tau \cong 5 \times 10^{-3}$ s, which means that $\tau_{VT} < \tau_S$. Since the mixture of nitrogen and water vapor contained also 0.4% of oxygen, the relaxation time τ_{VT} is still smaller [18]. Hence, under these experimental conditions, an intensive vibrational relaxation takes place, which results in an increase in the gas temperature in the plasma. Owing to the steep character of the dependence of the vibrational relaxation constant on temperature $k_{VT}(T)$, this effect leads to a further increase in the gas temperature, and so on. In this way, the process of nonlinear amplification of sound in a plasma proceeds according to the theory of this phenomenon considered in [10]. The growth of the sound intensity in a discharge in nitrogen above $J_0 > 75$ dB is accompanied by a decrease in the magnitude of jump of the amplification factor. This is connected with the formation of an acoustic streaming in the discharge [19] with an accompanying vortex motion and increase in heat removal. When the sound intensity is $J_0 \geq 88$ dB, the depinching of the discharge is observed, the visible boundary of the column increases more than tenfold, and the gas temperature at the discharge axis is considerably reduced. The measurements show that the gas temperature at the tube axis at a sound intensity of 85 dB drops by more than 100°. The decrease in the gas temperature in the plasma decelerates the processes of vibrational relaxation. The very process of constriction is eliminated along with the jump in the sound amplitude. Nevertheless, when an intense sound wave propagates along the discharge in which an intensive mixing of plasma takes place, the sound is amplified.

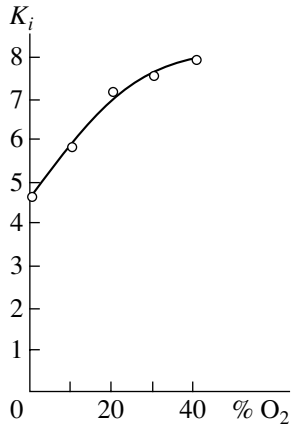

Fig. 4. Dependence of the amplification factor of the sound wave in the process of constriction of the discharge on the percentage of oxygen in its mixtures with nitrogen at the pressure in the tube P = 78 torr. The sound intensity is J_0 = 72 dB.

Now, we consider the effect of oxygen on the sound amplification factor in the discharge in nitrogen. When comparing the sound amplification factor in the discharge in nitrogen with the discharge in the N_2 + 10%O_2 mixture, we can see that, for the mixture, the sound amplification factor just before the constriction is $K_{i01} = 2.56$ m^{-1} (Fig. 3), whereas for pure nitrogen, it is $K_{i01} = 2.2$ m^{-1} (Fig. 2). Figure 4 demonstrates the dependence of the sound amplification factor in the process of constriction of the discharge on the percentage of O_2 in mixtures with N_2. One can see that, for the 40% content of O_2, the jump of the amplification factor is 8 m^{-1}, while for pure N_2, it is about 4.75 m^{-1}. This result is explained by the fact that the constant of vibrational relaxation of nitrogen by oxygen is two orders of magnitude greater than the constant of relaxation of nitrogen by nitrogen [18]. In a depinched discharge in the N_2 + 10%O_2 mixture, the amplification factor corresponding to the current of 120 mA is $K_i = 4$ m^{-1}, while for the same conditions in nitrogen, it is equal to 2.56 m^{-1}.

Thus, when a sound wave propagates along a discharge of a molecular gas, a smooth increase in the amplification factor with current is observed according to the linear theory [7–9], whereas, at the constriction

of the discharge, a sharp increase in the amplification factor takes place (a nonlinear amplification [10]).

The value of the sound amplification factor in a diffusive discharge of molecular gas (depending on its nature) is several times greater than its value for an atomic gas under similar conditions [5, 6].

REFERENCES

1. L. D. Tsendin, Zh. Tekh. Fiz. **35**, 1972 (1965) [Sov. Phys. Tech. Phys. **10**, 1514 (1965)].
2. U. Ingard, Phys. Rev. **145** (1), 41 (1966).
3. I. P. Zavershinskiĭ, E. Ya. Kogan, and N. E. Molevich, Akust. Zh. **38**, 702 (1992) [Sov. Phys. Acoust. **38**, 387 (1992)].
4. A. R. Mkrtchyan and O. S. Torosyan, Akust. Zh. **45**, 633 (1999) [Acoust. Phys. **45**, 562 (1999)].
5. M. Hasegawa, J. Phys. Soc. Jpn. **37** (1), 193 (1974).
6. G. A. Galechyan, A. R. Mkrtchyan, and É. G. Divanyan, Akust. Zh. **36**, 364 (1990) [Sov. Phys. Acoust. **36**, 200 (1990)].
7. H.-J. Bauer and H. E. Bass, Phys. Fluids **16** (7), 988 (1973).
8. E. Ya. Kogan and V. N. Mal'nev, Zh. Tekh. Fiz. **47**, 653 (1977) [Sov. Phys. Tech. Phys. **22**, 391 (1977)].
9. A. I. Osipov and A. V. Uvarov, Inzh.–Fiz. Zh. **55** (1), 149 (1988).
10. A. V. Eletskiĭ and E. V. Stepanov, Khim. Fiz. **8** (9), 1247 (1989).
11. N. L. Aleksandrov, A. P. Napartovich, A. F. Pal', *et al.*, Fiz. Plazmy (Moscow) **16** (4), 862 (1990).
12. Z. I. Avdus' *et al.*, *Practical Course for General Physics*, Ed. by V. F. Nozdrev (Prosveshchenie, Moscow, 1970), p. 84.
13. G. A. Galechyan, A. R. Mkrtchyan, and L. B. Tavakalyan, Fiz. Plazmy (Moscow) **19** (11), 1400 (1993).
14. G. A. Galechyan, Usp. Fiz. Nauk **165**, 1357 (1995) [Phys. Usp. **38**, 1309 (1995)].
15. A. V. Eletskiĭ, in *Plasma Chemistry* (Energoatomizdat, Moscow, 1982), Vol. 9, pp. 151–178.
16. A. V. Eletskiĭ, L. A. Palkina, and B. M. Smirnov, *Transport Phenomena in Weekly Ionized Plasma* (Nauka, Moscow, 1982).
17. M. Whitson and R. McNeal, J. Chem. Phys. **66** (8), 2696 (1977).
18. V. N. Kondrat'ev, *Kinetics of Chemical Gas Reactions* (Akad. Nauk SSSR, Moscow, 1958).
19. L. D. Landau and E. M. Lifshitz, *Course of Theoretical Physics*, Vol. 6: *Fluid Mechanics* (Nauka, Moscow, 1986; Pergamon, New York, 1987).

Translated by A. Svechnikov

Acoustical Physics, Vol. 48, No. 3, 2002, pp. 273–278. Translated from Akusticheskiĭ Zhurnal, Vol. 48, No. 3, 2002, pp. 319–324.
Original Russian Text Copyright © 2002 by Gromasheva, Zakharov.

Estimation of the Underwater Explosion Depth from the Modified Cepstral Analysis of Sea Reverberation

O. S. Gromasheva and V. A. Zakharov†

Pacific Oceanological Institute, Far East Division, Russian Academy of Sciences, ul. Baltiĭskaya 43, Vladivostok, 690041 Russia

e-mail: gromasheva@poi.dvo.ru

Received February 2, 2000

Abstract—A mathematical model of the signal produced by an underwater explosion is used to obtain the dependence of the explosion depth on the argument T_k at which the cepstrum of the signal reaches its maximum. The algorithm evaluating the parameter T_k on the basis of the cepstral analysis of reverberation is substantiated. The proposed method of estimating the explosion depth is tested by experimental data to demonstrate its high accuracy. © *2002 MAIK "Nauka/Interperiodica".*

When processing experimental data obtained with the use of sound sources in the form of concentrated explosive charges, it is often necessary to know the spectrum of signals produced by underwater explosions. An explosion signal is difficult to record in its pure form because of the multipath propagation. Therefore, to obtain its spectrum, it is expedient to use a mathematical model of an explosion signal. In such mathematical models, the initial data are the distance from the point of observation to the point of the explosion, the mass of the explosive charge, and the explosion depth [1]. The latter can be estimated unambiguously when direct signals arriving from long distances through the underwater sound channel, or the surface channel, are available; i.e., when a great number of ray paths terminate at the reception point. In this case, from the autocorrelation function of the direct signal, one determines the period of the first fluctuation T_1 in the explosion signal [2] and then estimates the explosion depth by the formula [3]

$$T_1 = 2.08W^{1/3}/(z + 10.07)^{5/6}, \quad (1)$$

where z is the explosion depth in meters, W is the mass of the explosive charge in kilograms, and T_1 is the period of the first fluctuation in seconds.

If the number of ray paths is small, the autocorrelation function contains several maxima whose relative positions on the time axis are determined by the delays in the signal arrival times corresponding to the signal propagation over different ray paths. For some time delays, this situation may lead to an ambiguity in the determination of the explosion depth, even when the rough estimate of the explosion depth is known beforehand. However, in some cases, e.g., in an experimental study of the reflection properties of underwater objects or when the sound-scattering properties of the sea medium are investigated, the direct signal is limited by the receiving channels of the measuring equipment. For these cases, we propose a method of estimating the explosion depth on the basis of the cepstral analysis of the sea reverberation, which is always present in this kind of measurements either as noise interfering with the desired signals or as the object of investigation. Any kind of reverberation can be used for this purpose, but the bottom reverberation is preferable because of its higher intensity. For the processing, it is desirable to choose the reverberation signal segments immediately after the bottom and bottom–surface reflections.

The reverberation is a nonstationary process, but it can be reduced to a random process that is stationary in the broad sense. For more efficient use of the information carried by the reverberation signal, the latter should be brought to the stationary form. Hence, before evaluating the reverberation energy spectrum used in the cepstral analysis, we preliminarily process the reverberation realization $f(t)$ that is determined by the sequence of readings $f(t_i)$ at the instants $t_i = i\Delta t$, where $i = 1, 2, \ldots, N$. From this realization, we eliminate the constant component, which can appear when the signal is recorded on a magnetic tape or when the signal is entered in the computer:

$$\hat{f}(t_i) = f(t_i) - \frac{1}{N}\sum_{i=1}^{N} f(t_i).$$

† Deceased.

1063-7710/02/4803-0273$22.00 © 2002 MAIK "Nauka/Interperiodica"

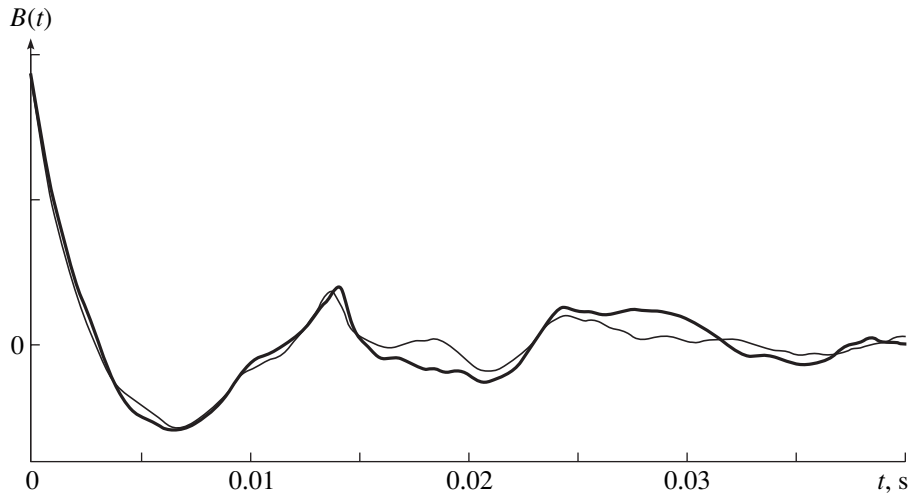

Fig. 1. Autocorrelation function of the bottom reverberation caused by the explosion of a 0.21-kg TNT charge at a depth of about 200 m (the thick line) and by an almost simultaneous explosion of two such charges fired at depths 198.5 and 206 m (the thin line).

Then, we bring the reverberation to the stationary form. For this purpose, we determine the absolute value of the function $\hat{f}(t_i)$ and, using the method of least squares, approximate it with a fifth-degree polynomial $F(t) = \sum_{j=0}^{5} e_j t^j$. Calculating $F(t_i)$, we obtain the reverberation signal in the stationary form: $s(t_i) = \hat{f}(t_i)/F(t_i)$. Then, we divide the realization $s(t_i)$ into M nonoverlapping adjacent segments, subject them to low-pass filtering, and calculate the energy spectra $|G_k(f_i)|^2$ of the filtered segments. As a result, we determine the statistically averaged spectrum $|G(f_i)|^2 = \frac{1}{M}\sum_{k=1}^{M}|G_k(f_i)|^2$.

The Fourier transform of this energy spectrum is the autocorrelation function $B(t)$ of the reverberation. This function is shown in Fig. 1 for one of the realizations of the bottom reverberation. It can be used for estimating the explosion depth by the well-known method, but the time shift corresponding to the correlation maximum cannot be determined with high accuracy because of the considerable width of this maximum.

The proposed method is free of this disadvantage and based on the similarity between the energy spectra of the sounding signal and the reverberation caused by it [4]. To justify the proposed method, we analyze the structure of the energy spectrum of an explosion signal. We consider the shock wave and the first fluctuation of the explosion signal within the time intervals where they have positive excess pressures in the coordinate system where they reach their peak values at $t = 0$. We denote their spectra by $G_0(f)$ and $G_1(f)$. Then, the spectrum $G(f)$ of the combination of the shock wave and the first fluctuation, which are separated in time by the first fluctuation period T_1, will have the form

$$G(f) = G_0(f) + G_1(f)\exp(-j2\pi f T_1), \qquad (2)$$

where j is the imaginary unit. Function (2) describes the main features of the spectrum of the explosion signal within almost the whole frequency range, because the contributions of the second and the following fluctuations to the spectrum are negligible and the phases of negative excess pressure manifest themselves only in the low-frequency region. From Eq. (2), we obtain the expression

$$\begin{aligned}|G(f)|^2 &= |G_0(f)|^2 + |G_1(f)|^2 \\ &+ 2|G_0(f)||G_1(f)|\cos[2\pi f T_1 - \Phi(f)],\end{aligned} \qquad (3)$$

where $\Phi(f) = \arctan\dfrac{j[G_0(f)G_1^*(f) - G_0^*(f)G_1(f)]}{G_0(f)G_1^*(f) + G_0^*(f)G_1(f)}$;

$G_0^*(f)$ and $G_1^*(f)$ are complex conjugate spectra.

The spectra $|G_0(f)|$ and $|G_1(f)|$ are functions slowly and monotonically decreasing with increasing frequency. Therefore, as one can see from Eq. (3), the energy spectrum contains a relatively slowly decreasing component $|G_0(f)|^2 + |G_1(f)|^2$ and a sinusoidal oscillation that is amplitude-modulated by another slowly decreasing function $2|G_0(f)||G_1(f)|$. The period of this oscillation $1/T_k$ slightly differs from $1/T_1$ because of the small additive introduced by the phase $\Phi(f)$; i.e., $T_k/T_1 = f(z) \approx 1$. This kind of spectrum structure allows us to formulate a fairly simple algorithm for estimating the quantity T_k: we eliminate the trend from the energy spectrum; we eliminate the amplitude modulation of the remaining sinusoidal oscillation; we calculate the spectrum of the resulting segment of the sinusoid; and, finally, we determine the position T_k of the maximum of

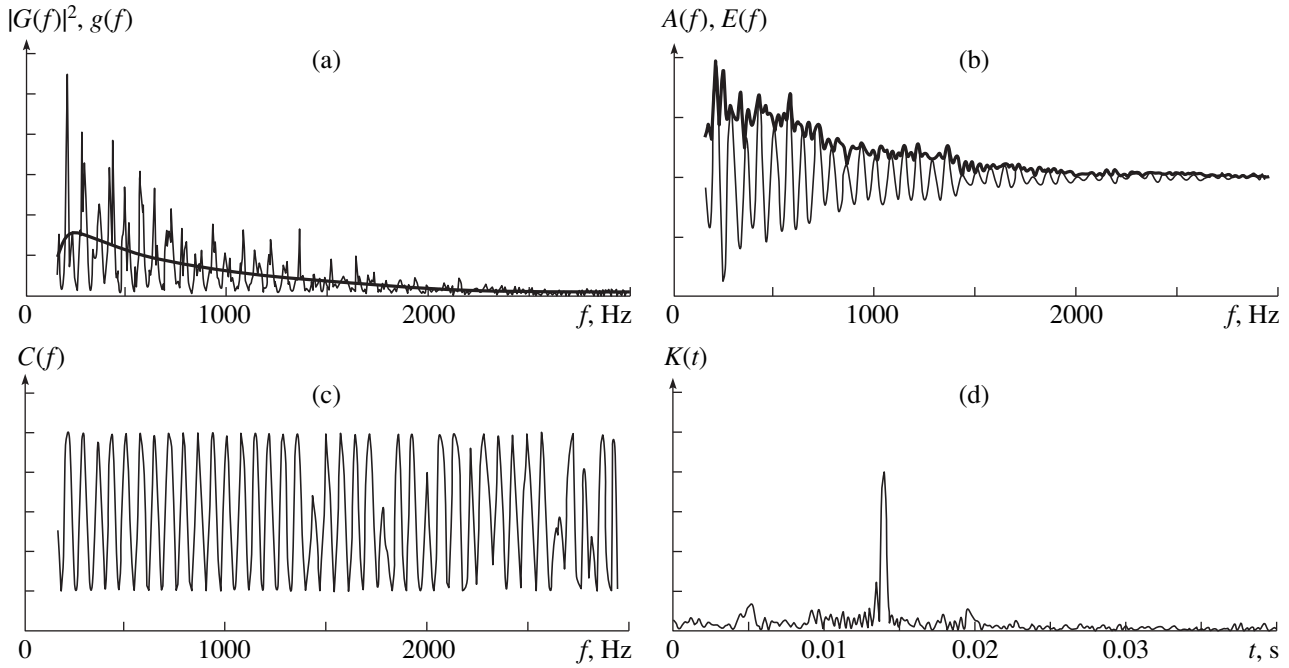

Fig. 2. Results of the cepstral processing of the realization of the bottom reverberation caused by the explosion of a 0.21-kg TNT charge at a depth of 200 m.

this spectrum on the abscissa axis. Hence, the processing of the statistically averaged reverberation spectrum $|G(f_i)|^2$ consists of the following operations:

(*i*) Applying the method of least squares, we approximate the energy spectrum within the transmission band of the low-pass filter, which was used for estimating the reverberation spectrum, by the rational function $g(f) = \sum_{j=-2}^{3} b_j f^j$ and eliminate the trend from the energy spectrum: $\hat{A}(f_i) = |G(f_i)|^2 - g(f_i)$. The energy spectrum of the bottom reverberation and the approximating function are shown in Fig. 2a.

(*ii*) The levels of the components of the reverberation energy spectrum have a wide dynamic range. Therefore, the function $g(f)$ does not eliminate the trend to the extent that one may ignore its residue. Hence, we filter the function $\hat{A}(f_i)$ in the time domain by a band-pass filter, which eliminates the high-frequency fluctuations of the function $\hat{A}(f_i)$.

(*iii*) We eliminate the amplitude modulation of the function $A(f_i)$. For this purpose, we use the Hilbert transform to calculate the conjugate function $\tilde{A}(f_i)$. Then, we determine the envelope $E(f_i) = [A^2(f_i) + \tilde{A}^2(f_i)]^{1/2}$ and divide the function $A(f_i)$ by this envelope: $C(f_i) = A(f_i)/E(f_i)$. The function $A(f)$ and its envelope are shown in Fig. 2b, and the function $C(f)$ is shown in Fig. 2c.

(*iv*) We apply the Fourier transform to the function $C(f_i)$. Determining the absolute value of the resulting function, we obtain the cepstrum $K(t_i)$ (see Fig. 2d).

(*v*) To increase the accuracy with which we determine the position of the cepstrum maximum on the time axis, we approximate the vertex of the cepstral peak by a second-degree polynomial and find the argument value $t = T_k$ corresponding to the maximal value of the polynomial.

Now, it is necessary to determine the expression relating the parameter T_k to the depth of the explosion.

In our previous publication [1], we showed that, when charges of different mass are exploded at the same depth, the signals generated by them and received at distances within which they propagate according to the laws of linear acoustics are similar in shape. At such distances, the ratio T_k/T_1 depends solely on the explosion depth z; i.e.,

$$T_k/T_1 = f(z).$$

Taking into account Eq. (1), we represent this ratio in the form

$$(z + 10.07)/[f(z)]^{6/5} = (2.08W^{1/3}/T_k)^{6/5}.$$

The values of the function $f(z)$ are close to unity. Therefore, the depth z is related to the quantity $x = (2.08W^{1/3}/T_k)^{6/5}$ by a dependence close to linear.

In some cases that require "whitening" of the spectrum of the probing explosion signal in a frequency range up to several kilohertz (e.g., when the response of the sound propagation channel is investigated or when the transient amplitude–phase characteristic of a

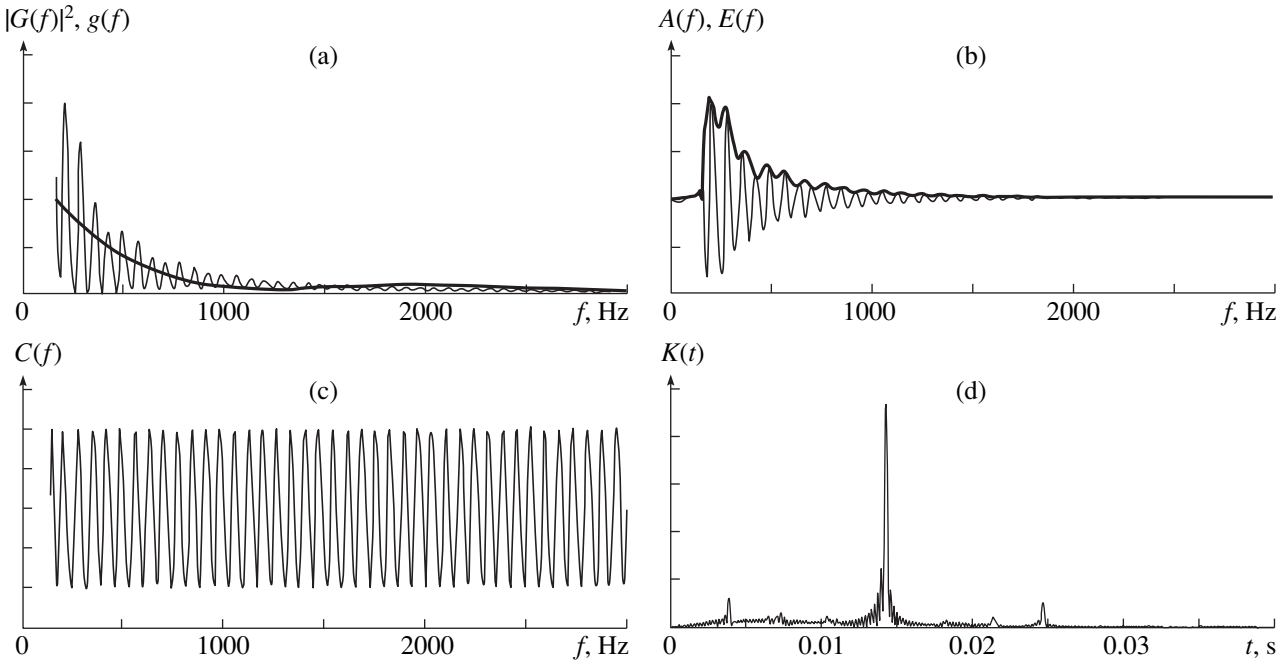

Fig. 3. Results of the cepstral processing of the signal generated by a 0.21-kg TNT charge fired at a depth of 200 m.

reflecting object is estimated), it is necessary to know the explosion depth with high accuracy. Therefore, we approximate the aforementioned dependence by a fifth-degree polynomial:

$$z = \sum_{j=0}^{5} a_j x^j. \tag{4}$$

To determine the coefficients a_j, we need to know a set of values T_{ki} corresponding to different explosion depths z_i.

Since the reverberation energy spectrum possesses all the characteristic features of the energy spectrum of the explosion signal, we can determine the pairs of values z_i and T_{ki} by using a mathematical model of the signal produced by an underwater explosion [1]. In this case, we perform the following operations: for a charge with a chosen mass and a given depth, we calculate the explosion signal, filter it through a low-pass filter, and determine the energy spectrum of the filtered signal. Then, we process the energy spectrum by the proposed method. Such calculations were performed for a charge of mass $W = 0.21$ kg and the explosion depths $z_i = i \times 25$ m, where $i = 2, 3, \ldots, 14$, in the frequency range up to 3 kHz. An example of the signal processing by the proposed algorithm is presented in Fig. 3. The pairs of values z_i and T_{ki} were used to determine the coefficients a_j of polynomial (4) by the method of least squares. As a result, we obtained the following formula for estimating the explosion depth by the parameter T_k:

$$z = -10.152 + 1.00289x - 3.8302 \times 10^{-5}x^2$$
$$- 3.1108 \times 10^{-8}x^3 + 6.0331 \times 10^{-10}x^4 - 9.101 \times 10^{-13}x^5;$$
$$x = (2.08W^{1/3}/T_k)^{6/5}.$$

In the proposed algorithm for the cepstral processing of reverberation, the operation of taking the logarithm of the energy spectrum, which is conventionally used in cepstral analysis, is replaced by the operations of eliminating the trend and eliminating the amplitude modulation of the resulting residual. This allows us to obtain a narrow cepstral peak on the background of a small random component and to measure the parameter T_k with high accuracy. Note that we did not analyze the effects of the frequency dependence of the sound attenuation and the reflectance of the sea bottom on the shape of the explosion signal, because these factors practically do not affect the positions of the maxima and minima of the explosion signal spectrum on the frequency axis, and their influence is eliminated by the aforementioned operations.

The proposed method for the determination of the explosion depth was tested using experimental data. The experiments were carried out in the Sea of Japan in a region with a flat bottom with a sea depth of 3000 m. The signals were received by three radiosonic buoys (RSB) positioned at the vertices of a square with sides 1000 m in length. The hydrophones of the buoys were

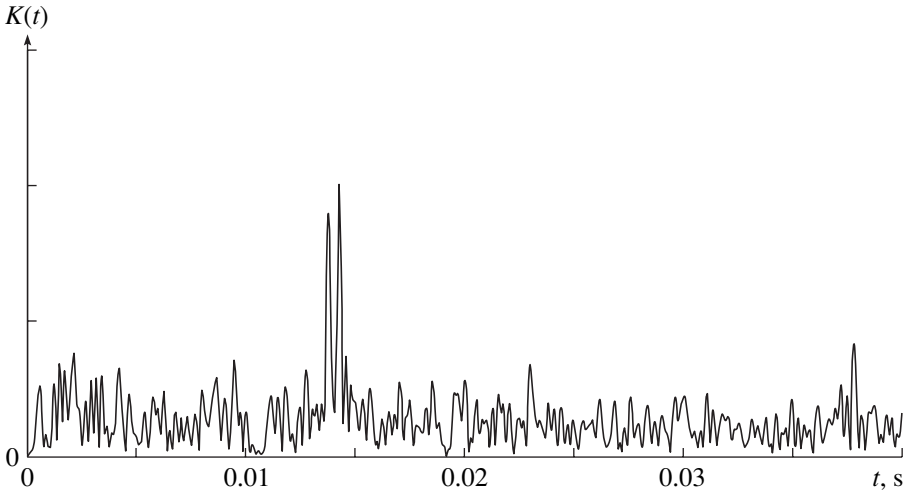

Fig. 4. Cepstrum of the bottom reverberation caused by an almost simultaneous explosion of two 0.21-kg TNT charges fired at the depths 198.5 and 206 m.

lowered to a depth of 100 m. Trinitrotoluene (TNT) charges of mass 0.21 kg were dropped from a ship moving outside this square. The charges were fired by hydrostatic blasters at a depth ~200 m. The distances between the points of explosion and the radiosonic buoys were within 2570–4350 m.

For processing, we selected the received signal segments that had a monotonically decreasing level of bottom reverberation immediately after the first bottom and bottom–surface reflections. The table presents the estimates obtained for the explosion depth, together with the average values of the explosion depth $\bar{z}$ calculated from the data of the three RSB in every experiment.

The accuracy of the proposed method is determined by the difference in the estimates obtained for the explosion depth from the reverberation signals received in every specific experiment by the different RSB. As one can see from the table, this difference is small: the standard deviation from the mean values is about 0.1 m, which testifies to the rather high accuracy of the proposed method of estimating the explosion depth on the basis of the data extracted from such a random process as sea reverberation. This method has one more advantage: it provides a high resolution in depth, which is confirmed by Fig. 4 showing the cepstrum of the reverberation caused by an almost simultaneous explosion of two charges fired at depths of 198.5 and 206 m. One can see that the cepstral peaks corresponding to different depths are well resolved; at the same time, these peaks cannot be resolved by the autocorrelation function (see Fig. 1).

The proposed method of estimating the explosion depth is based on the similarity between the energy spectra of an explosion signal and the reverberation caused by it and on the use of such an important property of spectra as the periodicity of the sequence of their maxima. In the experiment described above, the energy spectrum of reverberation generally reproduces the energy spectrum of the explosion signal, which can be seen from a comparison of Figs. 2a and 3a. However, in the case of a dissected bottom relief, the scattered signal may contain rather intense reflections that give rise to an additional periodic structure of the spectrum and, hence, to the appearance of additional peaks in the cepstrum (e.g., as in the case of hydroacoustic measurements in seismology [5]). In this situation, one faces the same problems as those encountered in estimating the period of the first fluctuation from the autocorrelation function of the direct signal in the case of a small number of ray paths. If the arguments of additional cepstral peaks differ considerably from T_k, the desired cepstral peak can be easily identified according to the known rough estimate of the explosion depth. Other-

Table

Experiment no.	Explosion depth z, m			$\bar{z}$, m
	RSB1	RSB2	RSB3	
1	198.5	198.4	198.4	198.4
2	196.9	196.9	197.0	196.9
3	199.9	199.8	199.8	199.8
4	201.9	201.7	201.9	201.8
5	203.8	203.9	203.8	203.8
6	206.1	206.0	206.0	206.0
7	201.0	200.7	200.8	200.8
8	196.3	196.8	196.5	196.5
9	198.7	198.8	198.7	198.7
10	198.0	197.9	198.2	198.0

wise, one has to either choose another segment of the reverberation signal or eliminate the most intense reflections from the reverberation realization before the preliminary processing.

Evidently, the proposed algorithm for estimating the explosion depth can also be applied to direct signals.

REFERENCES

1. O. S. Gromasheva and V. A. Zakharov, Nauchn. Tr. Dal'rybvtuza (Vladivostok), No. 11, 38 (1998).
2. V. M. Baronkin, M. V. Zheleznyakov, and R. Yu. Popov, in *Acoustics in the Ocean* (Nauka, Moscow, 1992), pp. 127–135.
3. R. H. Cole, *Underwater Explosions* (Princeton Univ. Press, Princeton, NJ, 1948; Inostrannaya Literatura, Moscow, 1950).
4. V. V. Ol'shevskiĭ, *Statistical Properties of Sea Reverberation* (Nauka, Moscow, 1966).
5. D. R. Baumgardt and Z. Der, Bull. Seismol. Soc. Am. **5** (IS4), 89 (1998).

Translated by E. Golyamina

Acoustical Physics, Vol. 48, No. 3, 2002, pp. 279–283. Translated from Akusticheskiĭ Zhurnal, Vol. 48, No. 3, 2002, pp. 325–330.
Original Russian Text Copyright © 2002 by Gusev.

Optimal Synthesis of Inhomogeneous Layered Structures

E. L. Gusev

Joint Institute of Physicotechnical Problems of the North, Yakutian Scientific Center, Siberian Division, Russian Academy of Sciences, ul. Oktyabr'skaya 1, Yakutsk, 677891 Russia

e-mail: e.l.gusev@ipng.yusn.ru

Received December 29, 2000

Abstract—The optimal synthesis problem for inhomogeneous acoustic structures is studied. The case is considered when a discrete set of materials is available. A possibility for efficiently designing inhomogeneous structures that realize the ultimate characteristics of acoustic media is studied. The extremal relationships between the parameters of optimal acoustic systems are obtained on the basis of a constructive analysis of the necessary optimum conditions. These relationships can be used to study the ultimate performance of inhomogeneous acoustic structures. © *2002 MAIK "Nauka/Interperiodica".*

1. FORMULATION OF THE PROBLEM

The problems of the optimal design of inhomogeneous structures with prescribed properties has received much attention in recent years [1–12]. The central problem in the optimal synthesis of inhomogeneous structures is the determination of the maximum potentialities in achieving the desired properties by choosing the appropriate design of the structure. To create composite structures, materials, and coatings with unique properties, it is necessary to study their potentialities in terms of achieving their ultimate performance. The latter corresponds to the limiting characteristics that can be achieved through a task-oriented control of the structure design.

The most general approach to the optimal synthesis of inhomogeneous structures is to use the variational method. In the variational formulation, the study of the potentialities amounts to creating efficient global optimization methods for solving particular optimal control problems, which are typical of the inhomogeneous structure synthesis and are usually combinatorial.

We study the problem in the following formulation. We restrict our analysis to considering the propagation of acoustic waves in the framework of linear acoustics. In this case, the propagation of acoustic waves in a layered medium is described by the system of equations

$$\begin{aligned} \frac{\partial \mathbf{v}_s}{\partial t} + \frac{1}{\rho_s}\nabla p_s &= 0, \\ \frac{\partial p_s}{\partial t} + \rho_s c_s^2 \operatorname{div} \mathbf{v}_s &= 0, \end{aligned} \tag{1.1}$$

where ρ_s is the density of the sth layer and p_s, $\mathbf{v}_s$, and c_s are the pressure, particle velocity vector, and wave velocity in it.

At the interface F between the sth and $(s-1)$th layers, the pressure and the normal component of the velocity are continuous:

$$(p^s - p^{s-1})\big|_F = 0, \quad (v_n^s - v_n^{s-1})\big|_F = 0.$$

The separation of variables and the Fourier transform reduce the problem of acoustic wave propagation in an inhomogeneous structure to the following boundary-value problem [13]:

$$\begin{aligned} &\frac{\partial^2 f_s(z,\omega)}{\partial z^2} + k_s^2(\omega) f_s(z,\omega) = 0, \\ &b_{s-1} \le z \le b_s \quad (s = 0, \ldots, N+1), \\ &f_s(b_{s-1},\omega) = f_{s-1}(b_{s-1},\omega), \\ &\frac{\partial f_s(b_{s-1},\omega)}{\partial z} = \frac{\rho_s}{\rho_{s-1}} \frac{\partial f_{s-1}(b_{s-1},\omega)}{\partial z} \\ &(s = 1, \ldots, N+1), \\ &\frac{\partial f_0(0,\omega)}{\partial z} + ik_0(\omega) f_0(0,\omega) = 2ik_0(\omega), \\ &\frac{\partial f_{N+1}(l,\omega)}{\partial z} - ik_{N+1}(\omega) f_{N+1}(l,\omega) = 0. \end{aligned} \tag{1.2}$$

The functions $f_s(z,\omega)(b_{s-1} \le z \le b_s, s = 0, \ldots, N+1)$ are the components of the complex pressure amplitudes and $k_s(\omega) = \omega(c_s^{-2} - c_0^{-2}\sin^2\vartheta_0)^{1/2}$ is the z component of the wave vector in the sth layer.

The energy transmission coefficient $T(\omega)$ is determined through the solution to boundary-value problem (1.2):

$$T(\omega) = \frac{c_0\rho_0\cos\vartheta_{N+1}}{c_{N+1}\rho_{N+1}\cos\vartheta_0}\left|f_{N+1}(l, \omega)\right|^2.$$

Here, ϑ_{N+1} is the angle at which the wave leaves the structure.

Let the structure be composed of a given discrete set of materials. Since the physical properties of these materials are not independent, we assume that a functional dependence $c = c(\rho)$ exists that uniquely determines the velocity of acoustic waves in the material by a given density of this material. Then, the density ρ alone is the independent physical parameter. Let Λ be the set of densities of the available materials.

Let the goal be the design of an acoustic structure that features the maximal reflection in one given spectrum region and the maximal transmission in another region. Then, in terms of the optimal control theory, the optimal design problem amounts to the minimization of the goal function

$$J = \int_{\omega_{\min}}^{\omega_{\max}} \tau(\omega)\mathrm{mod}^2 f_{N+1}(l, \omega)d\omega \qquad (1.3)$$

over the solutions of the system of equations (1.2). Here, $\omega_{\min}$ and $\omega_{\max}$ are the lower and upper bounds of the filtered frequency range, and $\tau(\omega)$ is the weighting function ($-1 \le \tau(\omega) \le 1$). In the synthesis of transmissive acoustic systems, the goal function is negative; in the synthesis of acoustic insulation materials, it is positive.

In keeping with the above formulation, we consider the problem of finding the complete set of inhomogeneous structures that realize the potentialities in achieving the required properties:

$$U^* = \{\rho^*(z) : J(\rho^*(z)) = \min_{\rho(z)} J(\rho(z))\}. \qquad (1.4)$$

Here, $\rho(z)$ is the density distribution across the structure ($0 \le z \le l$): $\rho(z) = \rho_s$, $b_{s-1} \le z \le b_s$, $s = 1, \ldots, N$.

It is important to derive the extremal relationships between the parameters of the optimal acoustic structures, which can be used to study the effect of individual parameter variations on the optimal structure.

Below, we will consider only the normal incidence of acoustic waves.

2. NECESSARY CONDITIONS IN PROBLEMS OF ACOUSTIC OPTIMAL SYNTHESIS

Let us formulate the necessary optimum conditions in the optimal control problem given by Eqs. (1.2) and (1.3). Consider the Hamiltonian function for the sth layer:

$$H(f_s, \dot{f}_s, \psi_s, \dot{\psi}_s; \rho)\big|_z = \int_{\omega_{\min}}^{\omega_{\max}} \frac{k^2(\rho, \omega)}{\rho}\alpha_s(z, \omega)d\omega + \int_{\omega_{\min}}^{\omega_{\max}} \rho\beta_s(z, \omega)d\omega, \qquad (2.1)$$
$$b_{s-1} \le z \le b_s, \quad s = 1, \ldots, N.$$

Here, $k(\rho, \omega) = \omega/c(\rho)$, $\rho \in \Lambda$,

$$\alpha_s(z, \omega) = -\frac{\rho_s}{k_s^2}\mathrm{Re}\,\dot{\psi}_s(z, \omega)\,f_s(z, \omega),$$

$$\beta_s(z, \omega) = \frac{1}{\rho_s}\mathrm{Re}\,\dot{f}_s(z, \omega)\psi_s(z, \omega),$$

and $\psi_s(z, \omega)$ ($b_{s-1} \le z \le b_s$, $s = 1, \ldots, N$) is a solution to the boundary-value problem conjugate to problem (1.2) [11].

Let $\rho^*(z)$ ($0 \le z \le l$) be the optimal density distribution across the layered structure and $f_s^*(z, \omega)$ and $\psi_s^*(z, \omega)$ ($b_{s-1} \le z \le b_s$, $s = 0, \ldots, N$) be the corresponding solutions to the original, Eqs. (1.2), and the conjugate systems of equations. Then, for the optimal solution, we have

$$H(*; \rho^*(z))\big|_z = \max_{\rho \in \Lambda} H(*; \rho)\big|_z, \quad 0 \le z \le l. \qquad (2.2)$$

(The omitted arguments of Hamiltonian function (2.2) refer to the optimal solution.)

Let us apply the necessary optimum conditions given by Eqs. (2.2) to the constructive synthesis of optimal acoustic systems. We will study this problem for monochromatic and nonmonochromatic acoustic waves separately.

3. MONOCHROMATIC ACOUSTIC WAVES

At the optimal solution for the monochromatic wave, the Hamiltonian function can be reduced to the form

$$H(*; \rho)\big|_z = \alpha_s^*(z)\rho\left[\frac{k^2(\rho)}{\rho^2} - \frac{k_s^{*2}}{\rho_s^{*2}}\right] + \frac{\rho}{\rho_s^*}L^*, \qquad (3.1)$$
$$b_{s-1}^* \le z \le b_s^*, \quad s = 1, \ldots, N^*,$$

where L^* is a constant independent of z.

Let us represent the amplitude transmission W and reflection V coefficients as

$$W = \tau\exp(i\vartheta), \quad V = \sigma\exp(i\varphi),$$
$$0 \le \tau, \quad \sigma \le 1, \quad 0 \le \vartheta, \quad \varphi \le 2\pi.$$

Consider the cases when the set of available materials consists of two and of several (more than two) different materials separately.

The Available Set Consists of Two Materials

The constructive analysis of necessary optimum conditions (2.2) yields the following extremal relationships between the parameters of the optimal structure.

The density of the first layer of the optimal structure satisfies the extremal relationship

$$\rho_1^* = \begin{cases} \arg\max\limits_{\rho\in\Lambda}[\rho(Z^2(\rho)-Z_0^2)], & \text{when} \quad 0<\varphi<\pi \\ \arg\min\limits_{\rho\in\Lambda}[\rho(Z^2(\rho)-Z_0^2)], & \text{when} \quad \pi<\varphi<2\pi. \end{cases} \tag{3.2}$$

We use here the following notations: $x^* = \arg\operatorname{extr}\limits_x f(x)$ if $f(x^*) = \operatorname{extr}\limits_x f(x)$, $Z(\rho) = 1/\rho c(\rho)$, and $Z_0 = 1/\rho_0 c_0$. The optimal thickness of the first layer satisfies the extremal relationship

$$\Delta_1^* = \frac{1}{2k_1^*}\arccos\left\{\frac{(Z_1^{*2}-Z_0^2)[2\rho_1^* Z_1^{*2}-\rho_2^*(Z_1^{*2}+Z_2^{*2})]\cos\gamma(\varphi)}{\rho_2^*(Z_0^2+Z_1^{*2})(Z_2^{*2}-Z_1^{*2})}\right\} - \frac{1}{2k_1^*}\gamma(\varphi). \tag{3.3}$$

Here,

$$\gamma(\varphi) = \arctan\left[\frac{2Z_0 Z_1^*\cot\varphi}{Z_1^{*2}+Z_0^2}\right],$$

$$Z_s = 1/\rho_s c_s.$$

The thicknesses of the first and second layers of the optimal structure are related through the extremal relationship

$$Z_2^*\cot y_2^* = -Z_1^*\sigma_{2,1}^*\cot(2y_1^*+\gamma(\varphi)) + \frac{Z_1^*\tau_{2,1}^*\tau_{0,1}^*\cos(\gamma(\varphi))}{\sigma_{0,1}^*\sin(2y_1^*+\gamma(\varphi))}. \tag{3.4}$$

Here, $y_s^* = k_s^*\Delta_s^*$, Δ_s^* is the optimal thickness of the sth layer,

$$\sigma_{i,j} = \frac{1}{2}(1+\delta_{i,j}^2), \quad \tau_{i,j} = \frac{1}{2}(1-\delta_{i,j}^2),$$

$$\delta_{i,j} = Z_i/Z_j.$$

It has been shown [13] that, when the excitation is monochromatic and the set of only two materials is available, the thicknesses of the internal layers of the optimal structure are related as

$$\Delta_s^* = \Delta_{s-2}^*, \quad s = 4, \ldots, N^*-1. \tag{3.5}$$

The above extremal relationships can be used to find the complete set U^* of optimal layered structures that realize the potentialities in achieving the required properties. This can be accomplished with the help of the procedure described below.

For each $\varphi(0 \le \varphi \le 2\pi)$, the following actions are performed:

(1) Find the material of the first layer from extremal relationship (3.2).

(2) Use formulas (3.3)–(3.5) to find the thicknesses of all layers of the structure.

(3) Calculate the amplitude transmission coefficient $V(\varphi)$ of the structure as a function of the scalar argument φ.

(4) Find the complete set of structures that satisfy the condition $\arg V(\varphi) = \varphi$.

(5) Consider the subset of such structures that correspond to the smallest goal function as the desired set of solutions that realize the potentialities in achieving the given properties.

The procedure described above can be extended to the case when the total thickness of the structure is not fixed and is allowed to vary within a specified range ($l_{\min} \le l \le l_{\max}$). Therefore, it can be used to study the optimal structure as a function of its total thickness.

The Available Set Consists of Several (More Than Two) Materials

As follows from the necessary optimum conditions (2.2), the constant L^* and the function $\alpha_s^*(z)$ in the Hamiltonian function (3.1) can be represented as

$$L^* = \frac{\tau(\omega)\omega^2\rho_0\rho_1^*}{k_0(\omega)}(Z_1^{*2}-Z_0^2)\left(\frac{(1-\rho^2)Z_0}{Z_{N^*+1}}\right)\rho\sin\varphi,$$

$$\alpha_s^*(z) = C_s^*\sin(2k_s^*(z-b_{s-1}^*)) + D_s^*\cos(2k_s^*(z-b_{s-1}^*)) + E_s^*,$$

$$b_{s-1}^* \le z \le b_s^*, \quad s = 1, \ldots, N^*,$$

where C_s^*, D_s^*, and E_s^* are real constants. For $s = 1$, these constants can be represented as

$$C_1^* = -\frac{\rho_1^*\tau(\omega)}{k_1^*(\omega)}\left(\frac{(1-\rho^2)Z_0}{Z_{N^*+1}}\right)\rho\cos\varphi,$$

$$D_1^* = \frac{\rho_0\tau(\omega)}{2k_0(\omega)}\left(1+\frac{Z_0^2}{Z_1^{*2}}\right)\left(\frac{(1-\rho^2)Z_0}{Z_{N^*+1}}\right)\rho\sin\varphi, \quad (3.6)$$

$$E_1^* = \frac{\rho_0\tau(\omega)}{2k_0(\omega)}\left(1-\frac{Z_0^2}{Z_1^{*2}}\right)\left(\frac{(1-\rho^2)Z_0}{Z_{N^*+1}}\right)\rho\sin\varphi.$$

The continuity conditions at the layer interfaces yield the following recurrent formulas, which relate the coefficients C_s^*, D_s^*, and E_s^* of the function $\alpha_s^*(z)$ that correspond to adjacent layers of the layered structure:

$$\begin{aligned} C_s^* &= \delta_{s-1,s}^*(C_{s-1}^*\cos 2y_{s-1}^* - D_{s-1}^*\sin 2y_{s-1}^*),\\ D_s^* &= \sigma_{s-1,s}^*(C_{s-1}^*\sin 2y_{s-1}^* + D_{s-1}^*\cos 2y_{s-1}^*)\\ &\quad + \tau_{s-1,s}^* E_{s-1}^*,\\ E_s^* &= \tau_{s-1,s}^*(C_{s-1}^*\sin 2y_{s-1}^* + D_{s-1}^*\cos 2y_{s-1}^*)\\ &\quad + \sigma_{s-1,s}^* E_{s-1}^*,\\ s &= 2, \ldots, N^*. \end{aligned} \quad (3.7)$$

These extremal relations can be used to determine the complete set of the structures that realize the potentialities in achieving the required properties with the help of the procedure described below.

For each value of the scalar parameter $\varphi(0 \le \varphi \le 2\pi)$, perform the following calculations:

(1) Find the density ρ_1^* of the first layer from relationship (3.2).

(2) Find the optimal thicknesses Δ_s^* ($s = 1, \ldots, N^*$) and the physical parameters ρ_s^* ($s = 1, \ldots, N^*$) of the layers from extremal relationships (2.2), (3.6), and (3.7) as follows. Let the optimal thickness Δ_{s-1}^* of the $(s-1)$th layer and the optimal density ρ_s^* of the sth layer be known. Determine C_s^*, D_s^*, and E_s^* from formulas (3.7) and calculate $\alpha_s^*(z)$. Determine the point z^* ($b_{s-1}^* < z \le l$) at which the function $H(*;\rho)|_z$ given by Eq. (3.1) peaks for two elements ρ_s^* and ρ^* simultaneously. Set $\Delta_s^* = z^* - b_{s-1}^*$ and $\rho_{s+1}^* = \rho^*$. Continue the calculations in a similar manner.

(3) For the structure found above, calculate the amplitude transmission coefficient $V(\varphi)$ as a function of the scalar parameter φ.

(4) Determine the set of structures that satisfy the condition $V(\varphi) = \varphi$.

(5) Consider the subset of these structures that correspond to the minimum of the goal function as the desired set of structures that realize the ultimate performance.

This procedure can be generalized to structures with an unfixed thickness, in which case it can be used to study the optimal structure as a function of its total thickness.

4. NONMONOCHROMATIC ACOUSTIC WAVES

Consider the general case of a nonmonochromatic acoustic wave.

We begin with the synthesis of acoustic systems whose energy transmission coefficient is closest to the desired value at a particular frequency $\omega^* \in [\omega_{min}, \omega_{max}]$. Let q be the closest possible value at $\omega = \omega^*$. Then, the optimal synthesis problem consists in finding the set of structures U^* [Eq. (1.4)] that realize the ultimate performance subject to the additional condition

$$T(\omega^*) = q. \quad (4.1)$$

However, the closest possible energy transmission coefficient at $\omega = \omega^*$ is achieved for the monochromatic excitation at this frequency. Let U_0^* be the complete set of inhomogeneous structures that correspond to the minimal value of goal function (1.3) for the monochromatic excitation at the frequency ω^*. Then, the set U^* of all inhomogeneous structures that solve the optimal synthesis problem described by formulas (1.2), (1.3), and (4.1) is a subset of the set U_0^*:

$$U^* = \left\{ u^* \in U_0^* : J(u^*) = \min_{u \in U_0^*} J(u) \right\}. \quad (4.2)$$

Thus, the optimal synthesis problem in this formulation can be solved completely.

Consider the general case.

In a fairly large number of optimal synthesis problems, a frequency $\omega^* \in [\omega_{min}, \omega_{max}]$ can be indicated at which the energy transmission coefficient of the inhomogeneous structure differs from the closest achievable value by a sufficiently small quantity δ. The closest achievable value of the energy transmission coefficient at the frequency ω^* is the closest attainable value for the monochromatic excitation at the frequency ω^*. Denote this value as $g_{\omega^*}^*(\omega^*)$. Then, the above condition can be written as

$$\left| g(\omega^*) - g_{\omega^*}^*(\omega^*) \right| \le \delta. \quad (4.3)$$

Consider the optimal synthesis problem given by Eqs. (1.2) and (1.3) with additional condition (4.3).

Let $V_\delta^*(\omega^*)$ be the set of solutions that realize the potentialities in attaining the required properties in optimal synthesis problem (1.2), (1.3) under additional condition (4.3). Let E_ω^* be the set of all solutions that

realize the ultimate performance in optimal synthesis problem (1.2), (1.3) for the monochromatic excitation at the frequency ω.

Then, we have

$$V_0^*(\omega^*) \subset E_{\omega^*}^*,$$

where, according to the notation introduced above, $V_0^*(\omega^*)$ is the set of all solutions that realize the ultimate performance in optimal synthesis problem (1.2), (1.3) under constraint (4.3), which corresponds to $\delta = 0$.

As follows from the theory of multivalued mappings [14, 15], for any $\alpha_0 > 0$, there exists such a $\delta_0 > 0$ that, for all $0 < \delta < \delta_0$, the condition

$$V_\delta^*(\omega^*) \subset S_{\alpha_0}(V_0^*(\omega^*)) \tag{4.4}$$

is satisfied. Here,

$$S_{\alpha_0}(V_0^*(\omega^*)) = \{u(.) : \rho_U(u(.), V_0^*(\omega^*))\} \le \alpha_0,$$

$$\rho_U(u(.), V_0^*(\omega^*)) = \inf_{v(.) \in V_0^*(\omega^*)} \rho_U(u(.), v(.)).$$

Thus, at a sufficiently small δ, the sets $V_0^*(\omega^*)$ and $V_\delta^*(\omega^*)$ are close in their structure. Property (4.4) can be used to construct the set $V_\delta^*(\omega^*)$ when the set $V_0^*(\omega^*)$ is known. The theory of multivalued mappings can be efficiently used in the optimal synthesis of inhomogeneous structures from a given discrete set of materials for a nonmonochromatic excitation under additional condition (4.3) to find the complete set of solutions that realize the ultimate performance when the complete set of solutions that realize the ultimate performance for the monochromatic wave is known.

CONCLUSION

One of the most important problems in studying acoustic fields in inhomogeneous structures is the problem of revealing the potentialities of controlling the acoustic characteristics through a task-oriented choice of the structure design (the physical properties of the layer materials, the thickness and number of layers, and the order of the layer arrangement in the structure). Since the number of inhomogeneous structure designs that have to be tested for optimum is very large, the problem cannot be solved by an exhaustive search through all possible designs, even using high-performance computers. Presently, there is no alternative to such an exhaustive search.

Extremal relationships that relate the parameters of optimal acoustic systems are derived on the basis of the constructive analysis of the necessary optimum conditions in acoustic optimal synthesis problems.

These extremal relationships can be used to study the effect of various parameters on the optimal structure and to develop methods for investigating the ultimate characteristics of acoustic structures.

REFERENCES

1. M. I. Imashev, R. K. Khanov, and Sh. D. Shamgunov, Dokl. Ross. Akad. Nauk **335**, 167 (1994) [Phys. Dokl. **39**, 161 (1994)].
2. E. L. Korotyaev, Dokl. Ross. Akad. Nauk **336**, 171 (1994) [Phys. Dokl. **39**, 291 (1994)].
3. K. Han-Pin and D. Ravi, Aerosp. Eng. **15** (4), 33 (1995).
4. S. Y. Sotrikhin and A. N. Shupikov, Int. J. Solids Struct. **32** (8, 9), 1247 (1995).
5. C. Huang and B. Kroplin, Eng. Comput. **12** (5), 403 (1995).
6. N. Ichiro and N. Akio, Trans. Jpn. Soc. Mech. Eng., Ser. C **61** (587), 2645 (1995).
7. J. S. Hesthaven, Comput. Phys. **142** (1), 129 (1998).
8. E. R. Michael, J. Acoust. Soc. Am. **104**, 3369 (1998).
9. A. N. Shupikov, N. V. Smetankina, and H. A. Sheludko, Mechanica **33** (6), 553 (1998).
10. J. K. Tomson, Sound Vibr. **33** (6), 12 (1999).
11. R. Maurizio, Atti Semin. Mat. Fis. Univ. Modena **47** (2), 479 (1999).
12. M. Grediac, J. Compos. Mater. **33** (20), 1939 (1999).
13. E. L. Gusev, *Mathematical Methods of the Layered Structure Synthesis* (Nauka, Novosibirsk, 1993).
14. V. K. Ivanov, Mat. Sb. **61** (2), 211 (1963).
15. O. A. Liskovets, Differ. Uravn. Ikh Primen., No. 4, 636 (1967).

Translated by A. Khzmalyan

Acoustical Physics, Vol. 48, No. 3, 2002, pp. 284–291. Translated from Akusticheskiĭ Zhurnal, Vol. 48, No. 3, 2002, pp. 331–339.
Original Russian Text Copyright © 2002 by Derov, Maximov.

Determination of Crack Orientation in the Vicinity of a Borehole by Vertical Seismoacoustic Profiling

A. V. Derov and G. A. Maximov

Moscow Engineering Physics Institute, Kashirskoe sh. 31, Moscow, 115409 Russia

e-mail: maximov@dpt39.mephi.ru

Received April 18, 2001

Abstract—Excitation of a Stoneley wave in a single fluid-filled crack of small wave size in a borehole under an external seismic wave incident on it at an arbitrary angle is considered. On the basis of the solution obtained, the feasibility of solving the inverse problem of reconstructing the crack orientation from the data of vertical seismoacoustic profiling by hydrophones with the use of minimal input data is demonstrated. © *2002 MAIK "Nauka/Interperiodica".*

The phenomenon of low-frequency Stoneley wave propagation in boreholes is well known [1–4]. The Stoneley waves can be generated at any kind of borehole inhomogeneities, including cracks and fractures crossing the borehole [5, 6].

In vertical seismic profiling (VSP), the low-frequency Stoneley waves are usually considered as noise. However, they can be useful as a means to detect and analyze cracks crossing a borehole. The Stoneley waves proved to be very sensitive to the presence of cracks. It was reported in [7] that permeable cracks cause attenuation of Stoneley waves due to the fluid flow into these cracks. The same mechanism gives rise to a reflected Stoneley wave. The ratio between the amplitudes of transmitted and reflected Stoneley waves can provide information on the parameters of a crack or a cracked zone. Therefore, the analysis of the reflection of Stoneley waves is unique among the logging techniques in its sensitivity to the appearance and extension of cracks.

A method of calculating the reflection of Stoneley waves from horizontal and inclined plane-parallel fractures was proposed in [8], on the assumption that the compressibility of the external medium could be neglected. A comparison with the experimental data showed that the proposed simple analytical model overestimates the reflection factor of Stoneley waves.

To take into account the effect of the elasticity of walls, a modal solution valid at low frequencies was used in [9] with the aim of deriving expressions for the transmission and reflection factors in the case of a horizontal plane-parallel crack. The reflection factors given by this model proved to be higher than those predicted for a rigid formation.

The recent works [10, 11] present a refined analytical model along with a finite-difference technique for calculating Stoneley waves' reflection from horizontal cracks crossing a fluid-filled borehole. It is shown, in particular, that gullies in a borehole cause reflections that are quantitatively similar to those caused by cracks. When combined with an open crack, these gullies can considerably affect the reflection factor of a Stoneley wave. The principal conclusion of these works is that the reflection of Stoneley waves from cracks in an elastic medium can be twice as great as a similar reflection in the case of a perfectly rigid medium. It is also found that a cracked zone and a permeable one are equivalent on a scale that is smaller than the Stoneley wavelength.

There is another well-known mechanism of Stoneley wave generation [5] that differs from the above-mentioned one: the incident seismic wave compresses the fluid-filled crack and injects fluid into the borehole. The Stoneley waves generated by this injection propagate up and down the borehole, their amplitude depending on the permeability of the cracked zone. In this case, the permeability of the cracked zone can be estimated from the amplitude ratio of the incident seismic wave and the generated Stoneley waves.

A model for describing the generation of tube waves on a plane-parallel porous permeable layer crossing a borehole under an incident external seismic wave is proposed in [12]. This model is used to determine the dependence of the amplitude ratio of the Stoneley wave and the longitudinal wave on the thickness, porosity, and permeability of the layer.

Below, we consider the excitation of a Stoneley wave at a single fluid-filled crack of a small wave size when an external seismic wave is incident on it at an arbitrary angle (see Fig. 1). We show that, on the basis of the solution obtained, it is possible to solve the inverse problem of reconstructing the crack orientation from the data of VSP with hydrophones by using minimal initial information.

In the long-wave approximation $\lambda \gg R$ (λ is the characteristic wavelength of the seismic wave and R is the borehole radius), we consider the problem of the

1063-7710/02/4803-0284$22.00 © 2002 MAIK "Nauka/Interperiodica"

wave field generation in a fluid-filled borehole under the effect of an incident seismic wave in the presence of a crack crossing the borehole shaft. The linear dimensions of the crack are considered to be small compared to the wavelength of the seismic wave, $\lambda \gg L$. The crack and the borehole can be considered as two subsystems with a hydraulic connection. The latter leads to a fluid flow between the borehole and the crack when they are deformed by the external seismic field. As this takes place, the conditions of equality of the fluid pressures and flows between the crack and the borehole must be satisfied at the point of their intersection.

The propagation of small-amplitude waves in the borehole fluid is described by the system of linearized equations of continuity, motion, and state:

$$\begin{aligned} \frac{\partial}{\partial t}\rho(r, z, t) + \rho_f \operatorname{div}\mathbf{V}(r, z, t) &= 0; \\ \rho_f \frac{\partial}{\partial t}\mathbf{V}(r, z, t) &= -\operatorname{grad} P(r, z, t); \\ P(r, z, t) &= c_f^2 \rho(r, z, t). \end{aligned} \tag{1}$$

Here, $P(r, z, t)$, $\rho(r, z, t)$, and $\mathbf{V} = \{V_r(r, z, t), 0, V_z(r, z, t)\}$ are the deviations of the local pressure, density, and mass velocity, respectively, from their equilibrium values; ρ_f and c_f are the equilibrium values of the fluid density and the speed of sound in the fluid. Since, as a rule, the frequency used in the VSP does not exceed several hundreds of hertz and the borehole diameter does not exceed 20 cm, the characteristic wavelengths in both the borehole fluid and the external medium are much greater than the borehole diameter.

In the long-wave approximation, it is natural to describe the acoustic wave field in the borehole in terms of the dynamic quantities averaged over the borehole cross section:

$$\begin{aligned} P(z, t) &= \frac{2\pi}{\pi R^2}\int_0^R r dr P(r, z, t), \\ \rho(z, t) &= \frac{2\pi}{\pi R^2}\int_0^R r dr \rho(r, z, t), \\ \mathbf{V}(z, t) &= \frac{2\pi}{\pi R^2}\int_0^R r dr \mathbf{V}(r, z, t). \end{aligned} \tag{2}$$

These expressions take into account that, in the long-wave approximation, the distribution of dynamic quantities in the borehole is axially symmetric, and averaging over the angle gives the factor 2π.

Averaged over the borehole cross section, the equations of continuity and motion (the projection of the latter onto the borehole axis) lead, according to Eqs. (2), to the following relations:

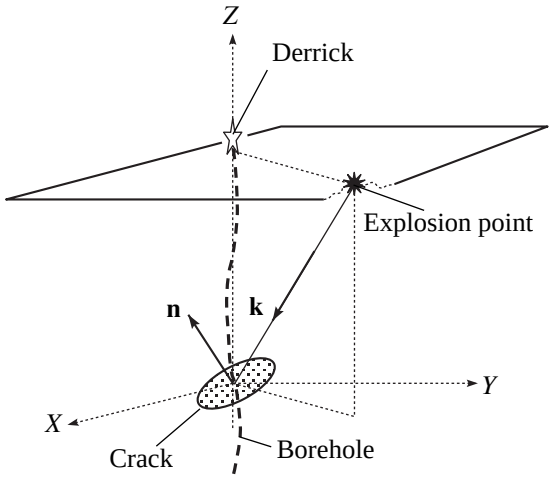

Fig. 1. Schematic diagram of VSP. **n** is the normal to the crack surface; **k** is the wave vector of the incident seismic wave.

$$\begin{aligned} \frac{\partial}{\partial z}V_z(z, t) &= -\frac{1}{\rho_f}\frac{\partial}{\partial t}\rho(z, t) - \frac{2}{R}V_r(r = R, z, t), \\ \rho_f \frac{\partial V_z(z, t)}{\partial t} &= -\frac{\partial P}{\partial z}. \end{aligned} \tag{3}$$

Combining these equations, we obtain an inhomogeneous wave equation for the pressure field in a fluid-filled borehole [13, 14]:

$$\frac{\partial^2 P}{\partial z^2} - \frac{1}{c_f^2}\frac{\partial^2 P_f}{\partial t^2} = \frac{2\rho_f}{R}\frac{\partial V_r(r = R, z, t)}{\partial t}. \tag{4}$$

If a fluid flow through the borehole wall is absent, the velocities of the borehole wall and the adjacent fluid coincide: $V_r(r = b, z, t) = \partial u_r/\partial t$, where u_r is the displacement of the borehole wall.

In the long-wave approximation, to obtain a closed equation for the pressure in the borehole, one can use the quasistatic relation between the applied pressure and the displacement of the borehole wall, which can be found on the basis of the solutions of the static equations of elasticity theory. For a cased borehole in the field of external static stress σ_{eff}, the relation between the radial displacement u_r, σ_{eff}, and P has the form [2]

$$\frac{u_r}{R} = \frac{P}{2M} + \frac{\sigma_{\text{eff}}}{E}, \tag{5}$$

where E is Young's modulus, and M is a modulus that depends on the presence of a borehole casing and equals either the shear modulus μ of the external medium for an uncased borehole or $M = \mu + E_{st}\Delta_{st}/(2R)$ when the borehole has a steel casing with the wall width Δ_{st} and Young's modulus E_{st}. The effective external dynamic stress σ_{eff} can be expressed in the cylindri-

cal coordinates in terms of the components of the external stress tensor σ_{eff} as [2]

$$\sigma_{\text{eff}} = \text{Sp}\,\sigma - (1+\nu)\sigma_{zz}, \tag{6}$$

where ν is Poisson's ratio of the elastic medium.

Substituting Eq. (5) into Eq. (4), we obtain an inhomogeneous wave equation describing the tube wave propagation under the effect of external dynamic stresses in a fluid-filled borehole [13, 14]:

$$\frac{\partial^2 P_f}{\partial z^2} - \frac{1}{c_{tw}^2}\frac{\partial^2 P_f}{\partial t^2} = \frac{2\rho_f}{E}\frac{\partial^2 \sigma_{\text{eff}}}{\partial t^2}. \tag{7}$$

Here, $c_{tw} = c_f(1 + K_f/M)^{-1/2}$ is the velocity of nondispersive Stoneley waves; $K_f = \rho_f c_f^2$ is the bulk modulus of the fluid.

At the intersection point of the borehole and the crack, the velocity V_r $(r = R, z, t)$ is determined by the fluid flow out of the crack, which can be found from the crack volume variation in the seismic wave field at a given fluid pressure. When linear dimensions of the crack are far less than the wavelength of the seismic wave $L \ll \lambda$, the crack shape is determined by the local values of the stress tensor of the medium σ_{ik} in the seismic wave and by the fluid pressure in the crack. This approximation allows one to determine the crack shape from the solution of the static equations of elasticity theory. To find the variation of the crack volume in the external seismic field, we use the static solution for the simplest model of an elliptic disk-shaped crack in an elastic medium [15]. In this case, the variation of the crack volume is related only to the stresses normal to the crack surface.

Then, the displacement of the crack edges with respect to the equilibrium position is described by the standard solution [15]:

$$u(r, L) = \frac{4(1-\nu^2)\sigma_\perp}{\pi E}\sqrt{L^2 - r^2}, \tag{8}$$

where $\sigma_\perp = P + n_i\sigma_{ik}n_k$ are stresses normal to the crack surface, $\mathbf{n}$ is the corresponding normal vector, P is the fluid pressure at the borehole–crack intersection point, and r is the distance from the symmetry axis of the crack.

The variation of the crack volume is found by integrating Eq. (8):

$$V(L) = \int_0^L 2\pi r u(r, L)\,dr,$$

which gives

$$V = V_0\frac{P + n_i\sigma_{ik}n_k}{E}, \tag{9}$$

where $V_0 = \frac{8}{3}(1-\nu^2)L^3$ is the effective volume of the crack.

Since, on a scale much smaller than the wavelength, the fluid can be considered incompressible, the crack volume variation leads to a corresponding mass flow from the crack through the borehole–crack intersection plane $S = 2\pi R\Delta z$ (Δz is the effective thickness of the crack):

$$\rho_f\frac{dV}{dt} = \frac{dm}{dt} = \rho_f V_r(r = R, z, t)S. \tag{10}$$

Relations (9) and (10) allow us to determine the radial component of the velocity at the borehole–crack intersection point:

$$V_r(r = R, z, t) = \frac{V_0}{S}\frac{\partial}{\partial t}\left(\frac{P + n_i\sigma_{ik}n_k}{E}\right). \tag{11}$$

In the limit $\Delta z \longrightarrow 0$, at a constant mass flow through the surface S, this relation gives the expression for the velocity in the form of a point source

$$V_r(r = R, z, t) = \frac{V_0}{2\pi R}\delta(z)\frac{\partial}{\partial t}\left(\frac{P + n_i\sigma_{ik}n_k}{E}\right), \tag{12}$$

where $z = 0$ is the borehole–crack intersection point.

Since, in the above-mentioned limit $\Delta z \longrightarrow 0$, the velocity related to the fluid flow out of the crack is nonzero at only one point, then, combining Eqs. (4), (5), and (12), one can obtain the resulting equation describing the wave field inside the borehole in the presence of a crack:

$$\begin{aligned}&\frac{\partial^2 P}{\partial t^2} - c_{tw}^2\frac{\partial^2 P}{\partial z^2}\\ &= -2\rho_f c_{tw}^2\frac{\partial^2}{\partial t^2}\frac{\sigma_{\text{eff}}}{E} - \rho_f c_{tw}^2\frac{\delta(z)V_0}{\pi R^2}\frac{\partial^2}{\partial t^2}\left(\frac{P + n_i\sigma_{ik}n_k}{E}\right).\end{aligned} \tag{13}$$

This equation differs from Eq. (7) by the presence of a point source at the borehole–crack intersection point.

Now, to find the solutions to Eq. (13) that meet the radiation condition at infinity, one should specify the external wave field describing the incident seismic wave.

We take the borehole and the crack to lie in the far wave zone so that both the wavelength and the linear dimensions of the crack are much smaller than the radius of curvature of the incident seismic wave front. Hence, the local interaction of the seismic field with the crack and the borehole can be considered in the plane-wave approxiation. Then, the displacement vector in the seismic wave can be represented in the form

$$\mathbf{u}(\mathbf{r}, t) = \mathbf{u}U(\mathbf{r})f\left(t - \frac{\mathbf{e}\times\mathbf{r}}{c}\right), \tag{14}$$

where $\mathbf{u}$ is the unit vector of the wave polarization, $U(\mathbf{r})$ is the local wave amplitude, $\mathbf{e}$ is the unit vector in the

direction of propagation, and c is the velocity of propagation depending on the wave type (longitudinal or transverse). From Eq. (14) for the external seismic field, with the use of Hooke's law

$$\sigma_{ij} = 2\mu\varepsilon_{ij} + \lambda\delta_{ij}\varepsilon_{ll}$$

and the expression for the strain tensor ε_{ij}

$$\varepsilon_{ij} = \frac{1}{2}\left(\frac{\partial u_i}{\partial x_j} + \frac{\partial u_j}{\partial x_i}\right),$$

we explicitly determine the components of the stress tensor σ_{ik} of the medium in the seismic wave:

$$\begin{aligned}\sigma_{ik} &= -(\lambda(\mathbf{u}, \mathbf{e})\delta_{ik} + \mu(u_i e_k + u_k e_i))f'(\xi)U/c,\\ \sigma_{zz} &= -(\lambda(\mathbf{u}, \mathbf{e}) + 2\mu(\mathbf{u}, \mathbf{e}_z))f'(\xi)U/c,\\ \sigma_{ll} &= -(3\lambda + 2\mu)(\mathbf{u}, \mathbf{e})f'(\xi)U/c,\end{aligned} \tag{15}$$

where λ and μ are the Lamé constants of the elastic medium, $\mathbf{e}_z$ is the unit vector along the borehole axis, and $\xi = t - \mathbf{er}/c$ denotes the time in the moving coordinate system. In Eqs. (15), we took into account that the slowly varying amplitude is not differentiated in the far wave zone.

Using Eqs. (15) for the components of the stress tensor, one can easily obtain the relations for the effective stress in Eq. (13):

$$\begin{aligned}&n_i\sigma_{ik}n_k\\ &= -\mu(((c_l/c_s)^2 - 2)(\mathbf{u}, \mathbf{e}) + (\mathbf{u}, \mathbf{n})(\mathbf{n}, \mathbf{e}))\frac{U}{c}f'(\xi),\\ &\sigma_{\text{eff}} = -E\left(\frac{1}{2}(c_l/c_s)^2(\mathbf{u}, \mathbf{e}) - (\mathbf{u}, \mathbf{e}_z)\right)\frac{U}{c}f'(\xi),\end{aligned} \tag{16}$$

where the relations $\mu = \rho c_s^2$, $\lambda + 2\mu = \rho c_l^2$, and $E = 3\lambda + 4\mu$ are used.

Introducing the angle of incidence of the seismic wave with respect to the borehole axis γ: $\cos(\gamma) = -(\mathbf{e}, \mathbf{e}_z)$ and the apparent velocity of the seismic wave propagation along the borehole c_w: $c_w = c/\cos(\gamma)$, we can write the phase of the wave as $\xi = t + z/c_w$. In the new notation, Eq. (13) can be rewritten as

$$\begin{aligned}&\frac{\partial^2 P}{\partial t^2} - c_{tw}^2\frac{\partial^2 P}{\partial z^2} = \rho_f c_{tw}^2\tilde{D}_w\frac{U}{c}f'''(t + z/c_w)\\ &-\frac{\rho_f c_{tw}^2}{E}\frac{\delta(z)V_0}{\pi R^2}\left(\frac{\partial^2 P}{\partial t^2} - \mu\tilde{D}_{tw}\frac{U}{c}f'''(t + z/c_w)\right),\end{aligned} \tag{17}$$

where $\tilde{D}_w$ and $\tilde{D}_{tw}$ denote the following geometric factors:

$$\begin{aligned}\tilde{D}_w &= (\mathbf{u}, \mathbf{e})(c_l/c_s)^2 - 2(\mathbf{u}, \mathbf{e}_z),\\ \tilde{D}_{tw} &= ((c_l/c_s)^2 - 2)(\mathbf{u}, \mathbf{e}) + (\mathbf{u}, \mathbf{n})(\mathbf{n}, \mathbf{e}).\end{aligned}$$

In the absence of the crack, which is described by the second term in Eq. (17), the external field, which locally is a plane wave, creates only a compressional wave propagating in the surrounding medium along the borehole with the velocity c_w. The compressional wave is described by a partial solution of the inhomogeneous equation (17) in the absence of the singular term on the right-hand side,

$$\frac{\partial^2 P}{\partial t^2} - c_{tw}^2\frac{\partial^2 P}{\partial z^2} = \rho_f c_{tw}^2\tilde{D}_w\frac{U}{c}f'''(t + z/c_w), \tag{18}$$

and has the form [7]

$$P_w(t, z) = \rho_f c_{tw}^2 D_w\frac{U}{c}f'(t + z/c_w), \tag{19}$$

where D_w denotes a dimensionless factor depending on the parameters of the medium and the geometry of the problem,

$$D_w = \frac{(c_l/c_s)^2(\mathbf{u}, \mathbf{e}) - 2(\mathbf{u}, \mathbf{e}_z)}{1 - (c_{tw}/c_w)^2}.$$

The validity of solution (19) is easily checked by substituting it into Eq. (18).

It should be noted that external plane seismic waves do not excite Stoneley waves described by the general solution of the homogeneous equation (17). The Stoneley waves can be excited only at local inhomogeneities, which in our case are represented by the crack. Taking into account the radiation condition that only outgoing waves can exist at infinity, one can write the general solution to the homogeneous equation (17) in the form

$$P_{tw}(t, z) = \begin{cases}P_{tw}^+(t - z/c_{tw}), & z > 0\\ P_{tw}^-(t + z/c_{tw}), & z < 0,\end{cases} \tag{20}$$

where $P_{tw}^+(t - z/c_{tw})$ and $P_{tw}^-(t + z/c_{tw})$ are unknown functions to be determined. Since the pressure should be described by a continuous function, the condition

$$P_{tw}^+(t, z = 0) = P_{tw}^-(t, z = 0) = P_{tw}(t) \tag{21}$$

should be satisfied at the point $z = 0$. This allows relation (20) to be rewritten in the form

$$P_{tw}(t, z) = \begin{cases}P_{tw}(t - z/c_{tw}), & z > 0,\\ P_{tw}(t + z/c_{tw}), & z < 0.\end{cases} \tag{22}$$

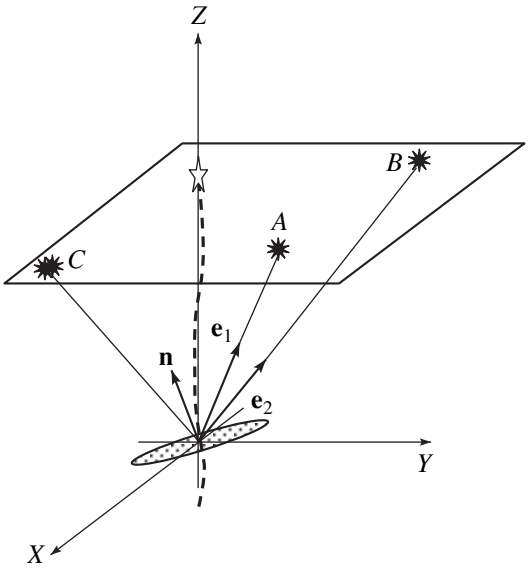

Fig. 2. Schematic diagram of the experiment on the determination of the crack normal.

The second condition for determining the functional dependence $P_{tw}(t)$ can be found by integrating Eq. (17) over a small vicinity of the point $z = 0$:

$$-c_{tw}^2\left(\frac{\partial P_{tw}(t - z/c_{tw})}{\partial z} - \frac{\partial P_{tw}(t + z/c_{tw})}{\partial z}\right)\Bigg|_{z=0} = \rho_f c_{tw}^2 \frac{V_0}{\pi R^2}\frac{\partial^2}{\partial t^2}\left(\frac{P_{tw}(t) + p_w(t) + n_i\sigma_{ik}n_k}{E}\right),$$

which can be finally written as

$$\ddot{P}_{tw}(t) + \frac{1}{\tau}\dot{P}_{tw}(t) = \rho_f c_{tw}^2 (D_{tw} - D_w)\frac{U}{c} f'''(t). \quad (23)$$

Here, we introduced the notations for the pressure relaxation time and the geometric factor D_{tw}:

$$\tau = \frac{\rho_f c_{tw}^2}{E}\frac{V_0}{c_{tw}\pi R^2}, \quad D_{tw} = \frac{\rho c_s^2}{\rho_f c_{tw}^2}\tilde{D}_{tw}.$$

After a single integration, Eq. (23) is reduced to a first-order equation

$$\dot{P}_{tw}(t) + \frac{1}{\tau}P_{tw}(t) = \rho_f c_{tw}^2 (D_{tw} - D_w)\frac{U}{c} f''(t), \quad (24)$$

whose solution at zero initial conditions can be written as

$$P_{tw}(t) = (D_{tw} - D_w)\int_0^t e^{-(t-\xi)/\tau} f''(\xi)\,d\xi. \quad (25)$$

Finally, the general solution of the inhomogeneous equation (17) can be represented in the form

$$P(t, z) = \begin{cases} P_w(t + z/c_w) + P_{tw}(t - z/c_{tw}), & z > 0 \\ P_w(t + z/c_w) + P_{tw}(t + z/c_{tw}), & z < 0, \end{cases} \quad (26)$$

where the functions $P_w(t)$ and $P_{tw}(t)$ are determined by Eqs. (19) and (25).

Consider now the procedure of reconstructing the crack orientation from the data of the VSP. The explicit analytical dependence of the amplitudes of Stoneley waves and compressional waves on the geometry of the problem allows one to formulate and solve the inverse problem of reconstructing the orientation of a crack crossing the borehole shaft by simultaneously measuring the amplitudes of both types of wave.

Let us examine the amplitude ratio of the Stoneley wave and the compressional wave:

$$\frac{P_{tw}(t_1)}{P_w(t_2)} = \left(\frac{D_{tw}}{D_w} - 1\right)Q(T, \tau), \quad (27)$$

where $Q(T, \tau)$ is a factor defined only by the pressure relaxation time τ and the time length of the incident seismic wave,

$$Q(T, \tau) = \frac{1}{f'(t_2)}\int_0^{t_1} d\xi\, e^{-(t_1 - \xi)/\tau} f''(\xi).$$

Amplitude ratio (27) relates the problem parameters to the measurable quantities, which allows us to solve the inverse problem. If the wave field in the borehole is excited by a longitudinal seismic wave, expression (27) can be rewritten as

$$\frac{P_{tw}}{P_w} = \left(\frac{\rho c_s^2}{\rho_f c_{tw}^2}\frac{1 - (c_{tw}/c_w)^2}{(c_l/c_s)^2 - 2(c_l/c_w)^2} \times ((c_{tw}/c_l)^2 - 2(1 - \cos^2\Theta)) - 1\right)Q(T, \tau), \quad (28)$$

where, again, $c_w = c/\cos(\gamma)$ is the apparent velocity of the compressional wave propagating along the borehole, and the angles γ and Θ define the orientation of the borehole and the crack normal, respectively, relative to the propagation direction of the longitudinal seismic wave: $\cos(\gamma) = (\mathbf{e}, \mathbf{e}_z)$, $\cos(\Theta) = (\mathbf{e}, \mathbf{n})$. All the quantities in Eq. (28) can be directly measured in a geophysical experiment, except for the angle Θ defining the crack orientation. It is this fact that allows one to pose and solve the problem of determining the crack orientation from hydrophone measurements.

On the basis of relation (28), we propose the following technique for reconstructing the crack orientation. The VSP data from three or more surface explosions is examined (see Fig. 2). The parameters ρ, ρ_f, c_l, and c_s are considered to be known from the borehole data.

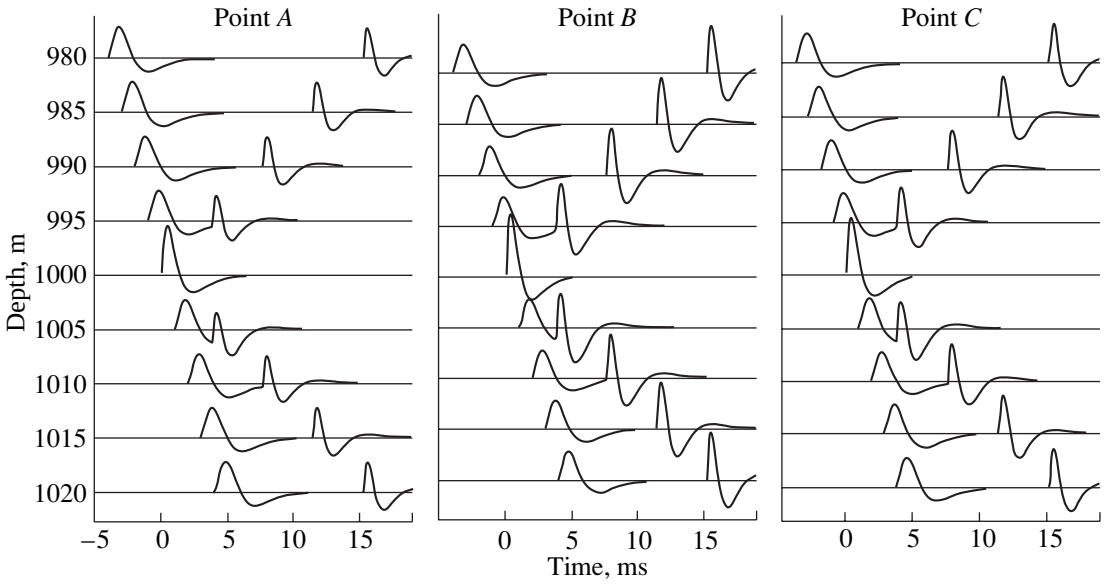

Fig. 3. Synthetic hydrophone profiles in the borehole after explosions at the points *A*, *B*, and *C*.

Then, from the VSP hydrophone data, one can determine the velocities c_w and c_{tw} and the amplitude ratio P_{tw}/P_w. In addition, if the frequency spectra of seismic waves coming from different explosion points differ only slightly, the factor $Q(T, \tau)$ can be considered to be constant. This can also be achieved by a proper frequency filtration of the seismograms so that the compressional waves spectrum be the same in all seismograms.

Then, we assume that, apart from the hydrophones, there is also a geophone in the borehole, which allows us to determine the direction of the longitudinal seismic wave arrival. For example, let three batches of seismograms from three different explosions be recorded so that $\mathbf{e}_1$, $\mathbf{e}_2$, $\mathbf{e}_3$ are local basis vectors of the propagation directions of seismic waves. Then, the cosines corresponding to these directions are $\cos(\Theta_i) = (\mathbf{e}_i, \mathbf{n})$, $i = 1, 2, 3$. Thus, there is a system of three equations in four quantities: $Q(T, \tau) = \text{const}$ and $\{\cos(\Theta_i)\}$, $i = 1, 2, 3$. To obtain a closed system of equations, we consider the vectors $\{\mathbf{e}_i\}$, $i = 1, 2, 3$ as a basis of an oblique coordinate system. Then, the normal unit vector $\mathbf{n}$ can be expanded in terms of this basis to obtain the relation

$$\cos(\Theta_j)\alpha_{ji}^{-1}\cos(\Theta_i) = 1. \tag{29}$$

Relation (29) can be obtained by the following transformations. Let $\mathbf{n} = n_i\mathbf{e}_i$. Then, the normalization condition can be written in the form

$$1 = (\mathbf{n}, \mathbf{n}) = n_i\mathbf{e}_i \times n_j\mathbf{e}_j = n_i(\mathbf{e}_i, \mathbf{e}_j)n_j,$$

or, introducing the matrix $\alpha_{ij} = \alpha_{ji} = (\mathbf{e}_i, \mathbf{e}_j)$, in the form

$$n_i\alpha_{ij}n_j = 1.$$

Besides, $\cos(\Theta_i) = (\mathbf{e}_i, \mathbf{n}) = (\mathbf{e}_i, n_j\mathbf{e}_j) = n_j\alpha_{ij}$.

If an inverse matrix α_{ij}^{-1} is introduced: $\alpha_{ik}^{-1}\alpha_{kj} = \alpha_{jk}\alpha_{ki}^{-1} = \delta_{ij}$, the condition $\cos(\Theta_i) = \alpha_{ij}n_j$ yields the equation $n_i = \alpha_{ij}^{-1}\cos(\Theta_j)$ leading, in turn, to relation (29).

The approximate values of $\{\cos(\Theta_i)\}$ ($i = 1, 2, 3$) can be found as a solution to the minimum problem for the function

$$F(\cos(\Theta_1), \cos(\Theta_2), \cos(\Theta_3)) = (G_1 - G_2)^2 + (G_1 - G_3)^2 + (G_2 - G_3)^2 + (1 - G_0)^2, \tag{30}$$

where

$$G_i = \frac{1}{Q(T, \tau)} = \frac{P_w}{P_{tw}}\left(\frac{\rho c_s^2}{\rho_f c_{tw}^2}\frac{1 - (c_{tw}/c_{wi})^2}{(c_l/c_s)^2 - 2(c_l/c_{wi})^2} \times ((c_{tw}/c_l)^2 - 2(1 - \cos^2\Theta_i)) - 1\right) \tag{31}$$

and c_{wi}, $i = 1, 2, 3$, is the apparent velocity of the seismic wave propagation along the borehole axis, i being the number of an explosion point. The last term in Eq. (30) that contains the function G_0,

$$G_0 = \cos(\Theta_j)\alpha_{ji}^{-1}\cos(\Theta_i), \tag{32}$$

appears due to the normalization condition (29).

After the minimum of $F(\cos(\Theta_i))$ is found, an estimate of the direction $\mathbf{n}$ can be made by the formula

$$\mathbf{n} = \cos(\Theta_j)\alpha_{ij}^{-1}\mathbf{e}_i. \tag{33}$$

To illustrate the proposed technique, we consider an example of reconstructing the crack orientation using

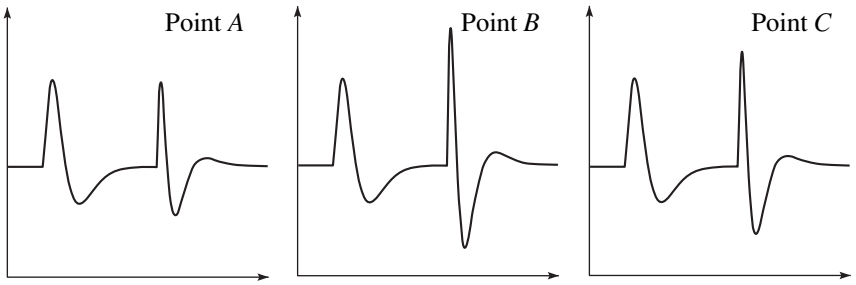

Fig. 4. Amplitude ratios of the tube wave and the compressional wave.

the synthetic seismograms obtained by solving the direct problem for Eq. (13). In solving the inverse problem, we assume that we have at hand the seismograms from three different surface explosions, which are recorded by the set of borehole hydrophones, and that we know the propagation directions of longitudinal waves from these explosions and the local properties of the external elastic medium and the borehole fluid, namely, the density and the velocities of longitudinal and transverse waves. Obtaining such a set of data in field conditions should present no great difficulties.

Thus, we consider a vertical borehole in a homogeneous medium and assume that, at a depth of 1 km, the borehole is crossed by a crack with the normal $\mathbf{n} = \{-0.882, 0.165, 0.441\}$ and the volume $V_0 = 0.1$ m^3. The external elastic medium has the parameters $\rho = 2.68 \times 10^3$ kg/m^3, $c_l = 4.64 \times 10^3$ m/s, and $c_s = 2.39 \times 10^3$ m/s; the fluid parameters are $\rho_f = 0.8 \times 10^3$ kg/m^3 and $c_f = 1.379 \times 10^3$ m/s; and the borehole radius is $R = 0.08$ m. The explosion points are located on the surface at the points $A = \{400\text{ m}, 0\text{ m}\}$, $B = \{-400\text{ m}, 200\text{ m}\}$, and $C = \{-400\text{ m}, -400\text{ m}\}$ in the Cartesian coordinate system with the center at the borehole axis. The wave field inside the borehole is measured by a chain of hydrophones spaced at 5-m intervals. The model time dependence of the displacement vector in the seismic wave has the form $f(t) = (t/T)^3\exp(-t/T)$, where $T = 0.65 \times 10^{-3}$ s is the effective duration of the seismic wave.

Figure 3 demonstrates the synthetic seismograms calculated for the three explosions with the parameters specified above. The seismograms show distinctly both the longitudinal compressional wave and two Stoneley waves generated at the crack–borehole intersection point.

In the framework of the homogeneous model of the external medium, for various explosion points, one can easily calculate the propagation directions $\mathbf{e}_i$ of the seismic wave front, the propagation velocities c_{tw} and c_{wi} of the Stoneley waves and compressional waves, and the ratio P_{tw}/P_w of their amplitudes taken from minimum to maximum. The results of these calculations are presented in Table 1.

In a real experiment, all measured data have limited precision. To simulate this situation, we determined the velocities of tube waves and compressional waves and their amplitude ratio by the graphic method from the synthetic seismograms shown in Fig. 3. The amplitude ratio of the Stoneley waves and compressional waves was found with the help of the scaled-up fragments of the seismograms shown in Fig. 4. The corresponding data are presented in Table 2.

Using the data from Table 2, we can write the expressions for the components of function (30) in the form

$$G_1 - G_2 = 2.3959 + 7.9928\cos^2(\Theta_1) - 4.8845\cos^2(\Theta_2),$$

$$G_1 - G_3 = 1.6429 + 7.9928\cos^2(\Theta_1) - 5.8614\cos^2(\Theta_3),$$

$$G_2 - G_3 = 0.7530 - 4.8844\cos^2(\Theta_2) + 5.8613\cos^2(\Theta_3),$$

$$G_0 = 2.1025\cos^2(\Theta_1) + 4.3000\cos^2(\Theta_2) + 3.9325\cos^2(\Theta_3) - 2.0647\cos(\Theta_1)\cos(\Theta_2) - 1.0827\cos(\Theta_1)\cos(\Theta_3) - 5.9782\cos(\Theta_2)\cos(\Theta_3).$$

Table 1. Calculated values of measurable parameters of the problem

Explosion points	$\mathbf{e}_i$	c_{tw}, m/s	c_w, m/s	P_{tw}/P_w
A	{0.371, 0.0, 0.928}	1315	4997	1.089
B	{–0.365, 0.182, 0.912}	1315	5082	1.814
C	{–0.348, –0.348, 0.870}	1315	5330	1.482

Table 2. Measured values of the problem parameters

Explosion points	$\mathbf{e}_i$	c_{tw}, m/s	c_w, m/s	P_{tw}/P_w
A	{0.371, 0.0, 0.928}	1400	5000	1.1
B	{–0.365, 0.182, 0.912}	1400	5000	1.8
C	{–0.348,–0.348, 0.870}	1400	5000	1.5

The minimum of the function $F(\cos(\Theta_1), \cos(\Theta_2), \cos(\Theta_3))$ was found numerically by the gradient-descent method. Two local minima were found.

At the first minimum with a value of 9×10^{-7}, the cosines of the angles in the oblique coordinate system were

$$\cos(\Theta_1) = -0.0030, \quad \cos(\Theta_2) = 0.7003,$$
$$\cos(\Theta_3) = 0.5294,$$

which, according to Eq. (32), corresponds to the following estimate of the crack normal:

$$\mathbf{n}^* = \{-0.896, 0.264, 0.355\}.$$

For the second minimum with a value of 8×10^{-8}, the respective values were

$$\cos(\Theta_1) = 0.5270, \quad \cos(\Theta_2) = 0.9721,$$
$$\cos(\Theta_3) = 0.8118, \quad \mathbf{n}_2^* = \{-0.566, 0.220, 0.794\}.$$

Note that exact values of the same quantities were

$$\cos(\Theta_1) = 0.0819, \quad \cos(\Theta_2) = 0.7549,$$
$$\cos(\Theta_3) = 0.6334,$$
$$\mathbf{n} = \{-0.882, 0.165, 0.441\}.$$

The quality of the reconstruction of the crack orientation can be assessed by the formula $\delta = \sqrt{1 - |(\mathbf{n}, \mathbf{n}^*)|}$, which gives $\delta_1 = 0.09$ in the first case and $\delta_2 = 0.33$ in the second case. In practice, an ambiguity in the reconstruction of crack orientation can be avoided by using data from another series of explosions.

Thus, the results presented above constitute a foundation for a method of determining the orientation of isolated cracks crossing a borehole by means of processing the hydrophone VSP data.

REFERENCES

1. M. A. Biot, J. Appl. Phys. **23**, 997 (2000).
2. J. E. White, *Underground Sound. Application of Seismic Waves* (Elsevier, Amsterdam, 1983; Nedra, Moscow, 1986).
3. C. H. Cheng and M. N. Toksoz, Geophysics **46**, 1042 (1981).
4. G. I. Petrashen', L. A. Molotkov, and P. V. Krauklis, *Waves in Layered Homogeneous Isotropic Elastic Media* (Nauka, Leningrad, 1985), Vol. 2.
5. C. F. Huang and J. A. Hunter, Pap.–Geol. Surv. Can., No. 81-1A, 361 (1981).
6. A. M. Ionov and G. A. Maksimov, Akust. Zh. **45**, 354 (1999) [Acoust. Phys. **45**, 311 (1999)].
7. F. L. Paillet and J. E. White, Geophysics **47**, 1215 (1982).
8. B. E. Hornby, D. L. Johnson, K. W. Winkler, and R. A. Plumb, Geophysics **54**, 1274 (1989).
9. X. M. Tang and C. H. Cheng, Geophys. Prospect. **41**, 165 (1993).
10. S. Kostek, D. L. Johnson, and C. J. Randall, Geophysics **63**, 800 (1998).
11. S. Kostek, D. L. Johnson, K. W. Winkler, and B. E. Hornby, Geophysics **63**, 809 (1998).
12. Y. D. Li, W. Rabbel, and R. Wang, Geophys. J. Int. **116**, 739 (1994).
13. A. M. Ionov and G. A. Maximov, Geophys. J. Int. **124**, 888 (1996).
14. A. M. Ionov, O. V. Kozlov, and G. A. Maksimov, Akust. Zh. **41**, 603 (1995) [Acoust. Phys. **41**, 529 (1995)].
15. V. Z. Parton and E. M. Morozov, *Mechanics of Elastic–Plastic Fracture* (Nauka, Moscow, 1974).

Translated by A. Kruglov

Acoustical Physics, Vol. 48, No. 3, 2002, pp. 292–296. Translated from Akusticheskiĭ Zhurnal, Vol. 48, No. 3, 2002, pp. 340–345.
Original Russian Text Copyright © 2002 by Zverev, Korotin.

Effect of Surface Reverberation on the Selection of a Diffracted Signal

V. A. Zverev and P. I. Korotin

Institute of Applied Physics, Russian Academy of Sciences, ul. Ul'yanova 46, Nizhni Novgorod, 603600 Russia

e-mail: zverev@hydro.appl.sci-nnov.ru

Received May 3, 2001

Abstract—An experiment is described in which a wave scattered by a rough water surface is the factor by virtue of which the signal diffracted by a moving scatterer is received with confidence. Experimental corroboration of this fact is presented, and the origin of this phenomenon is revealed. © *2002 MAIK "Nauka/Interperiodica".*

For acoustic detection and ranging, a signal scattered by the water surface is an essential interference. This interference is of particular significance for the forward-scattering location [1–4] and bistatic sonar, which is close to the forward-scattering location. We were, then, very surprised with the result of an experiment in which we recorded a signal identified by the majority of indexes as the signal scattered by the water surface, and it appeared that this signal favored the selection of the scatterer rather than hindered the reception of the weak diffracted signal.

First, we describe the experiment and give its result. Then, we advance a hypothesis on the role that surface reverberation plays in the reception of a diffracted signal and argue for this hypothesis.

The case of interest is the experiment whose geometry and part of the results are described in our previous papers [4–6]. An acoustic path 300 m in length was realized in a lake. The lake depth along the path was about 15 m. The source was positioned near the bottom, a horizontal receiving array was submerged to a depth of 4 m, and a similar vertical array was installed near it. The experiment was carried out in summer, when the water temperature exceeded 20°C near the surface and was equal to 4°C near the bottom. This temperature difference resulted in a sound velocity gradient that favored, due to the refraction, the formation of a bottom sound channel. In the experiment under consideration, a scatterer was mounted across the path of sound propagation at a distance of about 50 m from the receiving arrays. The scatterer was a plugged cylindrical tube filled with ballast; its length was about 5 m and diameter, 0.5 m. The scatterer traveled at a depth of 7 m with a constant velocity of about 0.6–0.65 m/s in such a manner that during the experiment it crossed twice the imaginary line connecting the source and the center of the receiving array (first, traveling in one direction and then, in the opposite direction). The duration of the scatterer motion in each direction was about 3 min with an inter-tack pause of a minute and a half.

The receiving arrays were 12-m-long chains of 64 equidistant hydrophones. The source operated in the polyharmonic mode and transmitted four discrete frequencies in the range between approximately 1.3 and 2.5 kHz. A tonal beacon with a frequency of 2.9 kHz was mounted on the scatterer. In what follows, the radiation at two frequencies will be our main concern; we will denote them frequency no. 1 (1373.29 Hz) and frequency no. 2 (2498.626 Hz).

The signals were received, recorded, and processed according to the procedures described in [4, 5]. For the signal processing, we used the dark field algorithm [4]. This algorithm subtracts the logarithms of the complex amplitudes of signals successively received by each element of the array at constant time intervals (this procedure safeguarded against reverberation). Then, we expanded the received signal in the Fourier series with respect to the spatial coordinates of the array elements (thus effectuating the angular scanning of the array pattern) and carried out a temporal filtration (for additional safeguard against reverberation, if required).

Figures 1 and 2 show the results obtained in this experiment. From these figures, one can see that the motion of the scatterer in the *sine of antenna scanning angle–time* coordinates is quite discernible for both frequency no. 1 and frequency no. 2. The motion is clearly seen for the lowest and highest frequencies of the range under investigation; for intermediate frequencies, the pattern is less distinct.

The fundamental point is the fact that different filters favoring the selection of the signal from the scatterer were used to ensure prominent target echoes in Figs. 1 and 2. The pattern of Fig. 1 is obtained using the dark field algorithm [4] without the subsequent filtering. In this case, the observed signal has a frequency band from –3 to +3 Hz relative to the carrier frequency. To obtain the scatterer motion pattern shown in Fig. 2,

1063-7710/02/4803-0292$22.00 © 2002 MAIK "Nauka/Interperiodica"

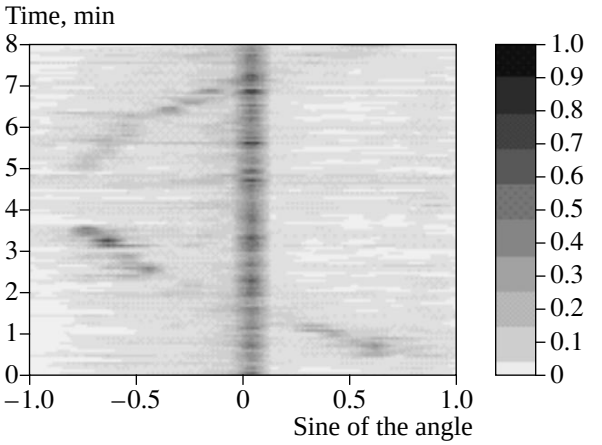

Fig. 1. Field of view of the array at frequency no. 1 for the scatterer traveling across the path of the sound propagation.

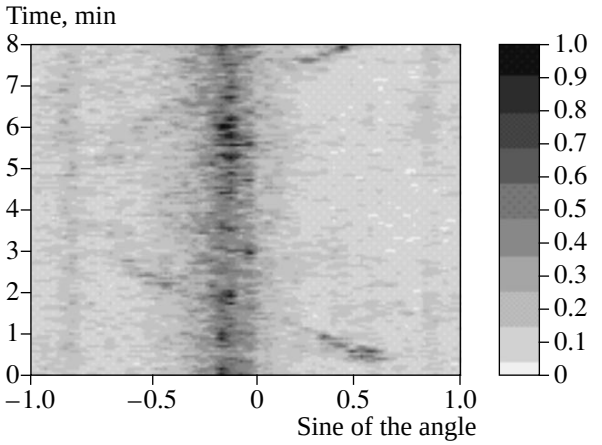

Fig. 2. Field of view of the array at frequency no. 2 for the scatterer traveling across the path of the sound propagation.

an additional frequency filtration is required in the frequency band from –1 to –0.6 Hz in order to make the scatterer motion more pronounced in the direction away from the array and in the frequency band from 0.6 to 1 Hz for the scatterer motion in the opposite direction. Without such a frequency filtration, the pattern in Fig. 2 will be masked with noise hiding the whole path of the scatterer.

To determine in more detail the origin of the difference between the signals received at frequencies nos. 1 and 2, we carried out additional studies.

Figure 3 shows the realizations of signals presented in Figs. 1 and 2 as functions of time for two bearings. We choose the angles so as to cover (for both frequencies 1 and 2) the scatterer path segments well discernible in Figs. 1 and 2. Additionally, Fig. 3 shows the instants at which these realizations were gated. The gate duration measured about 5 s. One gate was set in place of the maximal signal that corresponded to the instant at which the traveling scatterer crossed the azimuth corresponding to the realization under consideration. The other gate corresponded to the instant at which the scatterer was at an angle far from the above azimuth. In the latter gate, we received only the interference. Figure 4 shows the signal spectra in these gates. It can be seen that the level is the only difference between the spectrum of the signal at frequency no. 1 and the reverberation spectrum. The shapes of the spectra of the signal and interference are almost coincident. At frequency no. 2, the signal and interference spectra coincide in shape and level everywhere except for the range from –1 to –0.6 Hz. In this frequency range, the signal spectrum drastically differs from the reverberation spectrum in its level.

This effect is clearly seen in Figs. 5 and 6. These figures show the current spectra of the temporal realizations shown in Fig. 3. To obtain the current spectrum, we divided the temporal realization into 5-s segments. Then, each segment was subjected to spectral analysis. Figures 5 and 6 show the whole set of the corresponding spectra in the *frequency–segment number (time)* coordinates. In Fig. 5, the instant at which the scatterer crosses a certain azimuth is seen as the light strip (at the 3.5-min point); in this case, the shape of the spectrum does not differ from the reverberation spectrum at the previous and following instants.

In Fig. 6, the instant at which the scatterer crosses the azimuth is seen as the light spot covering a narrow

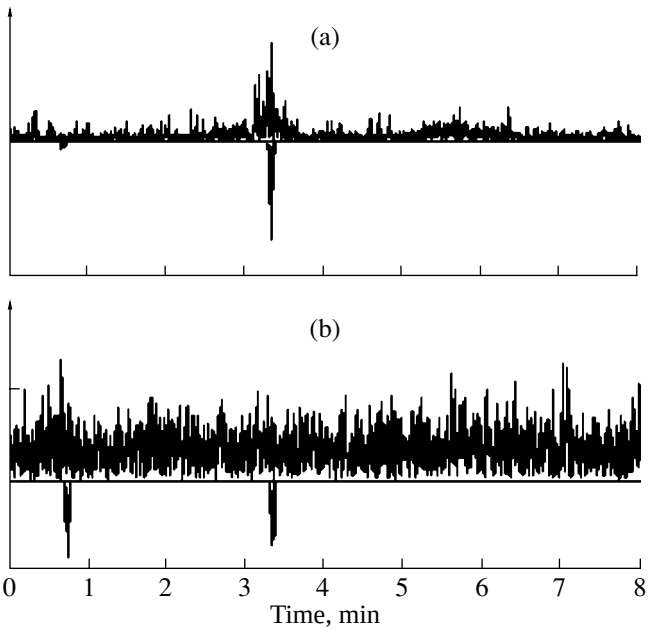

Fig. 3. Array responses for two bearings as a function of time. (a) The upper plot corresponds to $\sin(\varphi) = -0.6$ at frequency no. 1 (Fig. 1). (b) The lower plot corresponds to $\sin(\varphi) = +0.6$ at frequency no. 2 (Fig. 2). The downward peaks correspond to the instants (gates) used later in the spectral analysis.

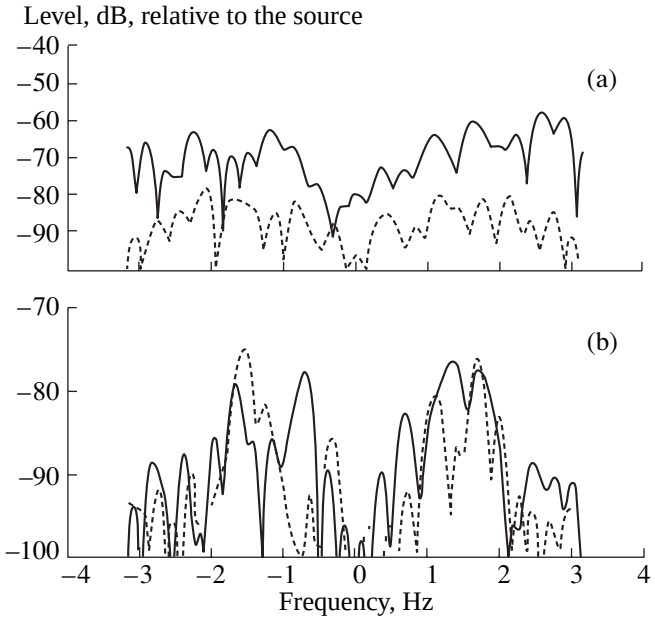

Fig. 4. Signal spectra for the gates shown in Fig. 3. The solid lines represent the spectra in the gates that contain the signals from the scatterer. The dashed lines show the spectra in the gates that contain the reverberation. (a) Spectra at frequency no. 1 and (b) spectra at frequency no. 2.

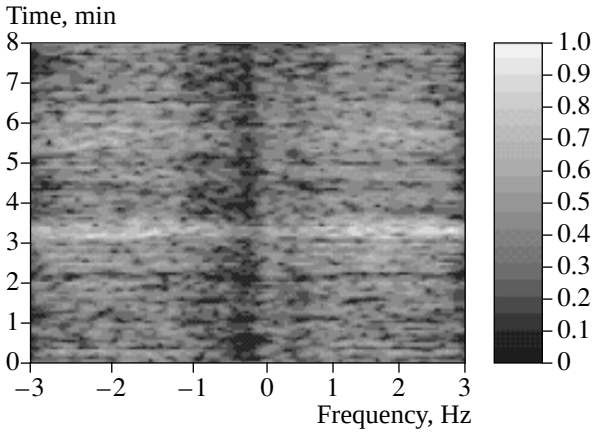

Fig. 5. Current spectrum of the signal shown in Fig. 3a.

portion of the spectrum; its coordinates are 0.5 min in time and slightly below –1 Hz in frequency.

We now come to the discussion of the experimental results. The expected result of the known physical nature was realized at frequency no. 2. The signal of the scatterer is distinguished against the background of reverberation due to the Doppler effect. The Doppler frequency is defined approximately (neglecting the ray bending) as

$$\Delta f = f\frac{v}{c}[\sin(\varphi_1) + \sin(\varphi_2)], \qquad (1)$$

where f is the frequency of transmitted sound, v is the velocity of the scatterer, c is the velocity of sound, $\sin(\varphi_1)$ is the function of the angle of observation (this quantity is plotted on the abscissa in Figs. 1 and 2), and $\sin(\varphi_2)$ is the function of the angle of sound incidence on the scatterer. If we set in Eq. (1) the parameters for the instant corresponding to the gate shown in Fig. 3 for frequency no. 2, we obtain approximately 0.8 Hz. The maximum of the spectrum shown in Fig. 4 for frequency no. 2 occurs at a frequency of about 0.7 Hz, and the width of this maximum at a level of 3 dB is about 0.2 Hz. Taking into account the accuracy with which we know the parameters used in Eq. (1) and the approximate nature of Eq. (1), this value can be considered as more or less coincident with the estimate obtained from Eq. (1).

The agreement between the spectrum of the signal received from the scatterer and the spectrum calculated by Eq. (1) unambiguously determines the physical model of the phenomenon. The main feature of this phenomenon is the fact that the field received from the scatterer is the field that is immediately diffracted by the scatterer body. We observed with confidence this model in the majority of other experiments. On the basis of just this model, we determined in [5] such parameters as the size of the scatterer and the angle in the vertical plane at which the field diffracted by the scatterer arrives at the horizontal array.

The situation is different for the result of the experiment at frequency no. 1. The trace of the scatterer path in Fig. 1 does not disappear after rejecting all frequencies below 1 Hz with a filter. Based on the fact that frequency no. 2 is lower than frequency no. 1 by a factor of almost 2, this frequency range covers the whole region of possible Doppler frequencies with a good safety margin. Therefore, the physical nature of the effect occurring at frequency no. 1 is totally different from that at frequency no. 2. This is not a hypothesis but an experimentally established fact.

We explain this fact with the use of the following model. The coincidence of the spectrum of the signal scattered at frequency no. 1 with the spectrum of reverberation suggests a relationship between the observed effect and the surface reverberation. The cause of this relationship may be as follows. The diffracted signal has a directional pattern that depends on the relationship between the scatterer size and the signal frequency. Hence, the diffracted field at higher frequency no. 2 is concentrated near the forward direction and does not touch the surface. At lower frequency no. 1, the scattering pattern significantly widens in the vertical plane; as a result, it touches the surface and the contribution of the surface reverberation of the secondary field increases. An additional point is that the portion of the energy scattered by the rough surface in the specular direction (i.e., in the forward direction) also increases with decreasing frequency. Collectively, these factors

make possible the selection of rays that touch the surface after scattering and those that do not.

An implementation of the frequency selection of the secondary field requires that the scatterer travels. The secondary field of a moving scatterer has the Doppler shift from the outset; after the reflection from the rough surface, its modulation spectrum is additionally widened, and the frequency features of the resulting spectrum appear different from those in the modulation spectrum of the surface reverberation of the primary field. Taking into account the general decrease in the reverberation interference for the lower frequency of location and the transfer of modulation frequencies in the region above the frequency of the direct signal modulation by the surface roughness, these frequency features make possible the selection of the scatterer in conditions under which the scatterer is not discernible in the direct scattering field because of the decreased scattering cross section.

From a comparison of the frequency spectra of signals at frequencies nos. 1 and 2, it follows that the level of the reverberation interference significantly decreases with increasing frequency. In the temporal spectrum of the signal at frequency no. 2, one can see intense peaks in the range between 1 and 1.5 Hz due to Bragg scattering by the surface roughness. No such peaks occur at frequency no. 1. For the experiment under consideration, the nature of the formation of the Bragg scattering is described in [6] along with the features of the reverberation spectrum in space and time. The surface regions responsible for the Bragg scattering in the experimental conditions for transmitted frequencies above 1.5–2 kHz are also determined in [6].

Simultaneous measurements with the use of the vertical array support the above hypothesis concerning the role of the surface scattering of the signal diffracted by the scatterer at frequency no. 1. These measurements demonstrate the experimental conditions of location with reference to the contributions of the bottom and surface reverberation and the direct ray. Figure 7 shows the spatial spectra of signals received with the vertical array as functions of time for the initial 2.5 min of the same tack. Figure 7a shows the signal of the omnidirectional (both in the vertical and horizontal planes) beacon mounted on the scatterer. The beacon signal significantly exceeded the reverberation interference and was discernible without the use of additional filters. Figure 7b shows the signal at frequency no. 1 after rejecting the carrier in the frequency band ±1 Hz. The signal at frequency no. 2 (Fig. 7c) was filtered in the frequency band from ±0.6 to ±1 Hz. The negative angles of arrival correspond to waves approaching the array from above (i.e., from the surface), and the positive angles correspond to waves approaching the array from below (i.e., from the bottom). Comparing Figs. 7a and 7b, one can see that, in both cases, most signals arriving at the array are reflected and scattered by the surface, the contribution of the bottom reverberation being small. It is

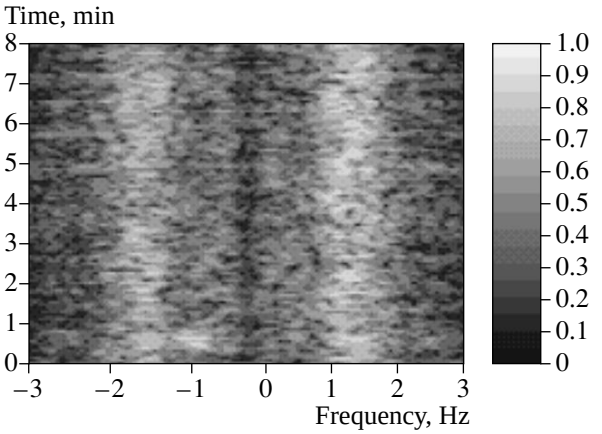

Fig. 6. Current spectrum of the signal shown in Fig. 3b.

clearly seen how the angle of wave arrival at the array decreases with increasing distance to the scatterer. At frequency no. 2 (Fig. 7c), the diffracted signal has a different structure; it is maximal at the instant of the bearing to the transmitted signal, because it is formed by the direct ray that touches neither the surface nor the bottom. Therefore, at lower frequency no. 1, the signal from the scatterer arrives at the array predominantly from the surface, while, at higher frequency no. 2, the scattered field arrives at the receiving array without touching the surface, and its Doppler shift is governed solely by the scatterer motion. The result of the experiment with the vertical array used to receive diffracted signals together with the beacon signal is not only a necessary but also a sufficient means for proving the suggested hypothesis about the physical nature of the signal at frequency no. 1.

Quantitative proof of the model of diffracted field formation in conditions of heavy surface roughness is a very difficult task, because the observed scattering effects are very small (they are discernible only with the use of the dark field method, which ensures a gain of about 50 dB [4]); in addition, only scarce data are available on the surface roughness.

In conclusion, we describe an additional, experimentally observed positive effect caused by the surface reverberation. During the measurements, we showed that, for the frequency range under consideration, the results of bistatic dark-field acoustic observations of the scatterer in conditions of heavy winds and, hence, heavy surface roughness appear to be better than in calm conditions. We observed the effect of the scattering cross section increase for roughness heights starting from 20–30 cm with the use of an omnidirectional insonifying radiator. In this case, the scatterer appears discernible with a good signal-to-noise ratio during the whole tack (+/–60° relative to the bearing to the insonifying radiator, i.e., to the bearing to the transmitted signal). Sometimes, this effect manifests itself in the fact that the scattering becomes discernible not only at the

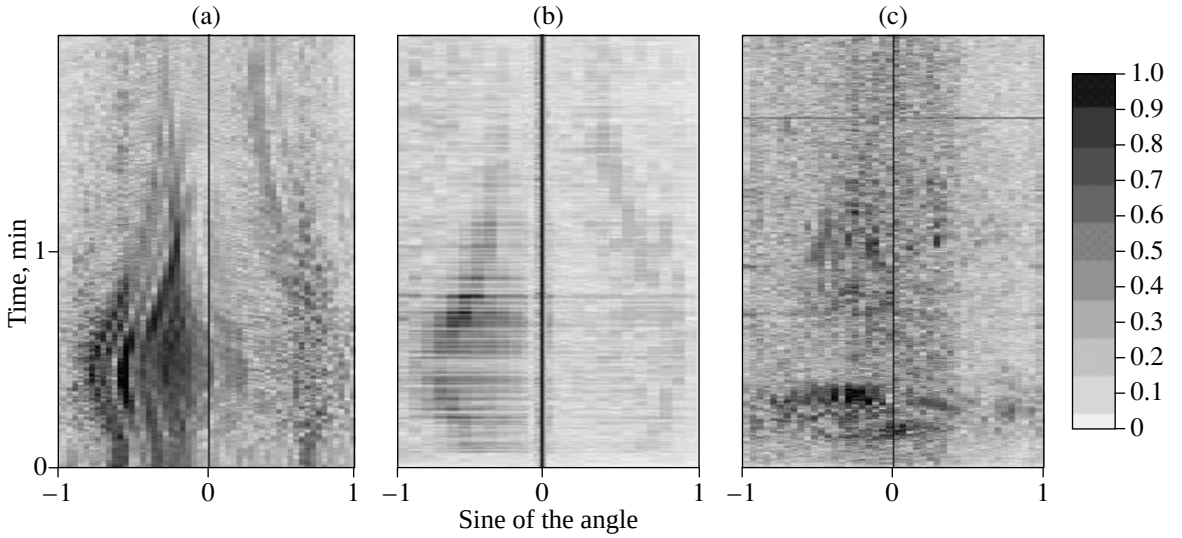

Fig. 7. Patterns of the spatial spectra of signals received by the vertical array at (a) the frequency of the radiator mounted on the traveling scatterer, (b) frequency no. 1, and (c) frequency no. 2 in the angle (spatial frequency)–time coordinates.

bearing to the transmitted signal, but also in bistatic observations for certain angular ranges (for large observation bearings). The magnitude of the effect of the scattering cross-section increase in the bistatic range of bearings measures about 5–6 dB when the tack-to-tack scatter of the scatterer response and the interference level in the same conditions measures about 2 dB. This means that the signal-to-noise ratio (both the interference and the scatterer response vary) at the tack during calm conditions differs by 5–6 dB from the tack during conditions with a wind velocity of 8–10 m/s.

This effect is related to the surface reverberation in conditions in which the bistatic signal from the scatterer becomes comparable with the scattered insonifying signal of the surface reverberation, which operates in the forward-scattering mode. In conditions of isotropic roughness and for an omnidirectional radiator, the surface reverberation increases more or less uniformly for all bearings of the receiving array; in these conditions, the scatterer appears to be more actively insonified by the surface for all angles in the horizontal plane, and its scattering cross section increases, which makes the scatterer discernible during the whole tack. In the case of anisotropic roughness, the angular dependence of the surface reverberation includes prominent peaks appearing in the horizontal plane and depending on the propagation direction of the surface roughness; correspondingly, reverberation at the receiving array also has peaks in its angular dependence. The effect of the reverberation insonification is maximal at the instant the scatterer crosses the surface scattering pattern peak directed to the receiving array; this is a version of the forward scattering situation but with the insonification by reverberation. This experimentally observed effect is of interest for further theoretical analysis and estimates, because it is of certain practical significance, e.g., in problems of the type considered in [7].

ACKNOWLEDGMENTS

We thank B.M. Salin, A.L. Matveev, and V.I. Turchin for the arrangement of the experiment and discussions. We also thank the anonymous reviewer whose essential remarks allowed us to improve the paper.

This work was supported by the Russian Foundation for Basic Research, project nos. 00-15-96741, 99-02-16401, and 01-02-17380.

REFERENCES

1. A. B. Gershman, V. I. Turchin, and V. A. Zverev, IEEE Trans. Signal Process. **43** (10), 2249 (1995).
2. V. A. Zverev, Akust. Zh. **42**, 220 (1996) [Acoust. Phys. **42**, 192 (1996)].
3. V. A. Zverev, Akust. Zh. **44**, 456 (1998) [Acoust. Phys. **44**, 389 (1998)].
4. V. A. Zverev, Akust. Zh. **46**, 75 (2000) [Acoust. Phys. **46**, 62 (2000)].
5. V. A. Zverev, P. I. Korotin, A. L. Matveev, *et al.*, Akust. Zh. **46**, 650 (2000) [Acoust. Phys. **46**, 569 (2000)].
6. V. V. Bredikhin, A. V. Lebedev, and B. M. Salin, Preprint No. 490, IPF RAN (Nizhni Novgorod Inst. of Applied Physics, Russian Academy of Sciences, 1999).
7. P. Runkle, L. Carin, L. Couchman, *et al.*, J. Acoust. Soc. Am. **106**, 605 (1999).

Translated by A. Vinogradov

Acoustical Physics, Vol. 48, No. 3, 2002, pp. 297–304. Translated from Akusticheskiĭ Zhurnal, Vol. 48, No. 3, 2002, pp. 346–353.
Original Russian Text Copyright © 2002 by Zlobina, Kasatkin.

Piston Acoustic Radiator in an Impedance Screen of a Pekeris Waveguide

N. V. Zlobina and B. A. Kasatkin

Institute of Marine Technology Problems, Far East Division, Russian Academy of Sciences, ul. Sukhanova 5a, Vladivostok, 690950 Russia

e-mail: kasatkas@marine.febras.ru

Received January 10, 2001

Abstract—A model problem of seismic hydroacoustics is studied for a piston radiator inserted in an impedance screen that coincides with the lower boundary of a Pekeris waveguide. The radiation resistance of the piston is numerically calculated as a function of the screen type and parameters of the radiator and the waveguide.
© 2002 MAIK "Nauka/Interperiodica".

The operation of directive receiving and transmitting systems in a waveguide has specific features that are governed by the mode structure of the sound field. These features have been studied in detail for horizontal and vertical linear arrays that operate in a waveguide with totally reflecting boundaries [1, 2]. The same is true for vertical cylindrical antenna arrays or a combination of them in the Pekeris waveguide [3, 4]. In particular, these studies analyze the frequency dependences of the radiation resistance for vertical cylindrical arrays, along with the distribution of the acoustic radiation power between the waveguide and the halfspace, this distribution being important in estimating the efficiency of low-frequency transmitting arrays operating in a shallow sea.

The operation of a piston radiator mounted in a rigid waveguide wall is considered in [5]. However, such a waveguide has a limited application in seismoacoustics.

In this paper, we analyze the operation of a piston radiator inserted in an impedance screen, which coincides with the lower boundary of the Pekeris waveguide. In doing so, we model seismoacoustic sound sources and directive piston-type radiators that operate near the sea bottom. The problem is solved in two stages.

At the first stage, we consider a piston radiator inserted in a rigid screen coinciding with the lower boundary of a waveguide whose upper boundary is free. The problem is formulated in the following way:

$$\begin{gathered}\Delta\varphi(r,z) + k_1^2\varphi(r,z) = 0,\\ z = 0, \quad p = 0,\\ z = h, \quad -\frac{\partial\varphi}{\partial z} = \begin{cases} -v_0, & r \le a \\ 0, & r > a. \end{cases}\end{gathered} \tag{1}$$

Here, φ and p are the velocity potential and the sound pressure, respectively; $k_1 = \omega/c_1$, where ω and c_1 are the cyclic frequency and the sound speed in the layer; and h is the waveguide thickness. The problem layout is sketched in Fig. 1a.

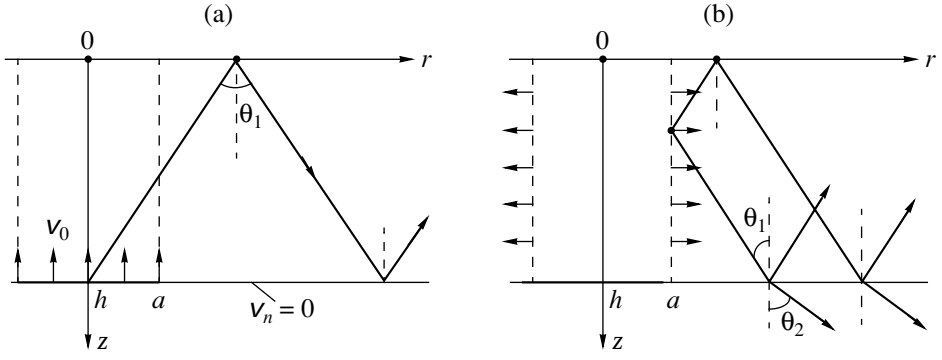

Fig. 1. Problem layout: (a) piston in a rigid screen; (b) secondary radiator in the Pekeris waveguide.

1063-7710/02/4803-0297$22.00 © 2002 MAIK "Nauka/Interperiodica"

By applying the Hankel transform to problem (1), we obtain the solution in the form of an improper integral:

$$\varphi(r, z) = -v_0 a \int_0^\infty \frac{J_1(\xi a) J_0(\xi r)}{k_{31} \cos(k_{31} h)} \sin(k_{31} z) d\xi, \quad (2)$$

where ξ is the transformation parameter and $k_{31}^2 = k_1^2 - \xi^2$. By using the well-known relations [6]

$$J_0(x) = \frac{1}{2}[H_0^{(1)}(x) + H_0^{(2)}(x)],$$

$$H_0^{(1)}(-x) = -H_0^{(2)}(x),$$

$$J_1(x) = \frac{1}{2}[H_1^{(1)}(x) + H_1^{(2)}(x)],$$

$$H_1^{(1)}(-x) = H_1^{(2)}(x),$$

we reduce solution (2) to the form:

$$\varphi(r, z) = \begin{cases} -\frac{v_0 a}{2} \int_{-\infty}^{\infty} \frac{J_1(\xi a) H_0^{(2)}(\xi r)}{k_{31} \cos(k_{31} h)} \sin(k_{31} z) d\xi, & r \geq a \\ -\frac{v_0 a}{2} \int_{-\infty}^{\infty} \frac{H_1^{(2)}(\xi a) J_0(\xi r)}{k_{31} \cos(k_{31} h)} \sin(k_{31} z) d\xi, & r \leq a. \end{cases} \quad (3)$$

Solution (3) can be used either to analyze the sound field produced by the radiator in the waveguide at $r > a$ (in particular, to calculate the acoustic radiation power by the far-field method) or to consider the near-field radiation at $r < a$ (in particular, to calculate the full resistance of the piston as the main power characteristic of the sound source).

By applying the theorem of residues to the lower integral in Eq. (3), we obtain for the region $r \leq a$:

$$\varphi(r, z) = v_0 i\pi a \left\{ \sum_n (-1)^{n+1} \frac{H_1^{(2)}(\xi_n^{(0)} a)}{\xi_n^{(0)} h} \times J_0(\xi_n^{(0)} r) \sin\left(\gamma_n \frac{z}{h}\right) - \frac{i}{\pi k_1 a} \frac{\sin(k_1 z)}{\cos(k_1 h)} \right\}, \quad (4)$$

$$\gamma_n = \frac{\pi}{2}(2n + 1),$$

$$\xi_n^{(0)} = \begin{cases} \sqrt{k_1^2 - (\gamma_n/h)^2}, & k_1 \geq \gamma_n/h \\ -i\delta_n, \quad \delta_n = \sqrt{(\gamma_n/h)^2 - k_1^2}, & k_1 \leq \gamma_n/h. \end{cases}$$

Solution (4) can be used to find the radiation resistance of the piston in a rigid screen:

$$Z_R = \frac{1}{v_0} \int_0^a p(r, h) 2\pi r dr = \rho_1 c_1 S Z_R',$$

$$S = \pi a^2, \quad p = i\omega\rho_1 \varphi,$$

where ρ_1 is the water density. For the normalized radiation resistance $Z_R' = r_R' + i x_R'$, we arrive at the expressions:

$$Z_R' = 2\pi k_1 h \sum_n \frac{J_1(\xi_n^{(0)} a)}{\xi_n^{(0)} h} \frac{H_1^{(2)}(\xi_n^{(0)} a)}{\xi_n^{(0)} h} + i \tan(k_1 h),$$

$$r_R' = \frac{\pi}{2} k_1 h a_1^2 \sum_{n=0}^{N-1} \Phi_n^2, \quad \Phi_n = \frac{2 J_1(\xi_n^{(0)} a)}{\xi_n^{(0)} a}, \quad (5)$$

$$a_1 = a/h,$$

$$x_R' = \tan(k_1 h)$$

$$+ 2\pi k_1 h a_1^2 \left\{ -\sum_{n=0}^{N-1} \frac{J_1(\xi_n^{(0)} a)}{(\xi_n^{(0)} a)^2} + \sum_{n=N}^{\infty} \frac{I_1(\delta_n a)}{(\delta_n a)^2} \frac{2}{\pi} K_1(\delta_n a) \right\},$$

where N is the number of normal waves with real propagation constants and $K_1(x)$ is the Macdonald function.

Figures 2a–2c illustrate the frequency dependence of the active component of the radiation resistance at different values of the geometric parameter a_1. Note that, at $a_1 \approx 10^{-3}$, the frequency dependence is close to that for a piston inserted in a rigid screen and operating in free space, and the mode structure of the sound field manifests itself in the discrete nature of the dependence. However, starting from $a_1 = 10^{-2}$, the discrete component considerably increases as the frequency parameter $k_1 h$ grows.

As the parameter a_1 increases, the active component rapidly increases to the value $r_R' \approx 1$ with a simultaneous increase in the discrete component. The frequency dependence itself becomes resonant and becomes mainly governed by the thickness oscillations of the liquid layer, which are damped by the sound radiation into the waveguide.

Figures 3a and 3b illustrate the frequency dependence of the reactive radiation component for different values of the parameter a_1. The reactive component exhibits an inertial behavior for low values of the parameters a_1 and $k_1 h$. However, as the frequency parameter grows, this component becomes alternating in sign and is mainly governed by the resonant thickness oscillations in the region $r \leq a$.

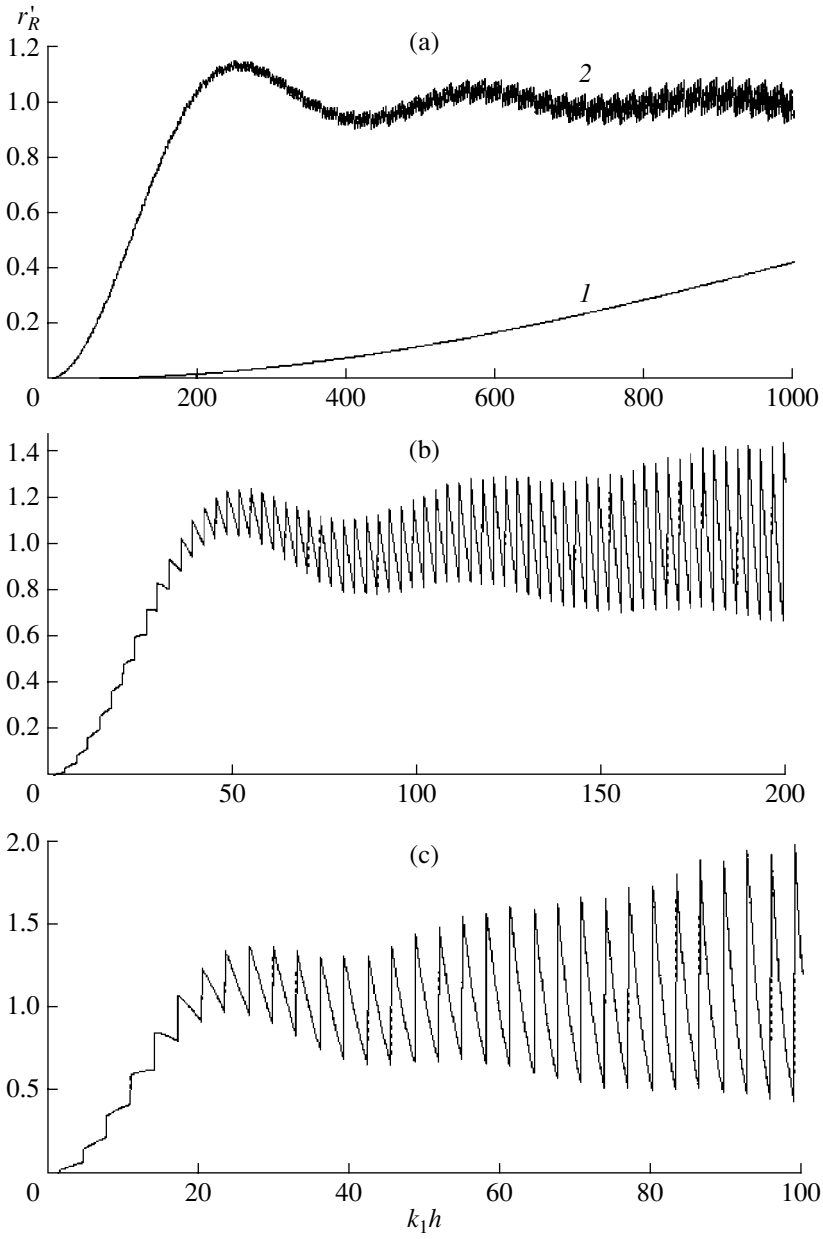

Fig. 2. Frequency dependence of the active component of the radiation resistance for a piston in a rigid screen: (a) $a_1 = (1)\ 10^{-3}$ and $(2)\ 10^{-2}$; (b) $a_1 = 5 \times 10^{-2}$; and (c) $a_1 = 10^{-1}$.

By applying the theorem of residues to the upper integral in Eq. (3), we obtain the solution for $r \geq a$:

$$\varphi(r, z) = iv_0 \frac{\pi}{2} a_1 a \sum_n (-1)^{n+1} \Phi_n \varphi_n^{(0)}(z) H_0^{(2)}(\xi_n^{(0)} r),$$
$$\varphi_n^{(0)}(z) = \sin\left(\gamma_n \frac{z}{h}\right). \tag{6}$$

With the representation $\xi_n^{(0)} = k_1 \sin\theta_{1n}$ (θ_1 is the incidence angle), the function $\Phi_n(\theta)$ represents the partial directivity characteristic of a circular piston for the nth normal wave.

Let us make use of solution (6) to specify the distribution of the normal component of the particle velocity at the surface of the cylinder determined as $r = a$, $z \in (0, h)$:

$$v_r(a, z) = v_0 f(z), \quad f(z) = i\pi a_1$$
$$\times \sum_n (-1)^{n+1} J_1(\xi_n^{(0)} a) H_1^{(2)}(\xi_n^{(0)} a) \varphi_n^{(0)}(z). \tag{7}$$

One may assume that distribution (7) of the particle velocity at the cylinder surface ($r = a$) is mainly governed by the source and the nature of the load in the

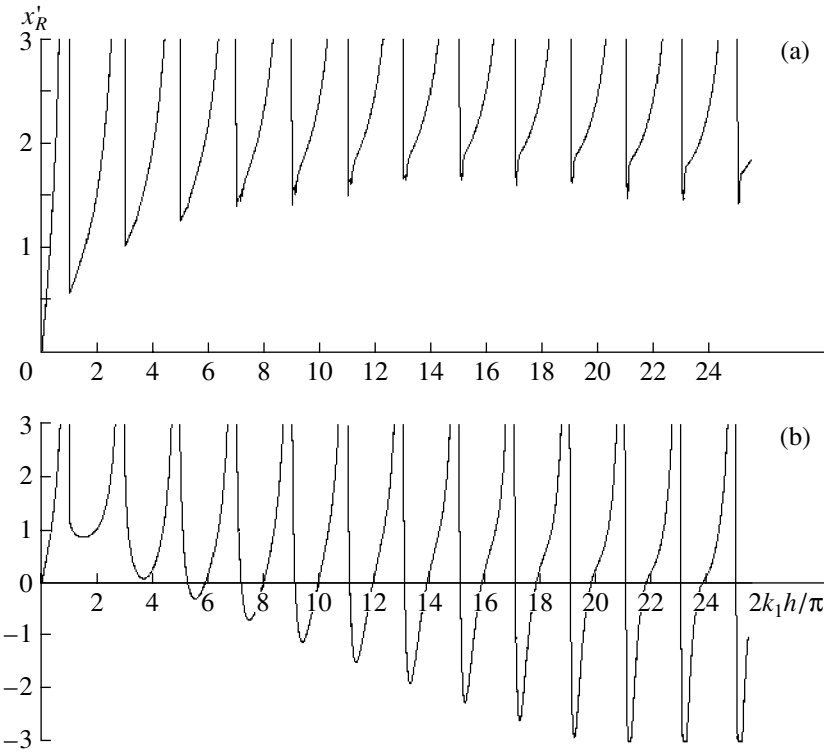

Fig. 3. Frequency dependence of the reactive component of the radiation resistance for a piston in a rigid screen: a_1 = (a) 5×10^{-2} and (b) 0.5.

region $r \le a$ of the waveguide but weakly depends on the load in the region $r > a$.

Naturally, at low frequencies ($k_1 a \ll 1$, $k_1 h \ll 1$), the load of the radiator as a source of particle velocity is low, and its distribution over the cylinder surface $r = a$ is solely determined by the law governing the outflow of an incompressible fluid with allowance for the boundary conditions at the source and at the opposite pressure-release surface in the region $r < a$ of the waveguide:

$$v_r(a, z) = v_0 az/h^2.$$

At high frequencies ($k_1 a \gg 1$), the radiation becomes directive, and distribution (7) again weakly depends on the boundary condition in the region $r > a$ of the lower boundary.

In this approximation, the cylinder $r = a$, with the normal particle velocity distribution specified at its surface, can be treated as a secondary radiator whose parameters do not change when the acoustic load varies, e.g., due to changes in the waveguide characteristic in the region $r > a$.

We assume that the Pekeris waveguide serves as the load imposed on the secondary radiator with distribution (7) of the boundary function. Then, we come to the second stage and formulate the following boundary-value problem for radiator (7) in the Pekeris waveguide:

$$\Delta\varphi(r, z) + k_1^2\varphi(r, z) = 0,$$
$$z = 0, \quad p = 0,$$
$$z = h, \quad p + \frac{\rho_2 c_2}{\cos\theta_2}\frac{\partial\varphi}{\partial z} = 0, \tag{8}$$
$$r = a,$$
$$v_r = v_0 f(z), \quad f(z) = f^{(1)}(z) + i f^{(2)}(z), \quad z \in (0, h).$$

Here, ρ_2 and c_2 are the density and sound speed in the halfspace, θ_2 is the refraction angle, and $f^{(1)}(z) = \mathrm{Re} f(z)$ and $f^{(2)}(z) = \mathrm{Im} f(z)$ are the quadric components of the boundary function $f(z)$. The problem layout is illustrated by Fig. 1b.

If one seeks a solution to problem (8) in the form

$$\varphi(r, z) = \varphi(z) H_0^{(2)}(\xi r), \tag{9}$$

one needs to find the eigenfunctions $\varphi_n(\xi_n, z)$ and eigenvalues of the propagation constant ξ_n for the operator corresponding to problem (8). This operator is known to be not self-conjugate, and its eigenfunctions do not form a complete system on the interval $z \in (0, h)$. The latter fact significantly complicates the problem of expanding an arbitrary function specified on the aforementioned interval into a series in the eigenfunctions of

the operator. This problem was solved in [4] by adding the eigenfunctions of the operator conjugate to operator (8) to those of operator (8). For quadric components $f^{(1)}(z)$ and $f^{(2)}(z)$, the expansion formulas take the form:

$$f^{(1)}(z) = \sum_m A_m^{(1)}\varphi_m(\xi_m, z),$$

$$f^{(2)}(z) = \sum_m A_m^{(2)}\varphi_m(\xi_m, z),$$

$$A_m^{1,2} = \frac{1}{h}\frac{(f^{(1,2)}, \varphi_m)}{E_m} = \pi a_1 \frac{x_m \cos x_m}{E_m}\sum_n \frac{G_n^{(1,2)}}{x_m^2 - \gamma_n},$$

$$(f, \varphi) = \int_0^h f(z)\varphi(z)dz,$$

$$E_m = 1 - \frac{\sin(2x_m)}{2x_m} - i\rho_{12}\frac{\sin^2 x_m}{k_{32,m}h}, \quad \rho_{12} = \frac{\rho_1}{\rho_2},$$

$$x_m = k_{31,m}h, \quad k_{32,m}^2 = k_2^2 - \xi_m^2, \quad k_2 = \omega/c_2,$$

$$G_n^{(1)} = \begin{cases} J_1(\xi_n^{(0)}a)N_1(\xi_n^{(0)}a), & k_1 \geq \gamma_n/h \\ -\frac{2}{\pi}I_1(\delta_n a)K_1(\delta_n a), & k_1 \leq \gamma_n/h, \end{cases}$$

$$G_n^{(2)} = \begin{cases} J_1^2(\xi_n^{(0)}a), & k_1 \geq \gamma_n/h \\ 0, & k_1 \leq \gamma_n/h, \end{cases}$$

where $\varphi_m(\xi_m, z)$ and ξ_m are the eigenfunctions and eigenvalues of the conjugate operators of problem (8). In the latter expression, the following waves contribute to the sum: the normal waves with real propagation constants ξ_m^- ($\mathrm{Im}k_{32,m} < 0$, $\mathrm{Re}k_{32,m} = 0$), the generalized normal waves with real propagation constants ξ_m^+ ($\mathrm{Im}k_{32,m} > 0$, $\mathrm{Re}k_{32,m} = 0$), and the leaky normal waves with complex propagation constants $\tilde{\xi}_m$ ($\mathrm{Im}\tilde{\xi}_m < 0$, $\mathrm{Re}k_{32,m} > 0$).

More detailed information on generalized waves of different types can be found in [7, 8] where the Stoneley–Scholte waves were theoretically and experimentally studied for the first time. In [9], the generalized normal waves were numerically studied and used to explain some experimental data obtained by other researchers.

The sound field generated by boundary function (7) (and by its quadric components) in the Pekeris waveguide is described by the expression

$$\varphi^{(1,2)}(r, z) = v_0\sum_m \frac{A_m^{(1,2)}\varphi_m(\xi_m, z)}{\xi_m H_1^{(2)}(\xi_m a)}\varepsilon_m^{(1,2)}H_0^{(2)}(\xi_m r), \tag{10}$$

$$\xi_m^{(1,2)} = \begin{cases} 1, \text{ for normal and generalized} \\ \text{normal waves } \xi_m^{\pm}, \\ 1 + \rho_{12}\frac{A_m^{(1,2)*}}{A_m^{(1,2)}}\frac{|\sin x_m|^2}{E_{1m}\mathrm{Im}k_{32,m}h}, \\ \text{for leaky normal waves } \tilde{\xi}_m, \end{cases}$$

$$E_{1m} = 1 - \frac{\sin(2x_m)}{2x_m}.$$

Let us use solution (10) to calculate the input resistance of the Pekeris waveguide at the cross section $r = a$:

$$Z_{\mathrm{in}} = \frac{1}{v_0}\int_0^h p(a) f^*(z) 2\pi a dz = \rho_1 c_1 S Z'_{\mathrm{in}}, \tag{11}$$

$$S = \pi a^2,$$

where $p(a) = i\omega\rho_1(\varphi^{(1)} + i\varphi^{(2)})$ and $f^*(z) = f^{(1)}(z) - if^{(2)}(z)$.

Substituting Eq. (10) into Eq. (11), we obtain

$$Z'_{\mathrm{in}} = 2\pi^2 k_1 h a_1 \sum_m \frac{iC_m H_0^{(1)}(\xi_m a)}{E_m \xi_m h H_1^{(2)}(\xi_m a)},$$

$$C_m = |x_m \cos x_m|^2 \{\varepsilon_m^{(1)}|F_m^{(1)}|^2 + \varepsilon_m^{(2)}|F_m^{(2)}|^2 + i(\varepsilon_m^{(2)} - \varepsilon_m^{(1)})F_m^{(1)}F_m^{(2)}\}, \tag{12}$$

$$F_m^{(1,2)} = \sum_n \frac{G_n^{(1,2)}}{x_m^2 - \gamma_n^2}.$$

In this case, the normal and generalized normal waves are responsible for the radiation into the waveguide, and the leaky normal waves govern the radiation into the halfspace.

By extracting the subset $m(1)$ of the normal waves and the subset $m(2)$ of the generalized normal waves from Eq. (12), we obtain the estimate for the corresponding component $Z'_{12} = r'_{12} + ix'_{12}$ of the total radiation resistance:

$$r'_{12} = 4\pi k_1 h \sum_{\substack{m(1) \\ m(2)}}^{M_1+M_2} \frac{C_m}{E_m(\xi_m h)^2 |H_1^{(2)}(\xi_m a)|^2},$$

$$x'_{12} = 2\pi^2 k_1 h a_1 \tag{13}$$

$$\times \sum_{\substack{m(1) \\ m(2)}}^{M_1+M_2} \frac{C_m[J_0(\xi_m a)J_1(\xi_m a) + N_0(\xi_m a)N_1(\xi_m a)]}{E_m \xi_m h |H_1^{(2)}(\xi_m a)|^2},$$

where M_1 and M_2 are the numbers of the normal and generalized normal waves, respectively.

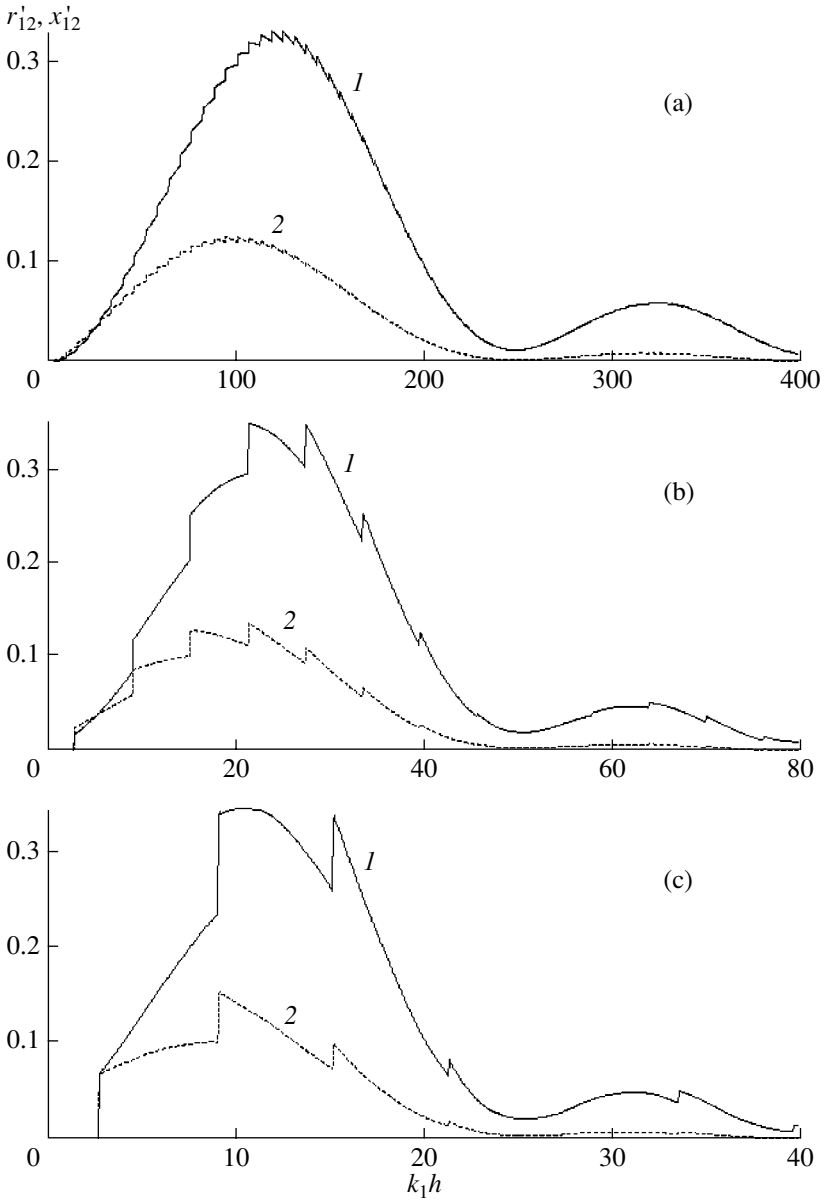

Fig. 4. Frequency dependence of the components (*1*) r'_{12} and (*2*) x'_{12} of the radiation resistance for the secondary radiator: a_1 = (a) 10^{-2}, (b) 5×10^{-2}, and (c) 10^{-1}.

By extracting subset $m(3)$ of the leaky normal waves from Eq. (12), we obtain the estimate for the corresponding component $Z'_3 = r'_3 + ix'_3$ of the total radiation resistance:

$$r'_3 = 2\pi^2 k_1 h a_1 \mathrm{Re} \sum_{m(3)} \frac{C_m i H_0^{(2)}(\xi_m a)}{E_m \xi_m h H_1^{(2)}(\xi_m a)},$$
$$x'_3 = 2\pi^2 k_1 h a_1 \mathrm{Im} \sum_{m(3)} \frac{C_m i H_0^{(2)}(\xi_m a)}{E_m \xi_m h H_1^{(2)}(\xi_m a)}. \quad (14)$$

Let us consider the results of numerical calculations performed for a waveguide with the parameters ρ_{12} = 1/1.6 and c_{12} = 1.5/1.75, which correspond to sandy sediments. Figures 4a–4c show the frequency dependences of the components r'_{12} and x'_{12} that are associated with the secondary radiation into the Pekeris waveguide at different values of the parameter a_1. The discrete nature of the dependences precisely corresponds to the mode structure of the sound field, and the global maximum of the component r'_{12} approximately corresponds to the condition $k_1 a \approx \pi/2$. The latter means

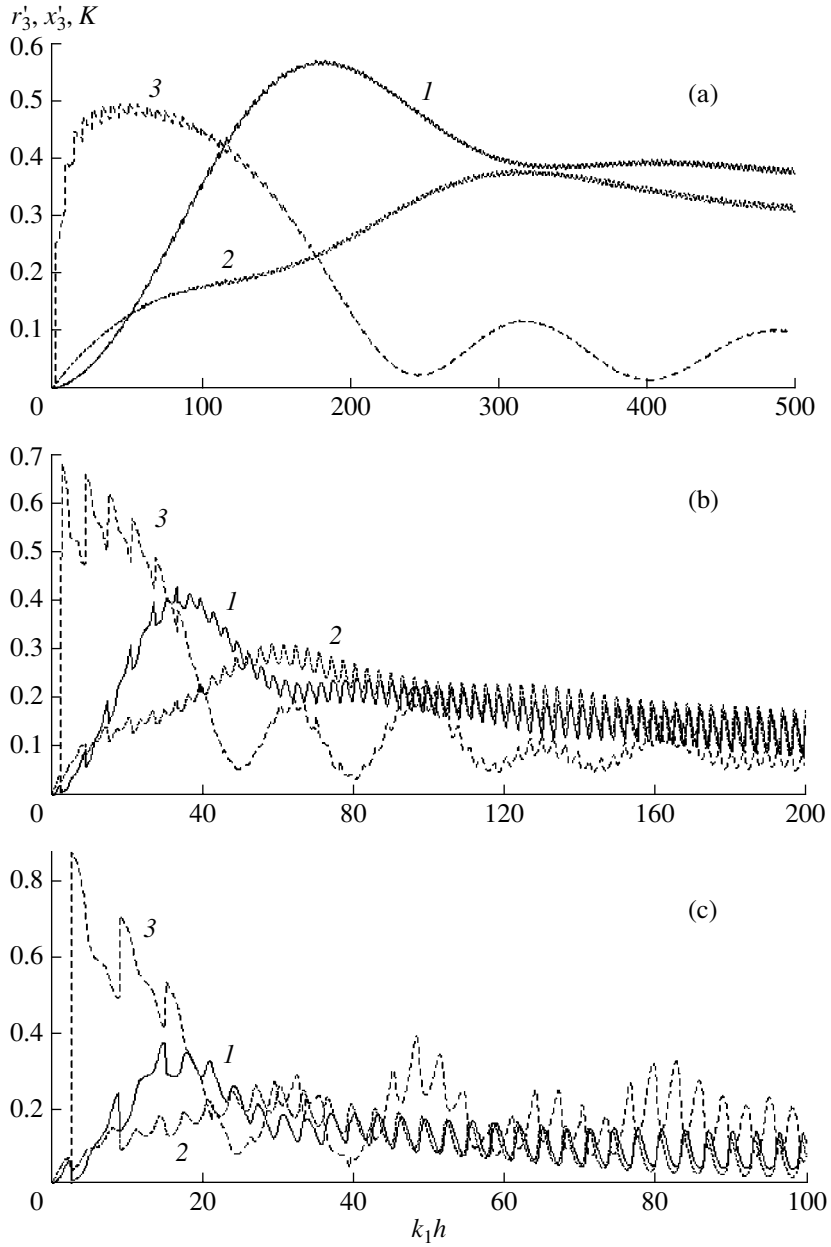

Fig. 5. Frequency dependence of the components (*1*) r'_3 and (*2*) x'_3 of the radiation resistance for the secondary radiator and (*3*) the factor K: a_1 = (a) 10^{-2}, (b) 5×10^{-2}, and (c) 10^{-1}.

that the radiation into the waveguide is maximal when a single Fresnel zone fits within the piston surface ($r \gg h$) for a distant ($2a \approx \lambda/2$) observer.

As the geometric parameter a_1 increases, the maximum of the component r'_{12} shifts towards lower frequencies with a simultaneous increase in the magnitude of the global maximum. When a single Fresnel zone fits along the piston surface at the first critical frequency $(k_1h)_{\text{crit, 1}} = 2.7$, $a_1 = 0.57$, the radiation resistance becomes maximal and $r'_{12} \approx 0.6$.

Figures 5a–5c show the frequency dependences of the components r'_3 and x'_3 that are associated with the radiation into the halfspace. The discrete nature of these dependences also corresponds to the mode structure of the sound field, but this time at frequencies that are limited by the condition $k_1a \le \pi/2$ from above. At higher frequencies, the interference component caused by the resonant phenomena in the thickness oscillations of the layer in the region $r \le a$ comes into play. These oscillations are damped by the radiation into the waveguide and the halfspace in the region $r > a$.

Since the power emitted by the piston radiator is exactly equal to that emitted by the secondary radiator, we can characterize the piston radiation into the waveguide by the value of the component r'_{12}. However, we are also interested in the distribution of the radiation power between the waveguide and the halfspace. Figure 5 also shows the dependences of the factor $K = \frac{r'_{12}}{r'_{12} + r'_3}$ that characterizes the fraction of the power radiated into the waveguide relative to the total radiation power. One can notice that the maximal value of K corresponds to the vicinity of the first critical frequency, while the maximum of the component r'_{12} corresponds to the frequency parameter $k_1 h = \pi/2a_1$. These two maxima are combined only when $(k_1 h)_{\text{crit, 1}} = 2.7$ and $a_1 = 0.57$. In this case, $r'_{12} \approx 0.6$ and $K \approx 1$, and such a piston radiator has the highest efficiency.

Let us compare the frequency dependences of the active component of the radiation resistance, r'_R, for the piston in a rigid screen and the component r'_{12} of the radiation resistance for the piston in an impedance screen. One can notice a considerable damping of the resonant processes associated with the thickness oscillations of the liquid layer because of the radiation into the halfspace. Moreover, the frequency dependences of the radiation resistance r'_{12} of a piston-type radiator inserted in an impedance screen of the Pekeris waveguide are close to the corresponding frequency dependences obtained in [10] for a piston radiator in a pressure-release screen of the same waveguide. In both cases, the maximal radiation into the waveguide occurs when $k_1 a \approx \pi/2$, but the efficiency of a piston radiator inserted in an impedance screen is much higher.

One may also assume that the efficiency of a piston radiating into the waveguide will increase with an increase in the acoustic stiffness of the sea floor.

REFERENCES

1. V. A. Eliseevnin, Akust. Zh. **25**, 227 (1979) [Sov. Phys. Acoust. **25**, 123 (1979)].
2. V. A. Eliseevnin, Akust. Zh. **27**, 228 (1981) [Sov. Phys. Acoust. **27**, 137 (1981)].
3. N. V. Zlobina, B. A. Kasatkin, and L. G. Statsenko, in *Proceedings of the VIII School–Seminar of Academician L. M. Brekhovskikh on Ocean Acoustics* (GEOS, Moscow, 2000), p. 118.
4. B. A. Kasatkin and L. G. Statsenko, *Energy and Field Characteristics of the Acoustic Antenna Arrays in Waveguides* (Dal'nauka, Vladivostok, 2000).
5. A. D. Lapin, Akust. Zh. **46**, 427 (2000) [Acoust. Phys. **46**, 367 (2000)].
6. L. M. Brekhovskikh, *Waves in Layered Media*, 1st ed. (Nauka, Moscow, 1957; Academic, New York, 1960).
7. J. H. Ansell, Pure Appl. Geophys. **194**, 172 (1972).
8. F. Padilla, M. de Billy, and G. Quentin, J. Acoust. Soc. Am. **106**, 666 (1999).
9. B. A. Kasatkin and N. V. Zlobina, *Nonclassical Solution of Classical Acoustic Problems* (Dal'nauka, Vladivostok, 2000).
10. N. V. Zlobina and B. A. Kasatkin, Akust. Zh. **48**, 61 (2002) [Acoust. Phys. **48**, 54 (2002)].

Translated by E. Kopyl

Acoustical Physics, Vol. 48, No. 3, 2002, pp. 305–308. Translated from Akusticheskiĭ Zhurnal, Vol. 48, No. 3, 2002, pp. 354–357.
Original Russian Text Copyright © 2002 by Karpova, Lobova, Paukov, Polunin, Postnikov.

Experimental Investigation of an Air–Magnetic-Liquid Resonator

G. V. Karpova*, O. V. Lobova*, V. M. Paukov*, V. M. Polunin*, and E. B. Postnikov**

**Kursk State Technical University, ul. 50 Let Oktyabrya 94, Kursk, 305040 Russia*

***Kursk State Pedagogical University, ul. Radishcheva 33, Kursk, 305416 Russia*

e-mail: postnicov@mail.ru

Received April 18, 2001

Abstract—Experimental results obtained by studying a vibratory system in which a magnetic liquid playing the role of a mass shuts off the cross section of a tube under the effect of a magnetic field and is spring-loaded by an air cavity and elasticity of ponderomotive type are discussed. An expression for the resonant frequency of vibrations is derived with allowance for both types of elasticity. The expression agrees well with the experimental data. © *2002 MAIK "Nauka/Interperiodica".*

This paper describes the results obtained by studying the elastic properties of a vibratory system in which a magnetic liquid (ML) playing the role of a mass shuts off the cross section of a tube under the effect of a magnetic field and is spring-loaded by an air cavity and an elasticity of ponderomotive type.

In papers [1, 2], a water–air resonator consisting of a vessel closed from above with a rigid cover and immersed in water is considered. The air inside the vessel is the elastic element of the resonator, and the water in the lower part of the vessel, together with the water near the open end, serves as the mass.

The application of ML in a water–air resonator endows it with new physical properties. In an air–magnetic-liquid resonator (AMLR), the liquid may be located above the gas cavity due to stabilization of the interphase boundary by a nonuniform magnetic field; a continuous adjustment of the resonance frequency is possible by both changing the volume of the air cavity and controlling the elasticity of the system with a magnetic field. For exciting mechanical vibrations in the system, an electrodynamic method can be used, and the indication of vibrations is possible by using an induction method.

The urgency of studying the AMLR is also connected with the fact that the results obtained may be useful for designing magnetic-liquid seals (MLS) and dampers that are widely used in mechanical engineering [3], as well as waveguides with control structural inserts [4]. In an MLS, a drop of magnetic colloid shuts off the clearance between a shaft and sleeve due to the effect of the magnetic field concentrated in the clearance area. However, in publications devoted to the MLS, the possibility of elastic vibrations of the magnetic-liquid plug is not taken into account, although it cannot be excluded, e.g., under conditions of instability of pressure in the working chamber or outside it.

The cutting off of the cross section of the tube connected with a vessel by a drop of ML can be realized by using a ring magnet enveloping the tube [5]. The magnetic field of a ring magnet magnetized along its axis is capable of stabilizing the position of the ML plug.

A schematic view of the investigated vibratory system is shown in Fig. 1. A drop of ML *1* shuts off the cross section of a glass tube *2* under the action of a ponderomotive force of a nonuniform magnetic field produced by a coaxial ring magnet *3*. The tube of the inner diameter *d* is attached to a glass vessel *4* filled with air. (Glass tubes of various lengths sealed at one end were also used.) Both free surfaces of the ML plug *5* have the form of a concave meniscus, which results from the nonuniformity of the magnetic field in the radial direction.

The ML used in the experiment was prepared by a standard technique on the basis of magnetite and kerosene with oleic acid as a stabilizer.

The physical parameters of the magnetic colloid are given in Table 1.

The designations are as follows: ρ is the liquid density, φ is the volume concentration of the solid phase, η_s is the static shear viscosity, and χ is the initial magnetic susceptibility.

The density and the viscosity were measured by using a pycnometer and an Ostwald viscosimeter, the magnetization was measured by a ballistic method, and the strength of magnetic field, by a Hall-type teslameter. All experiments were performed at room temperature ($20 \pm 1°C$).

Unlike the films formed by usual liquids (e.g., soap films), the ML plug is characterized by a high stability

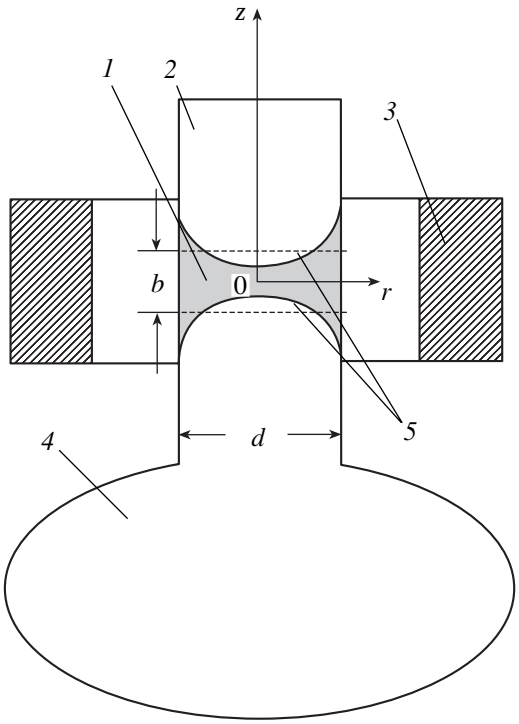

Fig. 1.

(its lifetime measures weeks and months), and its most remarkable feature is that it has the possibility of self-recovery [5]. After a forced breakage, the plug rather quickly restores its continuity and shape. The pressure jump arising in this case disturbs the vibratory system from equilibrium. For breaking the ML plug, it is sufficient to change the volume of the gas cavity within 0.1% by displacing the magnetic system along the tube or the piston inside the tube. The described phenomenon serves as the basis of the procedure of the vibration excitation in the system under study.

The indication of damped vibrations is carried out by an induction method. For this purpose, an inductance coil is installed coaxially inside the ring magnet. The body of the coil is fixed to the magnet, but between the body and the tube, there is an air clearance, which allows the magnetic system to move freely along the axis.

The electromotive force induced in the coil is fed to an oscilloscope operating in the mode of external synchronization. An electromechanical unit provides a uniform motion of the magnet system (the piston) with a predetermined low velocity at which the superposition of the system vibrations caused by two sequential impulses is impossible. In this case, the oscilloscope displays a stable waveform by which the frequency ν and the attenuation coefficient β of vibrations are determined. The error of measurement of ν and β by this method is 5 and 20%, respectively.

Table 1

ρ, kg/m^3	φ, %	η_s, Pa s	M_s, kA/m	χ
1499	16.2	8×10^{-3}	50 ± 1	1 ± 0.1

Figure 2 shows the results of measurement of the frequency of vibrations ν of the AMLR as a function of the volume of the air cavity V_0 (the dots).

Table 2 presents the results of measurement of the attenuation factor β for the vibrations of the system.

It should be noted that, in the upper part of the investigated frequency range (80–200 Hz), in some cases the waveforms have an irregular character, unlike the exponential decrease typical of the amplitude of damped vibrations. This apparently results from the effect produced on the ML plug by the sound vibrations arising in the air cavity near the open end of the tube and in the inner isolated volume. This phenomenon is of special interest and requires further investigation. Therefore, Table 2 contains no data for the frequencies exceeding 63 Hz.

We analyze the results of the experimental study of the AMLR on the basis of the vibratory system model with lumped parameters. We assume that both free surfaces of liquid are flat (the dashed lines in Fig. 1) and are spaced at the distance *b*. The liquid is viscous but incompressible and non-heat-conducting. The oscillations of the gas density have an equilibrium character. The modulus of elasticity *k* of the system is determined by the sum

$$k = k_g + k_p, \tag{1}$$

where k_g and k_p are the coefficients of gas and ponderomotive elasticity. The expression for k_g is known [1, 2]:

$$k_g = \rho_g c^2 S^2 / V_0, \tag{2}$$

where ρ_g is the air density, *c* is the sound velocity in air, *S* is the area of the cross section of the tube, and V_0 is the volume of the air cavity.

To determine k_p, we assume that the center of mass of the ML drop, which has the form of a cylinder of radius *R*, performs small oscillations along the *z* axis about the equilibrium position at the point $z = 0$ (Fig. 1). When the center of mass is displaced by Δz, every element of the magnetic-liquid cylinder experiences the force caused by magnetic field [6]

$$d\mathbf{f} = 2\pi\mu_0(\mathbf{M}\nabla)\mathbf{H} r dr dz,$$

where μ_0 is the permeability of the vacuum and $\mathbf{M}(z, r)$ is the magnetization of the liquid. For the axial component of the force, we obtain

$$\Delta f_z = 2\pi\mu_0 \int_{-\frac{b}{2}+\Delta z}^{\frac{b}{2}+\Delta z} \int_0^R \left[M_r \frac{\partial H_z}{\partial r} + M_z \frac{\partial H_z}{\partial z} \right] r dr dz, \tag{3}$$

where M_z and M_r are the radial and axial components of **M**. The relation between the linear dimensions of the magnetic-liquid cylinder and the ring magnet is such that the first term in the brackets and the dependence of the second term on the radial coordinate can be neglected. For materials with a small magnetic susceptibility, it is possible to use the linear equation of magnetic state

$$\mathbf{M} = \chi\mathbf{H}$$

and neglect the degaussing field. Taking this into consideration, Eq. (3) can be written as

$$\Delta f_z = \frac{1}{2}\mu_0\chi S \int\limits_{-\frac{b}{2}+\Delta z}^{\frac{b}{2}+\Delta z} \frac{\partial H_z^2}{\partial z} dz.$$

By virtue of the symmetry of the magnetic field about the plane $z = 0$, we have

$$\Delta f_z = -2\mu_0\chi S\left(H_z\frac{\partial H_z}{\partial z}\right)_{z=-b/2}\Delta z,$$

$$\text{or} \quad \Delta f_z = -2\mu_0 S\left(M_z\frac{\partial H_z}{\partial z}\right)_{z=-b/2}\Delta z,$$

which yields

$$k_p = 2\mu_0 S\left(M_z\frac{\partial H_z}{\partial z}\right)_{z=-b/2}. \quad (4)$$

If the ML is magnetized to saturation level, we obtain

$$k_p = 2\mu_0 S M_s\left(\frac{\partial H_z}{\partial z}\right)_{z=-b/2}. \quad (5)$$

Using Eqs. (2) and (4), we determine the expression for the frequency of vibrations

$$\nu = \frac{1}{2\pi}\sqrt{\frac{\rho_g c^2 S}{\rho b V_0} + \frac{2\mu_0 M_z}{\rho b}\frac{\partial H_z}{\partial z}}. \quad (6)$$

In the absence of a magnetic field, we have

$$\nu = \frac{c}{2\pi}\sqrt{\frac{\rho_g S}{\rho V_0}}. \quad (7)$$

The reciprocating motion of a viscous drop inside a tube can be described by the well-known Poiseuille or Helmholtz models [7]. The Poiseuille model is applicable when $2\lambda' > \pi d$, where $\lambda' = 2\sqrt{\pi\eta/\nu\rho}$ is the viscous wavelength.

In our case, the Helmholtz model is preferable, since the requirement of smallness of the viscous wavelength, $\pi d/2\lambda' > 10$, is satisfied. With this condition, the complex impedance R' of the tube is approximately equal to

$$R' \approx db\sqrt{\pi^3\rho\eta\nu} + i\frac{\pi^2 d^2\rho\nu}{2}\left(1 + \frac{2}{d}\sqrt{\frac{\eta}{\pi\nu\rho}}\right). \quad (8)$$

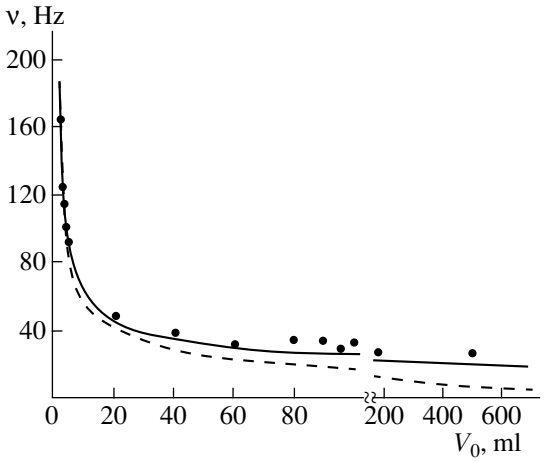

Fig. 2.

The active resistance has the form

$$r' = db\sqrt{\pi^3\rho\eta\nu} \quad (9)$$

and it increases with ν. Expression (9) was first derived by Helmholtz [8]. The second term in parenthesis in Eq. (8) can be neglected, which shows the absence of the associated mass due to the viscosity. The attenuation coefficient, according to the Helmholtz model, is calculated by the formula

$$\beta_t = \frac{2}{d}\sqrt{\frac{\pi\nu\eta}{\rho}}. \quad (10)$$

It should be noted that the viscous oscillatory motion of the ML drop can be described by a model theory with the same degree of approximation as for the case of an ordinary liquid, because the shear viscosity of the magnetic colloid hardly depends at all on its magnetization [9].

The reduced values of the attenuation coefficient $\beta/\sqrt{\nu}$ and the values β_t calculated by formula (10) are presented in Table 2. The values of β_t differ from the experimental data almost by an order of magnitude. Beyond the measurement errors, an increase in the attenuation coefficient with frequency is observed, although the proportionality $\beta \sim \sqrt{\nu}$ is not confirmed by the results of measurements. Thus, the Helmholtz model is not quite adequate to describe the dissipative properties of the investigated vibratory system.

Table 2

ν, Hz	28	29	35	37	40	49	63
β, s^{-1}	10	10	20	22	26	28	45
$\beta/\sqrt{\nu}$, $s^{-1/2}$	1.9	1.9	3.4	3.6	4.1	4	5.7
β_t, s^{-1}	2.7	3.8	3.0	3.1	3.3	3.6	4.1

The dependence of the frequency ν_t calculated by Eq. (6) on the volume of the air cavity V_0 is presented graphically in Fig. 2 by the solid line. The plot was obtained using the following experimental data: M = 25 kA/m, $\partial H_z/\partial z = 4.6 \times 10^6$ A/m^2, $S = 2 \times 10^{-4}$ m^2, the volume of the ML equal to 3 cm^3, and the known numerical values of ρ_g and c.

The dashed line in Fig. 2 corresponds to the dependence $\nu'(V_0)$ obtained by formula (7).

The comparison of the conclusions of the model theory with the experimental results suggests that, at the upper frequencies of the investigated range, the elasticity of the AMLR is governed by the elasticity of the gas cavity, and at the lower frequencies, by the elasticity of ponderomotive type.

Considering the model of ponderomotive elasticity described as the first approximation, we can use it as a basis to evaluate the resonance frequency ν_r of an MLS. For this purpose, we use the expression for the critical pressure ΔP_c of a "one-tooth" seal [3]:

$$\Delta P_c = \mu_0 M_s (H_{max} - H_{min}),$$

where H_{max} and H_{min} are the maximal and minimal strengths of the magnetic field at the free surfaces of the ML plug. Taking into consideration only the ponderomotive elasticity calculated by Eq. (5), we obtain

$$\nu_r = \frac{1}{2\pi b}\sqrt{\frac{2\Delta P_c}{\rho}}.$$

For $\Delta P_c = 0.75 \times 10^5$ Pa, $b = 2$ mm, and $\rho = 1.5 \times 10^3$ kg/m^3, the resonance frequency is $\nu_r \approx 800$ Hz.

REFERENCES

1. V. I. Sorokin, Akust. Zh. **4**, 187 (1958) [Sov. Phys. Acoust. **4**, 188 (1958)].
2. V. A. Arkhipov, I. P. Zhukov, and M. A. Mironov, Akust. Zh. **33**, 395 (1987) [Sov. Phys. Acoust. **33**, 232 (1987)].
3. D. V. Orlov, Yu. O. Mikhalev, N. K. Myshkin, *et al.*, *Magnetic Liquids in Mechanical Engineering*, Ed. by D. V. Orlov and V. V. Podgornov (Mashinostroenie, Moscow, 1993).
4. B. R. Mace, R. W. Jones, and N. R. Harland, J. Acoust. Soc. Am. **109**, 1417 (2001).
5. V. M. Polunin, V. M. Paukov, G. V. Karpova, *et al.*, in *Proceedings of 9th International Conference on Magnetic Liquids, Pless, Russia* (IGÉU, Ivanovo, 2000), pp. 145–147.
6. L. D. Landau and E. M. Lifshits, *Electrodynamics of Continuous Media*, 2nd ed. (Nauka, Moscow, 1982; Pergamon, Oxford, 1984).
7. S. N. Rzhevkin, *Lectures on the Theory of Sound* (MGU, Moscow, 1960).
8. J. W. S. Rayleigh, *The Theory of Sound*, 2nd ed. (Macmillan, London, 1926; GITTL, Moscow, 1955), Vol. 2.
9. V. E. Fertman, *Magnetic Liquids: Natural Convection and Heat Transfer* (Nauka i Tekhnika, Moscow, 1978).

Translated by A. Svechnikov

Acoustical Physics, Vol. 48, No. 3, 2002, pp. 309–320. Translated from Akusticheskiĭ Zhurnal, Vol. 48, No. 3, 2002, pp. 358–370.
Original Russian Text Copyright © 2002 by Kosobrodov.

Acoustic Waves Propagating in a Fluid-Filled Spherical Shell Placed in a Liquid

R. A. Kosobrodov

All-Russia Research Institute of Physico-Technical and Radio-Engineering Measurements, p/o Mendeleevo, Solnechnogorskiĭ raĭon, Moscow oblast, 141570 Russia

e-mail: myagkov@ntmdt.ru

Received March 6, 2001

Abstract—Acoustic waves arising in a fluid-filled elastic spherical shell placed in a liquid are considered. It is demonstrated that, in general, none of the four types of waves possible in such a system (subsonic and supersonic antisymmetric Lamb waves, symmetric Lamb waves, and whispering galleries) is realized separately, but an interaction between the waves of different types takes place. © *2002 MAIK "Nauka/Interperiodica".*

The problem of the scattering of a plane acoustic wave by an elastic spherical shell belongs to the so-called standard problems, for which analytical solutions are obtained. These problems are important for the evaluation of approximate and numerical methods and contribute to the understanding of the physical processes of acoustic wave interaction with elastic bodies. The purpose of this paper is to analyze acoustic waves arising as a result of the sound scattering by a fluid-filled spherical shell and to study the mechanism of interaction between waves of different types.

The problem of sound scattering by an air-filled elastic spherical shell was considered for the first time by Junger [1], who used the theory of thin shells to describe shell motion. Later [2], it was demonstrated that this theory did not adequately describe the flexural vibrations of a shell. The solution of the problem on the basis of the exact theory of elasticity was proposed in [3], where a shell placed in an ideal liquid and filled with the same liquid was considered. The generalization for the case of different liquids can be readily obtained and is described, e.g., in [4]. A solution for a shell partially filled with a liquid was obtained recently [5].

In the monograph [6], the scattered field is expressed in terms of the mechanical impedance of a shell and the impedances of radiation into the external and internal regions. Exact and approximate expressions for determination of the mechanical impedance are given there.

This paper uses the results by Goodman and Stern [3] and Murphy *et al.* [4], which are true not only for thin shells but also for an elastic spherical layer of arbitrary thickness.

Let a plane monochromatic sound wave described by the expression

$$p_0 = p\exp(ikr\cos\theta) \tag{1}$$

be incident upon a shell. In Eq. (1), p is the amplitude of the sound pressure, k is the wave number in the external liquid, r is the distance from the shell center, and θ is the angle measured relative to the direction of wave incidence. Figure 1 explains the problem geometry. A plane wave is incident in the direction opposite to the direction of the x axis in the figure. The densities of the internal and external liquids are denoted by ρ_1 and ρ_2, respectively, and the velocities of sound propagation, by c_1 and c_2. In Eq. (1) and in what follows, the factor $\exp(-i\omega t)$ is omitted for brevity.

For the incident wave p_0, the scattered wave $p_2^{(s)}$, and the field within the shell p_1, the following expansions are valid:

$$p_0 = p\sum_{n=0}^{\infty}(2n+1)i^n j_n(kr)P_n(\cos\theta), \tag{2}$$

$$p_1 = p\sum_{n=0}^{\infty}(2n+1)i^n a_n j_n(k_1 r)P_n(\cos\theta), \tag{3}$$

$$p_2^{(s)} = p\sum_{n=0}^{\infty}(2n+1)i^n b_n h_n^{(1)}(kr)P_n(\cos\theta). \tag{4}$$

Here, j_n and $h_n^{(1)}$ are the spherical Bessel and Hankel functions of the nth order, $P_n(x)$ is the Legendre polynomial, and $k_1 = \omega/c_1$. The numerical coefficients a_n and b_n and four coefficients c_n, …, f_n in the expressions for shell displacements are determined from six boundary conditions, i.e., the conditions of continuity of displacements at the external and inner surfaces of the shell, the conditions of equality of the total sound pressure and the normal component of shell stress (taking into account the sign), and the conditions of the absence of tangential stress at the shell surfaces [3, 4]. The

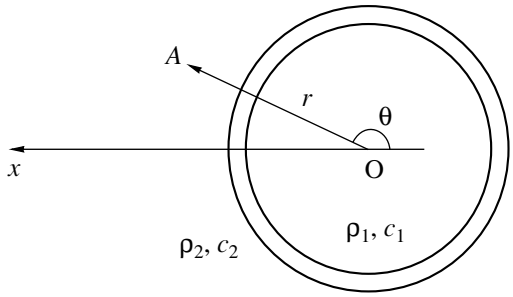

Fig. 1. Geometry of the problem.

determination of the coefficients is reduced to solving a system of six linear equations in six unknowns,

$$\|m_{ij}\|_n[a_n, b_n, c_n, d_n, e_n, f_n]^T = [\alpha_1, 0, \alpha_3, 0, 0, 0]^T.$$

Expressions for α_1 and α_3 and the matrix elements m_{ij} are given in the appendix.

Thus, the coefficients a_n and b_n depend on the frequency, the parameters of the external and internal media (ρ_1, c_1, ρ_2, c_2), the density of the shell material, and the Lamé constants, as well as on the radius and thickness of the shell.

As a rule, the form function f determined through the sound pressure $p_2^{(s)}$ of the scattered wave in the direction opposite to the direction of the wave incidence ($\theta = \pi$) at an infinite distance from the shell center ($r \longrightarrow \infty$) is analyzed. Using the asymptotic expression $h_n^{(1)}(x) \approx (-i)^{n+1}\exp(ix)/x$ and taking into account the fact that $P_n(-1) = (-1)^n$, it is possible to write down the form function f and $p_2^{(s)}$ as

$$f = \frac{2}{ika}\sum_{n=0}^{\infty}(2n+1)(-1)^n b_n,$$
$$p_2^{(s)} = p\frac{ae^{ikr}}{2r}f, \quad (5)$$

where a is the external radius of the shell. Another quantity that is often used is the scattering cross section σ, which is also expressed through the form function:

$$\frac{\sigma}{\pi a^2} = |f|^2.$$

Table 1. Parameters used in calculations; c_L and c_T are the velocities of longitudinal and transverse waves in titanium, respectively

	Density, kg/m^3	Sound velocity, m/s
Air	1.293	346
Ether	713.5	985
Water	1000	1500
Titanium	4540	$c_L = 5718.8$; $c_T = 3056.8$

Various techniques were suggested to analyze the form function [7]. The Sommerfeld–Watson method of integral transformation is widely used [8, 9]. The transformation is applied to a series of partial modes of the type of Eq. (4), which provides an opportunity to speed up the calculation of this slowly convergent series. Moreover, this method makes it possible to obtain the contributions of individual wave types to the scattered sound field.

Another frequently used method is the utilization of the theory of resonance scattering [10, 11] taken from quantum mechanics. The basic idea lies in the fact that a scattered field can be formally represented as a sum of two components: the resonance component related to the elastic resonances of the shell in a vacuum and the background component caused by the so-called diffraction modes. The sound field scattered by a perfectly rigid or soft sphere is often used as the background component. The choice of a suitable background component, the subtraction of which yields the resonance part in the classical Breit–Wigner form, is the main difficulty of this method. The background component for thin shells corresponds to the scattering by a soft sphere, and for very thick shells, by a rigid sphere. Some researchers suggested using an intermediate background constructed from the solutions for soft and rigid spheres [4, 11]. This approach provided somewhat better results but did not solve the problem completely.

A new technique for the separation of the resonance component is proposed in a series of papers [12–14] and applied to a cylindrical shell in [15]. According to this technique, the resonance component is separated not by subtracting a certain background but is obtained as a result of the numerical determination of the poles of form functions (the roots of the dispersion equation $\det\|m_{ij}\| = 0$) on the complex plane of frequency at a given mode number $n = 0, 1, 2, \ldots$ in such a way that each partial mode in Eq. (5) is analyzed separately. Frequency is commonly expressed in terms of the dimensionless complex quantities ka. If the pole positions and the partial mode number are known, it is easy to determine the phase velocity and to plot the dispersion curves. The analysis of the dispersion curves makes it possible to identify the resonances according to the type of motion (wave) they belong to. All results given in this paper were obtained using just this technique.

Many papers devoted to the interaction of elastic and acoustic waves in both classical [16–18] and more complex [19–22] systems have recently been published. This study was to a large extent stimulated by [15], where flexural waves propagating in a fluid-filled cylindrical shell were investigated. This study expands the results obtained in [15]. Consideration is not only

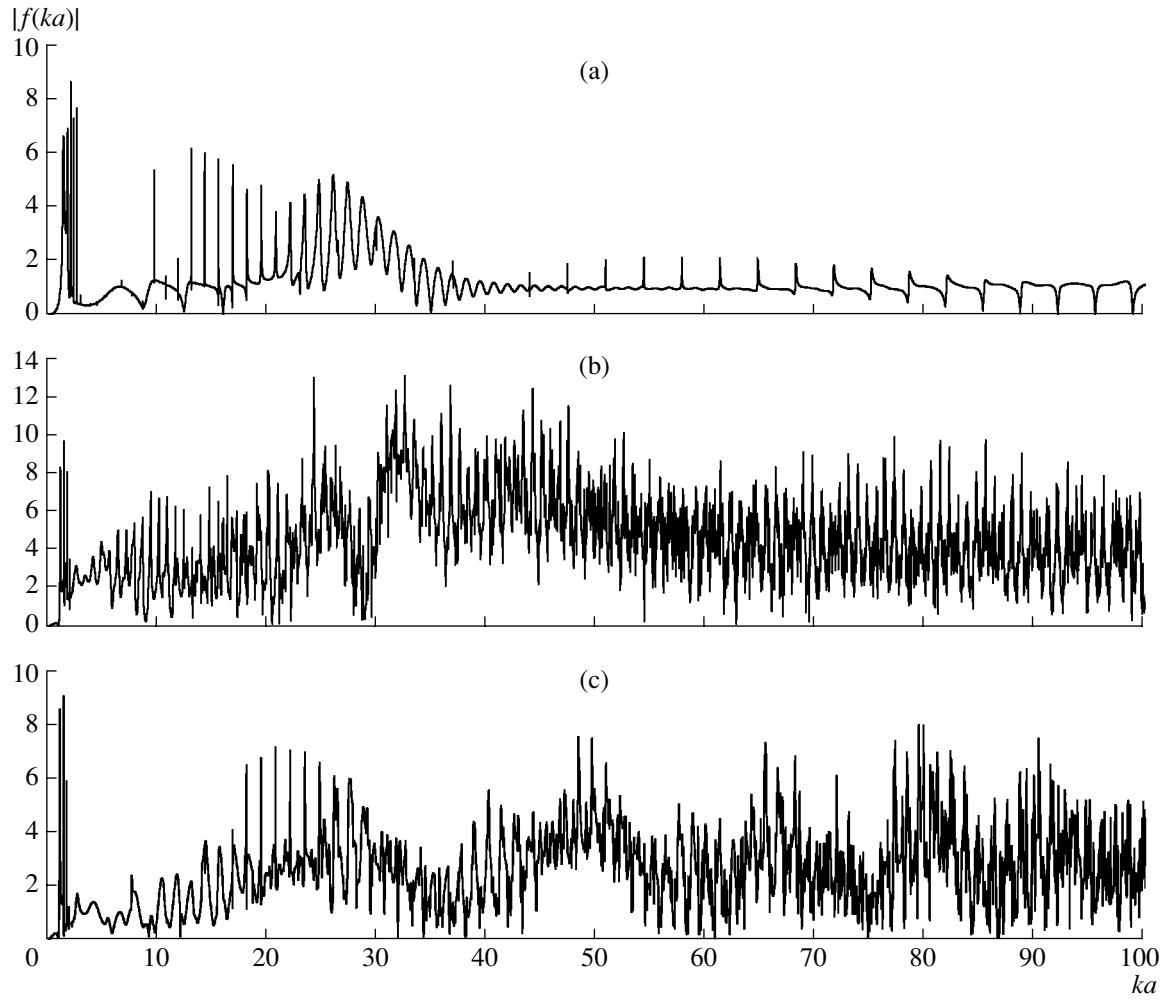

Fig. 2. Moduli of the form functions for (a) an empty shell, (b) a shell filled with ether, and (c) a shell filled with water.

given to waves of flexural type: longitudinal waves are also analyzed. Calculations are conducted in a wider range of dimensionless frequencies. Moreover, the results for a hollow shell, which were first obtained in [12, 14], are briefly discussed. This provides an opportunity to represent the interaction mechanism for various types of waves more clearly.

The numerical determination of the pole positions x_{nq} on the complex plane of the dimensionless frequency ka was performed using the Cauchy theorem of residues [23]. The rectangular region $0 < \mathrm{Re}(ka) < 100$, $0 < \mathrm{Im}(ka) < 5$ was partitioned by a rectangular grid. The following integral was calculated in each grid mesh at a given value of n:

$$I_0 = \oint_C b_n(ka)d(ka),$$

where C is the mesh boundary and $b_n(ka)$ is the coefficient involved in expansion (5) and represented as a function of frequency. If I_0 is nonzero (within the accuracy of calculations), the pole position x_{nq} is determined [11] from the ratio of integrals,

$$x_{nq} = \frac{1}{I_0}\oint_C ka b_n(ka)d(ka).$$

The index n in the pole notation corresponds to the number of a partial mode and q determines the wave type. The calculations were performed using a code designed with the help of the MATLAB 5.2 software package.

The relative phase velocity c_{nq}^{ph}/c_2 by definition [4, 24] is

$$\frac{c_{nq}^{ph}}{c_2} = \frac{\mathrm{Re}(x_{nq})}{n + (1/2)}.$$

The calculations were performed for a spherical shell made of titanium, with the ratio of the thickness (h) to the radius $h/a = 0.042$. Water, ether, and air were

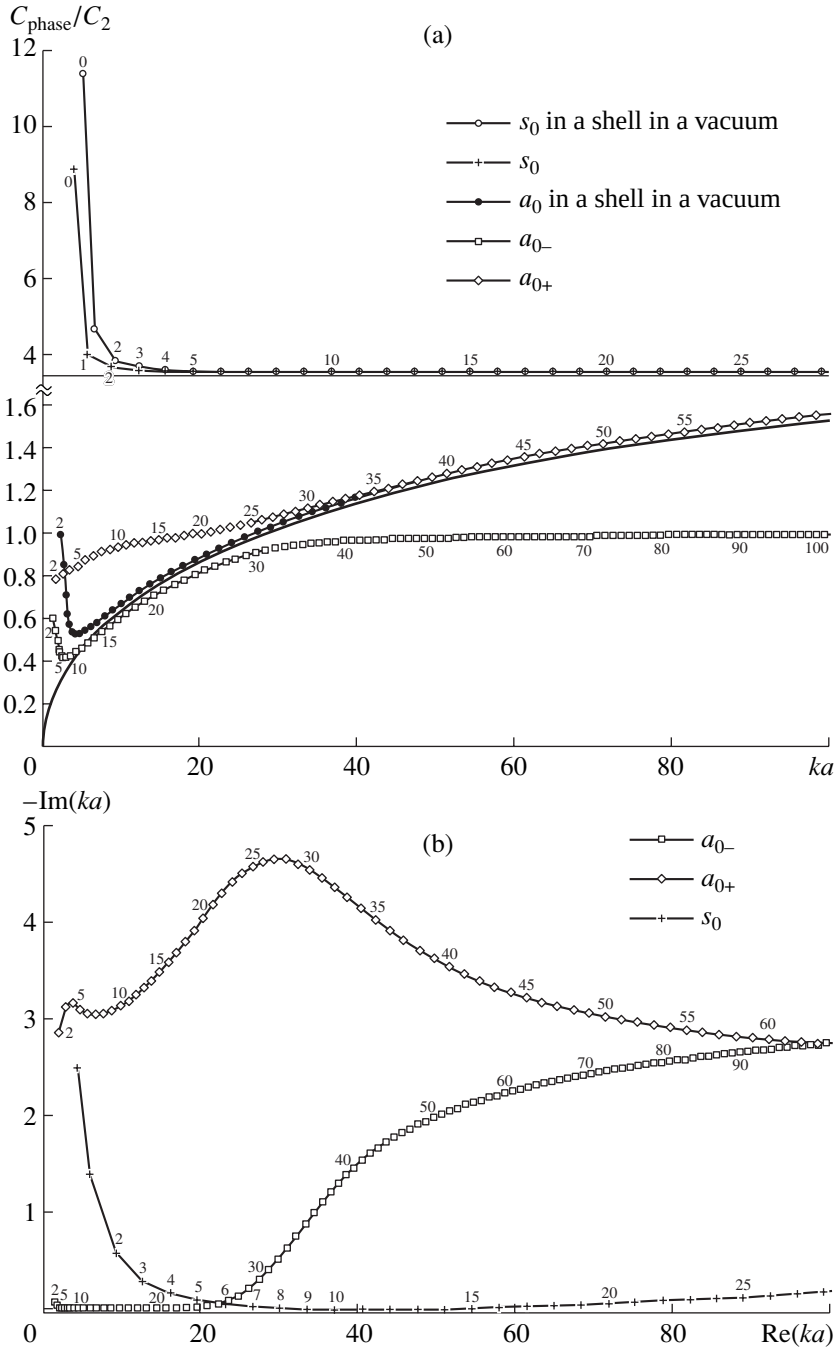

Fig. 3. (a) Dispersion curves and (b) pole positions on the complex plane of the dimensionless frequency *ka* for the antisymmetric and symmetric Lamb waves in a shell in a vacuum and in an empty shell in water. The solid lines show the wave velocities in a titanium plate of the same thickness. The numbers near the curves indicate the mode numbers.

taken as the shell fillers. The numerical parameters used for calculations are given in Table 1.

Let us first consider a simple system: a hollow spherical shell immersed in water. Its detailed analysis can be found in [12, 14], and here we give only the results of calculations and some conclusions.

The modulus of the form function is given in Fig. 2a. Two characteristic regions can be separated in the rather complex frequency dependence of $|f|$: several intense resonance peaks are present at small values of frequency $1 < ka < 4$, and, in the range of *ka* from approximately 20 to 35, several wide overlapping resonance peaks are observed, which produce a characteristic enhancement. When the frequency is higher than $ka \approx 50$, the form function fluctuates near unity with noticeable peaks and dips.

The irregularity of the form function is caused by the excitation of elastic waves in the shell. Two elastic waves propagate in the shell in a vacuum in the considered frequency range. These waves were named antisymmetric a_0 and symmetric s_0 Lamb waves by analogy with waves in a plate [12]. Figure 3a shows the dispersion curves for the Lamb waves in a shell in a vacuum and in a plate of equal thickness [25]. The lowest mode at which the excitation of the wave a_0 in a shell is possible is the second mode. At low frequencies ($ka < 10$ in our case), waves in a shell differ essentially from waves in a plate, and their name is a matter of convention. For example, it is impossible to excite the wave a_0 at low frequencies in a real shell in the absence of the symmetric wave [6].

The phase velocity of the wave s_0 changes weakly if the shell is immersed in a liquid (Fig. 3a). As one can see, the presence of an external liquid tells noticeably on the resonance frequencies of the zeroth and first modes only, where the wave slows down to a certain extent. Starting from the fourth mode, the curves almost merge, and the wave s_0 exhibits almost no dispersion.

The situation with the antisymmetric Lamb wave is entirely different. The phase velocity of this wave in a shell in a vacuum decreases rapidly at small values of ka, then passes through a minimum near $ka \approx 5$, after which it increases, and starting from $ka \approx 27$ exceeds the sound velocity in water. When a shell is immersed in water, one can observe the interesting phenomenon of the splitting of the wave a_0 into two components, which are called in [12] subsonic a_{0-} and supersonic a_{0+} components (in other papers, e.g., in [15], the supersonic branch is called the "A wave," but we will use the notations introduced in [12]).

The dispersion curves for the waves a_{0-} and a_{0+}, which are calculated for the numerical parameters indicated above, are also given in Fig. 3a. The positions of the poles corresponding to the waves s_0, a_{0-}, and a_{0+} are demonstrated in Fig. 3b.

The interaction mechanism for the two branches of the antisymmetric Lamb wave can be represented as follows. At low frequencies ($ka < 20$ in our case), the wave a_{0+} behaves as a diffraction wave and propagates in water near the shell surface. Its poles are located far from the real axis (Fig. 3b), and it contributes little to the scattered field. In the low-frequency range, the wave a_{0-} propagates in the shell, which differs little from the flexural wave a_0 in a "dry" shell. The phase velocity of the wave a_{0-} decreases to a certain extent in comparison with the wave a_0 (Fig. 3a) because of the influence of the added mass of the liquid surrounding the shell. The poles connected with the wave a_{0-} lie very close to the real axis (Fig. 3b).

In the frequency range, where the phase velocity of a flexural wave in a dry shell approaches c_2 ($20 < ka < 40$), the exchange of branches occurs. The velocity of the subsonic wave a_{0-} begins to grow slowly tending to c_2, while the dispersion curve of the branch a_{0+} approaches the curve for a_0. Starting from $ka \approx 20$, the poles of the branch a_{0-} move away from the real axis rapidly, and the wave transforms into a diffraction wave. Oppositely, the branch a_{0+} transforms into a flexural wave propagating along the shell. In the frequency range where the exchange of branches occurs the form function exhibits a characteristic rise.

If a shell is filled with a liquid (or gas), one more type of motion is possible in it, namely, the wave of the "whispering gallery" type, *wg* [25]. The dispersion equations for the waves of this type in a spherical cavity with the radius a_2 and perfectly rigid and perfectly soft boundaries are written down in the form $j_n'(k_1a_2) = 0$ and $j_n(k_1a_2) = 0$, respectively.

The resonances connected with this type of wave make the form function much more complex. Figures 2b and 2c demonstrate the moduli of the form functions for shells filled with ether and water. As one can see from Fig. 2c, apart from the characteristic rise in the range of ka from 20 to 35, the form function has some similar features in the ranges $40 < ka < 55$, $65 < ka < 75$, etc. However the form function for a shell filled with ether has an entirely different form. The rise in the range of ka from 20 to 35 is not as pronounced as in Figs. 2a and 2c, and it extends to a larger frequency interval, approximately from $ka = 20$ to $ka = 60$.

Let us consider in more detail the case of a shell filled with water. The pole positions were determined for it, and the dispersion curves can be seen in Fig. 4. The wave a_{0-} can be easily identified, since it almost does not change its form in comparison with the wave a_{0-} in an empty shell. Naturally, the velocity of this wave decreases to a certain extent because of the influence of the filler. If the minimal relative velocity of the wave a_0 in a dry shell is equal to 0.520, then, in an empty shell immersed in water, it decreases to as low as 0.406 and becomes equal to 0.345 in a water-filled shell.

The supersonic branch of the antisymmetric wave a_{0+} changes considerably. The interaction with the slowest wave of the whispering gallery type, wg_0, occurs in the frequency range $40 < ka < 55$. After that, the relative phase velocity of the branch a_{0+} stops rising and levels off at approximately 1.08. The velocity of the wave wg_0 propagating in a cavity with perfectly soft or perfectly rigid boundaries is well known to decrease monotonically. In our case, the phase velocity of wg_0 begins to grow smoothly near the region of interaction with a_{0+}, and in the range of ka from 35 to 55, this wave replaces a_{0+} in a certain way. Then, when the velocity of wg_0 approaches the velocity of the next whispering gallery wave wg_1, the interaction occurs again, and the wave wg_0 transforms into wg_1. The same process takes place for the following waves: wg_1, wg_2, etc. This interesting phenomenon was first noticed probably by Veksler [15] for the case of a cylindrical shell.

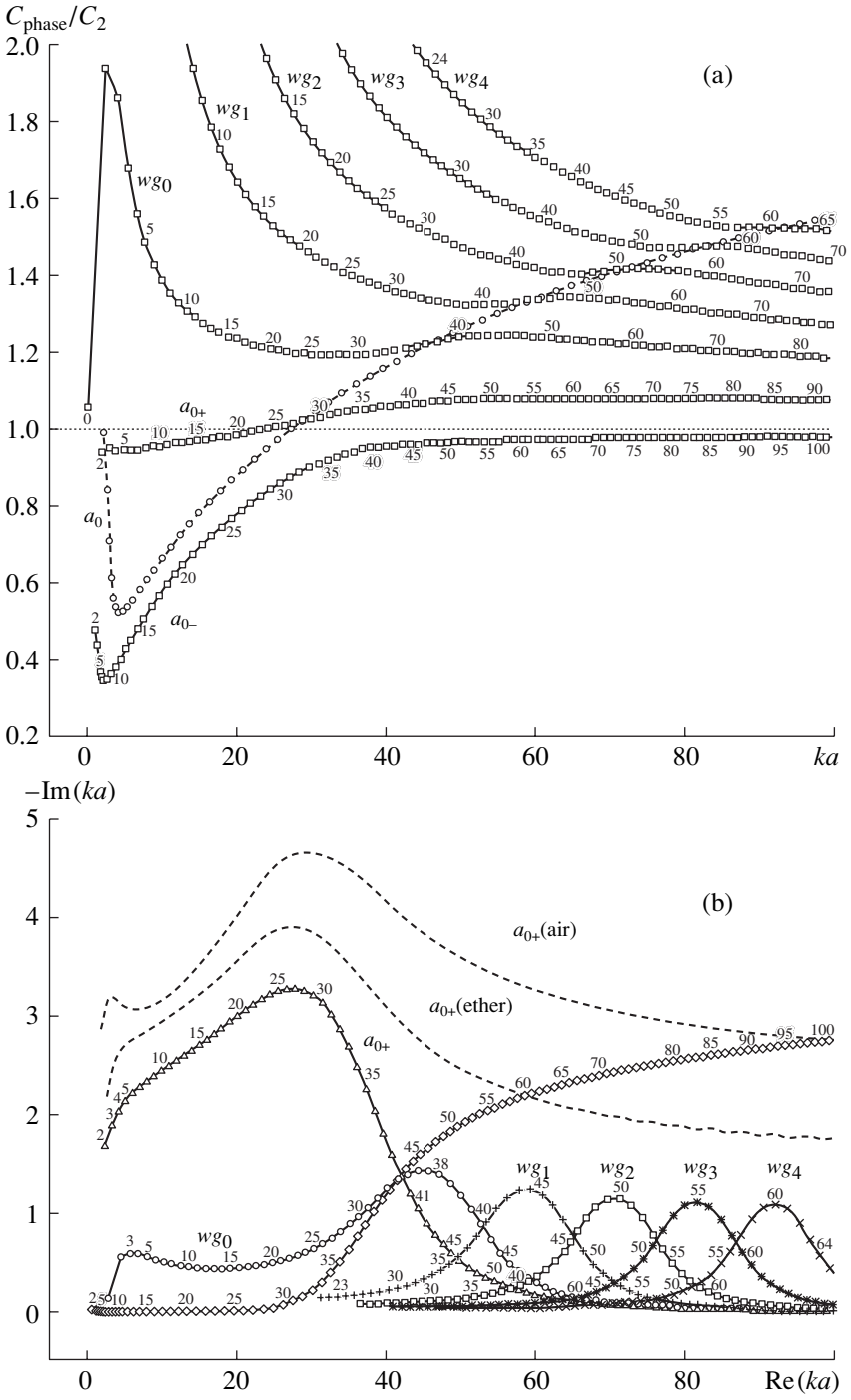

Fig. 4. (a) Dispersion curves and (b) pole positions for the waves a_{0-} and a_{0+} and the waves of the whispering gallery type, *wg*, for a water-filled shell. The relative phase velocity of the wave a_0 in a shell in a vacuum and the positions of the poles of the wave a_{0+} in shells filled with air and ether are given for comparison. The poles belonging to the waves wg_1–wg_4 are shown starting from $ka > 30$.The numbers near the curves indicate the mode numbers.

Thus, the antisymmetric Lamb wave (the flexural wave) alone does not propagate in a fluid-filled shell immersed in a liquid medium. The flexural wave is obtained as the result of the interaction between the waves of the a_{0-}, a_{0+}, and *wg* types. One can see readily that the form function has special features in the regions of interaction (branch exchange) between the waves of different types.

It is interesting to trace the change of pole trajectories for waves of different types (Fig. 4b). Comparing Figs. 3b and 4b, it is easy to see that the trajectory of the poles of a_{0-} changes little. On the contrary, the poles of

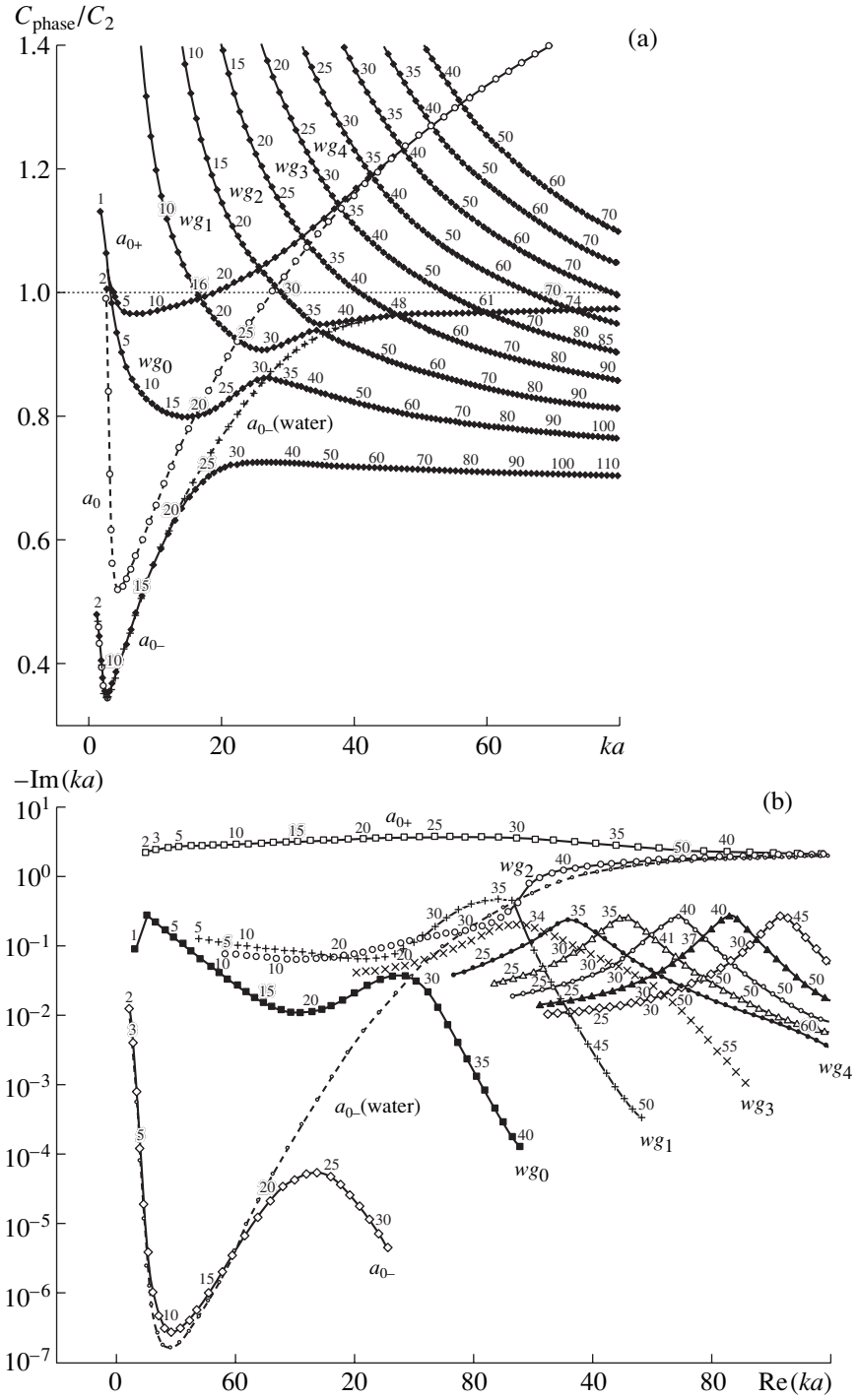

Fig. 5. The same as in Fig. 4 but for a shell filled with ether. The relative phase velocity of the wave a_0 in a shell in a vacuum and the curves corresponding to the wave a_{0-} in a water-filled shell are given for comparison.

the wave a_{0+} rapidly approach the real axis at $ka > 30$. This confirms the assumption that, at these frequencies, the wave changes its character and becomes a *wg* wave with poles that, as a rule, have a small imaginary part.

The poles of the waves wg_0–wg_4 smoothly move away from the real axis in the frequency range of wave interaction and then approach the real axis again. The poles at the maximal distance from the axis correspond exactly to the intersection of the dispersion curves for the *wg* waves and the wave a_0 (Fig. 4). The trajectories of the poles of the wave a_{0+} propagating in a shell filled with air and ether are also plotted in Fig. 4b to make it more illustrative. One can see that the increase in the

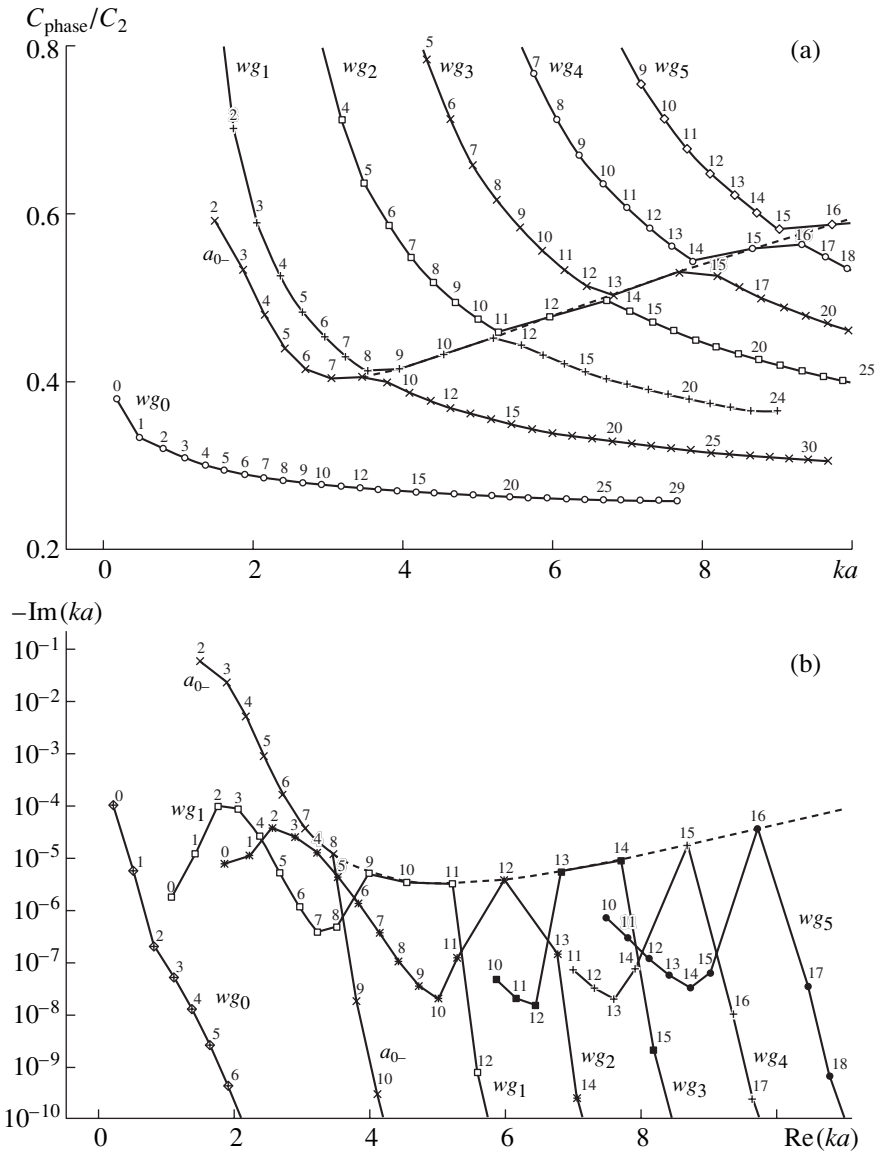

Fig. 6. (a) Dispersion curves and (b) pole positions for the waves of the a_{0-} and *wg* types for an air-filled shell. The dashed line corresponds to the wave a_{0-} in an empty shell.

filler density leads to a decrease in the width of resonances for this wave.

If a shell is filled with a liquid in which the sound velocity is smaller than in the surrounding medium, e.g., with ether, the situation becomes more complex. In this case, the interaction of the *wg* waves with both waves a_{0+} and a_{0-} can occur.

The dispersion curves for the waves propagating in a shell filled with ether are shown in Fig. 5a. The same figure presents the curves of the relative phase velocity for the waves a_0 in a shell in vacuum and a_{0-} in a shell filled with water. The velocities of the waves a_{0-} in a shell with ether and in a shell filled with water are almost the same at the frequencies $ka < 13$. At higher frequencies, the interaction with the wave wg_0 occurs. Up to the frequency $ka \approx 35$, the dispersion curve of the wave a_{0-} is realized in the form of segments of the waves wg_0 and wg_1. At higher frequencies, its character apparently changes. Proceeding from the pole positions shown in Fig. 5b, we can conclude that, starting from $ka \approx 35$, the interaction does not occur, since the trajectory of wg_2 starts to move away from the real axis and passes near the trajectory of the wave a_{0-} propagating in a shell filled with water.

The form of the dispersion curves also indicates the absence of interaction (Fig. 5a). As was demonstrated in [15], the behavior of the dispersion curves near the intersection with the curve for the wave a_0 is deter-

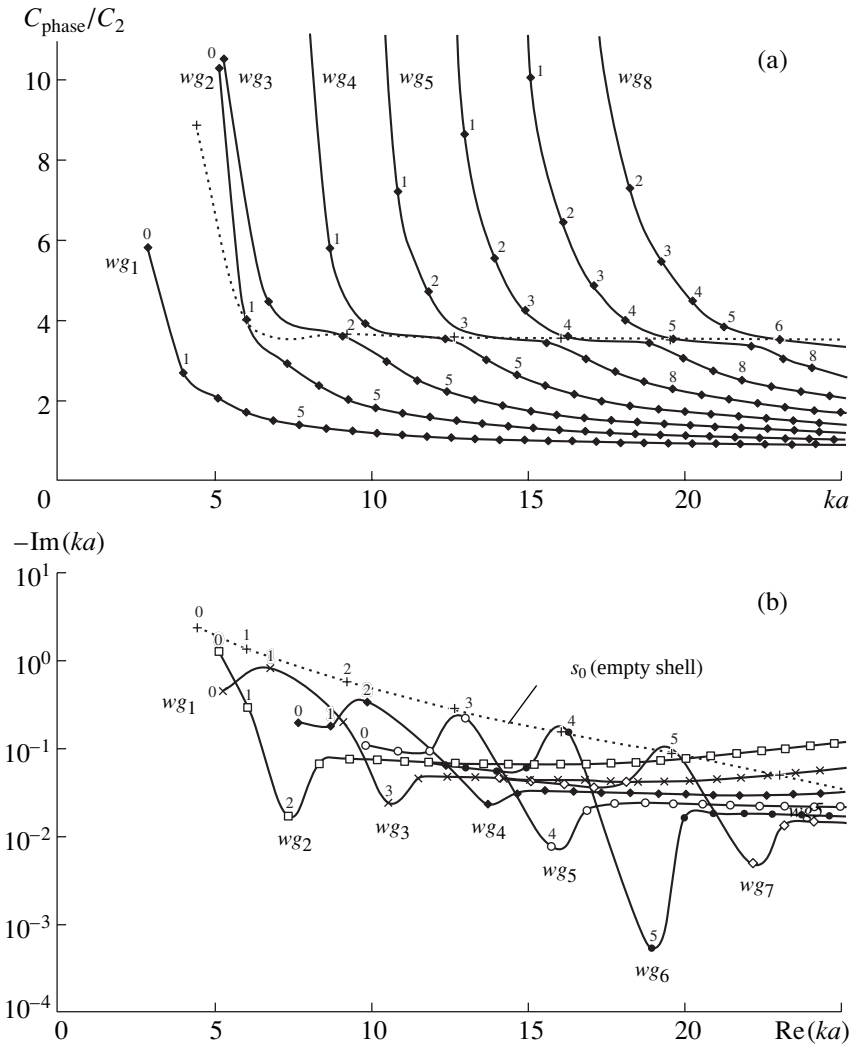

Fig. 7. (a) Dispersion curves and (b) pole positions for a shell filled with ether. The dotted lines correspond to a symmetric wave in an empty shell in water.

mined by the filler density. The lighter the filler is, the closer the curves for the *wg* waves approach the curve for a_0. The same conclusion can be drawn by comparing Figs. 4a and 5a. However, the shapes of the curves for wg_3, wg_4, etc., almost do not change at the intersection with the curve for wg_1, which points to the absence of interaction.

The wave a_{0+} was separated as an individual type of motion for the same reasons (Fig. 5).

In conclusion, without any detailed analysis, we present the dispersion curves and the pole positions for a shell filled with air (Fig. 6). This example illustrates, first, the dependence of the shapes of the dispersion curves on the filler density and, second, the assumption that the interaction between the waves of different types occurs when the trajectories of the poles of these waves are close to each other. The form function for this case is not given, since it differs little from the one plotted in Fig. 2a.

Certain difficulties arose in the identification of the poles determining the symmetric Lamb wave s_0. Sometimes, it was difficult to determine which of the two closely located poles corresponded to this wave. Table 2 gives the results of calculations for several first poles of the wave s_0 for a shell in vacuum and in water and with different fillers. For example, in the case of a shell filled with ether, the pole trajectory for the wave s_0 can pass through the points $5.1544 - 1.2674i$, $6.0487 - 0.2946i$, $9.1039 - 0.2104i$, …, as well as through the points $5.2791 - 0.4580i$, $6.7402 - 0.8382i$, etc. Similar difficulties also arose with the poles for the waves of the *wg* type.

An assumption was made that the wave s_0 also interacts with the waves of the whispering gallery type and does not exist alone in the system under study but

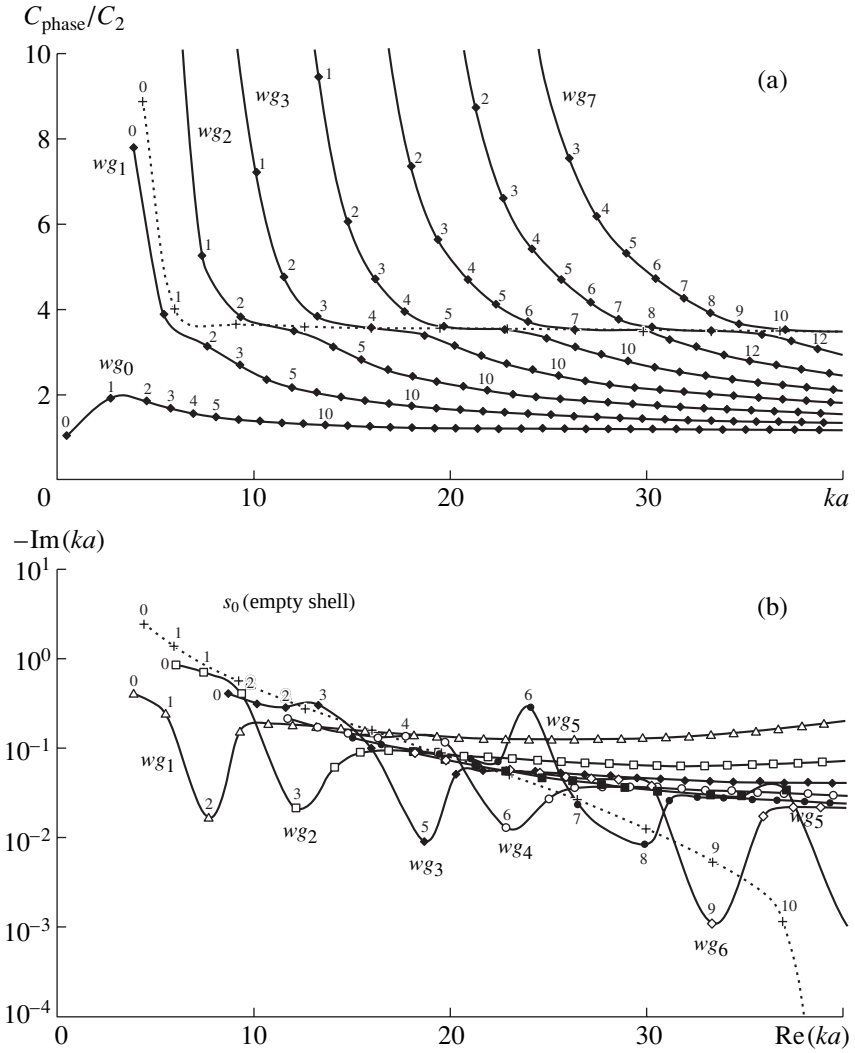

Fig. 8. The same as in Fig. 7 but for a shell filled with water.

results from the interaction of the *wg* waves. Figures 7a and 8a show the dispersion curves for shells with ether and water, respectively, which illustrate the above hypothesis. The dotted line and crosses demonstrate the curve for the relative phase velocity of the wave s_0 in an empty shell immersed in water.

If this assumption is correct, the trajectories of the poles of the *wg* waves have the form given in Figs. 7b

Table 2. Dimensionless complex pole frequencies *ka* determining the symmetric Lamb wave s_0. Two closest poles are given for shells with water and ether

Mode	Shell in vacuum	Empty shell in water	Shell with ether	Shell with water
0	5.6823	4.4494 – 2.5016*i*	5.1544 – 1.2674*i*	3.9221 – 0.4227*i*
			5.2791 – 0.4580*i*	6.0701 – 0.8611*i*
1	6.9511	6.0319 – 1.3931*i*	6.0487 – 0.2946*i*	5.5152 – 0.2388*i*
			6.7402 – 0.8382*i*	7.4481 – 0.7111*i*
2	9.5726	9.2103 – 0.5746*i*	9.1039 – 0.2104*i*	7.7202 – 0.0167*i*
			9.8137 – 0.3553*i*	9.4238 – 0.4052*i*
3	12.7789	12.6373 – 0.2855*i*	12.4002 – 0.0669*i*	12.1449 – 0.0223*i*
			13.0210 – 0.2282*i*	13.3383 – 0.3034*i*
4	16.1568	16.0945 – 0.1567*i*	15.7118 – 0.0078*i*	16.0331 – 0.1005*i*
			16.2895 – 0.1575*i*	

and 8b. In the case of ether (Fig. 7b), the picture is more illustrative. The trajectories have breakpoints near the corresponding poles of the wave s_0 in an empty shell. If we connect the poles of wg_2, $n = 0$ with those of wg_3, $n = 1$, and so on, we obtain the trajectory of the apparent wave s_0, which almost coincides with the trajectory for s_0 starting from $n = 4$.

CONCLUSION

Acoustic waves arising in a fluid-filled elastic spherical shell were studied in this paper. The propagation of two Lamb elastic waves, i.e., symmetric (longitudinal) and antisymmetric (flexural) waves, is possible at low frequencies in a shell in a vacuum. When an empty shell is immersed in a liquid, an interesting phenomenon is observed: the splitting of the antisymmetric wave into two branches.

If a shell is filled with a gas or a liquid, one more type of motion becomes possible in it: waves of the whispering gallery type. These waves propagate in the inner volume of the shell. As it has been demonstrated in this paper, none of the motion types (the waves a_0 and s_0 and the *wg* waves) is realized alone in this system in the general case, but they are possible as a result of the interaction of different waves. The interaction mechanism is analogous to the exchange of branches between the waves a_{0-} and a_{0+} in an empty shell.

The condition for such an interaction is the intersection of the dispersion curves of the waves propagating in solitary systems and, apparently, the closeness of the widths of the resonance peaks corresponding to different waves (closeness of the pole trajectories).

APPENDIX

Elements of the matrix m_{ij}:

$$m_{11} = 0, \quad m_{12} = (2n+1)i^n h_n^{(1)\prime}(ka)\frac{pa}{\rho_2 c_2 \omega},$$

$$m_{13} = -\mu_{L1} j_n'(\mu_{L1}), \quad m_{14} = -\mu_{L1} n_n'(\mu_{L1}),$$

$$m_{15} = n(n+1) j_n(\mu_{T1}), \quad m_{16} = n(n+1) n_n(\mu_{T1}),$$

$$m_{21} = (2n+1)i^n j_n'(k_1 a_2)\frac{pa_2}{\rho_1 c_1 \omega}, \quad m_{22} = 0,$$

$$m_{23} = -\mu_{L2} j_n'(\mu_{L2}), \quad m_{24} = -\mu_{L2} n_n'(\mu_{L2}),$$

$$m_{25} = n(n+1) j_n(\mu_{T2}), \quad m_{26} = n(n+1) n_n(\mu_{T2}),$$

$$m_{31} = 0, \quad m_{32} = (2n+1)i^n h_n^{(1)}(ka) pa^2,$$

$$m_{33} = 2\mu\mu_{L1}^2 j_n''(\mu_{L1}) - \lambda\mu_{L1}^2 j_n(\mu_{L1}),$$

$$m_{34} = 2\mu\mu_{L1}^2 n_n''(\mu_{L1}) - \lambda\mu_{L1}^2 n_n(\mu_{L1}),$$

$$m_{35} = 2\mu n(n+1)(j_n(\mu_{T1}) - \mu_{T1} j_n'(\mu_{T1})),$$

$$m_{36} = 2\mu n(n+1)(n_n(\mu_{T1}) - \mu_{T1} n_n'(\mu_{T1})),$$

$$m_{41} = (2n+1)i^n j_n(k_1 a_2) pa_2^2, \quad m_{42} = 0,$$

$$m_{43} = 2\mu\mu_{L2}^2 j_n''(\mu_{L2}) - \lambda\mu_{L2}^2 j_n(\mu_{L2}),$$

$$m_{44} = 2\mu\mu_{L2}^2 n_n''(\mu_{L2}) - \lambda\mu_{L2}^2 n_n(\mu_{L2}),$$

$$m_{45} = 2\mu n(n+1)(j_n(\mu_{T2}) - \mu_{T2} j_n'(\mu_{T2})),$$

$$m_{46} = 2\mu n(n+1)(n_n(\mu_{T2}) - \mu_{T2} n_n'(\mu_{T2})),$$

$$m_{51} = 0, \quad m_{52} = 0, \quad m_{53} = 2\mu_{L1} j_n'(\mu_{L1}) - 2j_n(\mu_{L1}),$$

$$m_{54} = 2\mu_{L1} n_n'(\mu_{L1}) - 2n_n(\mu_{L1}),$$

$$m_{55} = -\mu_{T1}^2 j_n''(\mu_{T1}) - (n^2+n-2) j_n(\mu_{T1}),$$

$$m_{56} = -\mu_{T1}^2 n_n''(\mu_{T1}) - (n^2+n-2) n_n(\mu_{T1}),$$

$$m_{61} = 0, \quad m_{62} = 0, \quad m_{63} = 2\mu_{L2} j_n'(\mu_{L2}) - 2j_n(\mu_{L2}),$$

$$m_{64} = 2\mu_{L2} n_n'(\mu_{L2}) - 2n_n(\mu_{L2}),$$

$$m_{65} = -\mu_{T2}^2 j_n''(\mu_{T2}) - (n^2+n-2) j_n(\mu_{T2}),$$

$$m_{66} = -\mu_{T2}^2 n_n''(\mu_{T2}) - (n^2+n-2) n_n(\mu_{T2}).$$

Components of the column of free terms:

$$\alpha_1 = -(2n+1)i^n j_n'(ka)\frac{pa}{\rho_2 c_2 \omega}, \qquad (35)$$

$$\alpha_3 = -(2n+1)i^n j_n(ka) pa^2.$$

Here, $j_n(x)$ and $n_n(x)$ are the Bessel and Neumann spherical functions of the *n*th order, the prime denotes a derivative with respect to x, $\mu_{L1} = \frac{\omega}{c_L} a$, $\mu_{L2} = \frac{\omega}{c_L} a_2$, $\mu_{T1} = \frac{\omega}{c_T} a$, and $\mu_{T2} = \frac{\omega}{c_T} a_2$.

REFERENCES

1. M. C. Junger, J. Acoust. Soc. Am. **24**, 366 (1952).
2. A. Kalnins, J. Acoust. Soc. Am. **36**, 74 (1964).
3. R. R. Goodman and R. Stern, J. Acoust. Soc. Am. **34**, 338 (1962).
4. J. D. Murphy, J. George, A. Nagl, and H. Überall, J. Acoust. Soc. Am. **65**, 368 (1979).
5. J. A. Fawcett, J. Acoust. Soc. Am. **109**, 508 (2001).
6. E. L. Shenderov, *Radiation and Scattering of Sound* (Sudostroenie, Leningrad, 1989).
7. L. M. Lyamshev, Akust. Zh. **45** (5), 693 (1999) [Acoust. Phys. **45** (5), 619 (1999)].
8. K. L. Williams and P. L. Marston, J. Acoust. Soc. Am. **78**, 1093 (1985).

9. K. L. Williams and P. L. Marston, J. Acoust. Soc. Am. **79**, 1702 (1986).
10. L. Flax, L. R. Dragonette, and H. Überall, J. Acoust. Soc. Am. **63**, 723 (1978).
11. G. C. Gaunaurd and M. F. Werby, J. Acoust. Soc. Am. **90**, 2536 (1991).
12. G. S. Sammelmann, D. H. Trivett, and R. H. Hackman, J. Acoust. Soc. Am. **85**, 114 (1989).
13. G. S. Sammelmann and R. H. Hackman, J. Acoust. Soc. Am. **89**, 2096 (1991).
14. R. H. Hackman and G. S. Sammelmann, J. Acoust. Soc. Am. **90**, 2705 (1991).
15. N. D. Veksler, J.-L. Izbicki, and J.-M. Conoir, Akust. Zh. **45**, 321 (1999) [Acoust. Phys. **45**, 279 (1999)].
16. B. T. Hefner and P. L. Marston, J. Acoust. Soc. Am. **107**, 1930 (2000).
17. Kohji Toda and Kenji Motegi, J. Acoust. Soc. Am. **107**, 1045 (2000).
18. F. Padilla, M. de Billy, and G. Quentin, J. Acoust. Soc. Am. **106**, 666 (1999).
19. J. K. Henry and R. L. Clark, J. Acoust. Soc. Am. **109**, 1456 (2001).
20. M. Tournour and N. Atalla, J. Acoust. Soc. Am. **107**, 2379 (2000).
21. K. S. Sum and J. Pan, J. Acoust. Soc. Am. **107**, 2021 (2000).
22. Pei-Tai Chen, J. Acoust. Soc. Am. **105**, 106 (1999).
23. V. I. Smirnov, *Course of Higher Mathematics* (Nauka, Moscow, 1974), Vol. 3, Part 2.
24. M. Talmant, H. Überall, R. D. Miller, *et al.*, J. Acoust. Soc. Am. **86**, 278 (1989).
25. L. M. Brekhovskikh, *Waves in Layered Media*, 2nd ed. (Nauka, Moscow, 1973; Academic, New York, 1960).

Translated by M. Lyamshev

Acoustical Physics, Vol. 48, No. 3, 2002, pp. 321–324. Translated from Akusticheskiĭ Zhurnal, Vol. 48, No. 3, 2002, pp. 371–374.
Original Russian Text Copyright © 2002 by Kudashev, Yablonik.

Simple Models of the Characteristic Functional in Hydrodynamic Acoustics

E. B. Kudashev* and L. R. Yablonik**

** Institute of Space Research, Russian Academy of Sciences, ul. Profsoyuznaya 84/32, Moscow, 117810 Russia*
e-mail: eco@iki.rssi.ru
*** NPO Polzunov Central Boiler and Turbine Institute, ul. Atamanskaya 3/6, St. Petersburg, 193167 Russia*
e-mail: lry@ckti.nw.ru

Received June 6, 2001

Abstract—Simple models of the characteristic functional are considered in the context of analyzing the probabilistic characteristics of turbulent pressure fluctuations. The Gaussian model of the spatial characteristic functional of wall-pressure fluctuations is shown to be more appropriate for jet flows, while the Poisson model better describes the characteristic features (splashes) of pressure fluctuations in a turbulent boundary layer. The suggestion is made that the representation of the characteristic functional as a superposition of simple models can reduce the experimental determination of the characteristic functional and the multidimensional distribution functions to measuring only a limited number of parameters and dependences characterizing the turbulent flow under study. *© 2002 MAIK "Nauka/Interperiodica".*

INTRODUCTION

Our present notion of the processes underlying the generation of turbulent wall-pressure fluctuations and the role of organized structures in a boundary-layer flow [1, 2] was formed as a result of the mutual influence of the correlation-spectrum methods of measurement and the physical models of turbulent pressure fields. The Corcos correlation model [3] of the turbulent pressure field in a boundary-layer flow is one of the known examples of such a fruitful interplay.

The models that most adequately describe the spatial structure of the field of wall-pressure fluctuations $p(\mathbf{x})$ are the continual statistical models specified by a characteristic functional [4, 5]

$$\Phi[\upsilon(\mathbf{x})] = \langle \exp\{i\int \upsilon(\mathbf{x})p(\mathbf{x})d\mathbf{x}\}\rangle,$$

which provide a complete statistical description of the random field of pressure fluctuations $p(\mathbf{x})$. Functional methods are often used in hydrodynamic acoustics and in statistical hydroacoustics, as well as in the analysis of the probabilistic structure of random processes and fields [6, 7].

In this paper, we analyze simple analytical representations of the characteristic functional of turbulent wall-pressure fluctuations.

FUNCTIONAL APPROACH TO THE MEASUREMENT OF TURBULENT PRESSURES

The functional approach to measuring turbulent pressures was suggested in our previous papers [8–12]. This approach provides an almost exhaustive description of the random field $p(\mathbf{x})$ on the basis of the experimentally measured characteristic functional of the turbulent pressure field in the boundary layer.

In the experimental measurements, the characteristic functional of the field, $\Phi[\upsilon(\mathbf{x})]$, is determined for a family of the functional arguments $\upsilon(x) = \lambda K(\mathbf{x})$, where λ is the sensitivity of the receiver of turbulent fluctuations and $K(\mathbf{x})$ is the impulse response of the receiver [8]. Because of the averaging effect of the receiving surface, the characteristic function of the signal of the turbulent pressure transducer

$$\varphi_s(\lambda) = \langle \exp(i\lambda s)\rangle$$

is actually an estimator of the characteristic functional of the field:

$$\varphi_s(\lambda) = \langle \exp(i\int \lambda K(\mathbf{x})p(\mathbf{x})d\mathbf{x})\rangle = \Phi[\lambda K(\mathbf{x})]. \quad (1)$$

When the turbulent fluctuation sensors have sufficiently small receiving areas and the impulse response can be approximated by the delta-function

$$\lambda K(\mathbf{x}) \longrightarrow \lambda\gamma_0\delta(\mathbf{x}-\mathbf{x}_0),$$

the characteristic functional $\Phi[\lambda K(\mathbf{x})]$ is expressed through the characteristic function

$$\varphi_s(\lambda) = \langle \exp\{i\lambda\gamma_0 p(\mathbf{x}_0)\}\rangle = \varphi_p(\lambda\gamma_0)$$

corresponding to the one-point probability distribution of fluctuating pressures.

1063-7710/02/4803-0321$21.00 © 2002 MAIK "Nauka/Interperiodica"

In the case of a receiver composed of n point sensors with a controlled sensitivity λ, the impulse response can be represented in the form

$$\lambda K(\mathbf{x}) \longrightarrow \sum \lambda_i \gamma_0 \delta(\mathbf{x} - \mathbf{x}_i) \equiv \sum \gamma_i \delta(\mathbf{x} - \mathbf{x}_i).$$

In this case, the characteristic functional takes the form of a characteristic function of the n-dimensional probability distribution

$$\varphi_s(\lambda_1, \ldots, \lambda_n) = \varphi_{x_1 \ldots x_n}(\gamma_1, \ldots, \gamma_n).$$

A method for measuring multidimensional distribution functions by using finite-dimension representations of the characteristic functionals was suggested in our previous papers [8–10]. We showed that the measurement of the characteristic functions of turbulent pressures makes it possible to reveal the deviation of the probability density function from the Gaussian form. Earlier, this deviation was mentioned in the papers [14, 15] reporting on the measurements of the asymmetry and excess coefficients and the probability distribution functions with the use of conventional procedures.

In the context of the functional approach, the choice of the functional models of turbulent pressure fields and the evaluation of the parameters of these models are of particular importance.

GAUSSIAN MODEL OF THE CHARACTERISTIC FUNCTIONAL

Turbulent flows characterized by the different statistical nature of their turbulent fluctuation generation are described by different functional models. In the case of jet flows, pressure fluctuations are generated by external turbulence. In this case, if the distance between the sources and the observation point is sufficiently long, the turbulent wall-pressure fluctuations can be represented as a sum of many statistically independent components related to different zones of the turbulent flow.

Random quantities of this type usually have a Gaussian asymptotic distribution, which leads to the model of the Gaussian field whose characteristic functional has the form

$$\Phi_G[\upsilon] = \exp\{-1/2 \iint \upsilon(\mathbf{x}_1)\upsilon(\mathbf{x}_2) R(\mathbf{x}_1, \mathbf{x}_2) d\mathbf{x}, d\mathbf{x}_2\}, \quad (2)$$

where $R(\mathbf{x}_1, \mathbf{x}_2)$ is the correlation function of the field $R = \langle p(\mathbf{x}_1) p(\mathbf{x}_2) \rangle$. In a homogeneous field, the correlation function depends only on the mutual arrangement of the correlated points, i.e., it is a function of the coordinate difference $\varepsilon = \mathbf{x}_1 - \mathbf{x}_2$.

In the case of the Gaussian model, the experimental investigation of the characteristic functional of the turbulent pressure field is reduced to measuring a limited number of parameters and dependences, namely, to determining the spatial correlation function of pressure fluctuations.

Taking into account Eq. (1), we obtain that, in the case of the Gaussian model, characteristic functional (2) can be represented in the form

$$\varphi_G = \Phi_G[\lambda K(\mathbf{x})] = \exp[-\lambda^2/2 \int \theta(\varepsilon) R(\varepsilon) d\varepsilon],$$

where $\theta(\varepsilon) = \int K(\mathbf{x}) K(\mathbf{x} + \varepsilon) d\mathbf{x}$ is the receiver influence function.

The characteristic function of the receiver signal in the wave representation has the form

$$\varphi_{sG} = \exp[-\lambda^2/2 \int S(\mathbf{k}) E(\mathbf{k}) d\mathbf{k}],$$

where $S(\mathbf{k}) = \int \theta(\varepsilon) \exp(-i\mathbf{k}\varepsilon) d\varepsilon$ is the wave characteristic of the receiver and $E(\mathbf{k})$ is the wave-number spectrum of turbulent pressure fluctuations [13, 14].

Measurements carried out in Russia [15] and abroad [16, 17] point to the fact that the actual probability distributions of turbulent pressure fluctuations differ from the Gaussian law. In many experiments, the measured value of the asymmetry coefficient differed from zero, while the measured value of the excess coefficient increased and steadily exceeded the value of three corresponding to the Gaussian distribution.

POISSON MODEL OF THE CHARACTERISTIC FUNCTIONAL

For the aforementioned reason, it is worthwhile to complicate the functional model of the turbulent pressure field by introducing the Poisson distribution. The Poisson model is close to the nature of pressure fluctuations in a turbulent boundary layer and can be useful for describing the wall pressures. It is known that, contrary to jet flows, turbulent wall-pressure fluctuations are governed by spontaneous splashes that are accompanied by the ejection of the liquid from the wall to the external region of the flow [2]. Assuming that the splashes are statistically independent and distributed over the surface according to the uniform probability law, we can approximately describe the field of wall-pressure fluctuations by Poisson statistics.

The corresponding spatial structure of turbulent pressures is conveniently characterized by the Poisson characteristic functional

$$\Phi_P[\upsilon(\mathbf{x})] = \exp\{\nu \int [\chi(\int g(\mathbf{x} - \mathbf{y}) \upsilon(\mathbf{x}) d\mathbf{x}) - 1] d\mathbf{y}\},$$

where ν is the average number of splashes per unit area, $\chi(\mu)$ is the characteristic probability distribution function of pressure fluctuations P in the splash core, pressure P characterizes a single splash and represents the fluctuation value in this splash, and $g(\mathbf{r})$ is the normalized ($g(0) = 1$) splash influence function determining the spatial correlation

$$R_{pp}(\mathbf{r}) = \nu \langle P^2 \rangle \int g(\boldsymbol{\rho}) g(\boldsymbol{\rho} + \mathbf{r}) d\boldsymbol{\rho}.$$

In this case, the turbulent wall-pressure fluctuation p generated by many splashes is the sum over all splashes (with the running index k) that occur at the wall at the points with the vector coordinates $\mathbf{x}_k$, where $\mathbf{x}$ is the running vector coordinate at the wall:

$$p(\mathbf{x}) = \sum P(\mathbf{x}_k) g(\mathbf{x} - \mathbf{x}_k).$$

In the Poisson field, the characteristic function of the signal at the output of a homogeneous receiver of area S (in this case, $K(\mathbf{x}) = K_0 = \text{const}$ at the receiver aperture) is representable in the form

$$\varphi_P(\lambda) = \exp\{\nu \int [\chi(\lambda K_0 \int g(\mathbf{x} - \mathbf{y}) d\mathbf{x}) - 1] d\mathbf{y}\}. \quad (3)$$

For small apertures S, the receiver can be considered as a point receiver and, according to the latter expression, we have

$$\varphi_P(\lambda) = \exp\{\nu \int [\chi(\lambda \gamma_0 g(\mathbf{y})) - 1] d\mathbf{y}\}. \quad (4)$$

By contrast, when the area of the receiving aperture S is much greater than the area $\sigma = \int g(\boldsymbol{\rho}) d\boldsymbol{\rho}$ of the influence region of a spontaneous splash, according to Eq. (3), we obtain

$$\varphi_P(\lambda) = \exp\{\nu S[\chi(\lambda \gamma_0 \sigma / S)] - 1\}.$$

In the latter case, the cumulants T_n of the random signal at the receiver output are representable in the form

$$T_n = (-i)^n (d_n \ln \varphi_P / d\lambda^n)_{\lambda = 0} = (-i)^n \nu S (\sigma / S)^n \times \gamma_0^n \chi^{(n)}(0) = (-i)^n (\nu\sigma)(\sigma / S)^{n-1} \gamma_0^n \langle P^n \rangle. \quad (5)$$

From Eq. (5), it follows that, in the case of a large receiver aperture $S/\sigma \gg 1$, all cumulants with $n > 2$ are small in comparison with the second cumulant T_2. Then, the probability distribution approaches the Gaussian law

$$\varphi_P(\lambda) \approx \exp[-1/2 \lambda^2 \gamma_0^2 \langle P^2 \rangle \nu \sigma^2 / S]. \quad (6)$$

A comparison of Eqs. (4) and (6) shows the extent to which the size of the receiver affects the statistical characteristics of the signal obtained from the measurements of pressure fluctuations in the turbulent boundary layer: when $S \gg \sigma$, the statistics is Gaussian irrespective of the fluctuation behavior observed for small scales. This fact was pointed out earlier in [14] and in our recent paper [10].

SUPERPOSITION OF SIMPLE MODELS

The experimentally observed differences in the regimes of turbulent wall pressures suggests the representation of the wall-pressure fluctuations in the form of a superposition of fields corresponding to different functional models, including the simple models considered above.

In particular, we can deal with wall-pressure fluctuations $p(x, y, z)|_{z=0}$ in the form of the sum

$$p(x, y, z)|_{z=0} = p_G(x, y, z)|_{z=0} + p_p(x, y, z)|_{z=0},$$

where the first component $p_G(x, y, z)|_{z=0}$ obeys Gaussian statistics and the second component $p_p(x, y, z)|_{z=0}$, Poisson statistics.

In this case, using the simple functional models, one can reduce the experimental determination of the characteristic functional and multidimensional distributions of the turbulent pressure field to the measurement of a limited number of parameters characterizing the turbulent flow under study. Namely, one should measure the spatial correlation function $R_G(\mathbf{x}_1, \mathbf{x}_2)$ of turbulent pressure fluctuations for the Gaussian field and the dependences ν_P, $\chi(\mu)$, and $g_P(\boldsymbol{\rho})$ for the Poisson component of the turbulent pressure field.

Evidently, a further development of the functional approach in hydrodynamic acoustics, which is based on our method of experimental determination of the characteristic functional in combination with an analysis of the functional models of turbulent wall pressures, should include a correlation of the results with experimental data obtained for different types of turbulent flows.

ACKNOWLEDGMENTS

This work was supported in part by the Russian Foundation for Basic Research, project no. 01-07-90008, and the program *Integratsiya*, project no. A-0030.

We are grateful to Yu.A. Kravtsov for useful remarks and fruitful discussions.

REFERENCES

1. M. K. Bull, J. Sound Vibr. **190**, 299 (1996).
2. B. J. Cantwell, Annu. Rev. Fluid Mech. **13**, 457 (1981).
3. G. M. Corcos, J. Fluid Mech. **18**, 353 (1964).
4. S. M. Rytov, Yu. A. Kravtsov, and V. I. Tatarskiĭ, *Introduction to Statistical Radiophysics* (Nauka, Moscow, 1978), Part 2.
5. A. S. Monin and A. M. Yaglom, *Statistical Hydromechanics* (Nauka, Moscow, 1967), Part 2.
6. V. I. Klyachkin, in *Proceedings of 5th All-Union School–Seminar on Statistical Hydroacoustics* (Novosibirsk, 1974), p. 5.
7. V. I. Klyachkin, Izv. Akad. Nauk SSSR, Mekh. Zhidk. Gaza, No. 1, 131 (1979).
8. E. B. Kudashev and L. R. Yablonik, Akust. Zh. **45**, 524 (1999) [Acoust. Phys. **45**, 467 (1999)].
9. E. B. Kudashev and L. R. Yablonik, in *Proceedings of X Session of the Russian Acoustical Society*, Vol. 3: *Architectural Acoustics. Noise and Vibration* (NIISF RAASN, Moscow, 2000), p. 113.
10. E. B. Kudashev and L. R. Yablonik, in *Abstracts of International Conference on Fluxes and Structures in Fluids* (St. Petersburg, Russia, 1999), p. 71.

11. E. B. Kudashev and L. R. Yablonik, in *Proceedings of 17th International Congress on Acoustics* (Rome, 2001).
12. E. B. Kudashev and L. R. Yablonik, in *Proceedings of XI Session of the Russian Acoustical Society*, Vol. 1 (Moscow, 2001), p. 262.
13. E. B. Kudashev and L. R. Yablonik, Akust. Zh. **23**, 615 (1977) [Sov. Phys. Acoust. **23**, 351 (1977)].
14. E. B. Kudashev, in *Abstracts of XI All-Union Symposium on Representation Methods and Instrument Analysis of Random Processes and Fields, Sukhumi, 1980* (Leningrad, 1980), Section 1, p. 58.
15. E. M. Greshilov, B. V. Lipatov, L. M. Lyamshev, and V. G. Tkachenko, in *Proceedings of Second All-Union Symposium on Physics of Acoustic-Hydrodynamic Phenomena and Optoacoustics, Suzdal', 1979* (Nauka, Moscow, 1982), p. 127.
16. G. Scheve, J. Fluid Mech. **134**, 311 (1983).
17. S. P. Gravante, A. M. Naguib, C. E. Wark, and H. M. Nagib, AIAA J. **36** (10), 1808 (1998).

Translated by A. Vinogradov

Acoustical Physics, Vol. 48, No. 3, 2002, pp. 325–330. Translated from Akusticheskiĭ Zhurnal, Vol. 48, No. 3, 2002, pp. 375–381.
Original Russian Text Copyright © 2002 by Kudryashov.

Correlation Processing of a Noise Signal in the Arrival-Time Acoustic Monitoring of the Water Medium in an Arctic Waveguide

V. M. Kudryashov

Andreev Acoustics Institute, Russian Academy of Sciences, ul. Shvernika 4, Moscow, 117036 Russia

e-mail: bvp@akin.ru

Received February 15, 2001

Abstract—The propagation of a noise signal is considered for an arctic-type waveguide with a varying sound speed profile. The profiles used in the calculations differ from each other due to different depth dependences of salinity. The shape of the envelope of the time correlation function is studied for the coherent and reference signals. For the latter, either the replica of the transmitted noise signal or one of the modes propagating in the waveguide is used. A characteristic feature of the proposed technique is the use of the time cross-correlation between the signals that traveled through the same path in the presence of different sound speed profiles. In this case, from the shape of the envelope of the signal correlation function, one can estimate the changes that occur in the sound speed profile on the path of signal propagation. © *2002 MAIK "Nauka/Interperiodica".*

Acoustic methods are commonly used in the climatic monitoring of the water bulk on long propagation paths [1–5], in underwater navigation, in the exploration of mineral resources at the bottom of shallow-water seas, and in other applications. Acoustic monitoring allows one to estimate the integral change in the sound speed within the path and the state of the ice cover, whereas direct instrumental observations from vessels or helicopters provide random point sections of the water bulk, which are few in number. In some cases, the location of a noise-generating object can only be determined by acoustic technique, if observation from an aircraft or satellite is difficult.

Nowadays, sound sources are widely used that transmit a noise signal into the water. Among such signals, artificial pseudorandom ones that are based on *M*-sequences [1–6] have become popular (these signals are abbreviated as MLS) [1]. The *M*-sequences can be reproduced with a high accuracy. Upon being time-correlated with a reference signal that is identical with the transmitted one, these signals form the impulse response of the waveguide. In this case, the pulses in the envelope of the time correlation function have high amplitudes due to the energy accumulated in the realization of a long-duration noise signal.

In generating the noise signal, one can use a natural realization of a stationary and ergodic process. This process modulates the acoustic oscillations of the carrier frequency f_0 to produce the acoustic and reference signals. In all situations, a "noise portrait" of the sound source is required. We assume that the time average (the first statistical moment) of the noise signal is zero. However, the time-average intensity of the signal is not equal to zero. In practice, the variance of the sound pressure is used. In the simplest case, the electric voltage picked off the receiving array is fed to a quadratic detector and then averaged by an integrator. Earlier, a low-pass filter was used as the integrator. Nowadays, analog devices are replaced by computer processing.

We express the sound pressure of a narrow-band noise signal as follows:

$$P_c(\mathbf{r}, z) = \sqrt{W\Delta f}\sum_{m=1}^{M} p_m(\mathbf{r})\Phi_m(z)F(t-t_m)\exp(-i\omega_0 t). \quad (1)$$

Each summand in Eq. (1) is a normal wave [1, 2, 7–9]. Here, we use the following notations: $\mathbf{r}$ is the vector horizontal coordinate, the coordinate origin coinciding with the acoustic center of the source; z is the vertical coordinate, the z axis being directed downwards and the origin $z = 0$ coinciding with the free water level; t is time; $\omega = 2\pi f$, where f is the sound frequency; $\omega_0 = 2\pi f_0$, where f_0 is the central (carrier) frequency; m is the ordinal number of the mode; W is the spectral density of the transmitted signal, which is normalized to the 1-Hz band; Δf is the signal frequency band determined by the bands of both the transmitted signal and the receiving filter; and the quantity $p_m(\mathbf{r})$ characterizes the spatial variability of the signal amplitude and phase relative to the unit level. The latter level is determined as

$$P_c\Big|_{R\to 0} = \frac{\exp(ik_0R - i\omega_0 t)}{R}, \quad (2)$$

where R is the distance from the phase center of the source.

If the parameters of the waveguide are constant in **r**, we have

$$p_m(\mathbf{r}) = i\pi\Phi_m(z_0)H_0^{(1)}(\zeta_m r), \quad k_0 = \omega_0/c(z_0), \quad (3)$$

where z_0 is the source depth and $\Phi_m(z)$ is the eigenfunction of the waveguide [8, 9], which corresponds to the longitudinal wave number ζ_m of the mth mode. If the waveguide parameters vary in **r**, ζ_m is a function of **r**, and the same is true for $\Phi_m(z)$. By assuming that $\Phi_m(z)$ varies slowly in **r**, one can neglect the energy transfer between modes of different numbers (the mode scattering), and the sound field can be described in the adiabatic approximation [10]. Then, Eq. (3) remains valid but $\zeta_m r$ is replaced by $\int_0^r \zeta_m(\eta)d\eta$. At different **r**, the quantity $\Phi_m(z)$ represents the eigenfunctions of the reference waveguide [8, 9], i.e., those of a planar stratified waveguide whose parameters coincide with those of the waveguide at hand along the vertical axis passing through the observation point. The functions $\Phi_m(z)$ produce an orthonormal system [8]. If the condition of orthonormality is violated for modes calculated for different **r**, the scattering of modes (energy transfer) is possible. Then, one can use the exchange approximation, which is also known as the method of coupled modes [9, 11–13]. The latter is usually based on the principle of vertical modes and horizontal mode-associated rays [10]. This method is rather common and implemented in the form of computer codes (one can find details in [11–13]).

The noise-like character of the signal is expressed by factor $F(t)$, which is a stationary and ergodic function of time t:

$$\overline{F(t)} = 0, \quad \overline{F(t)F(t-\tau)} = B(\tau), \quad B(0) = 1,$$

where $F(t)$ is determined by parameters of the sound source and the receiving filter. The overbar denotes time averaging [14], and t_m is the time of propagation of the mth mode from the source to the receiver. In a planar stratified waveguide, $t_m = r/v_m$, where v_m is the group velocity of the mode [9]. In the adiabatic approximation, $t_m = \int_0^r d\eta/v_m(\eta)$.

The signal has a zero mean value: $\bar{P}_c(\mathbf{r}, z) = 0$. The variance of the acoustic pressure and its time correlation function $K(\mathbf{r}, z, \tau)$ (τ is the delay between the signals at the correlator input) are both nonzero. In the simplest case, the correlator consists of a device multiplying the voltages that are fed to two (or more) inputs equipped with delay circuits. The signal from the correlator output is integrated (averaged) by an integrator. The output signal of the correlator is a deterministic process (a correlation function) accompanied by a fluctuating component. The higher the value $\Delta f T$ (T is the duration of the signal entering the correlator), the smaller the variance of the fluctuating component. The reliability of estimating the correlation function is governed by the extent to which the fluctuating component is suppressed. The variance of the latter determines the detection limit for the desired signal [15, 16].

In monitoring applications, a method [1] is often used whereby one feeds the signal to be analyzed to one input of the correlator and the signal $F(t-\tau)\exp[i\omega_0(t-\tau)]$ to another input. As a result, the deterministic component of the correlator output signal takes the form [17]:

$$K_c(\mathbf{r}, z, \tau) = \sqrt{W\Delta f}\,\mathrm{Re}\sum_{m=1}^{M} p_m(\mathbf{r})\Phi_m(z) \times B(\tau - t_m)\exp(-i\omega_0\tau). \quad (4)$$

Equation (4) is a pulsed signal in which the frequency spectrum of the signal is replaced by the power spectrum of the noise signal. The only difference between this and an ordinary impulse response of a waveguide is that the running time t is replaced by the delay τ.

Figure 1a shows the vertical sound speed profile $c(z)$ that was used in calculating the sound field. Figure 1b presents the variations of $c(z)$, where the numbers *1* and *2* correspond to the variations of the salinity S (Fig. 1c) in the near-ice water layer.

Figures 2 and 3 show the examples of the envelope (4) calculated for a noise signal with the central frequency $f_0 = 65$ Hz and the frequency band $\Delta f = 5$ Hz. The source and receiver depths are both 60 m. The sound speed profiles are constant in **r**, and Figs. 2 and 3 correspond to the vertical sound speed profiles labeled by *1* and *2* in Fig. 1b, respectively. We assume the ice cover to be two-component [17], with a 65% fraction of flat ice. The flat ice has the mean thickness $h_1 = 2.6$ m, and the variance of the ice draught is $\sigma_1 = 2.8$ m. For the upper boundary of the ice, the corresponding value is $\hat{\sigma}_1 = 0.4$ m, i.e., $\hat{\sigma}_1 = \sigma_1/4.5$. The hummocky ice has the mean thickness $h_2 = 6.6$ m with $\sigma_2 = 3.3$ m. According to the histogram, the correlation scale of flat ice is 120 m, and that of hummocky ice is 44 m. The velocity of longitudinal waves in the ice material is $3500(1 - i0.04)$ m/s, the velocity of shear waves is $1800(1 - i0.04)$ m/s, and the ice density is 0.91 relative to the water density.

The envelopes of the correlation function (4) are plotted in Figs. 2 and 3 for the profiles $c(z)$ shown in Figs. 1a and 1b. The function $F(t)$ is generated by the M-sequence without filtration. Figure 4 shows the signal that is analogous to that presented in Fig. 3 but processed with a rectangular filter, the pass band $\Delta f = 5$ Hz of the filter being narrower than the frequency band of the transmitted signal. Narrow-band filtration leads to side peaks in the envelope of the correlation function, but the positions of its main maxima do not change. Below, we use the same calculation technique, because we are interested in the most adverse situation, so as the initial signal spectrum does not differ from that of a

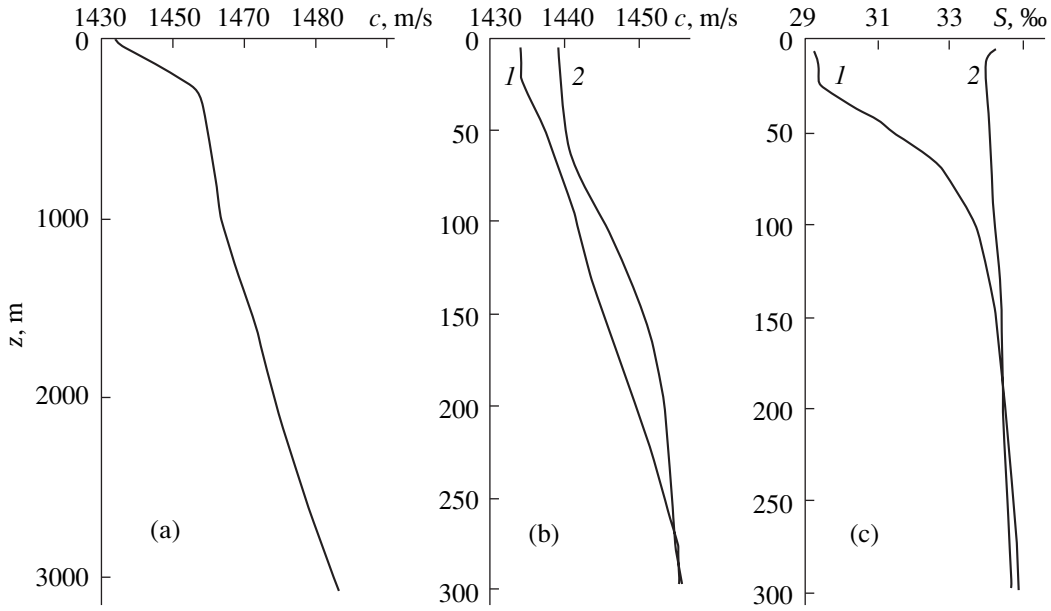

Fig. 1. Profiles of the (a, b) sound speed and (c) water salinity in the arctic waveguide.

white noise within the band of filtering. Then, at the filter output, we have

$$B(\tau) = \frac{\sin(\pi\Delta f\tau)}{\pi\Delta f\tau}.$$

Here, we do not consider the full correlation function of the noise signal: the term $\cos(\omega_0\tau)$ in the carrier frequency is not presented in the figures, the same being also true for further plots. The vertical arrows indicate the position of the first water mode on the scale of delays.

The delay (time) structure of the waveguide impulse response is typical of a deep-water region of an arctic sea. This structure is governed by the vertical profile

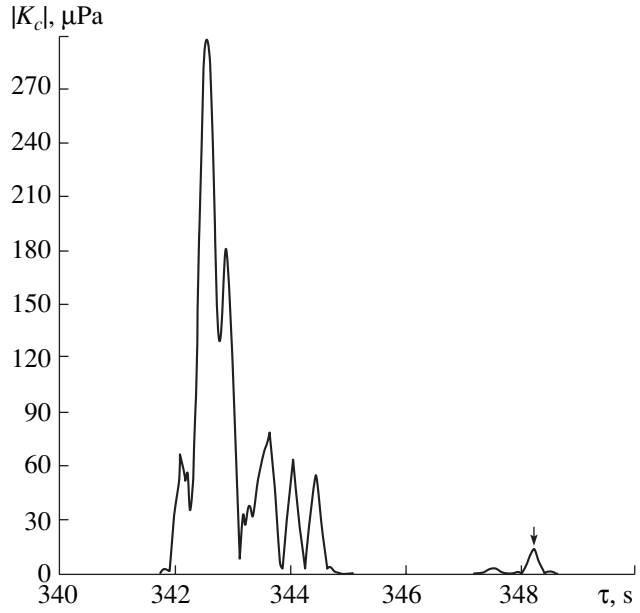

Fig. 2. Envelope of the time cross-correlation function of the received noise signal and reference signal for sound speed profile *1* of Fig. 1b and for the unfiltered signal generated with the use of the MLS.

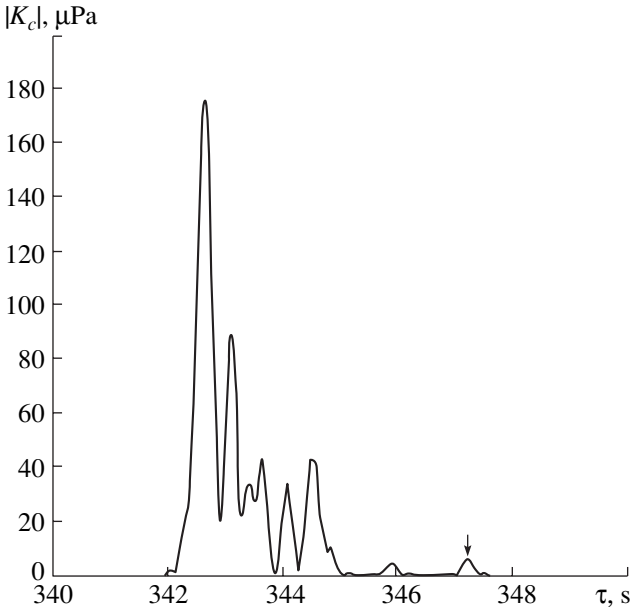

Fig. 3. Same as in Fig. 2 for sound speed profile *2* of Fig. 1b.

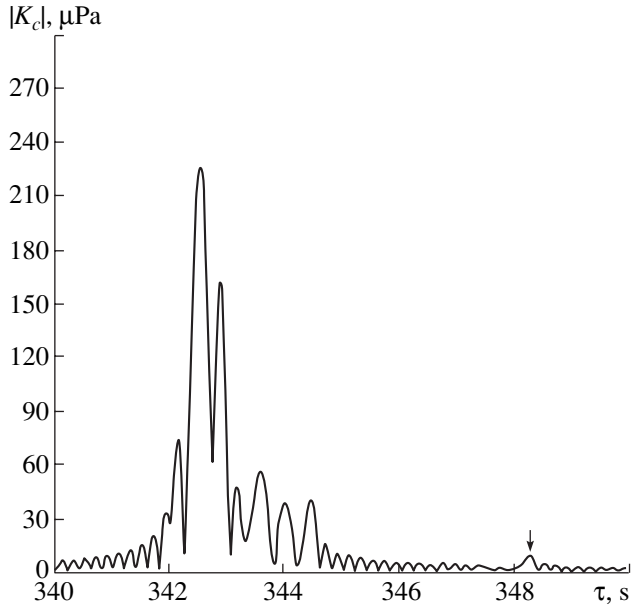

Fig. 4. Same as in Fig. 3 for white noise filtered in the frequency band Δf.

$c(z)$ of the sound speed. According to Fig. 1, the upper water layer up to the ice cover is desalinated both because of the melting of the ice, which has a salinity lower than that of water, and the intrusion of the waters of the great rivers of Siberia. The near-ice profile of the sound speed is governed by the salinity profile. In the upper water layer, the sound speed rapidly grows in depth and forms a channel that can capture part of the water modes of low numbers. For instance, at the frequency 65 Hz, the first water mode is fully concentrated within the near-ice water layer, and deeper Atlantic waters slightly influence the parameters of this mode. Below the nearly isospeed layer of the Atlantic waters, a layer of arctic waters exists with a positive sound speed gradient that is close to the hydrostatic one. The water temperature and salinity are stable in this layer within the whole sea region.

In view of the aforementioned facts, let us consider the shapes and arrival times of the pulses shown in Figs. 2–4 for the 500-km propagation path. Waves of higher numbers are the first to arrive, because they are mainly concentrated within the deep-water layers of the waveguide, where the sound speed has its maximal values. The pulse shape is a result of the interference of modes that are close in their group velocities. Hence, the resulting pulses exhibit insignificant differences, and the time structure remains nearly unchanged.

Modes of low numbers, which are captured by the sound channel, are the last to arrive. Among them, the first water mode prevails. For this mode, the difference in its arrival time reaches almost 1 s for the sound speed profiles at hand. This value is governed by the difference in the salinity of the near-ice layer, and, hence, it can be used to monitor the variations in water salinity. The difference in the arrival times of modes is sufficiently high to be detected: it is higher than the possible error in measuring the mode arrival time.

In practice, the difficulty of estimating the arrival time of the first mode consists in the fact that the attenuation coefficient is highest for this mode. Therefore, the observed mode amplitude can be hidden under the "tails" of high-number modes. Note that Figs. 2–4 correspond to a purely coherent signal. In practice, the pulse is masked by the ambient interfering noise. The latter can be attenuated by using a directive antenna array. To the second correlator input, a signal arrives that is free from interfering noise [1–6]. The interfering noise produced by independent signals has no effect on the correlation function (which is a time-averaged quantity), if the time of averaging is long enough. Hence, realizations of maximal length T, for which both signal and noise remain statistically stationary, ergodic, and independent, are advantageous.

In an arctic waveguide, the coherent component of the signal generated by the sound source is added by one that is stochastically scattered by the ice cover. The latter can be higher than the coherent component in its intensity. The stochastically scattered component carries information on the scatterers but not on the sound source. Therefore, in the correlation processing, the stochastic component, though being correlated with the reference signal, produces a background that is spread over delays; this background can also mask the weak pulse of the first mode. To eliminate the background accompanying the correlation function in the input circuit, one can use, e.g., a horizontal antenna array [17].

In monitoring applications, the experiment on the time variability of the water bulk usually lasts for years. It is important to know how the signal changes after propagating over the same path at different times. One can act in a direct way: to record the signal for a long time and then compare the results obtained at different instants. However, there is an alternative approach. Let us take a record of the sound pressure, which is obtained in one of the measurements, as a reference. In the reference measurement, it is desirable that the first mode have maximal intensity and minimal noise level. If we have a set of signal realizations that differ in their reception times, we can construct the cross-correlation function for the reference signal and other signal realizations. The advantage of this approach is that it enables one to increase the signal-to-noise ratio at the output of the processing device. The essence of the idea is that the desired coherent (in the sense of stochastic scattering) signal is described by nearly the same function $F(t)$ in all experiments, and different realizations of the signal are well correlated. The noise levels produced by the medium are, for the most part, statistically independent in time for long time intervals, and, hence, they have no effect on the shape of the correlation function. This statement is also true for the stochastically scattered component, because the realizations of the ice

cover significantly change from one measurement to another. With the previous method, the interfering noise of this type cannot be suppressed, although such a suppression is extremely important for sound frequencies of several tens of hertz, when the intensity of the scattered component is high relative to that of the coherent component.

Since the first water mode has a simple vertical structure that exhibits a single maximum and is concentrated within the near-ice layer, it can be easily extracted from a narrow-band signal by using a vertical receiving array. Experiments of this type have been repeatedly performed in the arctic waveguide to yield good results owing to the orthogonality of the modes.

The mode extracted from the reference signal is, in turn, used as the reference in the correlation processing. To one of the correlator inputs, the voltage is fed that corresponds to the sound pressure (1) plus an additive noise. To another correlator channel, as in Eq. (4), the reference signal is fed. As a result, the electric analog of the cross-correlation function takes the following form:

$$\tilde{K}_c(\mathbf{r}, z, t) = W\Delta f \mathrm{Re}\left\{ \tilde{p}_N^*(\mathbf{r}) \exp(-i\omega_0\tau) \times \sum_{m=1}^{M} p_m(\mathbf{r})\Phi_m(z) B(\tau + \tilde{t}_N - t_m) \right\}. \quad (5)$$

Here, the factor $\tilde{p}_N^*(\mathbf{r})$ corresponds to the extracted mode of number N with the propagation time $\tilde{t}_N$.

The first water mode is not the only one that can be extracted. If other water layers are to be studied, a mode can be selected that is most sensitive to changes in the sound speed in those layers.

In Eq. (5), the eigenfunction of the Nth mode is absent, because it vanishes in the extracting procedure due to the normalization of modes.

Figure 5 shows the envelope of the function $\tilde{K}_c(\mathbf{r}, z, \tau)$ for the same conditions as in Fig. 4. Here, the signal itself, or, more precisely, its first mode, is used as the reference. By comparing Figs. 4 and 5, one can see that the envelope shapes are nearly the same, but the curves are shifted in delays relative to each other. The maximum corresponding to the extracted mode is at $\tau = 0$. The shifts of other maxima are the same relative to the maximum of the reference mode.

Figure 6 presents a similar plot for which the reference mode corresponds to sound speed profile *1* (Fig. 1), and the signal corresponds to profile *2* (Fig. 1b). This plot shows that the maximum of the first water mode is shifted by about 1 s in delay τ. This difference in the arrival time of the first mode can be noticed in Figs. 2 and 3 as well. However, with the proposed approach, the error in measuring the difference in the travel time of the mode at hand is lower than with the previous techniques. This higher accuracy can probably be

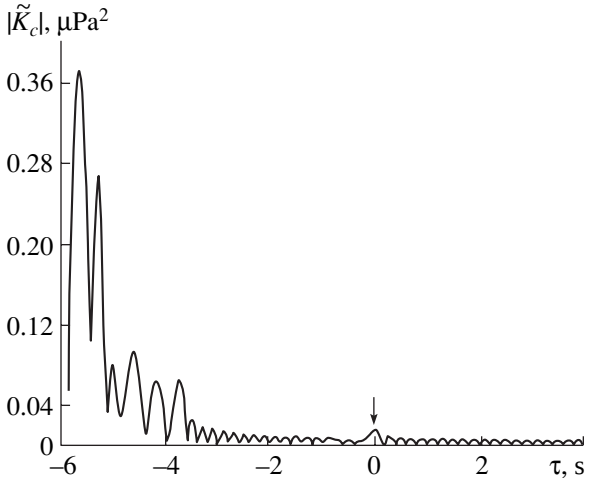

Fig. 5. Cross-correlation function of the signal and its first water mode for sound speed profile *2* of Fig. 1b.

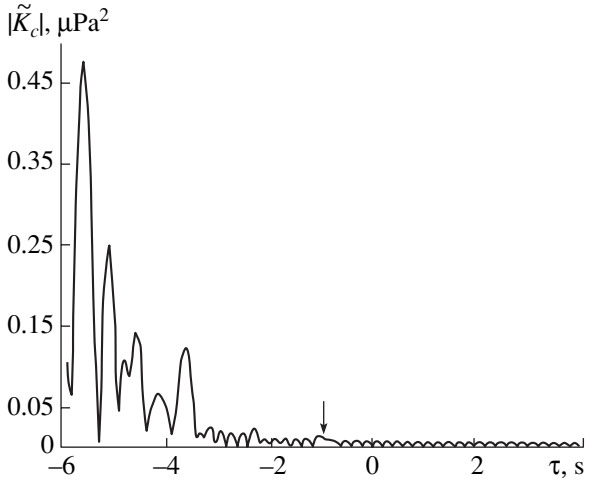

Fig. 6. Same as in Fig. 5 for the first water mode corresponding to sound speed profile *1* of Fig. 1.

related to the fact that the near-ice layer weakly affects the propagation times of higher modes. The latter statement is confirmed by both calculated propagation times of the modes and the shape of the envelope of the cross-correlation function for signal (1) corresponding to sound speed profiles *1* and *2* (Fig. 1).

The calculations presented above show that the proposed technique can be used in performing experiments on monitoring the time variability of the sound speed profile. With such experimental data, one can quantitatively compare the changes in the parameters of the medium and the time relations in the correlation function. The expected changes in the correlation function are evidently higher than the experimental error, but for estimating the accuracy of solving the inverse problem (i.e., the reconstruction of the changes in the medium

from those in the signal), additional studies that are beyond the scope of this paper are necessary.

REFERENCES

1. P. N. Mikhalevsky, A. N. Gavrilov, and A. B. Baggeroer, IEEE J. Ocean. Eng. **24** (2), 183 (1999).
2. A. N. Gavrilov and P. N. Mikhalevsky, in *Proceedings of the 3rd European Conference on Underwater Acoustics* (Heraklion, 1966), p. 851.
3. A. N. Gavrilov, M. M. Slavinskiĭ, and A. Yu. Shmelev, Usp. Fiz. Nauk **165** (7), 836 (1995) [Phys. Usp. **38**, 797 (1995)].
4. V. M. Kudryashov, Akust. Zh. **46**, 798 (2000) [Acoust. Phys. **46**, 700 (2000)].
5. G. N. Kozubskaya, V. M. Kudryashov, and K. D. Sabinin, Akust. Zh. **45**, 250 (1999) [Acoust. Phys. **45**, 217 (1999)].
6. A. K. Morozov, Akust. Zh. **42**, 829 (1996) [Acoust. Phys. **42**, 733 (1996)].
7. V. M. Kudryashov, Akust. Zh. **42**, 438 (1996) [Acoust. Phys. **42**, 386 (1996)].
8. L. M. Brekhovskikh, *Waves in Layered Media*, 1st ed. (Akad. Nauk SSSR, Moscow, 1957; Academic, New York, 1960).
9. L. M. Brekhovskikh and Yu. P. Lysanov, *Fundamentals of Ocean Acoustics* (Gidrometeoizdat, Leningrad, 1982; Springer, New York, 1991).
10. R. Burridge and H. Weinberg, in *Wave Propagation and Underwater Acoustics*, Ed. by J. B. Keller and J. S. Papadakis (Springer, New York, 1977; Mir, Moscow, 1980).
11. V. M. Kudryashov, Akust. Zh. **33**, 55 (1987) [Sov. Phys. Acoust. **33**, 32 (1987)].
12. V. M. Kudryashov, Akust. Zh. **34**, 117 (1988) [Sov. Phys. Acoust. **34**, 63 (1988)].
13. B. G. Katsnel'son and V. G. Petnikov, *Acoustics of a Shallow Sea* (Nauka, Moscow, 1997).
14. A. A. Kharkevich, *Spectra and Analysis* (Gostekhteorlit, Moscow, 1957).
15. A. M. Tyurin, *Introduction to the Theory of Statistical Methods in Hydroacoustics* (VMA, Leningrad, 1963).
16. *A Handbook on Hydroacoustics*, Ed. by A. P. Evtyukhov *et al.* (Sudostroenie, Leningrad, 1988).
17. F. I. Kryazhev and V. M. Kudryashov, Akust. Zh. **30**, 790 (1984) [Sov. Phys. Acoust. **30**, 469 (1984)].

Translated by E. Kopyl

Acoustical Physics, Vol. 48, No. 3, 2002, pp. 331–338. Translated from Akusticheskiĭ Zhurnal, Vol. 48, No. 3, 2002, pp. 382–390.
Original Russian Text Copyright © 2002 by Kuz'kin, Petnikov.

Variability of the Vertical Interference Structure of the Sound Field in a Shallow Sea

V. M. Kuz'kin and V. G. Petnikov

General Physics Institute, Russian Academy of Sciences, ul. Vavilova 38, Moscow, 117942 Russia

e-mail: gera@kapella.gpi.ru

Received January 22, 2001

Abstract—Dynamics of the spectral intensity oscillations that occur in the vertical plane because of the time variability of the medium along the propagation path is described. The errors arising in measuring the frequency shifts of the interference structure are considered. For low-frequency broadband signals received on a stationary propagation path, experimental data on the shifts of their frequency spectra due to the variation of the reception depth are presented. The number of interfering modes and their arrival directions in the vertical plane are estimated from the measured frequency shifts of the spectral intensity oscillation. *© 2002 MAIK "Nauka/Interperiodica".*

Data presented in the literature on the frequency shifts of spectral intensity oscillations caused by the change of conditions along the propagation path usually do not contradict existing theories. The fundamentals of these theories can be found in [1–5]. The majority of experimental studies devoted to this subject treated the space–frequency interference pattern in a horizontally homogeneous waveguide from the point of view of its particular features related to the direction of the lines of extreme levels (lines of equal phase) in the coordinate system using the wave frequency and the relative increments of the source–receiver distance [1, 6–9]. The exception is our previous paper [9] that presents experimental data on the shifts of the frequency spectra of low-frequency broadband signals in a shallow sea, which were recorded on a stationary propagation path. The shifts of local interference peaks in frequency can be used in monitoring shallow-water regions of the ocean for the determination of their integral average and statistical characteristics [4, 5, 9]. Now, this phenomenon is also used for controlling the field focusing in a shallow sea on the basis of phase conjugation [10–12].

This paper develops the results obtained in the previous studies [1–5, 9]. The dynamics of the spectral intensity oscillations that occur in the vertical plane because of the time variability of the medium along the propagation path is described. The errors arising in the measurement of the frequency shifts of the interference structure are considered. Experimental data on the shifts of the frequency spectra of low-frequency broadband signals due to the variations in the reception depth are presented for the case of the propagation along a stationary path. The number of interfering modes and the directions of their arrivals in the vertical plane are estimated on the basis of the measured frequency shifts of spectral intensity oscillations.

Let us first consider the frequency shifts of the intensity oscillations in the vertical plane. The propagation conditions in the ocean are such [13] that the local interference structure, which is stable to changes in the propagation conditions, is formed effectively by a small number of interfering modes of the same type. We assume that, in this interval of mode numbers, we can restrict our consideration to a linear expansion of the propagation constant (the horizontal component of the wave vector) h_m into a series in the vicinity of the number of the lth mode:

$$h_m = h_l + \alpha(m - l), \tag{1}$$

where $\alpha = \partial h_l/\partial l = -2\pi/S_l$ and S_l is the cycle length of the ray corresponding to the lth mode [14]. In this case, for the group of the interfering modes detected at the time point t, the interference invariant η [1], which describes the direction of the lines of the extreme level values in the coordinate system formed by relative increments of the reception depth and frequency, can be represented as

$$|\eta| = \left|\frac{\Delta\omega}{\omega_0}\Big/\frac{\Delta z}{r_0}\right| = |\beta|\cot\chi_l, \tag{2}$$

where

$$\beta = \frac{\Delta\omega}{\omega_0}\Big/\frac{\Delta r}{r_0} = -\alpha(\omega_0, r_0)r_0/\omega_0\int_0^{r_0}\frac{\partial\alpha(\omega_0, r)}{\partial\omega}dr \tag{3}$$

is the interference invariant of the group of in-phase modes, which characterizes the direction of the lines of the extreme level values in the coordinate system of the relative increments of the horizontal source–receiver distance r_0 and the frequency ω_0 [1, 3]; χ_l is the glancing angle of the Brillouin ray of the mode with the number l at the interval of the reception depth measurement Δz. To distinguish the glancing angles of the Brillouin rays propagating downwards and upwards, the corre-

1063-7710/02/4803-0331$22.00 © 2002 MAIK "Nauka/Interperiodica"

sponding quantities in Eq. (2) are represented by their absolute values. To derive Eq. (2), it is sufficient to assume $\Delta r = \Delta z \cot\chi_l$ in Eq. (3). A more consistent derivation of Eq. (2) is given in [1]. Physically, the angle χ_l determines the arrival direction in the vertical plane for the group of modes localized in the vicinity of the Brillouin ray of the lth mode. In other words, the angle χ_l can be interpreted as the arrival angle of the ray corresponding to the interference peaks of the group of modes with close numbers. The value of Δz is limited by the size ρ, within which normal modes are plane, i.e., their refraction in the vertical plane can be ignored. Ignoring the amplitude variations of normal modes, this condition can be written in the form of an inequality [15]

$$(\Delta z)^2 \ll \rho^2 = 4\lambda L_n \sin\chi_l/\pi n, \tag{4}$$

where $L_n = n(z)/|\nabla_z n(z)|$ is the characteristic vertical scale of the refractive index variation $n(z)$ within the size Δz, and λ is the wavelength.

Let us describe the pattern of the frequency shifts of the vertical interference structure of the sound field due to the time variability of the medium along the propagation path. We represent the propagation constant $h_m(t, \tau)$ at the time point $t + \tau$ at the frequency ω in the form

$$h_m(\omega, t+\tau) = h_m^{(0)}(\omega, t) + h_m^{(1)}(\omega, \tau), \quad \left|h_m^{(1)}\right| \ll h_m^{(0)}. \tag{5}$$

The correction $h_m^{(1)}$ to the unperturbed value $h_m^{(0)}$ at the time point t, which is assumed to be known, can be determined in the framework of the WKB approximation using the perturbation theory [16]. In this case, using Eqs. (2) and (5), we obtain the following expression for the variations of the frequency shift of intensity oscillations $\delta\omega(t, \tau)$ within the time interval from t to $t + \tau$ in the linear approximation:

$$|\delta\omega(t,\tau)| = |\Delta\omega(t+\tau) - \Delta\omega(t)| = |\Delta\omega(t)||\Delta\beta(t,\tau) + \Delta(\cot\chi_l(t,\tau))|, \tag{6}$$

where $\Delta\omega(t) = \beta\omega_0\Delta z \cot\chi_l/r_0$ is the frequency shift of intensity oscillations that is caused by the change of the reception depth; $\Delta\beta(t, \tau)$ and $\Delta(\cot\chi_l(t, \tau))$ are the relative corrections to the values of $\beta(t)$ and $\cot\chi_l(t)$ that are caused by perturbations of the water medium: $\Delta\beta = \beta_1 + \beta_2$, $\beta_1 = \alpha_1/\alpha_0$, $\beta_2 = -\int_0^{r_0} dr \frac{\partial\alpha_1}{\partial\omega} \Big/ r\frac{\partial\alpha_0}{\partial\omega}$, $\alpha_0 = \partial h_l^{(0)}/\partial l$, and $\alpha_1 = \partial h_l^{(1)}/\partial l$ [3]; and $\Delta(\cot\chi_l) = -2\Delta\chi_l/\sin 2\chi_l$ and $\Delta\chi_l = \chi_l(t + \tau) - \chi_l(t)$ are the variations of the sound arrival angle in the vertical plane during the time τ. Equation (6) provides an opportunity to estimate the variations of the direction of sound arrival in the vertical plane by using the measured variations of the frequency shift of spectrum oscillations and the hydrological data.

The results of measuring the frequency shifts of the interference pattern of the field with variations of the reception depth make it possible to determine such parameters of the received group of modes as their total number N and the direction of sound arrival in the vertical plane χ_l provided that the value of the invariant β is known. Indeed, from Eq. (2) we obtain

$$\cot\chi_l = |\eta/\beta|. \tag{7}$$

The minimal frequency period of oscillations Θ in the horizontal plane, which is determined by the range of the propagation constants h_m of the modes forming the field, has the form [3]

$$\Theta = \frac{2\pi}{\left|\int_0^{r_0} (\partial h_{1N}/\partial\omega) dr\right|},$$

where $h_{1N} = h_1 - h_N$ and N is the maximal number of the mode that makes a noticeable contribution to the field. With allowance for the expansion (1), the minimal period is determined by the expression

$$\Theta = \frac{2\pi}{(N-1)\left|\int_0^{r_0} (\partial\alpha/\partial\omega) dr\right|}. \tag{8}$$

Then, from Eqs. (3) and (8), we obtain an expression for the number of modes:

$$N = [1 + |2\pi\beta\omega_0/\Theta\alpha r_0|] = [1 + |\beta\omega_0 S_l/\Theta r_0|]. \tag{9}$$

Here, the square brackets mean the integer part of a number. Note that it is possible to use expressions other than Eq. (9) to estimate the number of constructively interfering modes (see, e.g., [17]).

An error in measuring the frequency shifts of the interference structure is generally caused by two factors: the error in detecting the extreme signal levels against the noise background and the instability of the distance between the source and the receiver.

Considering the error in the indication of the extreme levels, we restrict our investigation to the case of the signal observation against an additive noise background. We assume that signal and noise are statistically independent and the error in the detection of the extreme intensity values is caused exclusively by noise. The error δI in the indication of the extremum I_{ex} gives rise to the error $\delta\omega$ in the determination of the frequency position ω_0 of the extreme intensity value that was observed at the time point t (Fig. 1). The relation between these errors can be obtained by calculating the total differential of the function $I(\omega)$ at the point $\omega = \omega_0$ and passing to finite increments. Restricting ourselves

to the terms of the second order of smallness and averaging the resulting expression, we obtain

$$\sigma^2_{\omega_0} = \frac{2\sigma^2_n}{|I''(\omega_0)|}, \quad (10)$$

because $I'(\omega_0) = 0$. Here, $\sigma^2_{\omega_0}$ and σ^2_n are the variance of the error in measuring the frequency ω_0 and the variance of noise, respectively. Further, we assume that, at the minimal frequency period of the interference beating Θ (Eq. (8)), the dependence $I(\omega)$ is described by the harmonic function

$$I(\omega) = I_0 + a^2\cos[\gamma(\omega - \omega_0)], \quad \gamma = 2\pi/\Theta.$$

In this case, Eq. (10) can be reduced to the form

$$\sigma_{\omega_0} = \Theta/2\pi q, \quad (11)$$

where the quantity $q = a/\sqrt{2}\,\sigma_n$ virtually determines the signal-to-noise ratio. Hence, the error in the indication of the extreme level increases with the increase in the frequency scale of the intensity variability and with the decrease in the signal-to-noise ratio.

Let a given local extremum be shifted during the observation time τ to the point $\omega = \omega_0 + \Delta\omega$ because of the time variability of the water medium. We assume that the time interval τ far exceeds the correlation time τ_* of noise: $\tau \gg \tau_*$. In this case, the variance σ^2_1 of the measurement error for the shift of the frequency spectrum, $\Delta\omega$, during the time τ is equal to

$$\sigma^2_1 = \sigma^2_{\omega_0}(t) + \sigma_{\omega_0+\Delta\omega}(t+\tau) \approx 2\sigma^2_{\omega_0}\left[1 + \frac{\delta\Theta}{\Theta}\right],$$

where $\delta\Theta = (\Delta\omega/\omega_0)\Theta$ is the variation of the quantity Θ during the time τ. Taking into account the fact that $\Delta\omega \ll \omega_0$, the expression obtained above can be represented as

$$\sigma_1 \approx \sqrt{2}\sigma_{\omega_0}. \quad (12)$$

The reliability of the results of the measurements is determined by the confidence coefficient [18]. For example, if the indication of the shift of the frequency spectrum is determined by the inequality $\Delta\omega \geq \sigma_1$, then, in the case of a normal distribution of noise, the corresponding confidence coefficient is $P \geq 0.683$, and when $\Delta\omega \geq 3\sigma_1$, the confidence coefficient is $P \geq 0.997$. Noise can make two local neighboring interference extrema (maxima or minima) irresolvable. For their reliable resolution, e.g., with the confidence coefficient $P \geq 0.997$, the condition $\sigma_{\omega_0} \leq \Theta/6$ must be satisfied. According to Eq. (1), this inequality takes the form $q \geq 3/\pi \approx 0.95$. Thus, the presence of noise imposes limitations on the source–receiver distance and on the width of the signal frequency range for which the frequency shifts of the intensity oscillations can be reliably measured. The lower bound of the frequency range is determined by the reliability of their measurement, and the upper bound, by the reliability of the resolution of neighboring local extrema. From this point of view, the use of wave front dislocations [19] for the detection of the frequency shifts of spectral intensity oscillations has a limited range of application.

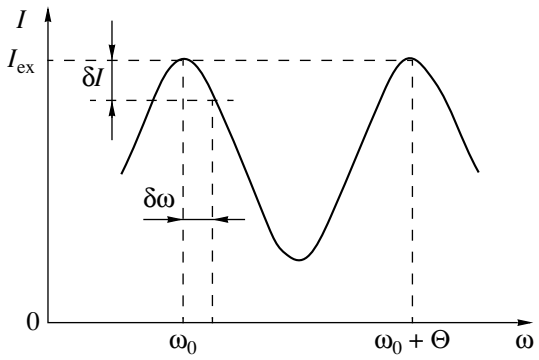

Fig. 1. Determination of the error in the indication of the extreme level.

Let us estimate the error in the determination of the length of the propagation path. The root-mean-square value of the frequency shift of intensity oscillations due to the instability of the distance r_0 between corresponding points is estimated according to Eq. (3) as

$$\sigma_2 = \beta\omega_0(\sigma_{\Delta r}/r_0), \quad (13)$$

where $\sigma_{\Delta r}$ is the root-mean-square value of the distance between the source of sound and the receiver.

The root-mean-square value of the total error σ arising in the detection of the frequency shift of the interference structure is equal to

$$\sigma = \sqrt{\sigma^2_1 + \sigma^2_2}, \quad (14)$$

where the quantities $\sigma_{1,2}$ are determined by Eqs. (12) and (13). In practice, the following substitutions must be made in Eqs. (12) and (13) to calculate the root-mean-square value of the error σ by Eq. (14): $\omega_0 \longrightarrow f_0 = \omega_0/2\pi$ and $\Theta \longrightarrow \theta = \Theta/2\pi$.

In addition to our previous publication [9], below we present the experimental data on the shifts of the frequency spectra of low-frequency broadband signals in the vertical plane, which were measured in 1990 during the expedition of the fourth voyage of the *Akademik Ioffe* research vessel and the seventh voyage of the *Akademik Sergeĭ Vavilov* research vessel.

DESCRIPTION OF THE EXPERIMENT

The conditions and data of the acoustically relevant characteristics of the experiment are described in detail in [9, 20]. The experiment was conducted on a stationary propagation path in the central part of the Barents Sea with two research vessels, each of them fixed by two anchored buoys (Fig. 2). A piston-type radiator was

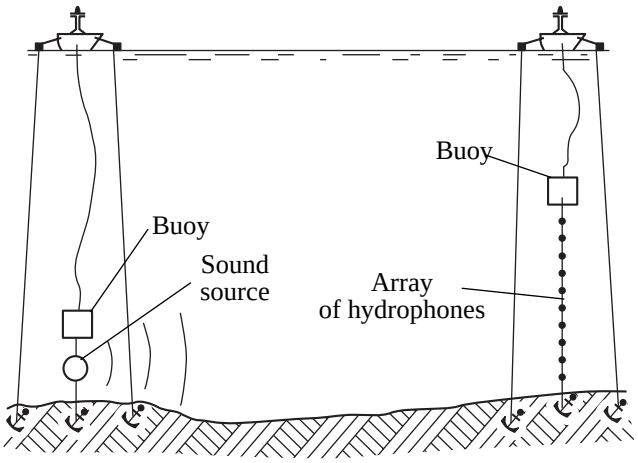

Fig. 2. Schematic representation of the experiment on a stationary propagation path.

submerged to a depth of 70-m from the stern of the *Akademik Ioffe* research vessel. The radiator excited broadband pulsed signals with linear frequency modulation in the frequency band 25–95 Hz. The length of each pulse was 40 s, and the repetition period was 60 s. The experiment duration was 101 min: sounding started at 5:20 p.m. and ended at 7:00 p.m. A vertical line array of ten equidistant hydrophones was lowered to the sea bottom from the stern of the *Akademik Sergeĭ Vavilov* research vessel. The array length was 66 m. The distance from the lower hydrophone to the anchor at the sea bottom was 18.5 m. The sea depth varied smoothly along the propagation path within 20 m and was equal to 170 m on average. The signal-to-noise ratios at the outputs of single hydrophones were no smaller than 12 dB (3.98). The experiment was conducted when the sea state was Beaufort 1 or less. The permanently recorded wind speed did not exceed 6 m/s.

The hydrological data are shown in Fig. 3a. As one can see from this figure, the distribution of the sound velocity in the region of the discontinuity layer (the seasonal thermocline) changed considerably within two hours. The boundary of the homogeneous upper layer lowered almost by 15 m, and the sound velocity gradient increased almost by a factor of 2. At the same time, in the depth interval from the lower boundary of the discontinuity layer to the sea floor (the main thermocline), the distribution of sound velocity did not change noticeably. Noticeable changes of sound velocity with time were caused by tidal variations. In this case, the semidiurnal changes in the depth value reached 1.5 m. The minimal, average (unperturbed), and maximal depths corresponded to the time points of 2:00, 5:00, and 8:00 p.m., respectively. It is essential that the tidal wave, on the one hand, perturbed the whole propagation path simultaneously and, on the other hand, inclined the receiving array in the plane perpendicular to the propagation path. The prevailing direction of tidal currents was normal to the propagation path. The inclination angle of the array with respect to the vertical line in the plane perpendicular to the direction of sound propagation did not exceed 9°. The latter fact allows us to assert that the horizontal variations of the positions of the array receivers were much smaller than 3 m and did not affect the variations of the distance between the corresponding points.

The distance between the ships measured accurate to 1 m by a Syledis radio rangefinder was 13834 m on average. The standard deviation of the distance between the radio beacons positioned in the central parts, at the bows, and at the sterns of both ships was

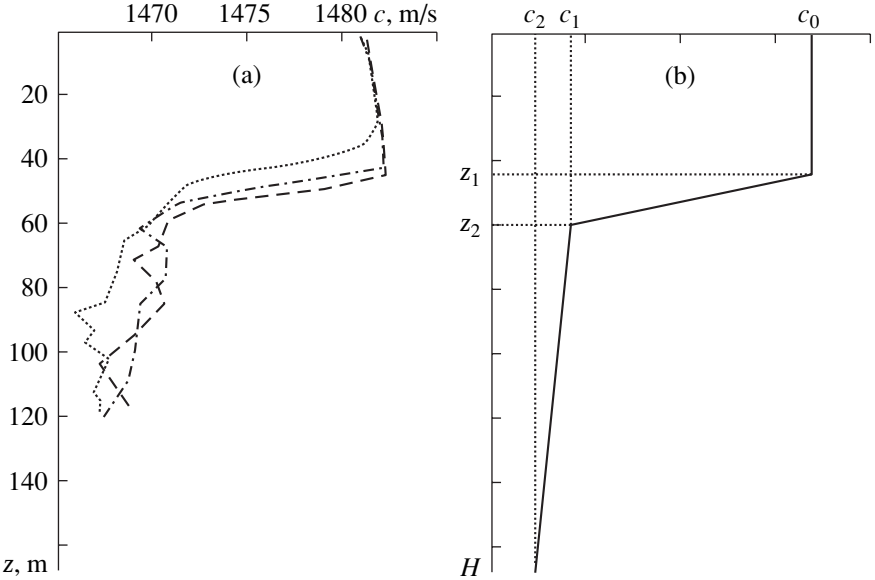

Fig. 3. Sound velocity profiles $c(z)$: (a) measured experimentally at the time points 5:12 (the dotted line), 6:04 (the dotted-and-dashed line), and 6:58 p.m. (the dashed line) and (b) used in the calculations.

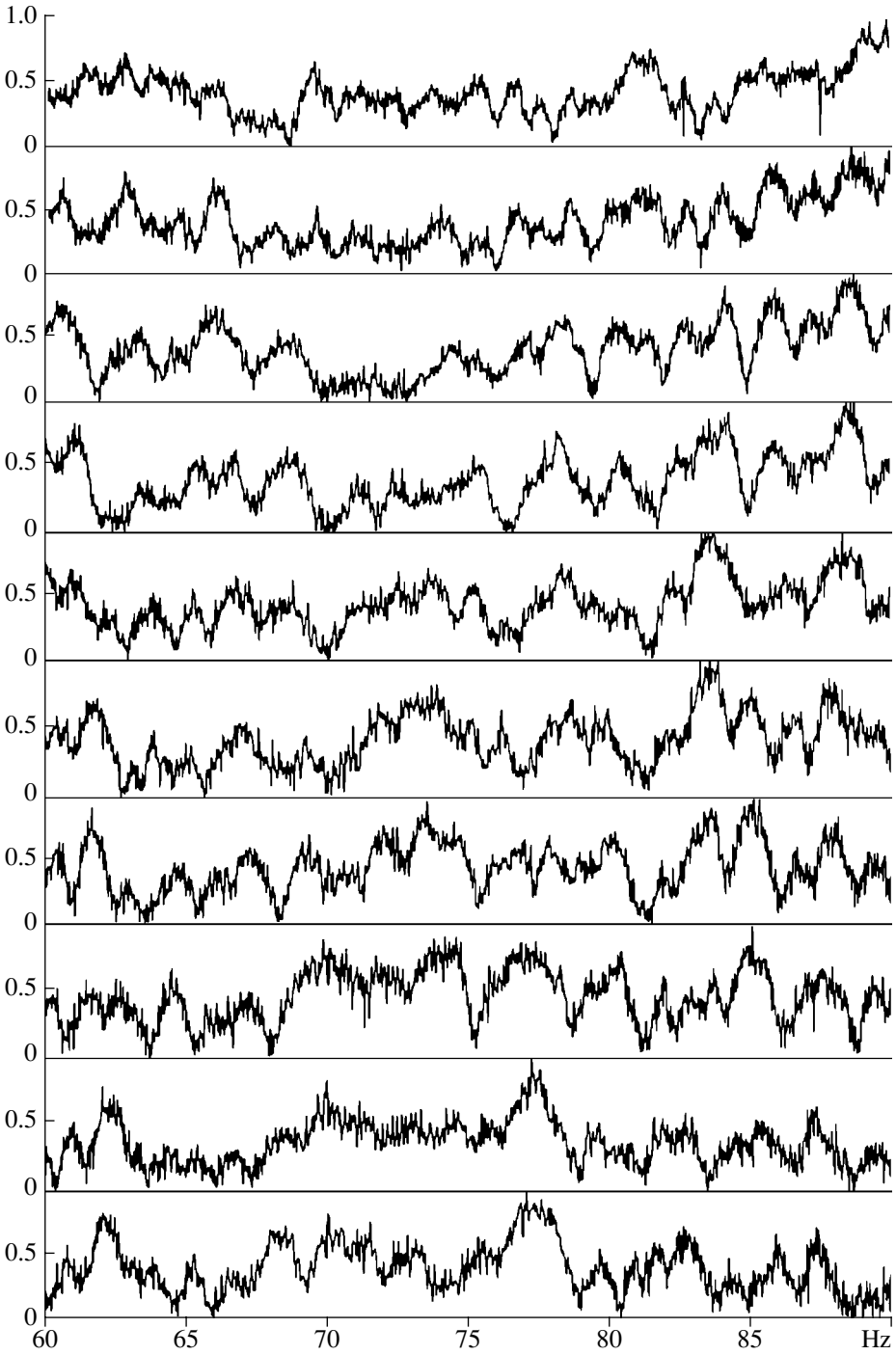

Fig. 4. Frequency spectra of the signal envelope at different depths at a fixed time point.

3 m during the experiment. One can assume that the horizontal variations of the source–receiver distance were approximately of the same value. Below, in discussing the experimental data, we take the distance between the ships for the distance between the source of sound and the receiving array without introducing any considerable error.

EXPERIMENTAL RESULTS

The signal processing included the calculation of the magnitude of the spectrum and the phase spectrum of the received pulsed signals at each receiver of the array [9]. Figures 4 and 5 present the normalized frequency spectra of the envelope and the derivative of the phase of a signal in the frequency band 60–90 Hz. The

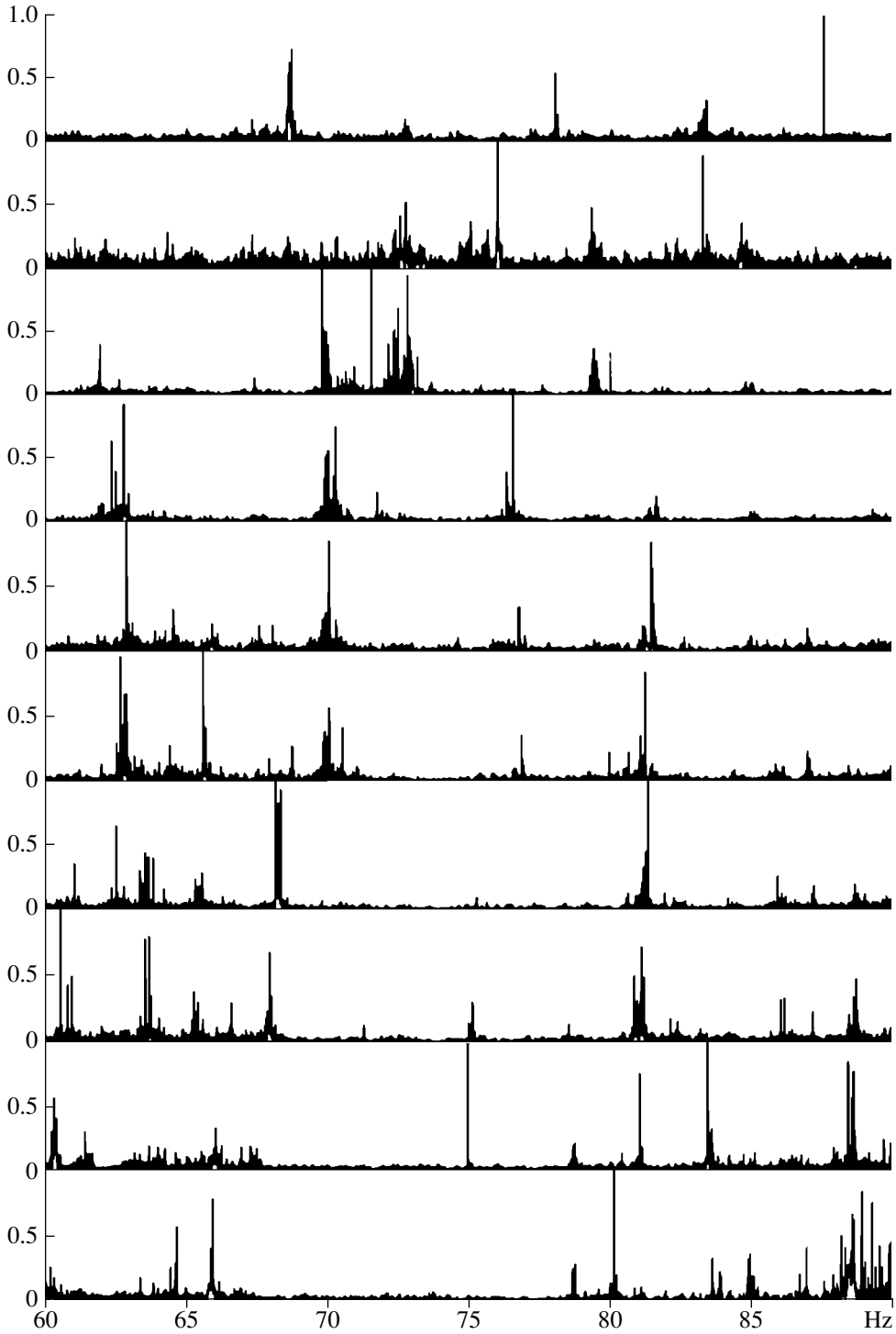

Fig. 5. Frequency spectra of the derivative of the signal phase at different depths at a fixed time point.

signal was received at 6:10 p.m. The lower curves in Figs. 4 and 5 correspond to the upper hydrophone and the upper curves, to the lower hydrophone. The indicated limited frequency range is related to the presence of strong discrete noise in the spectrum of the received signals at frequencies lower than 60 Hz due to the noise of the receiving ship. Oscillations of spectral intensity with the minimal period in frequency $\theta \approx 1.3$ Hz manifest themselves noticeably. Phase jumps correspond to deep interference minima of intensity, when the signal level drops approximately down to the noise level, which testifies to the presence of dislocations of the wave front of

sound fields at these points [19]. A regular shift with the relative value estimated at the array length as $\Delta f/f_0 \approx 2.06 \times 10^{-2}$ can be distinguished against the background of random frequency shifts of the interference structure. Approximately analogous results were obtained at other time points, which points to the insignificant effect of the perturbation of the water medium on the variations of the frequency shift with varying reception depth.

DISCUSSION

The direction of the lines of sound intensity level η [Eq. (2)] in the coordinate system formed by the relative increments of reception depth and frequency is estimated, according to the results of measurements, on average as $|\eta| \approx 4.38$. In the calculations, it was assumed that the projection of the array length l on the vertical is $\Delta z = 65$ m ($\Delta z = l\cos 9°$, $l = 66$ m), the average horizontal distance between the ships is $r_0 = 13834$ m, and the relative frequency shifts are $\Delta f/f_0 = 2.06 \times 10^{-2}$.

A simple analysis shows that the extrema of the sound field observed in the experiment are caused by a stable interference of the group of modes belonging to the bottom–surface rays, which are reflected from the bottom and from the upper boundary. Indeed, let us denote the glancing angle of a ray near the bottom by χ_* and assume that, later on, this ray touches the surface. According to [14], this angle is equal to $\chi_* = \sqrt{2\Delta c/c_0}$, where c_0 is the sound velocity at the surface and Δc is the difference in the sound velocities at the surface and the bottom. Substituting the values $c_0 = 1482.1$ m/s and $\Delta c = 15.6$ m/s in this expression, we estimate the value of the angle χ_*. Finally, we obtain $\chi_* = 8.4°$ so that the glancing angles at the bottom for the bottom rays are $\chi_b \le 8.4°$ and for the bottom–surface rays, $\chi_{b\text{–}s} > 8.4°$. A set of rays with the same value of the angle χ can be associated with each normal mode. The total number of propagating normal modes is approximately equal to $2H/\lambda$, and the angles χ that correspond to them lie within the interval $(0, \pi/2)$, where H is the sea depth. In this case, the number of normal modes within the interval of essential values $(0, \chi_*)$ is estimated as $N_b \approx [4\chi_* fH/\pi c_0]$ [14]. Assuming $H = 170$ m, we obtain that the number of bottom modes for the upper boundary of the frequency range $f = 90$ Hz is $N_b \approx 1$. Thus, the sound field within the considered frequency range is formed by the modes corresponding to bottom–surface rays with the glancing angles $\chi > \chi_*$. For this group of modes, it is possible to ignore the refraction and take the interference invariant $\beta \approx \cos^2\chi_l$ and the cycle length of the ray $S_l \approx 2H\cot\chi_l$ [1, 9]. In this case, for the direction of sound arrival in the vertical plane (Eq. (7)) and for the number of modes (Eq. (9)), we obtain the following estimates:

$$\eta \approx \cos^3\chi_l/\sin\chi_l,$$

$$N \approx [1 + (2Hf_0\eta/r_0\theta)].$$

Substituting the experimental data $\eta = 4.38$, $r_0 = 13834$ m, $\theta = 1.3$ Hz, and $H = 170$ m in these expressions and taking $f_0 = 75$ Hz, we obtain $\chi_l \approx 12.3°$ and $N \approx 7$. The latter estimate of the number of modes is close to the value $N = 8$, which was used in the numerical modeling of the variability of the spectra of signals with linear frequency modulation that were observed in the experiment under discussion [21].

The sound velocity profiles measured in the experiment are adequately approximated by a piecewise-linear function $c(z)$ given in Fig. 3b. The values of the sound velocity at the bottom, $c(H) = c_2$, and in the mixed upper layer, c_0, are constant and time-independent. In the case of such a dependence, perturbations of the water medium lead to changes in the boundaries of the seasonal and main thermoclines and the sea depth, i.e., to variations in the parameters c_1, z_1, z_2, and H. The parameters approximating the sound velocity profile are estimated as $c_1 = 1468.9$, 1471.0, and 1471.1 m/s; $z_1 = 35.2$, 43.4, and 48.3 m; and $z_2 = 54.2$, 54.6, and 55.3 m at constant $c_0 = 1482.1$ m/s and $c_2 = 1466.5$ m/s. Here, the values of c_1, z_1, and z_2 correspond to the respective time points of hydrological measurements (see Fig. 3a). According to these data, for the average value of the characteristic scale of the refractive index variation in the region of the main thermocline where the receiving array was positioned, we obtain the estimate $L_n \approx 4.5 \times 10^4$ m. Restricting our consideration to the upper sound frequency $f = 90$ Hz and taking $\chi_l = 12.3°$, we obtain from inequality (4) an estimate for the allowed value of the depth variation $\rho \approx 4.5 \times 10^2$ m. As one can see, condition (4) is satisfied, i.e., within the vertical length of the array $\Delta z = 65$ m, we can ignore the refraction of the Brillouin ray of the lth mode.

Let us estimate the error of the measurement of the frequency shifts of the interference pattern. According to the experimental data, from Eqs. (12) and (13), we obtain $\sigma_1 \approx 7.25 \times 10^{-2}$ Hz and $\sigma_2 \approx 1.86 \times 10^{-2}$ Hz, so that $\sigma_1 \gg \sigma_2$. In calculating the value of σ_2, we assumed that $f_0 = 90$ Hz (the upper estimate), $\sigma_{\Delta r} = 3$ m, and $r_0 = 13834$ m. As a result, the total error σ given by Eq. (14) is estimated as $\sigma \approx 7.58 \times 10^{-2}$ Hz. This is more than an order of magnitude smaller than the values of the frequency shifts detected in the experiment.

Thus, experimental data testify that the frequency shifts of the spectrum oscillations in the vertical plane reach considerable values and can be reliably measured. In conditions of multimode propagation, the interference effects often make it difficult or impossible to draw any definite conclusions concerning the relation between the parameters of the oceanic medium and the observed variability of the sound field characteristics. In the case considered above, the frequency shifts

of the interference pattern are completely determined by the dispersion characteristic of the sound channel and can be easily predicted. It is demonstrated that the frequency shifts of the local interference extrema can be used for the determination of the number of interfering modes and their arrival directions in the vertical plane.

ACKNOWLEDGMENTS

This work was supported by the Russian Foundation for Basic Research, project no. 99-02-17671.

REFERENCES

1. S. D. Chuprov, in *Ocean Acoustics: State of the Art*, Ed. by L. M. Brekhovskikh and I. B. Andreeva (Nauka, Moscow, 1982), pp. 71–91.
2. E. F. Orlov, in *Problems of Ocean Acoustics*, Ed. by L. M. Brekhovskikh and I. B. Andreeva (Nauka, Moscow, 1984), pp. 85–93.
3. V. M. Kuz'kin, Akust. Zh. **41**, 344 (1995) [Acoust. Phys. **41**, 300 (1995)].
4. V. M. Kuz'kin, Akust. Zh. **45**, 258 (1999) [Acoust. Phys. **45**, 224 (1999)].
5. V. M. Kuz'kin, Akust. Zh. **46**, 365 (2000) [Acoust. Phys. **46**, 310 (2000)].
6. A. N. Barkhatov, N. V. Gorskaya, N. M. Gromoglasov, *et al.*, in *Interference of Broadband Sound in the Ocean*, Ed. by V. A. Zverev and E. F. Orlov (Inst. Prikl. Fiz., Akad. Nauk SSSR, Gorki, 1984), pp. 73–81.
7. V. N. Golubev, V. A. Lazarev, E. F. Orlov, *et al.*, in *Interference of Broadband Sound in the Ocean*, Ed. by V. A. Zverev and E. F. Orlov (Inst. Prikl. Fiz., Akad. Nauk SSSR, Gorki, 1984), pp. 93–132.
8. V. N. Golubev, V. I. Il'ichev, E. F. Orlov, *et al.*, in *Acoustic Waves in the Ocean*, Ed. by L. M. Brekhovskikh and I. B. Andreeva (Nauka, Moscow, 1987), pp. 100–111.
9. V. M. Kuz'kin, A. V. Ogurtsov, and V. G. Petnikov, Akust. Zh. **44**, 94 (1998) [Acoust. Phys. **44**, 77 (1998)].
10. W. A. Kuperman, W. S. Hodgkiss, and H. C. Song, J. Acoust. Soc. Am. **103**, 25 (1998).
11. H. C. Song, W. A. Kuperman, and W. S. Hodgkiss, J. Acoust. Soc. Am. **103**, 3234 (1998).
12. W. S. Hodgkiss, H. C. Song, and W. A. Kuperman, J. Acoust. Soc. Am. **105**, 1597 (1999).
13. V. N. Kulakov, N. E. Mal'tsev, and S. D. Chuprov, Akust. Zh. **29**, 74 (1983) [Sov. Phys. Acoust. **29**, 41 (1983)].
14. L. M. Brekhovskikh and Yu. P. Lysanov, *Fundamentals of Ocean Acoustics* (Gidrometeoizdat, Leningrad, 1982; Springer, New York, 1991).
15. V. M. Kuz'kin, Akust. Zh. **47**, 483 (2001) [Acoust. Phys. **47**, 591 (2001)].
16. I. K. Kobozev, Yu. A. Kravtsov, and A. V. Ogurtsov, Akust. Zh. **34**, 109 (1988) [Sov. Phys. Acoust. **34**, 58 (1988)].
17. A. L. Virovlyanskiĭ, Preprint No. 120, IPF AN SSSR (Gorki Inst. of Applied Physics, USSR Academy of Sciences, 1985).
18. D. J. Hudson, *Statistics. Lectures on Elementary Statistics and Probability* (Geneva, 1964; Mir, Moscow, 1970).
19. V. A. Zhuravlev, I. K. Kobozev, and Yu. A. Kravtsov, Akust. Zh. **35**, 260 (1989) [Sov. Phys. Acoust. **35**, 156 (1989)].
20. B. G. Katsnel'son, L. G. Kulapin, A. A. Migulin, and V. G. Petnikov, Akust. Zh. **38**, 308 (1992) [Sov. Phys. Acoust. **38**, 164 (1992)].
21. V. A. Grigor'ev, B. G. Katsnel'son, and V. G. Petnikov, Akust. Zh. **42**, 712 (1996) [Acoust. Phys. **42**, 627 (1996)].

Translated by M. Lyamshev

Acoustical Physics, Vol. 48, No. 3, 2002, pp. 339–346. Translated from Akusticheskiĭ Zhurnal, Vol. 48, No. 3, 2002, pp. 391–399.
Original Russian Text Copyright © 2002 by Lebedev.

Method of Linear Prediction in the Ultrasonic Spectroscopy of Rock

A. V. Lebedev

Institute of Applied Physics, Russian Academy of Sciences, ul. Ul'yanova 46, Nizhni Novgorod, 603950 Russia
e-mail: swan@hydro.appl.sci-nnov.ru

Received April 19, 2000

Abstract—The possibility of using the resonant acoustic spectroscopy method for testing the internal state of rock is considered. This method can be used for the determination of the concentration of defects and their spatial distribution. A rock specimen with defects is characterized by a high loss of vibrational energy, which leads to the overlapping of the resonant responses. In this case, the complex resonant frequencies are determined as the parameters of a model that describes the measured transfer function of the response of the mechanical system. The linearity of the vibratory system is used as the *a priori* information for presetting the functional dependences of the model. An algorithm is developed for the determination of the parameters of the resonances in conditions of their partial overlapping. Examples are presented to demonstrate the possibility of analyzing the complex elastic constant tensor of rock by the acoustic spectroscopy method. The proposed method of experimental data processing provides the possibility for the determination of the weak anisotropy that occurs in the velocity of sound because of a partial fracture of rock. © *2002 MAIK "Nauka/Interperiodica"*.

Elastic moduli are fundamental parameters of solids. Knowledge of the elastic constant tensor is important, specifically, in geophysics, where the analysis of the values of its components and their ratios provides information on the internal structure of rock. In the linear approximation and in the absence of gyrotropic forces, the number of independent components of the elastic constant tensor is equal to 21 in the general case [1]. When the internal structure of a solid contains preferred axes or symmetry planes, this number is reduced.

The anisotropy of rock is usually attributed to a disturbance of the uniform distribution of internal macroscopic defects (cracks, pores, etc.) [2]. At the initial stages of rock fracture, the anisotropy of the elastic constant tensor manifests itself in the deviations of its components from those corresponding to an isotropic body within approximately 1%. Therefore, the search for experimental methods that provide a reliable detection of such small deviations is of major interest from the point of view of their possible applications.

A description of the methods used for the determination of elastic moduli and their comparative analysis can be found in [3, 4]. The method called resonant ultrasonic spectroscopy (RUS) was shown to provide the highest accuracy of the elastic constant measurements [4]. This method was developed in the 1960s–1970s and first used for analyzing the elastic properties of small-sized crystal specimens [5, 6]. Later on, RUS was successfully used for measuring the internal friction in solids [7], analyzing the phase transitions in superconducting materials [8], and so on. The history of RUS and its applications is reviewed in [4].

It should be noted that the problems of acoustic spectroscopy noticeably differ from the problems of modal analysis, which have been much studied in recent years [9] and for which considerable progress was achieved in computational technique [10]. First of all, the problems of acoustic spectroscopy (and, specifically, of resonant acoustic spectroscopy) are essentially inverse problems. The ultimate goal of acoustic spectroscopy is the reconstruction of the desired parameters of the material of which the specimen is made rather than the description of the response of a mechanical system of complex geometry with allowance for the effects of sound radiation and other factors complicating the calculations. Therefore, the geometry of the specimen is usually chosen so as to minimize the possible errors due to the irregular geometric shape (i.e., specimens in the form of a cylinder, a parallelepiped, or a sphere are preferred). In some publications (e.g., [5]), one can find diagrams representing the distributions of normalized displacements, but they contain no analysis of the modes of vibration in the framework of acoustic spectroscopy.

By contrast, in the applied problems of modal analysis, the viscoelastic parameters of the parts forming a structure are known, and the mathematical model is intended to describe the specific features of the response (in the general case, it can be the response to a finite-amplitude perturbation [10]) that are most important for applications. In this case, knowledge of the distributions of both displacements and stresses is of fundamental significance, because variations of the individual elements of the mathematical model allow one to optimize the structure of the vibratory system for a specific applied problem.

1063-7710/02/4803-0339$22.00 © 2002 MAIK "Nauka/Interperiodica"

The RUS method is based on the fact that the eigenfrequencies and the Q factor are related to the components of the elastic constant tensor. The eigenfrequencies of a specimen of a given geometry are determined from the condition of the minimal value of the action function expressed through the superposition of the basis functions [4]. The elastic constant tensor is determined from the condition of the minimal discrepancy between the measured and calculated frequencies. The condition of applicability of RUS is the need to determine all the eigenfrequencies without skips in the frequency range of interest. In this case, it is necessary to use reliably measured resonant frequencies whose total number is five times that of the independent components of the elastic constant tensor [4].

The possibility of detecting a weak anisotropy depends on the accuracy of the determination of the elastic constant tensor components. In turn, the accuracy of the determination of the elastic constant tensor depends on the number of basis functions in use and on the error in measuring the resonant frequencies and the Q factor. The maximal number of basis functions is limited by the performance and memory capacity of the computer. Hence, an increase in the accuracy of calculations presents a technical problem that can be easily solved. The accuracy of the resonant frequency measurement depends not only on the quality of the instruments used for this purpose, but also on the methods of processing the experimental data.

As was noted above, the RUS method was developed for the determination of the elastic constant tensor of crystal specimens. Crystals are characterized by the absence, or by a small amount, of internal defects, which results in a small loss and a high Q factor of vibrations. In this case, all resonances manifest themselves in the form of well-resolved peaks, and the interference of the responses is negligibly small. The determination of the resonant frequency and the Q factor presents no difficulties, because these parameters are uniquely related to the position on the frequency axis and to the width of the peak of the power spectral density. A characteristic feature of rock, as compared to crystals, is the high vibrational energy loss due to internal defects (cracks, pores, etc.). The frequency responses of individual resonances may overlap. In this case, the positions and widths of the peaks of the power spectral density depend on the positioning of the points of vibration excitation and detection. As a result, part of the resonant frequencies can remain undetermined or determined with uncontrolled errors. Since the overlapping of resonance responses is unrelated to the resolution of the spectral analysis, the problem cannot be solved by increasing the accumulation time or other evident methods.

A possible variant of the solution can be the analysis of the response of the mechanical system in a broad frequency band and the representation of this response in the form of a model. The model can be chosen in the form of the superposition of the contributions of resonances with unknown amplitudes, phases, and complex frequencies that satisfy a certain criterion. One of the reasonable criteria for the accuracy of the determination of the model parameters is the minimal error of prediction, which is determined as the sum of the squared absolute values of the difference between the measured and calculated spectral amplitudes. This paper analyzes the possibilities of using this approach to increase the accuracy of RUS as applied to specimens with relatively high losses. However, the losses in the mechanical system under study are assumed to be low enough to consider its resonance properties and to use RUS (i.e., the Q factor should be $\mathcal{Q} \gg 1$). When the condition $\mathcal{Q} \gg 1$ is satisfied, the difference between the eigenfrequencies and the resonant frequencies is negligible, and in the following analysis, this difference is ignored.

RECONSTRUCTION OF THE FREQUENCY CHARACTERISTIC OF A DISTRIBUTED VIBRATORY SYSTEM

Let us formulate the problem to be solved. Assume that, in a frequency band between $\mathcal{F}_{\min}$ and $\mathcal{F}_{\max}$, a vector of length N defines the complex response of the vibratory system to a harmonic excitation with a variable frequency. A discrete frequency sweep is made in such a way that, at every frequency belonging to the frequency spectrum, steady-state vibrations are recorded. Then, the problem consists in finding all resonances between $\mathcal{F}_{\min}$ and $\mathcal{F}_{\max}$ and in the determination of their parameters, namely, the complex frequencies and the complex amplitudes.

The measured transfer characteristic of a linear vibratory system is a superposition of the resonance responses (a superposition of standing waves) and has the form[1]

$$\mathcal{R}(p) = \sum_{l=1}^{M} C_l \mathcal{G}(p, \delta_l, \omega_l) = \frac{Q_{2\tilde{M}}(p)}{P_{2M}(p)}. \qquad (1)$$

Here, M is the number of resonances in the frequency band of analysis (from $\mathcal{F}_{\min}$ to $\mathcal{F}_{\max}$); $p = i\omega$; $\mathcal{G}(p, \delta_l, \omega_l) = \frac{1}{p^2 + 2\delta_l p + \omega_l^2}$; and $Q_{2\tilde{M}}(p)$ and $P_{2M}(p)$ are polynomials where $\tilde{M} < M$. The latter condition provides the alternation of the resonances and antiresonances of the vibratory system [11]. The resonance amplitudes are determined from the solution of the system of linear equations

$$\chi_{kl} C_l = \mathcal{Y}_k, \qquad (2)$$

[1] Representation (1) uses *a priori* information on the linearity of the vibratory system, which makes it possible to represent each resonance response involved in the sum as a certain functional dependence (the Lorentz curve).

where $\chi_{kl} = \sum_{j=1}^{N} \mathcal{G}^*(p_j, \delta_k, \omega_k)\mathcal{G}(p_j, \delta_l, \omega_l)$, $\mathcal{Y}_k = \sum_{j=1}^{N} \mathcal{G}^*(p_j, \delta_k, \omega_k)\mathcal{R}(p_j)$, $p_n = i2\pi(\mathcal{F}_{\min} + \mathcal{B}n/N)$, $\mathcal{B} = \mathcal{F}_{\max} - \mathcal{F}_{\min}$, and $(\ldots)^*$ denotes the complex conjugation.

To determine the positions of the resonances (δ_l, ω_l), it is necessary to turn to the modified methods of linear prediction for signals preset in the time domain [12]. The first L ($L \geq M$) values in the array of equidistant time readings ζ_n corresponding to the transfer function $\mathcal{R}(p_n)$ are used as the initial conditions for the prediction filter. The remaining $N - L$ readings are used to determine the error of the prediction. The change from the frequency domain of definition of the function $\mathcal{R}(p_n)$ to the time domain is performed through the Fourier transform. To eliminate the ambiguity of the transformation $\mathcal{R}(p_n) \longrightarrow \zeta_n$, the function $\mathcal{R}(p_n)$ is preliminarily weighted. In this paper, we use a window from the cosine window class [13].

The coefficients of the characteristic polynomial (g_k) for the data vector ζ_n can be determined from the condition that the prediction error be zero:

$$a_{jk}g_k + h_j = 0, \tag{3}$$

where $a_{jk} = \zeta_{L-k+j}$; $h_j = \zeta_{L+j}$; $j = 1, \ldots, N - L$, $k = 1, \ldots, L$. The polynomial $\mathcal{H}(z) = 1 + \sum_{k=1}^{L} g_k z^{-k}$, where $z = \exp(-\delta\tau)\exp(i\omega\tau)$ and $\tau = 1/\mathcal{B}$, determines the filter with which the convolution of the signal yields zero in the absence of noise when the choice of the filter order is correct, $L = M$. The points where the polynomial $\mathcal{H}(z)$ takes zero values, $z_l = \exp(-\breve{\delta}_l\tau)\exp(i\breve{\omega}_l\tau)$, determine the positions of the poles of Eq. (1). It should be noted that, strictly speaking, Eq. (3) corresponds to the frequency characteristic

$$\breve{\mathcal{R}}(p) = \sum_{l=1}^{M} \frac{\breve{C}_l}{p + \breve{\delta}_l - i\breve{\omega}_l},$$

which differs from Eq. (1). In the general case, when $\mathcal{F}_{\min} > 0$, the function $\breve{\mathcal{R}}(p)$ does not include the contribution of the "negative" frequencies. In addition, the very fact of presetting the frequency characteristic in the interval between $\mathcal{F}_{\min}$ and $\mathcal{F}_{\max}$ implies the presence of an error in the determination of the position z_l because of the contribution of resonances lying outside the frequency range $\mathcal{F}_{\min}$–$\mathcal{F}_{\max}$. However, if we do not consider the vibrations of systems with anomalously high dissipative losses when the width of the resonance curves $\Delta f_l = \delta_l/\pi$ is comparable to the analyzed frequency band $\mathcal{B}$, it is natural to assume that the effect of the aforementioned factors will be smaller the better the condition $\Delta f_l \ll \mathcal{B}$ is satisfied. The quantities $\delta_l \simeq \breve{\delta}_l$ and $\omega_l \simeq \breve{\omega}_l$ are calculated through the zero points of the characteristic polynomial, and the amplitudes C_l are determined from Eqs. (2). The numerical example considered in the following section shows that the effect of the resonant frequencies lying outside the frequency band $\mathcal{B}$ causes almost no changes in the resulting values of the complex resonant frequencies within the band $\mathcal{B}$ when the aforementioned limitations are met.

If the number of resonances M in the analyzed frequency band is unknown and $M < L$, the system of equations (3) is overdetermined, and its solution can be obtained in the sense of the minimal standard error. To determine the number of resonances, the following considerations can be used [12]. In the absence of loss ($\delta_l = 0$), the matrix $\hat{a}^+\hat{a}$ (the superscript $^+$ denotes the Hermitian conjugation) of dimension $L \times L$ has the rank M. The first M eigenvalues of this matrix are positive: $\Lambda_k > 0$, where $k = 1, \ldots, M$; the remaining $L - M$ values are equal to zero. The presence of noise in the data ζ_j causes the matrix $\hat{a}^+\hat{a}$ to have the full rank L. In this case, small eigenvalues correspond to noise. The difference between the magnitudes of the eigenvalues corresponding to the "signal" and the "noise" was used in [12] for the determination of the number of discrete components in the spectrum. Note that the method proposed in [12] was used to resolve continuous-wave harmonic signals with a limited-length sampling. To achieve a "superresolution," the *a priori* information on the absence of attenuation was used.

In the presence of loss ($\delta_l \neq 0$), the eigenvalues Λ_n of the autocorrelation matrix that correspond to the signal and noise subspaces do not differ considerably in their values. In this case, the boundary between the subspaces can be determined by the break in the spectrum of eigenvalues Λ_n (see the following section). The subscript n corresponding to the position of the break determines the number of resonances M in the analyzed frequency band.

In the presence of an additive Gaussian noise, the amplitude estimate given by Eqs. (2) and obtained as the solution to the system of linear equations in the sense of the minimal standard error will be unbiased. The estimate of the positions of the poles of Eq. (1) will also be asymptotically unbiased in the case of a sufficient sampling length: $N \gg L$ [14]. The condition $N \gg L$ means that the number of frequency readings at which the measurements are performed must multiply exceed the expected number of resonances. The possibility of the decomposition of the response into components given by Eq. (1) is realized owing to the redundancy of the information carried by the amplitude distribution $\mathcal{R}(p)$. In the case of clearly defined resonance responses, it is sufficient to determine the positions and widths of the peaks of the power spectral density. If the resonance responses overlap, the analysis of the local features of $\mathcal{R}(p)$ cannot provide the determination of the true positions and Q factors of the resonances. In this case, it is necessary to analyze $\mathcal{R}(p)$ in the whole

frequency band $\mathcal{B}$ (to use the whole information available).

RECONSTRUCTION OF THE FREQUENCY CHARACTERISTIC IN THE ACOUSTIC SPECTROSCOPY PROBLEMS

Let us consider a numerical example illustrating the possibilities of the proposed method of experimental data processing as applied to the problems of acoustic spectroscopy. Assume that the object under study is a sandstone rectangular parallelepiped with dimensions that are close to each other: $L_1 = 0.09$ m, $L_2 = 0.10$ m, and $L_3 = 0.11$ m. The density and velocities of elastic waves are taken from the reference data [2]: $\rho = 2510$ kg/m^3, $V_P = 4670$ m/s, and $V_S = 3060$ m/s. These values correspond to the average characteristics of dry sandstone with minimal porosity (the volume content of pores is 5%). The values of the Q factor of different types of vibrations are set to be equal: $Q = 50$. In this case, as one can see from the plots presented below, the frequency responses of individual resonances overlap, and the problem of determining the resonances becomes nontrivial. Thus, we use the results of calculations for the vibratory system with known parameters as "experimental" data. Comparing the calculated values of the frequencies and the Q factor with the values obtained from the reconstruction of transfer function (1), it is possible to test the efficiency of the algorithm as applied to the problems of acoustic spectroscopy.

Concerning the quantities L_1, L_2, L_3, and Q mentioned above, it should be noted that, in reality, the Q factor of vibrations in sandstone-type rock may exceed the value set above by a factor of 2–4 [3]. The dimensions of the specimen may have arbitrary values that are not necessarily close to each other. In the example under study, we deliberately make the problem of the determination of the resonance parameters more complicated to test the algorithm developed on the basis of the previous section.

To preset the response of the specimen to a localized harmonic action, we represent the displacement as a superposition of the contributions of normal modes [11]:

$$\boldsymbol{\zeta}(\mathbf{x}, \omega) = \begin{cases} \sum_{k=0}^{K} \mathcal{A}_k \dfrac{\boldsymbol{\Psi}_k(\mathbf{x})}{-\omega^2 + \omega_k^2} & \omega \geq 0 \\ \sum_{k=0}^{K} \mathcal{A}_k^* \dfrac{\boldsymbol{\Psi}_k(\mathbf{x})}{-\omega^2 + \omega_k^{*2}} & \omega < 0, \end{cases} \tag{4}$$

where ω is the real cyclic frequency of the harmonic action, ω_k is the complex cyclic frequency of the kth resonance, and $\boldsymbol{\Psi}_k(\cdot)$ are the eigenfunctions of the corresponding boundary-value problem (they are determined through the eigenvectors by solving the matrix problem of RUS). The algorithms used in this study for calculating the frequencies and modes are described in [15]. The ratio $Q_k = \dfrac{\omega_k'}{2|\omega_k''|}$ (where $\omega_k' = \mathrm{Re}(\omega_k)$ and $\omega_k'' = \mathrm{Im}(\omega_k)$) determines the Q factor of each individual resonance. The mode excitation amplitudes for a unit-amplitude force acting along a vector $\boldsymbol{\epsilon}$ are determined by the following evident expression:

$$\mathcal{A}_k = \frac{(\boldsymbol{\Psi}_k(\mathbf{x}_A) \times \boldsymbol{\epsilon})}{\|\Psi_k\|^2}, \tag{5}$$

where $\mathbf{x}_A$ corresponds to the coordinates of the extraneous force (Fig. 1) and $\|\Psi_k\|^2$ stands for the norms of the eigenfunctions of the boundary-value problem for which representation (4) is constructed.

Let us choose the total number of resonances K so as to satisfy the condition $\dfrac{\omega_K}{2\pi} > \mathcal{F}_{\max}$. In Eq. (4), the values of $\omega_K/2\pi$ and $\mathcal{F}_{\max}$ are 100 and 33 kHz, respectively. The step in frequency is selected to satisfy the condition $\Delta f \ll \dfrac{\omega_1}{2\pi Q} \simeq 250$ Hz,[2] which determines the requirements for the spectral resolution. Setting $\Delta f = 25$ Hz for definiteness, we obtain $N = 1080$ for the frequency range between $\mathcal{F}_{\min} = 6$ kHz and $\mathcal{F}_{\max} = 33$ kHz. Since, according to the calculations, the number of resonances in this frequency band is $M = 30$, the sampling length evidently satisfies the criterion $N \gg M$, and the resulting frequency estimates must be unbiased. To imitate the measurement errors, data in the form of Eq. (4) were supplemented with noise. The signal-to-noise ratio (SNR) can have a preset value, because the noise level in the course of the measurements depends on the accumulation time. The choice of the specific value SNR = 80 dB simulates the conditions at which the measurements are performed accurately, and all the details (peaks and dips) of the transfer function are recorded for all variants of excitation. Thus, we model the minimal requirements for the spectral resolution and the dynamic range of the measuring system. The inclusion of resonances lying outside the analyzed frequency band in the calculations by Eq. (4) allows one to estimate their possible effect on the accuracy of the reconstruction.

Figures 2–4 present the initial [calculated by Eqs. (4) and (5)] and reconstructed responses of an elastic parallelepiped to a harmonic action with a variable frequency. The force is applied at the corner point A (Fig. 1) with the dimensionless coordinates $x_j = (+1, -1, -1)$. The displacements are detected at the corner point B (Fig. 1) with the coordinates $\bar{x}_j = (-1, +1, +1)$ in the

[2] The first resonance frequency is approximately 12.5 kHz (Table 1).

direction of the force vector. This choice of the excitation conditions allows one to record vibrations of any polarization, irrespective of whether the mode of vibration is symmetric or antisymmetric about the geometric symmetry axes of the specimen. The setup shown in Fig. 1 is conventionally used in RUS [4].

One can easily notice the good agreement between the preset and reconstructed responses for all three variants of excitation. The errors in the reconstruction of the minima of the transfer functions (Figs. 3, 4) are caused by the effect of resonances with frequencies higher than $\mathcal{F}_{max}$ = 33 kHz (the positions and depths of the antiresonances of the mechanical system are determined by the contribution of a large number of nonresonant modes [11]).

The spectrum of the eigenvalues of the autocorrelation matrix $\hat{a}^{+}\hat{a}$ is presented in Fig. 5. The dissipative loss leads to the absence of great differences between the amplitudes Λ_n corresponding to resonances and the eigenvalues corresponding to noise. However, the components Λ_n corresponding to the noise subspace are identified with confidence and lie at a level of 1/SNR. This fact makes it possible to use the method of separating the noise and signal subspaces [12] for the determination of the number of resonances in mechanical systems with losses.

The accuracy of the reconstruction can be judged from Table 1. The analysis of the results obtained for each variant of excitation shows that maximal errors occur when the resonance amplitudes $\mathcal{A}_k$ are small compared to the average values taken over three variants of the source and the detector positions. These situations correspond to a weak excitation of resonances because of the discrepancy between the excitation conditions and the polarization of individual modes. Therefore, the complex frequencies were averaged with the weights equal to the resonance amplitudes, which made it possible to take into account the difference in the excitation coefficients for different variants of the "transducer" positioning.

The rms difference between the initial and determined frequencies is σ_F = 0.13%. This value is of the same order of magnitude as the error of RUS in the analysis of the elastic constants of crystals [4, 6]. Summarizing the values of δF and δQ, we obtain $\sum_{j=1}^{M}\delta F_j/M = 10^{-3}\%$ and $\sum_{j=1}^{M}\delta Q_j/M = -0.9\%$, which is less than the variance of the estimate of the aforementioned parameters. This result suggests that the estimates of the complex resonant frequencies are unbiased.

The rms difference between the frequencies corresponding to the peaks and the initial values of the resonant frequencies is 0.47%. However, the determination of all resonant frequencies as the frequencies corresponding to the peaks of the response is impossible:

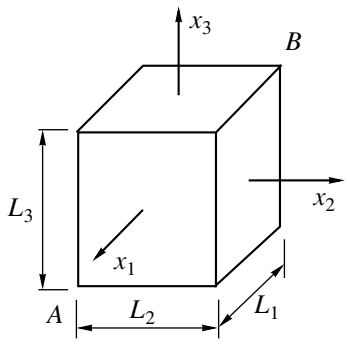

Fig. 1. Measuring setup used in the RUS method: *A* is the point of excitation and *B* is the point of vibration detection. The origin of coordinates coincides with the center of mass of the parallelepiped. The normalized coordinates are determined by the ratio $\bar{x}_j = 2x_j/L_j$, $x_j \in [-L_j/2, +L_j/2]$.

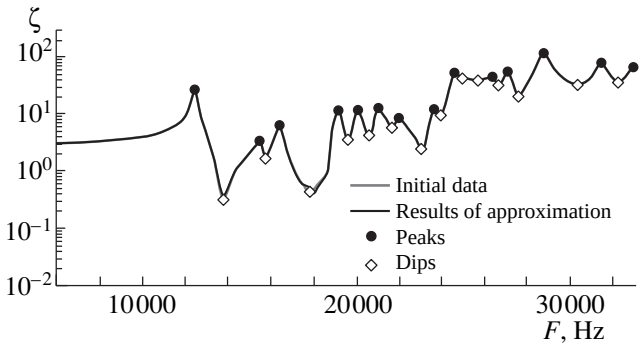

Fig. 2. Excitation along the x_1 axis.

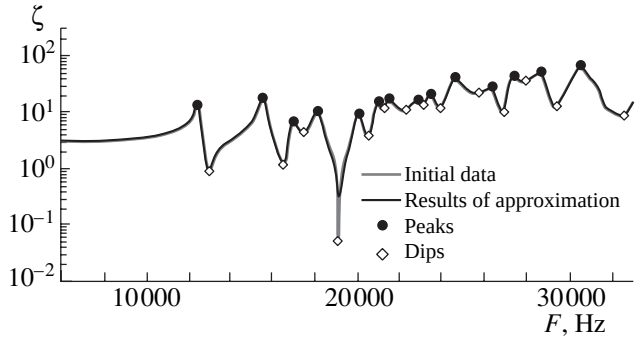

Fig. 3. Excitation along the x_2 axis.

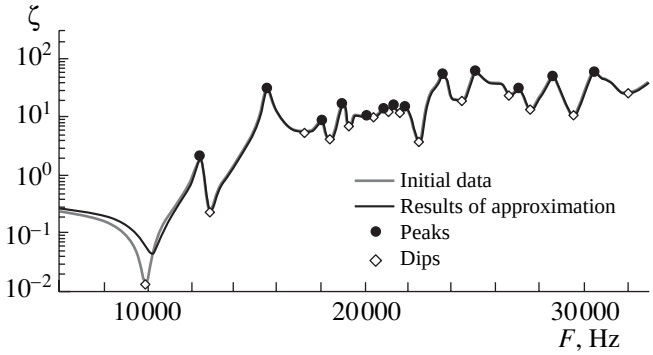

Fig. 4. Excitation along the x_3 axis.

Table 1. Estimates of the resonant frequencies and Q factors of a sandstone specimen for which the model calculations were performed from the reconstruction of the response to a force action of variable frequency

No.	True values	Frequencies corresponding to peaks		Results of the reconstruction			
	F(kHz)	F(kHz)	δF(%)	F(kHz)	δF(%)	Q	δQ(%)
1	12.4537	12.4333	+0.16	12.4512	+0.02	49.78	–0.44
2	15.5390	15.5151	+0.15	15.5370	+0.01	49.84	–0.31
3	16.4020	16.3893	+0.08	16.3982	+0.02	49.00	–2.00
4	16.9395	16.9859	–0.27	16.9364	+0.02	49.90	–0.20
5	18.1063	18.0740	+0.18	18.1034	+0.02	49.86	–0.29
6	18.9322	18.9781	–0.24	18.9293	+0.02	49.89	–0.21
7	19.1992	19.1489	+0.26	19.1960	+0.02	49.80	–0.40
8	19.3831	–	–	19.3814	+0.01	49.80	–0.40
9	20.0660	20.0711	–0.03	20.0607	+0.03	49.85	–0.30
10	20.2603	20.1304	+0.65	20.2565	+0.02	49.70	–0.60
11	20.9836	20.9789	+0.02	20.9778	+0.03	48.83	–2.35
12	21.4389	21.4531	–0.07	21.4306	+0.04	52.48	+4.97
13	21.9013	21.9381	–0.17	21.8880	+0.06	46.12	–7.75
14	22.5558	–	–	22.5511	+0.02	48.78	–2.44
15	22.9449	–	–	22.9473	–0.01	51.13	+2.26
16	23.3672	23.4634	–0.41	23.4029	–0.15	54.54	+9.07
17	23.6520	23.6431	+0.04	23.6520	+0.00	48.99	–2.03
18	24.2568	–	–	24.2557	+0.00	50.00	+0.00
19	24.5761	24.6357	–0.24	24.5834	–0.03	51.64	+3.27
20	25.0455	25.1172	–0.29	25.0468	–0.01	49.83	–0.34
21	26.4100	26.3519	+0.22	26.4082	+0.01	48.20	–3.60
22	26.5124	–	–	26.4903	+0.08	46.07	–7.87
23	26.7925	–	–	26.7835	+0.03	42.71	–14.58
24	27.1603	27.0836	+0.28	27.1076	+0.19	43.65	–12.68
25	27.2730	27.4078	–0.49	27.2519	+0.08	50.32	+0.64
26	28.7180	28.6819	+0.13	28.7122	+0.02	50.42	+0.84
27	30.4847	30.5216	–0.12	30.4772	+0.02	49.91	–0.19
28	31.0302	–	–	31.0241	+0.02	50.83	+1.67
29	31.4355	31.4105	+0.08	31.4266	+0.03	50.16	+0.32
30	32.6128	33.2381	–1.88	32.8268	–0.65	53.88	+7.77
Standard deviation			0.47		0.13		4.89

some resonances do not manifest themselves as peaks of the power spectral density because of the strong overlapping of the resonance responses for all three variants of the source and detector positions. For the same reason, it is impossible to obtain any reliable estimates of the Q factor.

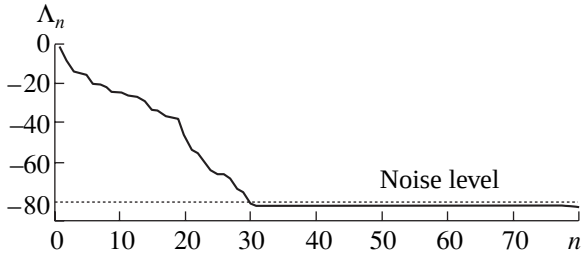

Fig. 5. Spectrum of the eigenvalues of the autocorrelation matrix. The values of Λ_n are normalized to the sum $\Lambda_1 + \Lambda_2 + \ldots + \Lambda_L$. The dotted line shows the noise level corresponding to SNR = 80 dB.

THE POSSIBILITY OF DETERMINING A WEAK ANISOTROPY OF ROCK BY RESONANT ULTRASONIC SPECTROSCOPY

Above, it was mentioned that the anisotropy of rock is governed by the specific features of the distribution of internal defects. In this respect, the anisotropy measurements by RUS are of particular interest. The reliability of weak anisotropy measurements is provided by the excess of the rms difference between the calculated and measured frequencies over the measurement error. Let us consider how the proposed method of resonant frequency measurement can be used for the determination of a weak anisotropy.

Table 2. Calculated frequencies for an isotropic sandstone specimen and for a weakly anisotropic one (with V_P = 4670 m/s along the symmetry axis and V_P = 4717 m/s across this axis)

No.	Isotropic F (kHz)	Anisotropi F (kHz)	δF (%)	No.	Isotropic F (kHz)	Anisotropi F (kHz)	δF (%)
1	12.4537	12.4542	$\frac{+0.00}{+0.02}$	16	23.3672	23.5882	$\frac{+0.95}{-0.15}$
2	15.5390	15.5419	$\frac{+0.02}{+0.01}$	17	23.6520	23.8524	$\frac{+0.85}{+0.00}$
3	16.4020	16.4247	$\frac{+0.14}{+0.02}$	18	24.2568	24.4096	$\frac{+0.63}{+0.00}$
4	16.9395	16.9532	$\frac{+0.08}{+0.02}$	19	24.5761	24.7330	$\frac{+0.64}{-0.03}$
5	18.1063	18.1086	$\frac{+0.01}{+0.02}$	20	25.0455	25.0493	$\frac{+0.02}{-0.01}$
6	18.9322	19.0378	$\frac{+0.56}{+0.02}$	21	26.4100	26.4279	$\frac{+0.07}{+0.01}$
7	19.1992	19.2000	$\frac{+0.00}{+0.02}$	22	26.5124	26.5981	$\frac{+0.32}{+0.08}$
8	19.3831	19.4545	$\frac{+0.37}{+0.01}$	23	26.7925	27.1271	$\frac{+1.25}{+0.03}$
9	20.0660	20.0854	$\frac{+0.10}{+0.03}$	24	27.1603	27.1891	$\frac{+0.11}{+0.19}$
10	20.2603	20.3328	$\frac{+0.36}{+0.02}$	25	27.2730	27.2974	$\frac{+0.09}{+0.08}$
11	20.9836	20.9866	$\frac{+0.01}{+0.03}$	26	28.7180	27.3776	$\frac{-4.67}{+0.02}$
12	21.4389	21.4982	$\frac{+0.28}{+0.04}$	27	30.4847	28.7711	$\frac{-5.62}{+0.02}$
13	21.9013	22.0233	$\frac{+0.56}{+0.06}$	28	31.0302	28.8196	$\frac{-7.12}{+0.02}$
14	22.5558	22.5733	$\frac{+0.08}{+0.02}$	29	31.4355	30.5119	$\frac{-2.94}{+0.03}$
15	22.9449	23.1015	$\frac{+0.68}{-0.01}$	30	32.6128	31.1843	$\frac{-4.38}{-0.65}$

A weak anisotropy is usually characterized by three quantities, each of which is smaller than unity in magnitude [2]:

$$\varepsilon = \frac{C_{11} - C_{33}}{2C_{33}}, \tag{6}$$

$$\gamma = \frac{C_{11} - C_{12} - 2C_{44}}{4C_{44}}, \tag{7}$$

$$\delta = \frac{(C_{13} + C_{44})^2 - (C_{33} - C_{44})^2}{2C_{33}(C_{33} - C_{44})}. \tag{8}$$

Here, C_{ij} are the components of the elastic constant tensor in terms of the standard two-index notation [1, 2].

We assume that a partial fracture gives rise to a maximum in the distribution of internal defects in a specific direction. This direction determines that of the symmetry axis. In Eqs. (6)–(8), we set $\gamma = \delta = 0$ and $\varepsilon = 0.01$, which corresponds to a difference of 1% between the sound velocity along the symmetry axis and across it when the velocity of shear waves is constant irrespective of the propagation direction and polarization. The results of the eigenfrequency calculations are presented in Table 2. The numerator δF corresponds to the relative difference between the resonant frequencies of

weakly anisotropic and isotropic specimens, and the numerator presents the errors of the reconstruction from Table 1. The rms difference between the resonant frequencies of anisotropic and isotropic specimens makes 2.2%. At the same time, as one can see from Table 1, the error in the reconstruction of the frequency response is 0.13%, i.e., 17 times smaller. Hence, a sound velocity anisotropy of 1% can be reliably measured by RUS with the use of the proposed method of experimental data processing.

CONCLUSION

Thus, we considered the possibilities of measuring the resonant frequencies and the Q factor of vibrations of rock specimens with the subsequent use of resonant ultrasonic spectroscopy for the determination of the complex elastic constant tensor. An algorithm is developed for the determination of the number of resonances falling within the frequency band under analysis and their parameters. The study described in this paper offers the following conclusions:

(i) The proposed measuring technique based on the modified method of linear prediction [12] allows one to reconstruct the parameters of a vibratory system in conditions of a partial or full overlapping of resonance responses;

(ii) The accuracy of RUS achieved in this case is close to that obtained for crystal specimens with a reliable resolution of every resonance response; and

(iii) The numerical example presented above demonstrates the possibility of weak anisotropy measurement, which allows one to test the internal state of rock at the initial stages of fracture.

ACKNOWLEDGMENTS

This work was supported in part by the Interdepartmental Center for Science and Engineering (project no. 1369) and by the Russian Foundation for Basic Research (project nos. 00-15-96741 and 00-05-64252).

REFERENCES

1. L. D. Landau and E. M. Lifshits, *Course of Theoretical Physics*, Vol. 7: *Theory of Elasticity*, 4th ed. (Nauka, Moscow, 1987; Pergamon, New York, 1986).
2. G. Mavko, T. Mukeji, and J. Dvorkin, *The Rock Physics Handbook. Tools for Seismic Analysis in Porous Media* (Cambridge Univ. Press, Cambridge, 1998).
3. J. E. White, *Underground Sound. Application of Seismic Waves* (Elsevier, Amsterdam, 1983; Nedra, Moscow, 1986).
4. A. Migliori and J. L. Sarrao, *Resonant Ultrasound Spectroscopy: Applications to Physics, Materials Measurements, and Nondestructive Evaluation* (Wiley, New York, 1997).
5. H. Demarest, J. Acoust. Soc. Am. **49**, 768 (1971).
6. Y. Sumino, I. Ohno, and M. Kumazawa, J. Phys. Earth **24**, 263 (1976).
7. W. P. Mason, K. J. Marfurt, D. N. Beshers, and J. T. Kuo, J. Acoust. Soc. Am. **62**, 1206 (1977).
8. A. Migliori, W. M. Visscher, and S. E. Brown, Phys. Rev. B **41**, 2098 (1990).
9. D. L. Brown, in *Proceedings of Second International Congress on Recent Developments in Air- and Structure-Borne Sound and Vibrations* (Mechanical Engineering Department, Auburn Univ., AL, USA, 1992), Vol. 3, p. 1555; see also: www.sem.org/downloads.htm.
10. K. Fyfe, B. McKay, A. Muradali, C. Sorensen, K. J. Geisler, T. Olofsson, P. Skoczylas, and R. Toogood, *Tutorials ANSYS Finite Elements Analysis*, Internet address: www.csa.ru/~slash/docs/ansys/tut2.
11. E. Skudrzyk, J. Acoust. Soc. Am. **67**, 1105 (1980).
12. D. W. Tuft and R. Kumare-Sun, Proc. IEEE **70** (9), 975 (1982).
13. R. K. Otnes and L. Enochson, *Applied Time Series Analysis* (Wiley, New York, 1978; Mir, Moscow, 1982).
14. T. W. Anderson, *The Statistical Analysis of Time Series* (Wiley, New York, 1971; Mir, Moscow, 1976).
15. L. A. Ostrovsky, A. V. Lebedev, A. L. Matveyev, *et al.*, J. Acoust. Soc. Am. **110**, 1770 (2001).

Translated by E. Golyamina

Acoustical Physics, Vol. 48, No. 3, 2002, pp. 347–352. Translated from Akusticheskiĭ Zhurnal, Vol. 48, No. 3, 2002, pp. 400–405.
Original Russian Text Copyright © 2002 by Mironov, Pislyakov.

One-Dimensional Acoustic Waves in Retarding Structures with Propagation Velocity Tending to Zero

M. A. Mironov* and V. V. Pislyakov**

** Andreev Acoustics Institute, Russian Academy of Sciences, ul. Shvernika 4, Moscow, 117036 Russia*
e-mail: mironov@akin.ru
*** Moscow Institute of Physics and Technology, Institutskiĭ per. 9,*
Dolgoprudnyĭ, Moscow oblast, 141700 Russia

Received July 17, 2001

Abstract—A retarding structure that allows the effective admittance of a tube wall to increase smoothly along the tube axis is considered. The sound velocity gradually decreases along a finite segment of the tube and finally vanishes at some cross section. The time of the sound propagation along this segment is infinitely long. A wave incident on the input cross section cannot reach the other end of the tube within a finite time, and, hence, it is not reflected from it. The wave is completely absorbed, the absorption being caused by the energy accumulation in the cross section where the velocity of sound vanishes, rather than by the energy transformation to heat, as in common sound absorbers. A differential equation is obtained to describe the sound propagation in a one-dimensional waveguide with a varying cross section and varying acoustic admittance of the walls. The solutions to this equation are analyzed in the WKB approximation. An exact solution is determined for the case of some specific functions describing the variations of the cross section and admittance. Calculated results for the input admittance of the waveguide are presented. A possible similarity to the problem of shear waves in sea sediments is pointed out. © *2002 MAIK "Nauka/Interperiodica".*

GENERALIZED WEBSTER EQUATION

The velocity of sound propagation in a narrow (in comparison with the wavelength) tube depends on the acoustic admittance of the tube wall [1]. The elastic-type wall admittance reduces the velocity of propagation. In what follows, we investigate longitudinal sound waves in a narrow waveguide of varying cross section with varying acoustic admittance of the walls. The waveguide provides a smooth decrease in the velocity of wave propagation, which, however, occurs rapidly enough for the propagation velocity to vanish within a finite distance. The possibility of creating specially tapered edges of plates and bars to eliminate the reflection of bending waves was considered earlier [2, 3]. Two conditions determine the choice of the tapering rate. On the one hand, the cross section should vary smoothly to cause no reflection. On the other hand, the cross section should vary rapidly enough for the velocity of a bending wave to vanish within the tapered segment of a finite length.

In the case of a narrow, axially symmetric waveguide of varying cross section and with varying wall admittance, the wave equation is derived as follows. We direct the x axis along the symmetry axis and denote by $S = S(x)$ the area of the waveguide cross section, by $r = r(x)$ the waveguide radius, and by $Y = Y(x)$ the admittance of the walls (Fig. 1). The Euler equation remains intact:

$$-\frac{\partial p}{\partial x} = \rho_0 \frac{\partial v}{\partial t}, \tag{1}$$

where v is the projection of the velocity on the x axis, p is the pressure, and ρ_0 is the density of the medium. The equation of continuity can be obtained from the conservation of matter in a thin layer of thickness dx (see Fig. 1)

$$d(\rho_0 S v) + (2\pi r v_\perp \rho_0)dx + \frac{\partial \rho}{\partial t} S dx = 0,$$

where $v_\perp$ is the projection of the velocity of liquid near the walls on the perpendicular to the symmetry axis and ρ is the acoustic component of the density. Substituting $v_\perp = Yp$, we obtain

$$-\frac{1}{\rho_0}\frac{\partial \rho}{\partial t} = v(\ln S)'_x + \frac{\partial v}{\partial x} + \frac{2Yp}{r}. \tag{2}$$

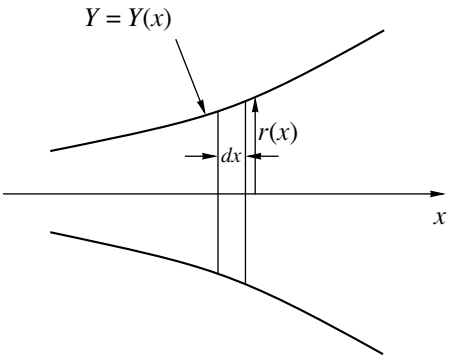

Fig. 1. Derivation of the generalized Webster equation. The waveguide with a varying cross section and varying wall admittance.

1063-7710/02/4803-0347$22.00 © 2002 MAIK "Nauka/Interperiodica"

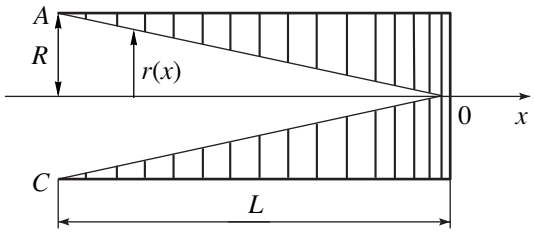

Fig. 2. Model of an acoustic black hole. The tube with rings whose inner radius $r(x)$ decreases to zero.

Taking into account the equality $\frac{\partial \rho}{\partial t} = \frac{1}{c^2}\frac{\partial p}{\partial t}$ and eliminating velocity v from Eqs. (1) and (2), we obtain the wave equation for the pressure:

$$\frac{1}{c^2}\frac{\partial^2 p}{\partial t^2} + \frac{2Y\rho_0}{r}\frac{\partial p}{\partial t} = \frac{\partial^2 p}{\partial x^2} + \frac{\partial p}{\partial x}(\ln S)_x'. \qquad (3)$$

For pressure varying harmonically in time, $p(x, t) = p(x)e^{-i\omega t}$, Eq. (3) takes the form of the generalized Webster equation

$$p'' + p'(\ln S)' + p\left(k_0^2 + \frac{2Y\rho}{r}(i\omega)\right) = 0, \qquad (4)$$

where $k_0 \equiv \omega/c$ and the prime denotes the derivative with respect to x. For zero-valued admittance Y, Eq. (4) transforms to the conventional Webster equation.

ACOUSTIC BLACK HOLE. THE WKB APPROXIMATION

For the sake of definiteness, we consider in what follows a particular structure of the waveguide with a varying cross section and varying wall admittance (Fig. 2). This structure is a segment of a perfectly hard cylindrical tube of radius R, inside which a number of perfectly hard rings are mounted rather close to each other. The inner radius $r = r(x)$ of the rings decreases according to a law satisfying the condition $\lim_{x \to -0} r(x) = 0$. The whole structure is located in the halfspace $x < 0$, and its right-hand wall lies in the plane $x = 0$. In this structure, the waveguide is the region AOC, while the remaining part of the tube between the rings forms the varying admittance of the walls of this waveguide. The admittance is determined by the compressibility of the medium between the adjacent rings. Simple calculations give

$$Y = (-i\omega)\frac{1}{\rho_0 c^2}\frac{R^2 - r^2}{2r}. \qquad (5)$$

Substituting expression (5) in Eq. (4) and taking into account the relationship $S = \pi r^2$, we obtain

$$p'' + 2p'(\ln r)' + k_0^2\frac{R^2}{r^2}p = 0. \qquad (6)$$

Note that this equation holds for a tube of varying radius R as well.

Following the cited papers [2, 3], we consider the solutions to Eq. (4) in the WKB approximation and determine the functional behavior $r(x)$ that can ensure the infinite time of propagation along a finite waveguide length. Note that the applicability of the WKB approximation assumes that waves propagating in different directions do not transform into each other. Substituting $p(x) \sim \exp(ikx)$ in Eq. (6), we obtain the following expression for the local wave number $k = k(x)$:

$$k(x) = \sqrt{k_0^2\frac{R^2}{r^2} - ((\ln r)')^2} = \frac{1}{r}\sqrt{k_0^2R^2 - (r')^2}. \qquad (7)$$

The WKB approximation is applicable if coefficients in Eq. (6) vary only slightly within distances about $k(x)^{-1}$:

$$\left|\frac{d(\ln r)'}{dx}\frac{1}{k}\right| \ll |(\ln r)'| \quad \text{and} \quad \left|\frac{d(\ln r)'}{dx}\frac{1}{k}\right| \ll \frac{1}{r^2}.$$

These inequalities can be rewritten in the form

$$|k| \gg \left|\frac{r''}{r'}\right|, \quad |k| \gg \left|\frac{r'}{r}\right|. \qquad (8)$$

Consider now the power-law function of x for the waveguide radius:

$$r(x) = \varepsilon x^n. \qquad (9)$$

In this case, both conditions (8) are identical,

$$|k| \gg 1/x, \qquad (10)$$

and the formula for the current wave number (7) takes on the form

$$k(x) = \frac{1}{\varepsilon x^n}\sqrt{k_0^2R^2 - \varepsilon^2 n^2 x^{2(n-1)}}. \qquad (11)$$

From relations (10) and (11), we obtain the following condition of applicability of the WKB approximation:

$$\left|\frac{1}{\varepsilon x^{n-1}}\sqrt{k_0^2R^2 - \varepsilon^2 n^2 x^{2(n-1)}}\right| \gg 1.$$

For $n > 1$, this condition holds for sufficiently small $|x|$ $\left(|x| \ll \left[\frac{k_0 R}{\varepsilon\sqrt{n^2+1}}\right]^{1/(n-1)}\right)$, and, for $n = 1$ and $\varepsilon \ll k_0 R$, it holds for any x. Below, we consider the case $n = 1$, when the waveguide radius decreases most slowly and the condition of applicability of the WKB

approximation holds uniformly in x. We choose the parameter ε as the ratio of the radius of the tube to the length L of the segment along which the waveguide radius decreases from R to zero (see Fig. 2): $\varepsilon = R/L$. From Eq. (11), we obtain

$$k(x) = -\frac{1}{x}\sqrt{k_0^2L^2 - 1}. \quad (12)$$

The minus sign corresponds to the wave propagating toward increasing x, i.e., from left to right. For $x \longrightarrow -0$, the wave number tends to infinity. In this case, both phase c_{ph} and group c_g velocities tend to zero,

$$c_{ph} = \frac{\omega}{k} = -\frac{\omega}{\sqrt{k_0^2L^2 - 1}}x, \quad c_g = -\frac{c^2\sqrt{k_0^2L^2 - 1}}{L^2\omega}x. \quad (13)$$

The propagation time T of a wave packet from the initial cross section $x = -L$ to cross section $x_1 = -l$ is

$$T = \int_{-L}^{x_1}\frac{dx}{c_g} = \frac{L^2\omega}{c^2\sqrt{k_0^2L^2 - 1}}\ln\left(\frac{L}{l}\right). \quad (14)$$

For $x_1 \longrightarrow -0$, we have $T \longrightarrow -\infty$. A wave incident on the left-hand cross section of the waveguide will never reach its right-hand cross section and, consequently, will never be reflected from the right-hand cross section. Thus, the structure under study is an acoustic black hole similar to the vibrational black hole considered in [2, 3] for bending waves in a bar of varying cross section.

EXACT SOLUTION

It turns out that Eq. (6) with $r(x) = -\frac{L}{R}x$ has a set of exact particular solutions in the form of power-law functions

$$p(x) = A_\alpha\left(\frac{x}{L}\right)^\alpha. \quad (15)$$

Indeed, after substituting Eq. (15) into Eq. (6), the power-law functions of x are canceled, and we obtain a quadratic equation in the exponent α, whose two solutions are

$$\alpha_{1,2} = -\frac{1}{2} \pm \sqrt{\frac{1}{4} - (k_0L)^2}. \quad (16)$$

For $k_0L < \frac{1}{2}$, these exponents are real-valued quantities, and the pressure field exhibits behavior of a nonwave type (pressures at different points are not shifted in phase relative to each other). For $k_0L > \frac{1}{2}$, the exponents have an imaginary part, and the pressure field demonstrates the behavior of a traveling wave (a finite phase shift is present). The correspondence of exact solutions (15) and (16) to the WKB approximation is obvious. The power-law function on the right-hand side of Eq. (15) can be rewritten as

$$x^\alpha \equiv x^{-1/2}\exp\left(\pm i\int_L^x\sqrt{k_0^2L^2 - (1/4)}\frac{dx}{x}\right). \quad (17)$$

Comparing this formula with expression (12) for the local wave number in the WKB approximation, one can see that Eq. (12) correctly describes the functional dependence on the parameter k_0L, except that the root argument has the term –1/4 in exact solution (17) instead of the term –1 in Eq. (12). Thus, the threshold frequency, i.e., the frequency starting from which the pressure field demonstrates the wave-type behavior, appears to be two times lower than the value predicted in the WKB approximation. The factor of the exponential in Eq. (17) describes the conservation of the energy flux.

SOUND REFLECTION FROM THE BLACK HOLE

Consider the sound reflection from the black hole and calculate its acoustic admittance. To take into account possible imperfection of the waveguide structure, we assume that the inner radius of rings decreases to a certain finite value, rather than to zero. Thus, the retarding structure occupies the region $-L < x < -l$, where $l > 0$. A unit-amplitude acoustic wave is incident on this structure from the half-infinite homogeneous tube $x < -L$ and is reflected with a coefficient V (see Fig. 3). Two waves are generated inside the black hole. They are described by relationship (15) and have the amplitudes A_1 and A_2. We specify the admittance Y in the cross section $x = -l$ (at the output of the black hole) and calculate the reflection coefficient V. At the input of the black hole ($x = -L$), the boundary conditions have the form

$$e^{-ikL} + Ve^{ikL} = A_1 + A_2, \quad (18)$$

$$\frac{1}{\rho_0 c}(e^{-ikL} - Ve^{ikL}) = -\frac{1}{i\rho_0\omega L}(\alpha_1A_1 + \alpha_2A_2). \quad (19)$$

At $x = -l$, the boundary condition is

$$A_1\left(\frac{l}{L}\right)^{\alpha_1} + A_2\left(\frac{l}{L}\right)^{\alpha_2} = \frac{v}{Y} = -\frac{1}{i\omega\rho_0 lY}\left(\alpha_1\left(\frac{l}{L}\right)^{\alpha_1}A_1 + \alpha_2\left(\frac{l}{L}\right)^{\alpha_2}A_2\right). \quad (20)$$

Solving Eqs. (18)–(20) simultaneously, we find the reflection coefficient V:

$$V = \frac{1 + W + \frac{c}{i\omega L}(\alpha_1 + W\alpha_2)}{1 + W - \frac{c}{i\omega L}(\alpha_1 + W\alpha_2)}e^{-2ikL}. \quad (21)$$

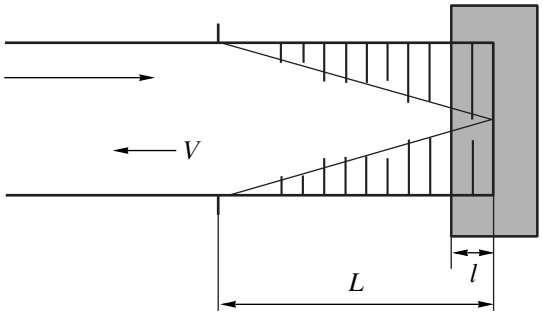

Fig. 3. Reflection of sound from an actual acoustic black hole. The distance l characterizes the imperfection of the black hole.

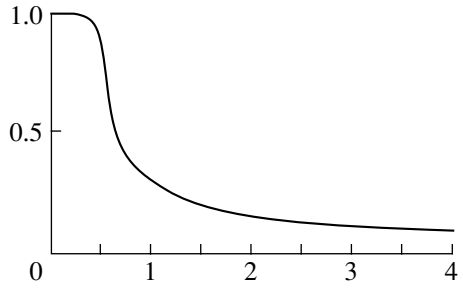

Fig. 4. Frequency dependence of the reflection coefficient of sound from an acoustic black hole in the case of a nonreflecting cross section at $x = -l$ (the frequency is given in k_0L units).

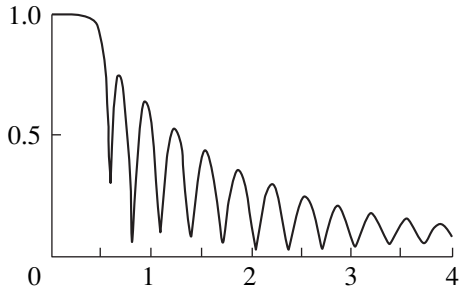

Fig. 5. Frequency dependence of the reflection coefficient of sound from an acoustic black hole in the case of a reflecting (perfectly hard) cross section at $x = -l$ with consideration for the energy loss in the course of the sound propagation in a liquid.

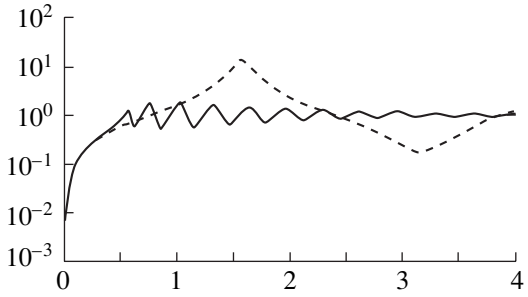

Fig. 6. Acoustic admittance of the black hole (the solid line) in comparison with the quarter-wavelength tube segment (the dashed line). The ordinate axis uses a logarithmic scale.

Here,

$$W \equiv \frac{A_2}{A_1} = -\left(\frac{l}{L}\right)^{\alpha_1-\alpha_2}\frac{1+\dfrac{\alpha_1}{i\omega\rho_0 lY}}{1+\dfrac{\alpha_2}{i\omega\rho_0 lY}} \qquad (22)$$

is the coefficient of reflection from the output cross section $x = -l$.

The acoustic admittance of the structure shown in Fig. 3 is expressed as follows:

$$Y_{Bh} = \frac{1}{\rho_0 c}\frac{e^{-ikL} - Ve^{ikL}}{e^{-ikL} + Ve^{ikL}} = \frac{1}{i\rho_0\omega L}\frac{\alpha_1 + W\alpha_2}{1+W}. \qquad (23)$$

If the waveguide is made so that no reflection occurs from the cross section $x = -l$, i.e., W is zero, then, we have

$$V = \frac{1+\dfrac{\alpha_1 c}{i\omega L}}{1-\dfrac{\alpha_1 c}{i\omega L}}e^{-2ikL}. \qquad (24)$$

Figure 4 shows the magnitude of the reflection coefficient $|V|$ as a function of ω. As expected, a sharp decrease can be seen in the reflection coefficient at $k_0L = 0.5$ [compare with Eq. (16)]. The fact that this curve is smoothed and does not exhibit stepwise behavior [which seemingly should appear in accordance with Eq. (16)] is explained by the reflection from the input cross section $x = -L$.

Now, let us assume that $W \neq 0$, $l = 5 \times 10^{-5}$, $L = 0.5$, and the boundary $x = -l$ is hard. We introduce a small energy loss by adding an imaginary part to the velocity of sound: $c = 340(1 - 0.05i)$. Figure 5 shows the corresponding magnitude of the reflection coefficient $|V|$ as a function of ω. The oscillations of the reflection coefficient are related to the resonance features of the black hole. Figure 6 shows the admittance of the black hole characterized by the same parameters as those used for Fig. 5 (the solid line) and the admittance of the standard quarter-wavelength tube segment (the dashed line). Both curves are normalized by $(\rho c)^{-1}$. First and foremost, the curves show that the retarding structure has many resonance peaks, the first resonance frequency being lower than the resonance frequency of the quarter-wavelength tube by a factor of about 3. Thus, the retarding structure increases the effective length of the tube.

With decreasing loss, the oscillation amplitude of $|Y_{Bh}|$ sharply increases. Figure 7 shows the same admittances $|Y_{Bh}|$ and $|Y_0|$ obtained for the sound velocity c

with the imaginary part decreased by four orders of magnitude.

PROPAGATION OF SHEAR WAVES

Note that a similar effect can appear in the case of a shear wave propagation in a medium with varying shear modulus.

To explain the experiments related to acoustic wave propagation in a shallow sea, a model was proposed [4] for a bottom composed of a sediment layer in which the shear modulus decreased as the bottom–water interface was approached. The shear modulus μ was described by the power-law function with the exponent 2ν:

$$\mu = \rho c_0^2 \left(\frac{z}{H}\right)^{2\nu}. \quad (25)$$

Here, c_0 is the velocity of a shear wave at $z = H$ and ρ is the sediment density (assumed to be constant). The shear wave propagation was investigated in a layer with this kind of depth-dependent shear modulus by assuming that the boundary conditions corresponded to the contact with a nonviscous liquid at $z = 0$ and to a hard boundary at $z = H$.

The wave equation for shear waves has the form

$$u'' + \frac{1}{\mu}\mu' u' + \frac{\rho\omega^2}{\mu} u = 0, \quad (26)$$

where the prime denotes the derivative with respect to z. The exact solution given in [4] for an arbitrary ν is expressed through the Bessel functions:

$$u = z^{1/2-\nu}\left[B_1 J_m\left(\frac{\omega}{c_0(1-\nu)}\left(\frac{z}{H}\right)^{1-\nu}\right) + B_2 Y_m\left(\frac{\omega}{c_0(1-\nu)}\left(\frac{z}{H}\right)^{1-\nu}\right)\right],$$

$$m = 2\nu - 1/[2(1-\nu)].$$

At $\nu = 1$, the index m of the Bessel functions is infinite; for this reason, this case was not considered in [4]. Let us consider this special, but interesting, case corresponding to a shear modulus varying with depth according to the quadratic law in the sediment layer:

$$\mu = \rho c_0^2 (z/H)^2. \quad (27)$$

In this case, wave equation (26) takes on a form similar to Eq. (6):

$$u'' + 2\frac{u'}{z} + \frac{\omega^2}{c_0^2}\left(\frac{H}{z}\right)^2 u = 0. \quad (28)$$

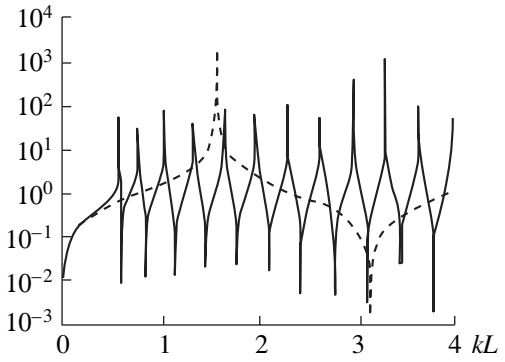

Fig. 7. Same as in Fig. 6 for a sound energy loss in liquid that is four orders of magnitude smaller.

Performing calculations similar to those described above for Eq. (6), we obtain an expression for the local wave number $k = k(z)$ in the WKB approximation:

$$k(z) = \frac{i}{z} \pm \frac{1}{z}\sqrt{\left(\frac{\omega}{c_0}\right)^2 H^2 - 1}. \quad (29)$$

The group and phase velocities of shear waves tend to zero when z tends to zero (i.e., when the sediment layer–water interface is approached), and the time T of the wave packet propagation from the initial cross section $z = H$ to the cross section $z = z_1$,

$$T = \left|\int_L^{z_1} \frac{dx}{c_g}\right| = \frac{H^2\omega}{c_0^2\sqrt{(\omega/c_0)^2 H^2 - 1}} \ln\left(\frac{L}{z_1}\right), \quad (30)$$

tends to infinity when $z_1 \longrightarrow 0$. A wave propagating from the bottom toward the sediment–water interface never reaches this interface. Thus, we obtain an effect similar to that considered above, i.e., the acoustic black hole. In this case ($\nu = 1$), the wave equation (28) for shear waves in the sediment layer also has a set of exact particular solutions in the form of power-law functions:

$$u(z) = A_\alpha (z/H)^\alpha, \quad (31)$$

$$\alpha_{1,2} = -\frac{1}{2} \pm \sqrt{\frac{1}{4} - \frac{\omega^2}{c_0^2} H^2}. \quad (32)$$

When the exponents are real, i.e., when $\omega < c_0/(2H)$, the field $u(z)$ exhibits no wave-type behavior, whereas, in the opposite case $\omega > c_0/(2H)$, the field given by Eq. (31) is a traveling wave.

CONCLUSIONS

1. We showed conceptually that there is a possibility of creating structures ensuring the total absorption of acoustic waves with the use of nonabsorbing materials only. The absorption occurs as a result of a gradual decrease in the velocity of sound along the waveguide

and the accumulation of acoustic energy at the point where the velocity vanishes.

2. In the special case corresponding to the uniform WKB asymptotics for such a retarding structure with varying parameters, exact solutions are described by power-law functions.

3. If an acoustic black hole is truncated, the retarding structure causes a sharp decrease in the resonance frequencies.

4. A similar effect can be observed for shear waves propagating in a medium with a varying shear modulus.

REFERENCES

1. M. A. Isakovich, *General Acoustics* (Nauka, Moscow, 1973).
2. M. A. Mironov, Akust. Zh. **34**, 546 (1988) [Sov. Phys. Acoust. **34**, 318 (1988)].
3. M. A. Mironov, in *Proceedings of XI All-Union Acoustic Conference, Moscow, 1991*, Section L, p. 23.
4. O. A. Godin and D. M. F. Chapman, J. Acoust. Soc. Am. **106**, 2367 (1999).

Translated by A. Vinogradov

Acoustical Physics, Vol. 48, No. 3, 2002, pp. 353–358. Translated from Akusticheskiĭ Zhurnal, Vol. 48, No. 3, 2002, pp. 406–411.
Original Russian Text Copyright © 2002 by Pankova, Tuzhilkin.

Errors in the Determination of the Amplitude and Arrival Times of Acoustic Pulses under Their Incomplete Resolution

S. D. Pankova and Yu. I. Tuzhilkin

Andreev Acoustics Institute, Russian Academy of Sciences, ul. Shvernika 4, Moscow, 117036 Russia

e-mail: bvp@akin. ru

Received May 22, 2001

Abstract—By the example of two overlapping pulses with a sinusoidal carrier and a gaussian envelope, errors in the determination of their amplitudes and positions on the time axis as functions of the extent of their overlapping are investigated. It is shown that, in the case of a considerable overlapping, the errors in the amplitude determination can exceed 100% (the pulses disappear); the greatest shifts of the maxima of the pulse envelopes are of the order of their half-width in the case of a half-pulse overlapping. *© 2002 MAIK "Nauka/Interperiodica".*

Most problems of experimental acoustics are associated with the measurements of the amplitudes and propagation times of signals. In simple cases of one-way propagation, these parameters are determined from the maxima of the envelope at the output of a filter matched with a probing signal [1]. The same approach can be used in the case of a multipath propagation, if the difference in the arrival times of the signals along different rays is greater than the inverse width of the signal spectrum. Difficulties arise in the experiments with relatively narrow-band signals, when the pulses at the output of the receiving filter more or less overlap. The determination of their arrival times from the envelope maxima becomes inapplicable, and more complicated processing procedures are needed. Among them, the most natural one is the procedure of the extension of the spectrum of the received signal [2]. The reception of wider band signals allows one to increase the resolution capability. The price for such an increase is the reduced noise stability of the reception and, as a consequence, higher power radiators are needed. It is shown [3] that, for tracing the variations of the signal propagation times over several paths, it is often more expedient to use the phase of the carrier frequency rather than the envelopes of the received signals. However, the problem of the exact determination of the arrival times at the beginning of tracing is still unsolved. A finer procedure of measurements is proposed in [4, 5]. It is based on the fact that the spectrum of a total signal arriving over several paths is modulated by frequencies proportional to the difference in the propagation times. These differences can be determined by calculating the spectrum of the logarithm of the initial spectrum (the cepstrum). It is clear that, for small time differences, the spectrum of a probing signal must be rather wideband to cover a sufficient number of modulation periods.

A more general approach to the solution of this problem is given in [6]. The amplitudes and arrival times of N overlapping pulses are determined as the greatest maximum of the likelihood function in the $2N$-dimensional space of the signal amplitudes and their propagation times. However, because of cumbersome calculations, this procedure is seldom used. In most experiments [7–14], the pulse amplitudes and arrival times are measured from the envelopes in spite of their partial overlapping. Such an approach is also promoted by the possibility of enhancing the signal-to-noise ratio by means of a signal accumulation over many series of measurements under conditions when the accumulation by the carrier frequency is ineffective because of the fluctuations.

The question arises as to the magnitude of errors in the determination of the signal amplitudes and arrival times from the maxima of the envelope of partially overlapping pulses at the output of the receiving filter. In this paper, we consider this problem for two pulses of different amplitudes with different degrees of overlapping.

The form of the first pulse is

$$y_1(t) = a_1 \exp\left[-\frac{\Delta t^2 (n-n_1)^2}{(\Delta t n_0)^2}\right] \cos 2\pi \frac{\Delta t}{T}(n-n_1), \quad (1)$$

where T is the period corresponding to the carrier frequency, a_1 is the pulse amplitude, Δt is the time step between signal samplings, and n is the number of the current reading. The pulse maximum corresponds to $n = n_1$, and the pulse half-width at the level $1/e$ is determined by $\Delta t n_0$. The second pulse $y_2(t)$ differs from the first one only by the amplitude a_2 and the position of the maximum, n_2.

The envelope of the sum of the pulses is calculated by the formula

$$Y(t) = \sqrt{[y_1(t) + y_2(t)]^2 + [\tilde{y}_1(t) + \tilde{y}_2(t)]^2}. \quad (2)$$

1063-7710/02/4803-0353$22.00 © 2002 MAIK "Nauka/Interperiodica"

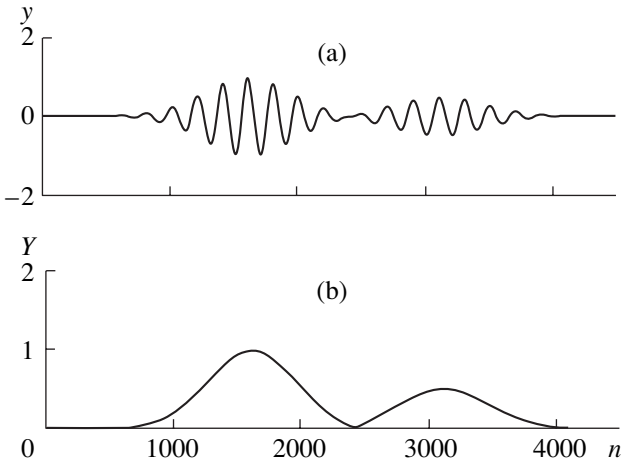

Fig. 1. (a) Form of the pulses in the case of a small overlapping and (b) the form of their envelopes.

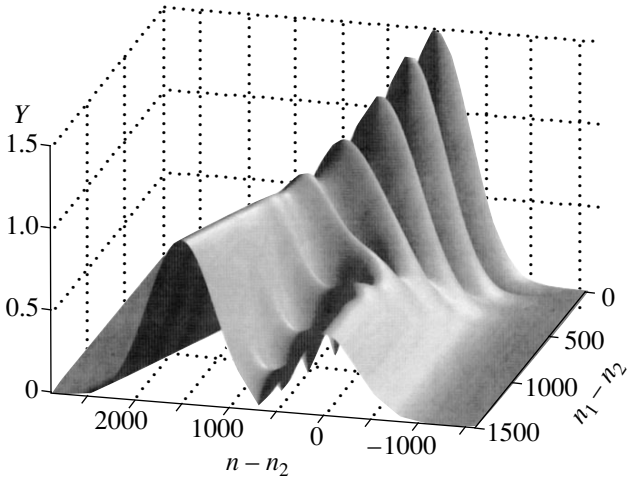

Fig. 2. Envelope of the sum of pulses with amplitudes equal to 1 and 0.5 as a function of the extent of their overlapping.

As $\tilde{y}_1(t)$ and $\tilde{y}_2(t)$, we took signals in the form of Eq. (1) with the cosines replaced by the sines of the same argument. The total signal for resolved pulses $y(t)$ and its envelope $Y(t)$ are shown in Fig. 1, where $\Delta t/T = 1/200$ and $n_0 = 500$, which corresponds approximately to five periods of the carrier frequency within the width of each pulse. Such pulses are typical of experiments using radiators with a moderate quality factor. The resonance properties of the radiators usually determine the spectrum of probing signals. Bear in mind that, in the frequency domain, the duration of a pulse is the inverse of the width of its spectrum Δf. Therefore, in terms of the number of the periods of the carrier frequency f_0, our pulse duration can be written as

$$(1/\Delta f) : (1/f_0) = f_0/\Delta f = Q,$$

where Q is the quality factor of the radiator. In our case, it is close to five. It is clear that the pulse will have the same form for different carrier frequencies on the condition that the bandwidth of its spectrum is 1/5 of f_0. The form of the received pulse does not change even when the probing signal is not a pulse but the reception is performed through a filter matched with this signal and the medium is dispersion-free.

Below, for completeness, we consider also the conditions of recording a pulse whose frequency is five times higher but whose envelope has the same form. In all cases, the latter is assumed to be gaussian, so that the signals at the output of the matched filter have no side lobes. In the experiments, probing signals with a gaussian spectrum are used for this purpose.

In the calculations, the position of one pulse was fixed, while the second pulse was shifted with a step of $10\Delta t$ from the total coincidence. In the case of the overlapping of the pulses shown in Fig. 1, an interference between their carriers should occur. In a constructive interference of pulses, their total width increases. At the total coincidence of the arrival times, the signal is described by Eq. (2) with the total amplitude. In a destructive interference of pulses, a minimum is formed within the overlapping portion, and the envelope maxima move away from each other. The pattern of this phenomenon is shown in Fig. 2. It was calculated for two pulses with the amplitudes equal to 1 and 0.5. The amplitude of the envelope of their sum is presented as a function of both the current time (in terms of the number of readings, starting from $n = n_2$) and the difference $n_1 - n_2$ between the positions of the maxima of both pulses in the absence of interference. When this difference is zero, the envelope of the total pulse with the amplitude equal to 1.5 is similar to that of a single pulse. As the difference $n_2 - n_1$ increases, the largest pulse moves away to the left, almost up to the complete resolution. In this case, the total pulse expands, and then a small maximum is singled out of it. It is significant that its separation begins when dips appear between the largest maxima. The dips between maxima along the time axis are visible only in the front part of Fig. 2.

Now, we consider the interaction between the pulses depending on the distance between them, $n_2 - n_1$, for various amplitude relations, a_1/a_2. The results of calculating the magnitude and position of the maximum of the envelope of the test pulse are presented in Figs. 3–5. The amplitude of the test pulse was assumed to be equal to unity, while that of the second pulse was 0.1, 0.5, and 0.95. The true position of the test pulse corresponds to the value $n_1 = 1$; the position of the second pulse varies from $n_2 = 1$ up to $n_2 = 1100$, which corresponds to the complete resolution. The plots represent (a) the amplitude and (b) the shift of the maxima of the envelope of the test pulse as functions of the position of the second pulse, where the shift is measured with respect to the

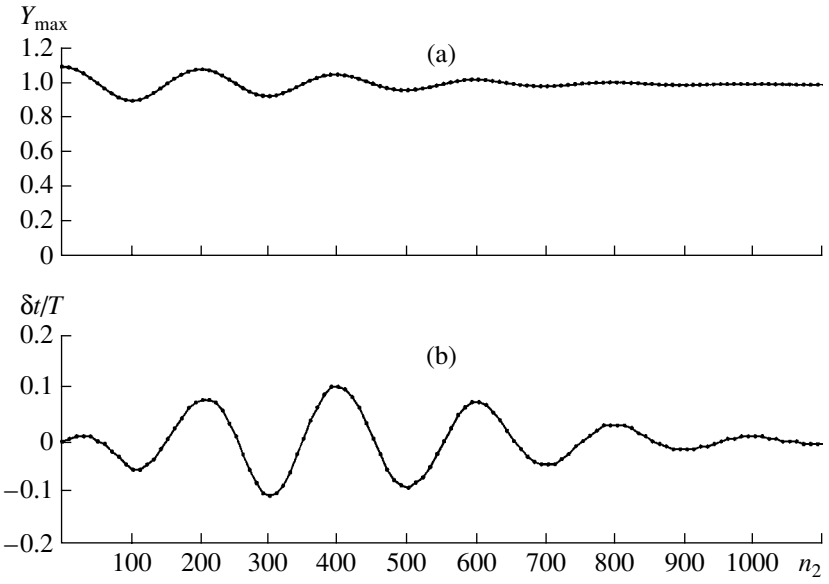

Fig. 3. (a) Amplitude and (b) position of the maximum of the envelope of the basic pulse as a function of the position of the second pulse. The amplitude of the second pulse is 0.1 of the basic pulse amplitude.

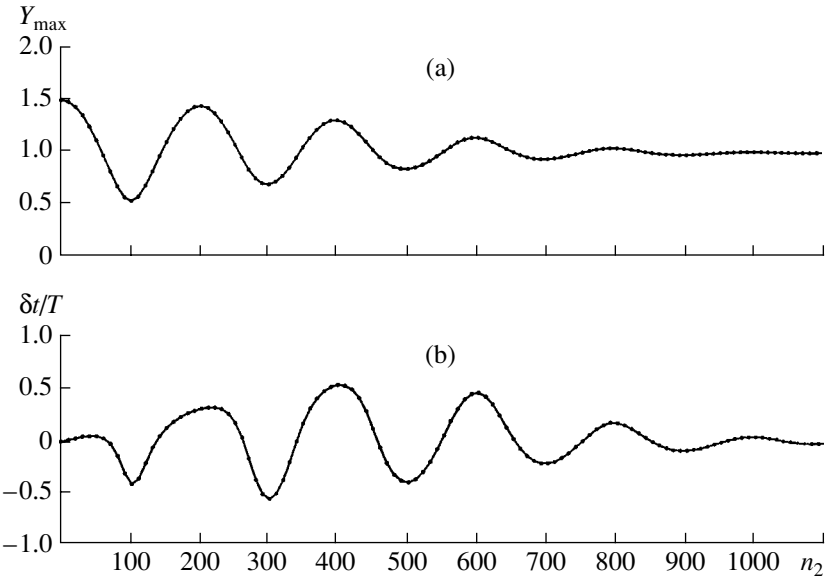

Fig. 4. The same as in Fig. 3 for the amplitude ratio 1 : 0.5.

true position and expressed in terms of the number of the periods of the carrier frequency, $\delta t/T$. As can be seen, its amplitude varies from 1.5 for $n_2 = n_1$ to 1 at the complete resolution. In this case, for a small amplitude of the second pulse, the envelope oscillations have a symmetric form. However, the symmetry is violated when both pulses have almost equal amplitudes.

As for the shift of the envelope maximum, the situation is more complicated. When the amplitude of the second pulse is an order of magnitude smaller than that of the basic pulse, the largest shift of the basic pulse (0.1 of the period of the carrier frequency) is observed for an approximately half-pulse overlapping. In this case, the oscillations of the shift of the envelope maximum are in phase with the amplitude variations. When the shifts are small, the influence of the second pulse is weak due to the considerable difference in the pulse amplitudes. The influence increases when the second pulse position corresponds to the slope of the basic pulse and then again decreases under an almost complete resolution. When the pulse carriers are combined in phase, the maxima of the pulses come closer

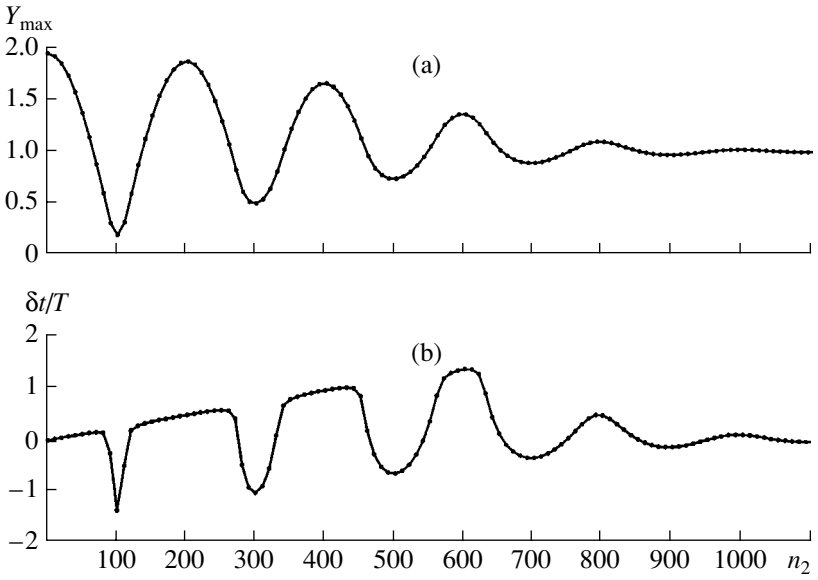

Fig. 5. The same as in Fig. 3 for the amplitude ratio 1 : 0.95.

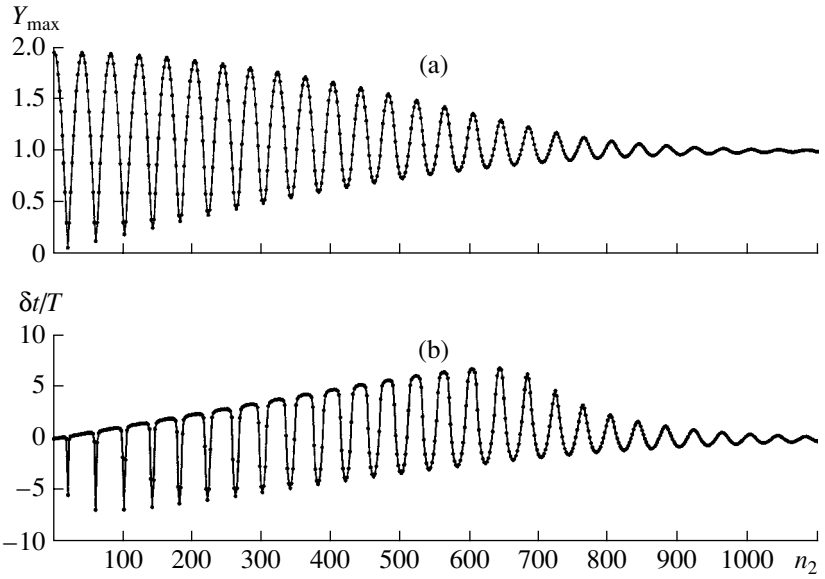

Fig. 6. The same as in Fig. 3 for the carrier frequency increased by a factor five and the amplitude ratio 1 : 0.95.

together, and when the carriers are in antiphase, the maxima move away from each other.

When the pulse amplitudes are close in magnitude, the oscillation form of the shift of the envelope maximum becomes more complicated (Fig. 5b). As the second pulse moves away, the shift of the first pulse increases almost linearly. The increase is periodically interrupted by sharp dips whose width increases as the pulses become more widely separated. The maximal shift, close to 1.5 periods of the carrier frequency, is observed for $n_2 = 600$. If we imagine both pulses on the time axis, we can easily see that, according to Eqs. (1) and (2), the unperturbed pulse envelope is equal to 0.24 in this case, and the pulses overlap at a level of 0.7.

The increase in errors that occur in the resolution of higher frequency pulses is illustrated in Fig. 6. As compared to Fig. 5, the pulses differ only in carrier frequency, which is five times higher, with the same envelope. As can be seen, the greatest shift of the maximum toward the second pulse is observed for the same value $n_2 = 600$ and equals 7.5 periods of the five times higher frequency. When the pulses are combined in antiphase, narrow segments (which are then extended) of the shifts

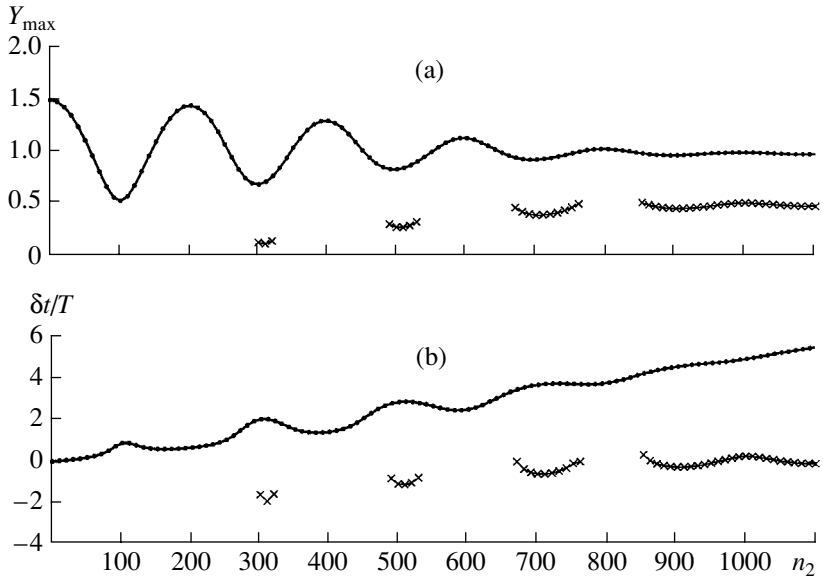

Fig. 7. (a) Amplitudes and (b) position of the maximum of the envelope for the amplitude ratio of interfering narrow-band pulses 0.5 : 1.

with the same magnitude but in the opposite direction are observed.

In some problems, one needs to measure the position of a pulse whose amplitude is not maximal. In this case, pulses with higher amplitudes play the role of noise. To estimate their influence, we carried out calculations for pulses with amplitudes equal to 0.5 and 1 and with low-frequency carriers. The results are presented in Fig. 7. Here, in contrast to Fig. 4, the pulse with the small amplitude is the fixed one. Figure 7a presents the amplitudes of both pulses: the small pulse (crosses) and the large pulse (dots); Fig. 7b shows the positions of the maxima of their envelopes. As one can see, when the overlapping is considerable, the large pulse has a predominant effect over the small pulse: the latter is virtually invisible. It begins to manifest itself first in short time intervals with strongly distorted amplitude values (0.125 instead of 0.5) and positions on the time axis (two periods of the carrier frequency instead of zero). One can also notice the inverse effect of the small pulse on the large one. The amplitude and position of the maximum of the large pulse envelope oscillate around the true values. The amplitude of these oscillations is nearly half as large as that for the small pulse. On the segments where the small pulse exists, the oscillations of the pulse amplitudes are in phase, whereas the shifts in time are in antiphase.

Let us summarize the results. The determination of the amplitudes and arrival times of signals from the magnitude and positions of the maxima of the pulse envelopes at the output of the receiving filter matched with the transmitted signal of an arbitrary form leads to errors when the pulses overlap. The errors in the amplitude estimates are maximal in the case of an almost complete overlapping of the pulses. For the arrival times, the errors are maximal when the overlapping is at the half-width of the envelope of the pulses. The error is not too large when the interfering pulse is small. In contrast, when the interfering pulse is close to the pulse under test, the errors in the amplitude estimates for a strong pulse overlapping approach 100% and decrease when the pulses become separated. As for the errors in the arrival times, they increase when the pulses move away from each other, and they reach the half-width of a pulse for a half-pulse overlapping. When the overlapping is strong, narrow negative spikes of errors are observed, which are due to the destructive interference of the pulses. For a half-pulse overlapping, errors that overestimate the signal propagation times are most probable. When the interfering pulse is larger than the pulse under test, the latter is visible only when destructive interference of the overlapping pulses takes place. The errors in the determination of the arrival times of the small pulse increase in this case.

REFERENCES

1. C. W. Helstrom, *Statistical Theory of Signal Detection* (Pergamon, New York, 1960; Inostrannaya Literatura, Moscow, 1963).

2. T. G. Birdsall and K. Metzger, Jr., J. Acoust. Soc. Am. **79**, 91 (1986).

3. V. R. D'yachenko and Yu. I. Tuzhilkin, Akust. Zh. **42**, 202 (1996) [Acoust. Phys. **42**, 176 (1996)].

4. V. A. Zverev, A. A. Pavlenko, A. D. Sokolov, and G. A. Sharonov, Akust. Zh. **47**, 76 (2001) [Acoust. Phys. **47**, 62 (2001)].
5. V. A. Zverev and A. A. Stromkov, Akust. Zh. **47**, 657 (2001) [Acoust. Phys. **47**, 572 (2001)].
6. J. E. Ehrenberg, T. E. Ewart, and R. D. Morris, J. Acoust. Soc. Am. **63**, 1861 (1978).
7. A. R. Kozel'skiĭ, A. A. Mazannikov, A. A. Migulin, *et al.*, Akust. Zh. **39**, 854 (1993) [Acoust. Phys. **39**, 451 (1993)].
8. A. V. Kulakov and R. Yu. Popov, Akust. Zh. **46**, 671 (2000) [Acoust. Phys. **46**, 588 (2000)].
9. P. F. Worcester, B. D. Cornuelle, J. A. Kuldebrant, *et al.*, J. Acoust. Soc. Am. **95**, 3118 (1994).
10. P. N. Mikhalevsky, A. N. Gavrilov, and A. B. Baggeroer, IEEE J. Ocean. Eng. **24** (2), 183 (1999).
11. D. E. Norris, J. L. Spiesberger, and D. W. Merdes, J. Acoust. Soc. Am. **103**, 182 (1998).
12. J. A. Simmen, S. M. Flatte, H. A. DeFerrari, *et al.*, J. Acoust. Soc. Am. **105**, 3231 (1999).
13. P. F. Worcester, B. D. Cornuelle, M. A. Dzieciuch, *et al.*, J. Acoust. Soc. Am. **105**, 3185 (1999).
14. J. A. Colosi, E. K. Scheer, S. M. Flatte, *et al.*, J. Acoust. Soc. Am. **105**, 3202 (1999).

Translated by Yu. Lysanov

Acoustical Physics, Vol. 48, No. 3, 2002, pp. 359–370. Translated from Akusticheskiĭ Zhurnal, Vol. 48, No. 3, 2002, pp. 412–424.
Original Russian Text Copyright © 2002 by Shvachko.

Long-Term Stability of the Sound Field Structure in the Central Part of the Eastern Atlantic

L. V. Shvachko

Andreev Acoustics Institute, Russian Academy of Sciences, ul. Shvernika 4, Moscow, 117036 Russia

e-mail: bvp@akin.ru

Received May 24, 2001

Abstract—Results of studying the angular and energy structures of the sound field formed in the first convergence zone as a result of the transmission of a continuous pseudonoise signal in the frequency range 0.8–1.5 kHz are presented for the case of the corresponding points lying in the upper ocean layer at depths between 150 and 500 m. The sound field characteristics were studied with the use of omnidirectional and narrow-beam (~2°) reception in the vertical plane. The variability of the basic experimental parameters of the field structure is analyzed using the data of three experiments carried out in the eastern part of the Atlantic Ocean, near the Canary Islands, over a period of 11 years. The experimental results are compared with ray calculations. It is shown that, in the region under investigation, the experimental characteristics of the field structure are relatively stable and the extent to which they agree with the calculated parameters is also stable. In addition, some data are presented to illustrate the effect of a small lens of Mediterranean water, which manifests itself in sound velocity variations at the channel axis, on certain field characteristics. © *2002 MAIK "Nauka/Interperiodica".*

In an experimental study of a sound field structure, one of the central problems is to determine the degree of agreement between the measured values and the corresponding parameters calculated using a model of sound propagation in the ocean. In addition, for acoustic forecasting, an essential point is the evaluation of the stability of the estimates obtained for the aforementioned agreement in different hydrological conditions.

After many years of oceanic investigations, researchers from the Andreev Acoustics Institute, Russian Academy of Sciences, have collected and analyzed a large body of experimental data on the basic parameters of the sound field structure in different regions of the ocean all over the world. The main body of experimental data on the angular and energy characteristics of sound fields in the ocean was obtained with the use of noise signals in the frequency range 0.5–5.0 kHz. For this reason, the most appropriate theoretical model for a computational analysis of the sound propagation was the ray model [1, 2]. Such an analysis showed that, in some situations, there is a discordance between the theoretical model and the measured field structure, the difference between them being observed not only for the elements of the fine structure, but also for the average characteristics of the structure [2–6]. The magnitude of this discrepancy essentially depends on the hydrological conditions and, for this reason, it is different in different regions of the ocean. For the average energy and angular characteristics of the field, including the case of relatively long paths, the best coincidence of experiment and calculation occurs for the regions characterized by sound velocity profiles $C(z)$ of tropical and subtropical types, i.e., in the presence of a single underwater sound channel whose axis lies at depths of 800–1000 m. However, even for this class of hydrological conditions, the best correspondence between the measured and calculated parameters occurs in regions of subtropical type, where the curve $C(z)$ is smoother in the upper ocean layers at depths of the thermocline.

In this paper, we present the results of studying the angular and energy structure of the field on the basis of the data obtained at different times in the eastern part of the Central Atlantic, i.e., in the region characterized by a subtropical type of sound velocity profile. In the conditions corresponding to the best agreement between the theoretical model and the experimental results, we quantitatively estimate their correspondence and analyze the long-term variability of individual parameters of the field structure. Similar problems concerning the stability of acoustic multipath in long-range propagation at the Western equatorial Pacific are considered in [7].

The experiments were carried out in three adjacent regions near the Canary Islands in 1980, 1988, and 1991. Figure 1 shows the hydrological characteristics of the regions of investigation and their geographic location. Figure 1b shows a map fragment, where the dots, crosses, and circles mark the experimental sites in the first, second, and third regions of investigation (1980, 1988, and 1991, respectively). One can see that all experimental regions are located near the meridian 24° W with a scatter of about 2° and, from south to north, they fall within an interval of about 7° (from 30° to 23° N). The sound velocity profiles for these regions are shown in Fig. 1a by the solid, dotted, and dashed lines, respectively, on a single scale for the whole depth

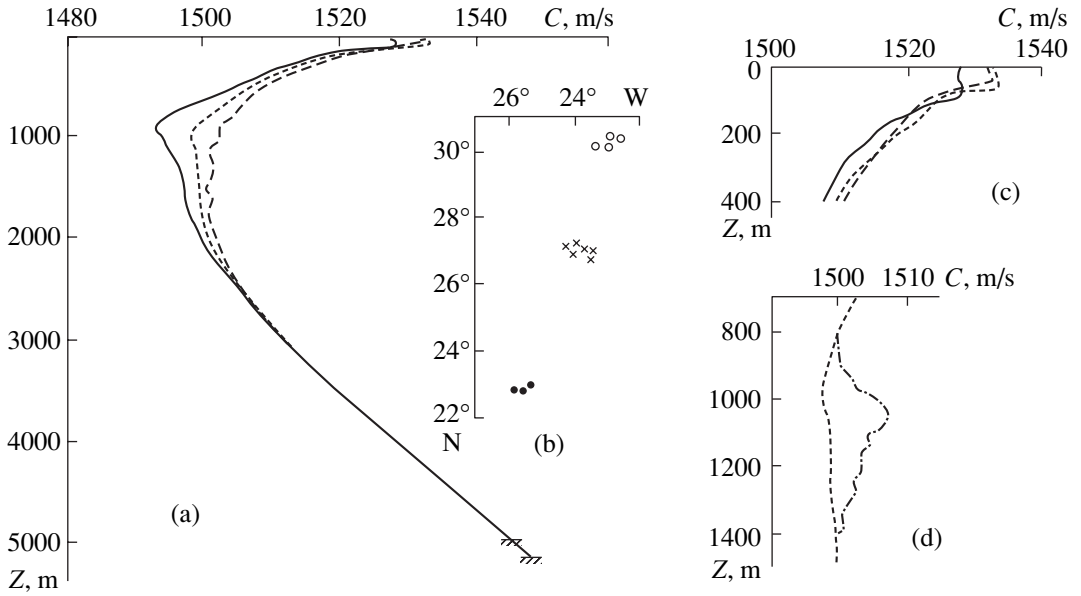

Fig. 1. Hydrological and geographic characteristics of the experimental regions: (a) the sound velocity profiles $C(z)$ in the first, second, and third regions (the solid, dotted, and dashed lines, respectively); (b) a map fragment with the experimental regions indicated; (c) the profiles $C(z)$ for the upper 400-m layer of the ocean; and (d) the change in $C(z)$ near the channel axis in the second region because of the lens of Mediterranean water.

range. Figure 1c shows in more detail the profiles $C(z)$ in the upper 400-m layer using the same types of lines. From Figs. 1a–1c, it follows that all three profiles $C(z)$ are close in their parameters. A weak surface channel is available for all regions in the upper mixed layer at depths of 50–80 m. For depths of 100–500 m, a fairly smooth discontinuity layer characteristic of subtropical-type profiles $C(z)$ is observed. In all cases, the channel axis is located at a depth varying from 900 to 1400 m. However, some regional and seasonal features also take place. The regional features are related to the fact that the farther south the region of investigation was, the more prominent the sound channel was, the shallower its axis, and the smaller the sound velocity at the channel axis (Fig. 1a). Seasonal variations occurred only in the uppermost surface layer (Fig. 1c), and they were caused by the fact that the water mass was warmer in November (the time of experiments in the second and third regions) than in March (the time of the experiment in the first region). Despite the above regional and seasonal features, the spatial distribution of the sound field behavior was generally the same, with clearly defined alternating shadow and convergence zones in all cases. For a source located at a depth of 200 m, the turning depth of the rays (this parameter specifies the location of the convergence zones) varied within only 250 m (from 3200 to 3450 m) for all three profiles $C(z)$, which means that the convergence zones were formed by rays propagating in the same ocean layers in all three cases. The above regularities offer an opportunity to consider these three different, but adjacent regions as a single combined region. In this case, the results obtained for the sound field structure in these regions can be considered as the manifestation of the variability of the field characteristics in the combined region within the period of investigations (11 years).

In all three regions, the experimental studies of the sound field structure were carried out according to the same procedure of experimentation in open ocean with the use of two research vessels equipped with specially designed facilities [2–6, 8]. The experiments were carried out using intense omnidirectional broadband pseudonoise sound radiation and omnidirectional and narrow-beam (~2°) reception in the vertical plane with the use of flexible extended (~40 m) arrays oriented in the vertical direction. During the measurements, the distance between the corresponding points slowly and continuously varied due to the counterdrift motion of the transmitting vessel, this distance being acoustically controlled [9] every minute. Owing to this fact, the distance between the points of transmission and reception (and not between the research vessels) was determined in the system of unified time by measuring the time (within 1 ms) during which a short pulse added to the noise signal under study traveled along the ray until it was received at some angle with the narrow-beam array. Then, the distance in question was calculated using the data on the profile $C(z)$ and, hence, on the sound velocity along this ray. The measurement error was about several tens of meters (~20 m).

Of the large body of experimental data obtained from the complex experiments in the three regions under consideration, we present only the results concerning the angular and energy structure of the field of a pseudo-noise source in the frequency range 0.8–1.5 kHz

in the first convergence zone, when the transmission occurred in the 150–200-m layer and the reception, in the 150–500-m layer.

The experiment in the first region was carried out in March 1980 with the use of a pseudonoise source with a mean frequency of 1.25 kHz at a depth of 200 m. The field structure was simultaneously measured with two flexible extended arrays whose centers were located at depths of 200 and 450 m. As follows from the data of Figs. 1a and 1c, all corresponding points of the experiment were located immediately below the layer of the maximal sound velocity gradient. Figure 2 shows the resulting angular structure of the field for both reception depths. In these plots and all similar plots below, the distance r in kilometers is plotted along the abscissa axis, and the angle of the signal arrival in the vertical plane α in degrees is plotted as the ordinate. The minus sign corresponds to the signals arriving at the receiver from below, and the plus sign, to the signals arriving at the receiver from above. The solid lines correspond to the calculated functions $\alpha(r)$ of the field of water rays, while the dots and crosses correspond to the experimental data: the dots are the marks for the angles of arrival of signals propagating along the water rays, and the crosses are the marks for the signals propagating to the receiver along the bottom or bottom–surface reflected rays. From the curves, it follows that, in regions where the calculated field $\alpha(r)$ exists, the experimental angles of the signal arrival along water rays are in satisfactory agreement with the calculation. A disagreement occurs for distances preceding the calculated boundary of the convergence zone. For example, at the reception depth 200 m, signals with angles of arrival corresponding to the water rays were recorded beginning from distances 55.5 km and, at the reception depth 450 m, they were recorded beginning from distances 52 km, which is ahead of the calculated boundary of the convergence zone by 1.0–1.5 and 2.5 km, respectively. The first few of these signals are fairly weak and are characterized by the propagation anomaly $A = -(15–20)$ dB. Their advance relative to the calculated zone boundary, which is usually determined as the position of the caustic, cannot be treated as the measure of mismatch between the beginning of the convergence zone measured experimentally and the one calculated by the ray model. In certain regions of the ocean, the magnitude of this advance reaches 4.0–4.5 km. Some mechanisms of insonification of the shadow zone at distances preceding the ray boundary of the convergence zone are discussed in paper [10].

To determine the degree of correspondence between the experimental and calculated field parameters in terms of the ray model, we should additionally invoke the data on the energy structure. Figure 3 shows the energy structure of the field in the region of experiments for omnidirectional reception at depths of 200 and 450 m. In these plots, and all similar plots below, the distance r in kilometers is plotted on the abscissa, and the intensity I in decibels is plotted as the ordinate, the level of 0 dB corresponding to the signal level at a 1-km distance under the assumption that the signal propagates according to the spherical law. The solid curves correspond to the measured intensity $I(r)$, the dashed and dotted lines correspond to the calculated results, and the dotted-and-dashed line corresponds to the spherical law with consideration for the spatial attenuation with the coefficient $\beta = 0.028 f^{3/2}$ dB/km (0.04 dB/km for f = 1.25 kHz) [11]. The horizontal dashed straight lines shown at distances corresponding to the end of the convergence zone mark the interference level. The basic features of the energy structure of the field follow from the features of the corresponding angular structure. For the sound field structure at the depth of the sound source, such a feature is the continuous spectrum of angles of signal arrival in the range of all water rays, from –12° to +12° (Fig. 2a). As follows from the curves of Fig. 3a, the energy structure of the field at the depth of the sound source (200 m) is characterized by the maximal level of intensity with the propagation anomaly A_{max} = +24.5 dB in the middle of the zone at a distance of 59.6 km. This maximum falls in the region where the field is formed by signals corresponding to the center of the continuous angular spectrum with nearly zero-valued angles of arrival. The beginning of the convergence zone is determined by the caustic characterized by the propagation anomaly A_c = +21 dB, which is located, according to the angular structure shown in Fig. 2a, at a distance of 56.9 km, when the signals arrive at the reception point at an angle of –5°. The energy structure of the field at a reception depth of 450 m below the source depth fundamentally differs from the pattern of $I(r)$ at a depth of 200 m. As follows from the angular field structure $\alpha(r)$ (Fig. 2b), even a small difference in the depths of the corresponding points (Δz = 250 m) transforms the continuous range of angles into two discrete ranges with negative and positive angles of arrival and gives rise to an angular sector $\alpha = \pm 5°$ in which signals cannot arrive at the reception depth along water rays. Correspondingly, the energy structure of the field appears as though it is split in two halves separated by a peculiar minimum in the field intensity at the center of the zone r = 60 km with the propagation anomaly 10–12 dB. As can be seen from Fig. 3b, the beginning of the convergence zone at the 450-m depth is determined by the caustic at the distance 54.3 km with the propagation anomaly A_c = +19.5 dB; the maximal intensity A_{max} = +(21–22) dB occurs at the distance r = 57.2 km in the first half of the zone, where the field is formed by signals with negative angles of arrival. Similarly, the second half of the zone is also characterized by a relatively high intensity with the maximal propagation anomaly A_{max} = +18 dB.

The experimental energy structure agrees well with the calculation for both reception depths. As follows from the curves of Fig. 3, this agreement refers not only to the general level of the field, but also to the details in the behavior of the experimental and calculated curves

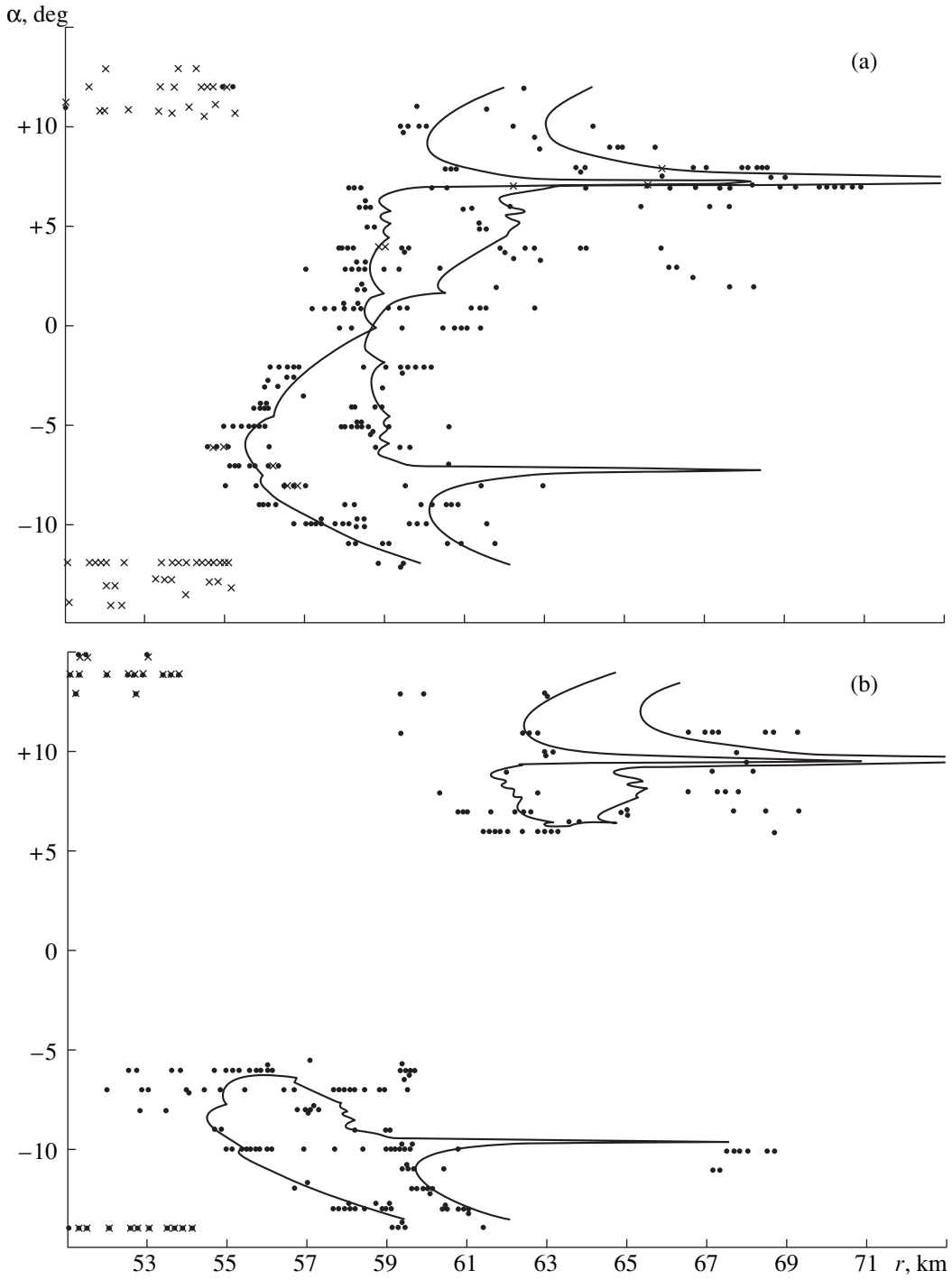

Fig. 2. Angular structure of the field in the first region for the source depth 200 m and the reception depths (a) 200 and (b) 450 m.

$I(r)$ along the entire zone. However, some relative displacement of these curves in distance is observed, and this displacement is most evident at the input in the convergence zone. The displacement magnitude Δr is not very large in this case, but it is just this quantity that serves as the measure of the mismatch between the experimental and calculated field structures in terms of the ray model. To correlate the results obtained in different regions of investigation, we should specify a procedure for determining the displacement magnitude Δr. As was shown in [6], the estimation of the experimental position of the beginning of the zone should be based on the fact that the field at the input of the convergence zone can be described by the Airy function, according to which the intensity $I(r)$ at the zone boundary in the ray approximation is by 3.5 dB lower than at the next,

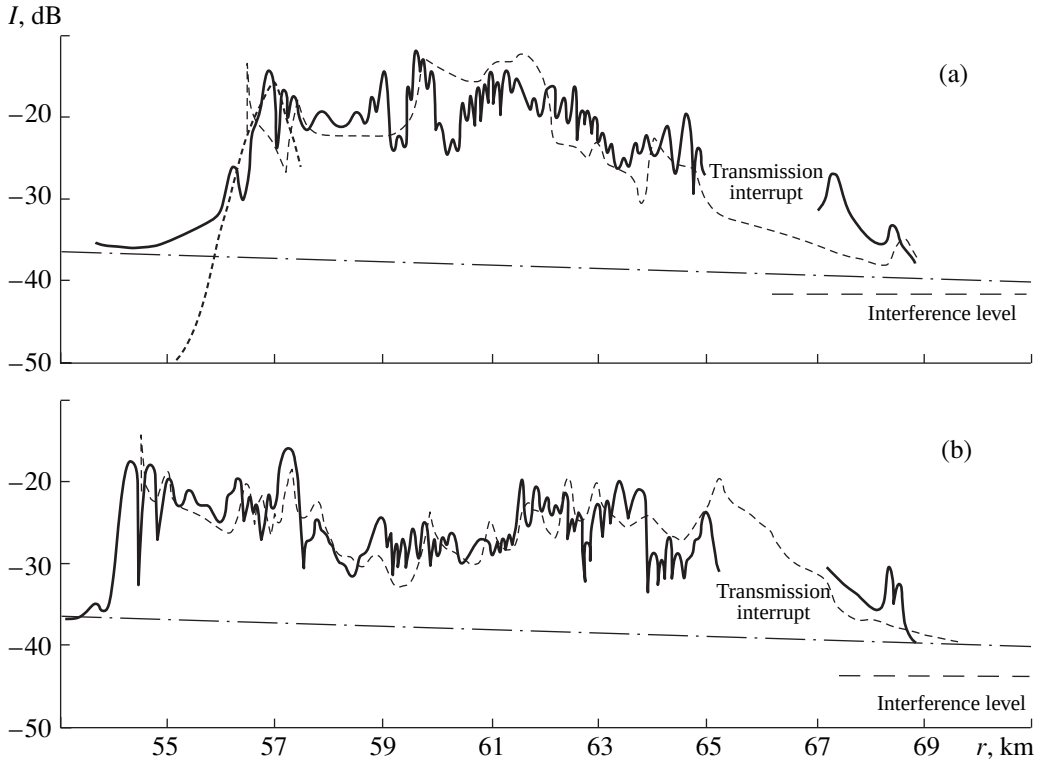

Fig. 3. Energy structure of the field in the first region in the case of an omnidirectional reception at the depths (a) 200 and (b) 450 m; the source depth is 200 m.

nearest in distance, peak at the zone input. Thus, the experimental boundary of the convergence zone is shifted toward the source in comparison with the position of the peak of $I(r)$ at the input of the zone. However, it is not always the case that the experimental behavior of $I(r)$ at the zone input is simple and can be unambiguously approximated by the Airy function.

Indeed, for the reception depth of 450 m, the experimental behavior of the intensity $I(r)$ at the zone input is simple (Fig. 3b), and, for this reason, it is a good example for the above procedure. According to this procedure, the experimental estimate of the distance to the beginning of the convergence zone is $r = 54.2$ km, i.e., 0.1 km shorter than the distance corresponding to the position of the peak of the intensity $I(r)$. According to the calculation, the beginning of the convergence zone is located at $r = 54.5$ km. Thus, the mismatch between the experiment and calculation measures $\Delta r = +0.3$ km (the plus sign corresponds to the situation when the experimental zone boundary lies at a shorter distance from the source than the calculated boundary, and the minus sign corresponds to its position at a longer distance from the source).

As for the reception depth of 200 m (Fig. 3a), the curve $I(r)$ at the input of the convergence zone exhibits a fairly complex behavior with two peaks of noticeably different intensity. As can be seen from Fig. 3a, the calculated position of the beginning of the zone is between these peaks. To refine the principal pattern of the field formation at the input of the zone, the ray calculation was compared with the calculation by the wave theory for a frequency of 100 Hz, the latter being considered as an estimator. The results of the wave calculation are given in Fig. 3a by the dotted line for distances between 55 and 57.5 km. This comparison made it possible to conclude that the beginning of the convergence zone should be identified with the second, most intense peak, starting from which the intensity of the field of water rays gradually decreases toward the shadow zone. Thus, the caustic determining the experimental estimate of the convergence zone was located at a distance of 56.8 km from the source, which is 0.1 km shorter than the distance from the position of $\max I(r)$ and 0.3 km longer than the distance from the position of the convergence zone boundary calculated by the ray theory; i.e., $\Delta r = -0.3$ km. Consequently, the parameters that characterize the degree of correspondence between the experiment and the calculation were equal in magnitude but had opposite signs. Note that the mismatch values obtained are relatively small, especially if we take into account the fact that they are determined on the most complex segment, where the mismatch between the experiment and calculation is usually maximal. Thus, the results of our analysis of the angular and energy structures of the field suggest that the experimental characteristics of the field in the region of inves-

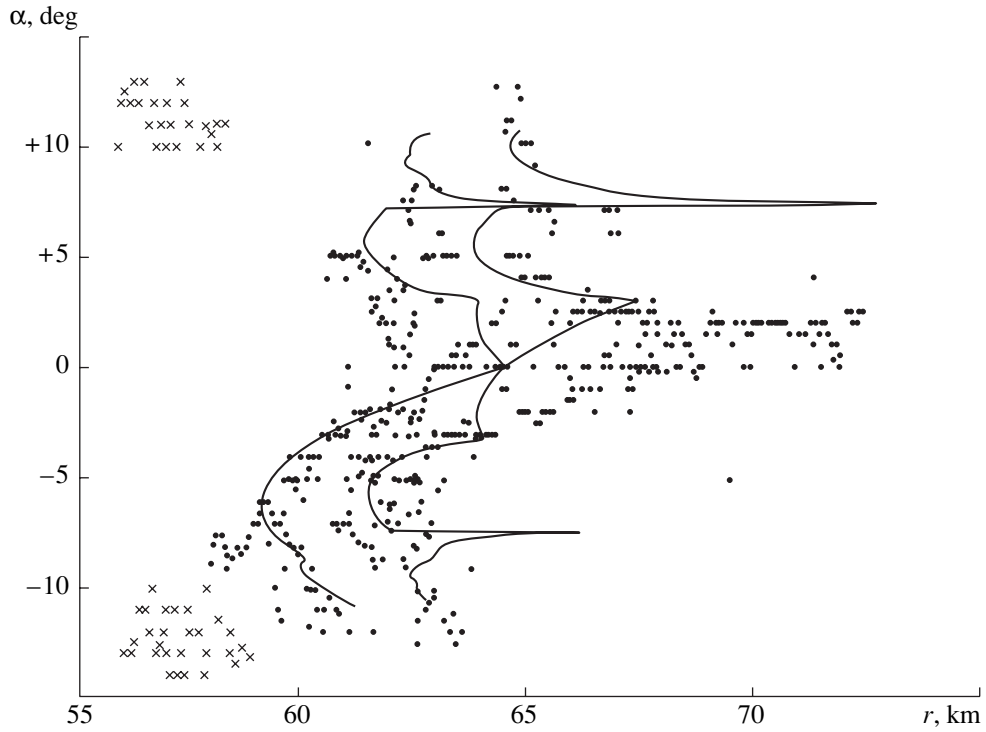

Fig. 4. Angular structure of the field in the third region for the source depth 150 m and the reception depth 150 m.

tigation agree rather well with the calculation by the ray theory.

Now, we describe the results obtained for the field structure in the third, northern region of experiments. The experiment was carried out in November 1991, using a pseudonoise source that had a mean frequency of 1.0 kHz and operated at a depth of 150 m. The field structure was measured with one extended flexible array, whose center was located at a depth of 150 m, and two omnidirectional systems positioned at the depths 250 and 500 m. According to the profile $C(z)$ given in Figs. 1a and 1c, all corresponding points were again located below the discontinuity layer. Figures 4 and 5 show the measured sound field structures, the first of which shows the angular characteristics of the field at a depth of 150 m and the second, the energy characteristics for the reception depths 150, 250, and 500 m. According to the data given in Figs. 4 and 5a, the experimentally determined field structures at the source depth in this region were almost identical with the field structures obtained in the first experimental region for transmission and reception depths of 200 m (see Figs. 2a, 3a). The maximal intensity A_{max} = +25 dB occurred in the middle of the convergence zone, at a distance of about 64 km, i.e., for distances where the sound field was formed by rays with nearly zero-valued angles of arrival. The beginning of the convergence zone was determined by signals with angles of arrival –(5°–6°) and the propagation anomaly at the caustics A_c = +20 dB. As for the correspondence between the experimental and calculated data, the calculated angular structure agreed fairly well with the measured angles of signal arrival along the entire zone. As in the first region, weak signals are ahead of the calculated boundary $\alpha(r)$ by about 1.0 km for $\alpha = -(6°–7°)$ and about 2.0 km for nearly zero-valued angles of arrival. The calculated energy structure of the field at the source depth agrees well with the experimental structure in the whole region where the calculated field exists. However, additional signals were recorded for distances exceeding 68 km, which was much greater than the calculated distance to the end of the zone. As for the beginning of the convergence zone, a perfect coincidence between the theory and the experiment occurs, i.e., we obtain $\Delta r = 0$.

From Figs. 5b and 5c, it follows that the experimental energy structure of the field for the reception depths 250 and 500 m, i.e., below the sound source, also agrees with the calculated curves $I(r)$ for all distances at which the calculated field exists. For these reception depths, the signal was again received at distances longer than the calculated distance to the end of the zone. The maximal intensity occurred in the middle of the zone and was characterized by A_{max} = +24 dB at r = 62 km for the reception depth 250 m and by A_{max} = +21.5 dB at r = 60.6 km for the reception depth 500 m. For distances 63.5–64.5 km, i.e., for distances at which rays with angles $\alpha = \sim 0$ formed a peak in intensity $I(r)$ at the reception depth 150 m, some decrease in the intensity level occurred at the reception depth 250 m, and this decrease was caused by the absence of signals with nearly zero-valued angles of arrival in the angular spec-

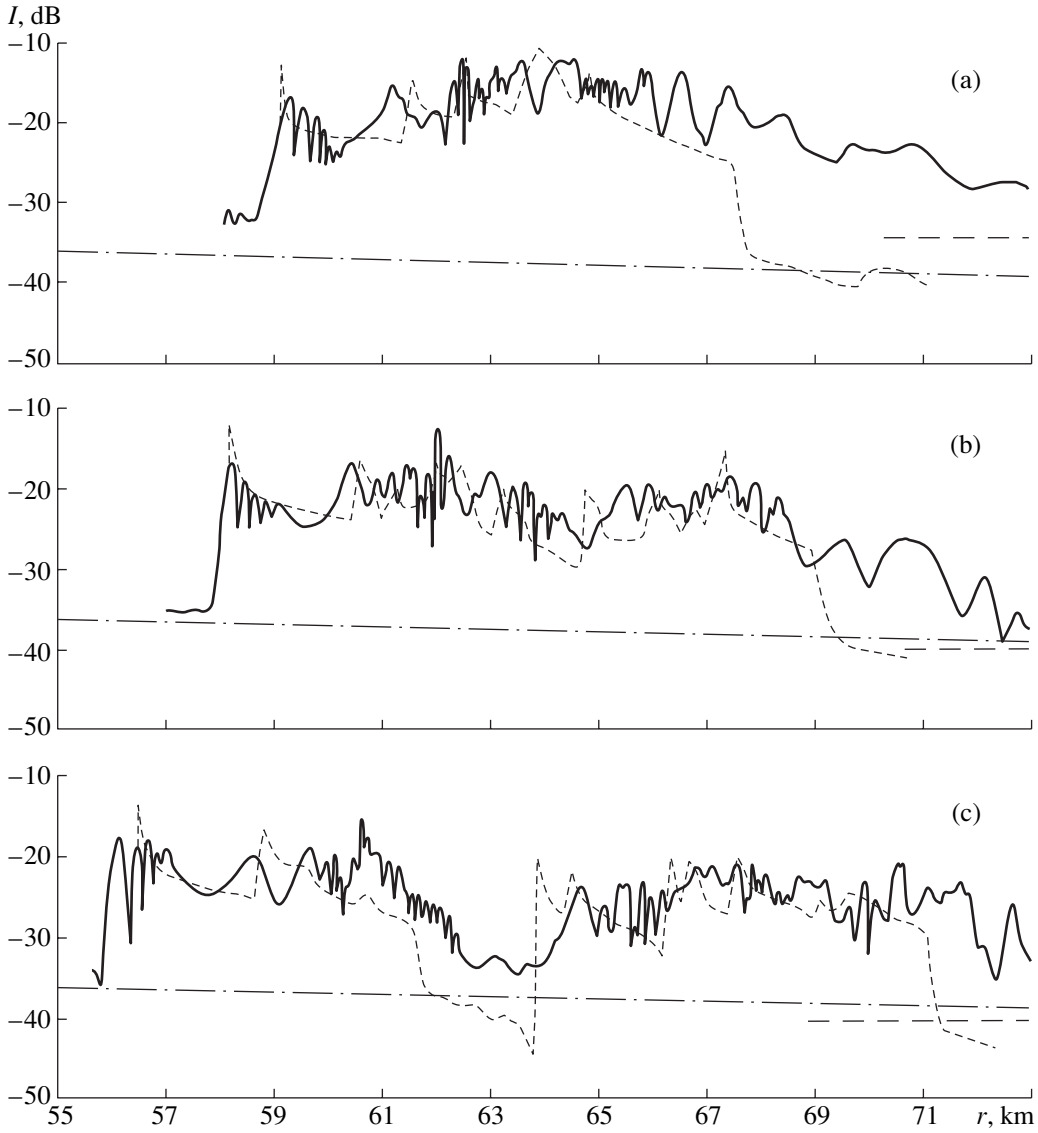

Fig. 5. Energy structure of the field in the third region in the case of an omnidirectional reception for the source depth 150 m and the reception depths (a) 150, (b) 250, and (c) 500 m.

trum. At the reception depth 500 m, the intensity in the middle of the zone decreased essentially because of the expansion of the angular sector around $\alpha = 0$, where no signal was present. This effect leads to the splitting of the convergence zone (both experimental and calculated) into two halves. For these reception depths characterized by the propagation anomalies at caustics A_c = +20 dB and A_c = +19 dB, respectively, an analysis of the degree of correspondence between the experimental and calculated distances to the beginning of the convergence zone showed that there is fairly good agreement with Δr = +0.1 km for the depth 250 m, whereas, for the depth 500 m, the difference between the experiment and the theory increases to Δr = +0.45 km. Thus, in this region of investigation, the experimental boundary of the beginning of the first convergence zone was located near the calculated boundary by either coinciding with it or being in advance of it so that the magnitude of the advance was the greater the deeper the reception point.

The experiment in the second region of investigation was carried out in November 1988 with the use of a pseudonoise source with the mean frequency f = 1.25 kHz at a depth of 200 m. The signals were simultaneously received with two vertical arrays, whose centers were located at depths of 180 and 220 m, and an omnidirectional system at a depth of 500 m. As in the above experiments, all corresponding points were again located below the continuity layer (see $C(z)$ in Figs. 1a, 1c). However, in this experiment, the structure of the field was investigated somewhat above (180 m) and somewhat below (220 m) the source depth, rather than at the source depth exactly. Figure 6 shows the resulting

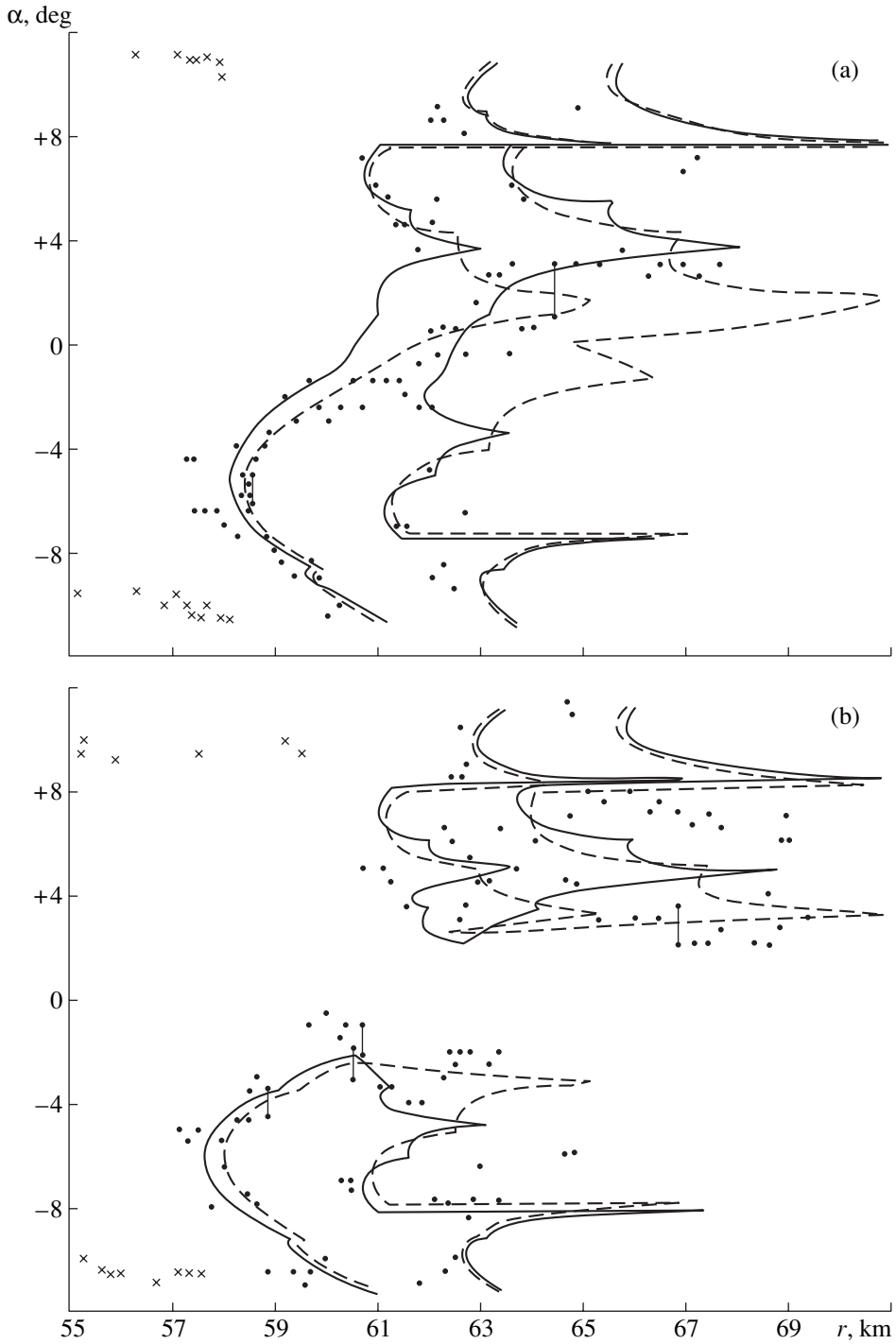

Fig. 6. Angular structure of the field in the second region for the source depth 200 m and the reception depths (a) 180 and (b) 220 m.

angular structure of the field, and Fig. 7 shows the resulting energy structure for the depths 180, 220, and 500 m (Figs. 7a–7c, respectively). In this experiment, it was possible to measure every 10–12 h the energy structure of the field at the reception depth 500 m with the use of omnidirectional reception for two transmissions through the first convergence zone. Figure 7c shows these two experimental realizations of $I(r)$ by heavy solid and dashed lines, respectively.

In contrast with the two experiments above, the experimental results on the angular and energy structures of the field in this region were compared with the calculations carried out for two profiles $C(z)$. The results calculated using the typical sound velocity pro-

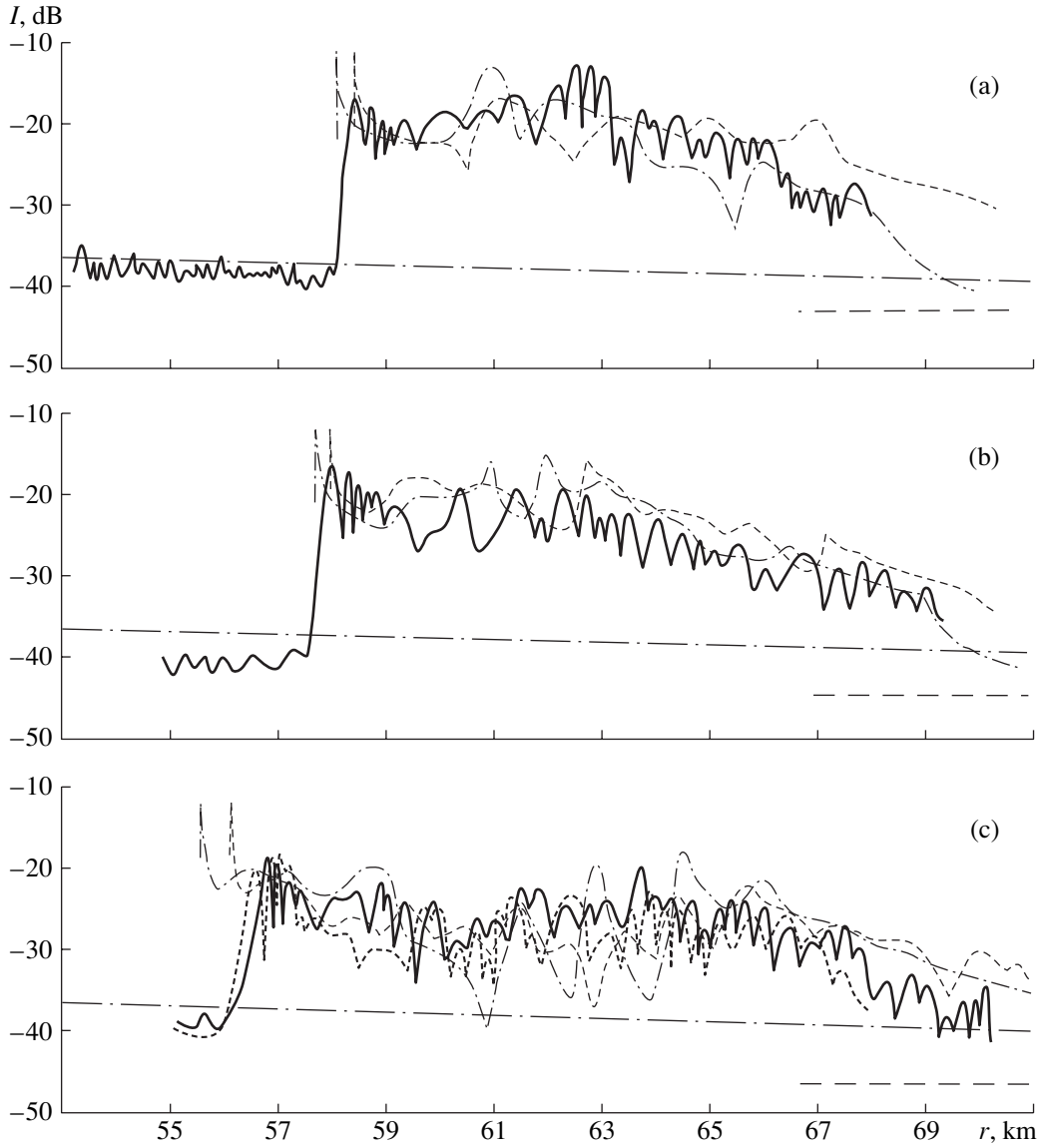

Fig. 7. Energy structure of the field in the second region in the case of an omnidirectional reception for the source depth 200 m and the reception depths (a) 180, (b) 220, and (c) 500 m.

file shown in Fig. 1a are given by solid lines for the curves $\alpha(r)$ (Fig. 6) and dotted-and-dashed lines for the curves $I(r)$ (Fig. 7). However, despite the ensemble of measured profiles $C(z)$ that consisted of nearly identical realizations, there were two profiles that showed an increased sound velocity near the channel axis. This increase in the sound velocity was caused by a lens of foreign water, namely, the saltier water that came from the Mediterranean Sea. The maximal change in the sound velocity profile $C(z)$ that occurred in one of these realizations is shown in Fig. 1d. The other realization showed only slight traces of such changes. As follows from Fig. 1d, the lens of Mediterranean water caused the maximal change in the profile $C(z)$ at the channel axis within approximately 8 m/s. This fact decreased the difference ΔC between the sound velocities at the channel axis and at the source depth ($\Delta C = \sim 21$ m/s), but it could not significantly affect the calculated pattern of the field. Nevertheless, we specially calculated the angular and energy structures of the field for $C(z)$ with the inclusion of the measured lens parameters (Fig. 1d). These results are shown in Figs. 6 and 7 by the light dashed lines.

An analysis of the experimental structure of the field in the second region of the experiment showed that its pattern is close to the corresponding patterns for two other regions. In this region, again, weak water signals were recorded at distances 1.0–1.5 km shorter than the calculated distance to the boundary of the zone. The maximal propagation anomaly $A_{max} = +25$ dB occurred in the middle of the zone ($r = 62.5$ km) at the reception depth 180 m (Fig. 7a), i.e., in the area where the field

was formed by the rays with nearly zero-valued angles of arrival (Fig. 6a). Despite the fact that the reception depth 220 m was only 20 m below the source, the interval of nearly zero-valued angles of arrival $\Delta\alpha$, which was absent in the spectrum of incoming water signals, measured 3°–4° (Fig. 6b). This reduced the maximum of the propagation anomaly in the middle of the zone to A_{max} = +19 dB (Fig. 7b). In this case, again, the energy structure of the field at the reception depth 500 m tended to split into two halves with the minimal intensity at r = 60 km, which was confirmed by both experimental realizations of $I(r)$. The maximal propagation anomaly inside both half-zones did not exceed +(16–18) dB. For all reception depths, the experimental beginning of the convergence zone was characterized, as usual, by caustics at which the propagation anomaly was A_c = +21 dB for the depths 180 and 220 m and A_c = 17–18 dB for the depth 500 m. The experimental distance to the zone boundary calculated according to these peak positions was r = 58.4 km and r = 58.0 km for the reception depths 180 and 220 m, respectively, and r = 56.7 km and r = 56.5 km for two field realizations at the reception depth 500 m.

A comparison of the experimental characteristics of the field structure with the calculated parameters obtained for the typical profile $C(z)$ shows a relatively good agreement for both angular characteristics throughout the basic range of the angles of arrival (Fig. 6) and for the total intensity level throughout the convergence zone (Fig. 7). In this case, the mismatch in the distance to the beginning of the zone was Δr = –0.25 km for the reception depths 180 and 220 m and Δr = –1.1 km and Δr = –0.9 km for the first and second field realizations at the reception depth 500 m. Thus, in the second region of investigation, the experimental boundary of the beginning of the zone was at longer distances than the calculated boundary for all reception depths. Summarizing the results obtained in all three experimental regions, we obtain that, in the case of the reception at a depth close to the source depth, mismatches between the experiment and the calculations are of the same order of magnitude and lie in the range $\Delta r = \pm 0.3$ km. For deeper reception (at a depth of 500 m), this measure increases slightly for the first and third regions and considerably for the second region.

Correlating the calculated functions $\alpha(r)$ and $I(r)$ shown in Figs. 6 and for different $C(z)$, we can estimate the effect of the lens on the calculated characteristics of the field structure. One can see that the differences in the calculated characteristics are mainly reduced to two effects. The first effect is related to the considerable difference between the calculated curves $\alpha(r)$ for nearly zero-valued angles of arrival. Indeed, the maximal difference between the curves calculated for the 180-m reception depth measures 4 km for rays with angles of arrival α = +1.5° (Fig. 6a). The second effect occurs in all angular and energy characteristics given above and is related to an increase in the calculated distance to the zone boundary relative to the source. Indeed, according to Fig. 7, the magnitude of this increase was 0.29, 0.30, and 0.60 km for the depths 180, 220, and 500 m, respectively. Thus, considering both effects simultaneously, we can deduce that the effect of the lens on the calculated field is reduced mainly to a certain lengthening of the ray paths, which is most prominent for rays with low grazing angles.

Despite the fact that only one of all measured realizations $C(z)$ showed a pattern characteristic of a lens, the effect of the lens on certain elements of the measured field is evident. Indeed, the effect on the angular structure follows from Fig. 6a, where the experimental points for the angles of arrival between $\alpha = -2°$ and $\alpha = -4°$ noticeably differ from the parameters calculated for typical conditions and agree much better with the curve $\alpha(r)$ calculated with consideration for the lens. No obvious effect of the lens on the energy structure of the field was observed in the convergence zone for omnidirectional reception (Fig. 7). However, the inclusion of the effect of the lens shifts the calculated beginning of the zone to longer distances from the source, which reduces the mismatches between the experiment and the theory for distances close to the zone input. For example, for the reception depths 180 and 220 m, i.e., near the source depth, we have Δr = 0 km, while, at the depth 500 m, Δr = –(0.3–0.5) km, or Δr = –0.4 km if we use the mean value of the distance to the experimental boundary of the zone for two field realizations.

In concluding the analysis of the results obtained in the second region of investigation, we again emphasize that the basic characteristics of the experimental angular and energy structures of the field are of the same order of magnitude as those in the first and third regions and agree fairly well with the calculation for the typical profile $C(z)$. Although the correction for the possible existence of a small lens slightly improves the quantitative parameters of the field structure, its basic pattern remains intact.

For estimating the long-term variability of the field structure in the whole region under investigation more descriptively, we summarized the main quantitative parameters obtained in the three above regions in two tables. Table 1 presents the maximal magnitudes of the propagation anomaly at the caustic at the input to the first convergence zone (A_c) and in the middle of this zone (A_{max}). Table 2 shows the values of the parameter Δr, which is the measure of the degree of agreement between the experimental and calculated distances to the beginning of the first convergence zone. In both tables, Z is the reception depth and Z_1 is the source depth.

From Table 1, it follows that, although the experimental data on the energy structure of the field were obtained during a long interval of time (more than 11 years), not only the basic pattern of the field structure remained intact within this period, but also the degree of the signal focusing in several parts of the first convergence zone. For example, the maximal propagation anomaly

Table 1

1	The 1st region, 1980			The 2nd region, 1988			The 3rd region, 1991		
2	Z_1 = 200 m			Z_1 = 200 m			Z_1 = 150 m		
3	Z (m)	A_c (dB)	A_{max} (dB)	Z (m)	A_c (dB)	A_{max} (dB)	Z (m)	A_c (dB)	A_{max} (dB)
4	200	221	24.5	180	21	25	150	20	25
5	–	–	–	220	21	19	250	20	24
6	450	19.5	21–22	500	17–18	16–18	500	19	21.5

Table 2

1	The 1st region, 1980		The 3rd region, 1991		The 2nd region, 1988			
2	Z_1 = 200 m		Z_1 = 150 m		Z_1 = 200 m			
3	$C(z)$ typical		$C(z)$ typical		$C(z)$ typical		$C(z)$ with the lens	
4	Z (m)	Δr (km)	Z (m)	Δr (km)	Z (m)	Δr (km)	Z (m)	Δr (km)
5	200	–0.3	150	0	180	–0.25	180	0
6	–	–	250	+0.1	220	–0.25	200	0
7	450	+0.3	500	+0.45	500	–1.0	500	–0.4
8	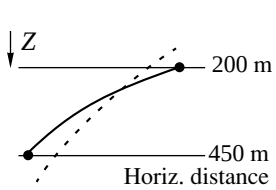		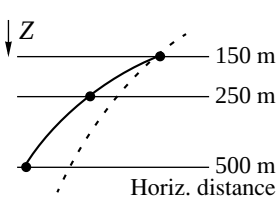		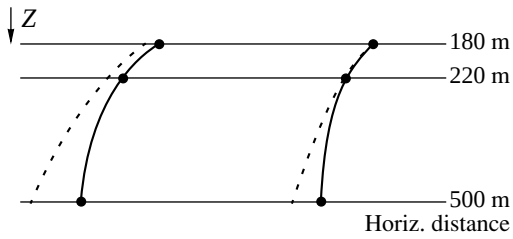			

A_{max} = +(24.5–25) dB always occurred in the middle of the zone at the depths where the field was formed by signals with nearly zero-valued angles of arrival, i.e., at the source depth or somewhat above the source depth. With a further increase in the reception depth, the level of A_{max} decreased and reached +(16–22) dB for the depths 450–500 m. For all regions, the magnitude of A_c characterizing the field level at the caustic at the input of the zone was +(20–21) dB for the depths close to the source depth and decreased to +(17–19.5) dB for the reception depths 450–500 m.

Table 2 presents the values of the measure Δr discussed earlier. From these values, it follows that the calculated and experimental positions of the beginning of the zone agreed well in the whole region under investigation. The largest mismatch between the experiment and the calculation was $\Delta r = \pm(0.3–0.45)$ km. The eighth row of Table 2 diagrammatically presents the resulting quantities Δr for every experimental region. The dashed lines correspond to the calculated boundaries of the zone for the depths used in the investigation, and the dots and lines passing through them correspond to the experimental boundaries of the zone relative to this calculation. From these diagrams, it follows that the experimental boundaries in the first and third regions have gentler slopes than the calculated boundaries. For the second region, Table 2 shows the measure Δr for two profiles $C(z)$ considered above (Figs. 1a, 1d). It is seen that the calculation with consideration for the lens better agrees with the experiment, because the lens shifts the boundary of the convergence zone to longer distances from the source, as was mentioned above. From these diagrams, it follows additionally that, contrary to other experimental regions, the experimental boundaries of the beginning of the zone in the second region have steeper slopes than the experimental boundaries for both profiles $C(z)$. According to the calculation, the profile $C(z)$ with consideration for the lens determines a steeper slope for the beginning of the zone as a function of depth then the typical profile of sound velocity. Therefore, we can suggest that it is the presence of the lens that causes the boundary of the beginning of the zone to be steeper in the second region.

A number of conclusions can be deduced from this investigation of the structure of the sound field generated in the frequency band 0.8–1.5 kHz by a continuous noise source in three experiments carried out over a period of 11 years.

The region of experiments located in the eastern part of the Central Atlantic, near the Canary Islands, should

be characterized as relatively stable during the whole time of the investigation. Both the close profiles $C(z)$ that determine the invariability of the spatial pattern of the sound field and the only slight variations of the angular and energy structures of the sound field in the first convergence zone are evidence in favor of this stability. Even the quantitative characteristics of the degree of signal focusing remain intact. Indeed, the maximal propagation anomaly was observed in the middle of the zone in all experiments with reception depths close to the source depth and was equal to +(24.5–25) dB. For deeper observation points, the propagation anomaly decreased and reached +(16–22) dB for the reception depths 450–500 m. The propagation anomaly at the caustic located at the input of the convergence zone also varied only slightly and was always in the range +(17–21) dB in the whole interval of depths under investigation (from 150 to 500 m).

A comparison of the experimental and calculated parameters of the field structure in the first convergence zone confirms their relatively good agreement for the profiles $C(z)$ of subtropical type. Indeed, the measure Δr determining the degree of mismatch between the experimental and calculated distances to the beginning of the first convergence zone did not exceed 300 m in absolute value for the reception depths close to the source depth in all experiments. With increasing reception depth, this measure tends to increase (to 450 m). Since the good agreement between the experiment and calculation is characteristic of the whole time of the investigation (11 years), we can conclude that the agreement between the experimental data and the theoretical model is stable in the region under consideration, which essentially simplifies the problem of acoustic forecasting.

ACKNOWLEDGMENTS

This work was supported by the Russian Foundation for Basic Research, project no. 00-02-17694.

REFERENCES

1. K. P. Bongiovanni, W. L. Siegmann, and D. S. Ko, J. Acoust. Soc. Am. **100**, 3033 (1996).
2. O. P. Galkin and L. V. Shvachko, Akust. Zh. **47**, 320 (2001) [Acoust. Phys. **47**, 268 (2001)].
3. O. P. Galkin, L. V. Shvachko, E. A. Kharchenko, S. D. Pankova, and A. M. Dymshits, in *Problems of the Ocean Acoustics* (Nauka, Moscow, 1984), pp. 118–133.
4. O. P. Galkin, L. V. Shvachko, E. A. Kharchenko, N. N. Komissarova, and A. M. Dymshits, in *Acoustics in the Ocean* (Nauka, Moscow, 1992), pp. 114–127.
5. O. P. Galkin and L. V. Shvachko, Akust. Zh. **44**, 192 (1998) [Acoust. Phys. **44**, 153 (1998)].
6. O. P. Galkin, E. A. Kharchenko, and L. V. Shvachko, Akust. Zh. **46**, 325 (2000) [Acoust. Phys. **46**, 274 (2000)].
7. H. Hachija, T. Nakamura, and I. Nukanj, Jpn. J. Appl. Phys., Part 1 **38** (5B), 3366 (1999).
8. L. V. Shvachko, Akust. Zh. **44**, 837 (1998) [Acoust. Phys. **44**, 729 (1998)].
9. A. V. Vedeneev, O. P. Galkin, I. S. Rogozhkin, and L. M. Filippov, Vopr. Sudostr., Ser. Akust., No. 15, 122 (1982).
10. V. S. Gostev, V. I. Neklyudov, S. D. Chuprov, L. V. Shvachko, and R. F. Shvachko, in *Acoustics of the Oceanic Medium* (Nauka, Moscow, 1989), pp. 88–97.
11. R. A. Vadov, Itogi Nauki Tekh., Ser.: Okeanol. **3**, 179 (1975).

Translated by A. Vinogradov

Acoustical Physics, Vol. 48, No. 3, 2002, pp. 371–373. Translated from Akusticheskiĭ Zhurnal, Vol. 48, No. 3, 2002, pp. 425–427.
Original Russian Text Copyright © 2002 by Kozhevnikov.

SHORT COMMUNICATIONS

Stationary Relaxation Stresses and "Domains" in a Cholesteric Liquid Crystal under the Effect of Ultrasound

E. N. Kozhevnikov

Samara State University, ul. Akademika Pavlova 1, Samara, 443114 Russia

e-mail: kozhev@ssu.samara.ru

Received July 4, 2001

The ordered structure of liquid single crystals is sensitive to acoustic and shear fields and exhibits a diversity of dissipative structures arising in sufficiently strong fields (see, e.g., [1, 2]). The effect of a homogeneous ultrasonic wave on a cholesteric liquid crystal (CLC) with the initial planar orientation is of a threshold nature and manifests itself at sound intensities exceeding a certain threshold value J_{th}. In this case, a spatially modulated domain structure of the "square lattice" type is formed in the crystal. The experimental values of J_{th} are frequency independent in the 1–10 MHz frequency range. The domain size d in a fully developed structure coincides with the size d_0 of domains formed under a static tension of the layer [3, 4].

A theoretical analysis of the domain structure in a CLC layer under the effect of ultrasound is performed in [5, 6]. The appearance of domains is explained by the oscillating vortex flows emerging in CLC due to a random periodic (along the layer) distortion of the structure, as well as by the phase lag of particle displacements in the flows due to the compression in the acoustic wave, which leads to the appearance of stationary moments and flows intensifying the initial distortion of the structure. The phase lag caused by both the viscous stresses in the oscillating flows [5] and the relaxation of the orientational order parameter [6] are taken into account.

The calculation of the domain structure in a CLC layer is performed in [5, 6] on the basis of linear hydrodynamics with the viscosity coefficients being considered as constant in the acoustic field. At the same time, the Leslie viscosity coefficients involved in the expressions for viscous stresses and moments depend on the orientational ordering of the crystal and change with it when the medium is compressed by an acoustic wave. The relaxation lag of these changes with respect to compression gives rise to stationary stresses and moments, which are not related to the oscillating flows and also can lead to observable macroscopic effects.

In this paper, the possibility of a macroscopic manifestation of the stationary relaxation stresses emerging in a cholesteric crystal in an acoustic field is considered using the example of a domain structure that is formed in a CLC layer with a planar initial alignment under the effect of ultrasound. The calculation of stationary relaxation stresses and moments is performed on the basis of a statistical analysis of the orientational molecular processes in the CLC in an acoustic field. For this purpose, the equation describing the rotation of a single molecule is written, and the corresponding microstresses are analyzed. Averaged over the angular distribution of molecular orientation, these stresses determine the contribution of relaxation processes to the viscous stresses. The averaging over the equilibrium density of the angular distribution leads to linear relations between the stresses and the strain rate in the medium, and, in particular, allows one to determine the Leslie viscosity coefficients α_k ($k \neq 4$), their dispersion in acoustic and viscous waves, the anisotropy of the sound velocity and attenuation in the crystal, etc. [7–10]. In this paper, the averaging is performed over the nonequilibrium density of the angular distribution of molecular orientation. This allows one to derive an expression for viscous stresses that includes the quadratic terms with respect to the strain rate, as well as to select the stationary component of stress. Such an approach to the nonlinear hydrodynamics of liquid crystals is applied for the first time.

Using the results of the previous publications [7, 8] and taking into account only the stationary relaxation stresses, we estimate the threshold intensity of ultrasound and the size of domains formed in the planar CLC layer at normal incidence of an ultrasonic wave. We apply the two-constant approximation for the Frank elastic energy ($K_{11} \neq K_{33} = K_{22}/\lambda$) and take the pitch P_0 of the cholesteric helix to be far less than the layer thickness h: $qh = 2\pi/P_0 h \gg 1$. The equation for the perturbations of hydrodynamic variables can be written in the form

$$\begin{gathered}
\gamma q^2 \Delta_\perp v_z \approx \Delta E \overline{\varepsilon^2} [\Sigma_{\alpha z} \Delta_\perp \theta - \Sigma_{z\alpha} \theta_{\alpha z,\, \alpha z^2}], \\
\gamma q v_z - K_{33}[(1 - \delta\delta_c)\Delta_\perp \varphi + \lambda \varphi_{2,\, zz} + 2q \langle n_\alpha \theta_{,\alpha} \rangle] = 0, \\
\gamma n_\alpha v_{z,\,\alpha} + K_{33}[\Delta\theta - q^2\theta - 2q n_\alpha \varphi_{,\alpha} \\
+ (\lambda - 1)(n_x^2 \theta_{,yy} + n_y^2 \theta_{,xx} - 2 n_x n_y \theta_{,xy})].
\end{gathered} \tag{1}$$

Here, φ and θ are the angle of molecular rotation in the cholesteric plane and the angle of departure from the

1063-7710/02/4803-0371$22.00 © 2002 MAIK "Nauka/Interperiodica"

plane; v is the flow velocity; the z axis defines the equilibrium orientation of the axis of the cholesteric helix and the propagation direction of the acoustic wave; $\alpha = x, y$; $\Delta_\perp = \partial_x^2 + \partial_y^2$; δ is the ratio of the layer extension to the critical one, δ_c, at which the CLC structure becomes unstable without external influence; and **n** is the director. In the stationary stresses involved in the right-hand side of the equation for the flows, ΔE is the local anisotropy of the elastic modulus of the CLC (i.e., the difference of the elastic moduli defined along and across the director); ε is the compression in the CLC layer under the acoustic field; the overbar means averaging over the period of the sound;

$$\Sigma_{z\alpha} \approx -1.5\left\{\frac{3}{2}\xi + (1 - d_T/7)[3(a_5 + a_6)R_{22} + 2a_1 Q]\right\};$$

$$\Sigma_{z\alpha} \approx 1.5\left\{\frac{3}{2}\xi - (1 - d_T/7)[3(a_5 + a_6)R_{22} + 2a_1 Q]\right\};$$

$$R_{22} = \langle P_2^2\rangle - \xi^2;$$

$$Q = \frac{2}{35} + \frac{3}{7}\xi - \xi^2 + \frac{108}{385}\langle P_4\rangle + \frac{18}{35}\langle P_6\rangle;$$

$P_n = P_n(\cos\psi)$ are Legendre polynomials; ψ is the angle between the long axis of the molecule and the director; the angular brackets mean the averaging over the equilibrium angular distribution of molecular orientation; $\xi = \langle P_2\rangle$ is orientational order parameter; and a_1, a_2, and a_3 are molecular parameters: $a_1 \approx 4.6$, $a_5 + a_6 \approx -1.4$ [6].

The appearance of the domain structure corresponds to the nonzero solution of the system of equations (1), this solution being periodic along the layer and satisfying the boundary conditions of zero v_z, θ, and φ. Such a solution is possible when the compression amplitude in the ultrasonic wave incident on the CLC layer exceeds a certain value ε_0. In the case when the first substrate of the CLC layer in the path of the wave is acoustically transparent and the second is rigid, the amplitude ε_0 is

$$\varepsilon_0 \approx \left[\frac{K_{33}(3 + \lambda)}{8\Delta E(\Sigma_{xz} - \Sigma_{zx})}\frac{(k^2 - k_0^2)^2 + 2(1 - \delta)k^2 k_0^2}{k^2}\right]^{1/2}. \quad (2)$$

Here, k is the wave number of the spatially modulated structure, which defines its periodicity along the layer, and $k_0 = \pi\sqrt{2/(hP_0)}\,[8\lambda(3 + \lambda)]^{1/4}$ is the wave number of the structure under the static extension of the layer.

The threshold value ε_{th} of the compression amplitude is determined by the minimization of ε_0 in k and is reached at $k = k_0$:

$$\varepsilon_{th} \approx \left[\frac{K_{33}(3 + \lambda)k_0^2(1 - \delta)}{4\Delta E(\Sigma_{xz} - \Sigma_{zx})}\right]^{1/2}. \quad (3)$$

The dependence of ε_{th} on cholesteric helix pitch and on the extension of the layer is determined by the relation $\varepsilon_{th} \sim \sqrt{(1 - \delta)/(P_0 h)}$, and its dependence on the sound frequency is determined by the anisotropy of the elastic modulus ΔE: $\Delta E \sim (\omega\tau)^2/[1 + (\omega\tau)^2]$, where τ is relaxation time of the orientational order.

Taking the typical parameters of a CLC cell to be $h = 60$ μm and $P_0 = 4$ μm and the physical parameters of the crystal to be similar to those of an MBBA nematic crystal [11, 12], at high frequencies $\omega\tau > 1$ and an extension $\delta = 0.8$, we obtain the following numerical estimates of the threshold values of the compression amplitude and the intensity of ultrasonic wave incident on the CLC cell: $\varepsilon_{th} = 0.76 \times 10^{-5}$ and $J_{th} = 0.02$ W cm^2.

Since, in the elastic energy of the CLC, we use only the terms that are quadratic with respect to perturbations, we obtain a degenerate threshold amplitude ε_{th}, at which only the wave number k of the spatially modulated structure inside the layer can be determined but not the type of the structure. With the structure of a "square lattice" type in mind, we obtain its period $d = \sqrt{2}\pi/k_0$, which is frequency independent and equal to the period d_0 of the structure formed under a static extension of the layer.

The threshold values of the sound intensity J_{th} are close to the experimental ones, and the domain size d coincides with the period of the fully developed structure observed in the experiment [3, 4]. The good agreement between the theory and the experiment indicates that the stationary stresses and moments emerging in liquid crystals in the process of structural relaxation in ultrasonic fields can play an important or even predominant role in the macroscopic hydrodynamic effects and should be taken into account in the theory of the corresponding phenomena.

ACKNOWLEDGMENTS

This work was supported by the Russian Foundation for Basic Research, project no. 00-02-17732.

REFERENCES

1. T. Mullin and T. Peacock, Proc. R. Soc. London **455**, 2635 (1999).
2. A. P. Krechov, T. Börsöoniy, P. Tóth, *et al.*, Phys. Rep., No. 337, 171 (2000).

3. A. P. Kapustin and O. A. Kapustina, *Acoustics of Liquid Crystals* (Nauka, Moscow, 1986).

4. I. N. Gurova and O. A. Kapustina, Akust. Zh. **43**, 338 (1997) [Acoust. Phys. **43**, 290 (1997)].

5. E. N. Kozhevnikov, Zh. Éksp. Teor. Fiz. **92**, 1306 (1987) [Sov. Phys. JETP **65**, 731 (1987)].

6. E. N. Kozhevnikov, in *VIII All-Russian Meeting on Theoretical and Applied Mechanics (Abstracts of Papers)* (Perm', 2001), p. 337.

7. E. N. Kozhevnikov and N. G. Dolmatova, Izv. Ross. Akad. Nauk, Ser. Fiz. **60** (4), 60 (1996).

8. E. N. Kozhevnikov and N. G. Dolmatova, Vestn. Samar. Univ., No. 2 (4), 142 (1997).

9. A. Chrzanowska and K. Sokalski, Z. Naturforsch. **18** (5), 817 (1994).

10. A. Chrzanowska, Phys. Rev. E **62**, 1431 (2000); Z. Naturforsch. **18** (5), 817 (1994).

11. E. Demus, in *Physical Properties of Liquid Crystals* (Wiley–VCH, Weinheim, 2000), Vol. 1, pp. 447–466.

12. C. A. Casto, A. Hikata, and C. Elbaum, Phys. Rev. A **17** (1), 353 (1978).

Translated by A. Kruglov

Acoustical Physics, Vol. 48, No. 3, 2002, pp. 374–375. Translated from Akusticheskiĭ Zhurnal, Vol. 48, No. 3, 2002, pp. 428–429.
Original Russian Text Copyright © 2002 by Lapin.

SHORT COMMUNICATIONS

Sound Absorption by a System of Resonators with Dissipation

A. D. Lapin

Andreev Acoustics Institute, Russian Academy of Sciences, ul. Shvernika 4, Moscow, 117036 Russia

e-mail: ras@akin.ru

Received April 18, 2001

An effective means for sound absorption is a resonance sound-absorbing structure in the form of a rigid wall to which identical resonators with dissipation are connected at small distances from each other [1–3]. The wall can be characterized by an effective impedance. At the resonance frequency, the impedance is a real quantity determined by the dissipative loss in the resonators. Assume that a plane sound wave is incident on the wall in the direction forming an angle θ with the normal to this wall. If the effective impedance is real and equal to $\rho c/\cos\theta$, where ρc is the wave impedance of the medium (air), the wave will be completely absorbed by the wall with resonators. It is of interest to consider the general problem on the absorption of a plane sound wave by a system of resonators forming a lattice with any (not small) spatial period and to determine the conditions at which this system represents an effective sound absorber.

Let the rigid wall coincide with the plane $z = 0$ and the resonators be placed at the points with coordinates $x = qL$, $y = sl$, where L and l are the lattice periods along the x and y axes, respectively, and q and s are arbitrary integers. All resonators are identical, and their dimensions are small relative to the sound wavelength. The cross-sectional area of the resonator neck is S_0. Each resonator is characterized by the impedance Z_0 equal to the ratio of the total external force acting on this resonator to its volume velocity. A plane harmonic sound wave incident on the system of resonators from the halfspace $z > 0$ is described by the pressure

$$p^{(0)} = A\exp[i(k_x^0 x + k_y^0 y - k_z^{00} z)], \qquad (1)$$

where k_x^0, k_y^0, and $(-k_z^{00})$ are the projections of the wave vector of the incident wave on the x, y, and z axes, respectively, and A is the wave amplitude. The total field formed above a rigid wall without resonators, $P^{(0)}$, is equal to the sum of the incident and reflected waves:

$$P^{(0)} = 2A\exp[i(k_x^0 x + k_y^0 y)]\cos(k_z^{00} z).$$

To determine the total field formed above a rigid wall with resonators, P, we represent it in the form $P = P^{(0)} + p^{(1)}$, where $p^{(1)}$ is the scattered field.

We denote the volume velocity of the resonator positioned at the origin of coordinates ($x = y = 0$) by V. The volume velocity of a resonator positioned at the point with the coordinates ($x = qL$, $y = sl$) is expressed as $V\exp[i(k_x^0 qL + k_y^0 sl)]$. The scattered field $p^{(1)}$ is equal to the field produced by a system of monopoles, and it satisfies the Helmholtz equation in the medium ($z > 0$) and the following boundary condition at $z = 0$:

$$\frac{dp^{(1)}}{dz} = i\omega\rho V\exp[i(k_x^0 x + k_y^0 y)] \times \sum_{q,s}\delta(x - qL)\delta(y - sl), \qquad (2)$$

where ω is the frequency of sound, $k = \omega/c$ is the wave number, ρ and c are the density of the medium and the sound velocity in it, and $\delta(x)$ is the delta-function. To calculate the scattered field, we use the Fourier method. As a result, we obtain

$$p^{(1)} = \sum_{m,n}\frac{k\rho cV}{Llk_z^{mn}}\exp[i(k_x^m x + k_y^n y + k_z^{mn} z)], \qquad (3)$$

where

$$k_x^m = k_x^0 + m\frac{2\pi}{L}, \quad k_y^n = k_y^0 + n\frac{2\pi}{l},$$

$$k_z^{mn} = \sqrt{k^2 - (k_x^m)^2 - (k_y^n)^2},$$

and the summation is performed over all integer m and n. According to Eq. (3), the scattered field $p^{(1)}$ consists of uniform and nonuniform Bragg spectra (plane waves). The spectrum (m, n) is a uniform plane wave when $(k_x^m)^2 + (k_y^n)^2 \le k^2$ and a nonuniform plane wave when $(k_x^m)^2 + (k_y^n)^2 > k^2$.

The volume velocity V can be determined from the impedance conditions at the scatterers. The structure of the scattered field is determined by the period of the scattering lattice. The field $P^{(0)} + p^{(1)}$ multiplied by $\exp[-i(k_x^0 x + k_y^0 y)]$ is a periodic function with the periods L and l along the x and y axes, respectively. Therefore, it is sufficient to satisfy the boundary condition for the resonator positioned at the origin of coordinates.

1063-7710/02/4803-0374$22.00 © 2002 MAIK "Nauka/Interperiodica"

The total external force acting on this resonator is equal to

$$-\int_{S_0}[P^{(0)} + p^{(1)}]_{z=0}dS,$$

where the integration is performed over the cross section of the resonator neck. At the resonator, the following condition is satisfied:

$$Z_0V = -\int_{S_0}[P^{(0)} + p^{(1)}]_{z=0}dS.$$

This condition can be represented in the form

$$(Z_0 + Z)V = -\int_{S_0}P^{(0)}_{z=0}dS, \quad (4)$$

where $Z = \frac{1}{V}\int_{S_0}p^{(1)}_{z=0}dS$ is the monopole radiation impedance. Taking into account Eq. (3), we arrive at the following expression for the radiation impedance:

$$Z = \sum_{m,n}\frac{k\rho c}{Llk_z^{mn}}\int_{S_0}\exp[i(k_x^m x + k_y^n y)]dxdy.$$

The real part of this impedance is called radiation resistance, and it is expressed as

$$R \equiv \mathrm{Re}\,Z \approx \sum_{m,n}{}' \frac{k\rho cS_0}{Llk_z^{mn}}, \quad (5)$$

where the prime marking the sum means that the summation is performed over all m and n for which k_z^{mn} is real.

The right-hand side of Eq. (4) is approximately equal to $-2AS_0$. Using this expression, we obtain the volume velocity of a monopole in the form

$$V = \frac{-2AS_0}{[(R_0 + R) + i(X_0 + X)]}, \quad (6)$$

where $X \equiv \mathrm{Im}Z$, and R_0 and X_0 represent the real and imaginary parts of the impedance Z_0, respectively. Substituting V in Eq. (3), we obtain the scattered field $p^{(1)}$. According to Eqs. (3) and (6), intense scattering occurs only when the reactive components of the impedances Z_0 and Z compensate each other, i.e., when the condition

$$X_0 + X = 0 \quad (7)$$

is satisfied. This condition determines the frequencies corresponding to resonance scattering. At a resonance frequency, the amplitude of a scattered uniform spectrum (m, n) is equal to

$$A^{(1)}_{mn} = \frac{k\rho cV}{Llk_z^{mn}} = -\frac{2S_0Ak\rho c}{Llk_z^{mn}(R_0 + R)},$$

where the quantity R is determined by Eq. (5).

Let the spatial periods of the lattice formed by the resonators be no greater than the half-wavelength. Then, all scattered spectra, except for the spectrum (0,0), are nonuniform, and the quantity R is equal to $\frac{k\rho cS_0}{Llk_z^{00}}$. The amplitude of the uniform spectrum (0,0) is $A^{(1)}_{00} = -\frac{2A}{1 + (R_0/R)}$. Combining the uniform reflected wave with the zero uniform scattered spectrum, we obtain a traveling uniform plane wave with the amplitude equal to

$$A + A^{(1)}_{00} = A\left[1 - \frac{2}{1 + (R_0/R)}\right].$$

In the case $R_0 = R = \frac{k\rho cS_0}{Llk_z^{00}}$, the amplitude $A + A^{(1)}_{00}$ is zero. This means that the system of resonators with dissipation completely absorbs the incident wave defined by Eq. (1).

Note that, when a single resonator placed in a free boundless medium has equal friction and radiation resistances, its absorption cross section is maximal and equal to its scattering cross section [4].

REFERENCES

1. S. N. Rzhevkin, *Course of Lectures on the Theory of Sound* (MGU, Moscow, 1960).
2. *Acoustics Handbook*, Ed. by M. J. Crocker (Wiley, New York, 1997).
3. W. J. Cavanaugh and J. A. Wilkes, *Architectural Acoustics: Principles and Practice* (Wiley, New York, 1999).
4. M. A. Isakovich, *General Acoustics* (Nauka, Moscow, 1973).

Translated by E. Golyamina

Acoustical Physics, Vol. 48, No. 3, 2002, pp. 376–377. Translated from Akusticheskiĭ Zhurnal, Vol. 48, No. 3, 2002, pp. 430–431.
Original Russian Text Copyright © 2002 by Bobrovnitskiĭ.

INFORMATION

5th International Conference on Vibration Problems

The 5th International Conference on Vibration Problems (ICOVP 2001) was held in Moscow, Russia, on October 8–10, 2001. It was organized by the Institute of Mechanical Engineering, Russian Academy of Sciences, together with the Institute of Mechanics Problems, Russian Academy of Sciences, with support from the Russian Academy of Sciences, the Russian Foundation for Basic Research, and other institutions. Full members of the Russian Academy of Sciences (academicians) K.V. Frolov and D.M. Klimov co-chaired the conference. In total, 180 researchers and experts from Russia, the USA, India, Sweden, the Czech Republic, Ukraine, and many other countries took part in the conference. The sessions included over 50 oral presentations and over 80 posters. A brief review of the conference and a description of some of the papers presented there are given below.

Vibrations play an exceptional role in nature and technology; therefore, a lot of scientific attention has always been given to the problems of vibrations. A multitude of new problems have appeared lately in this area due to the development of space-technology, aeronautics, rapid-transport systems, and also as the result of studies in geology, biological systems, and new technologies. Specialized research journals devoted to these issues are published, and scientific conferences on national and international levels, such as the annual INTER-NOISE conferences, congresses on noise and vibrations, the EUROMECH thematic conferences, and other meetings are organized. The distinctive feature of the 5th conference held in Moscow, as well as of the preceding four conferences, was its orientation toward the development of modern and frequently very complex mathematical and numerical methods of vibration theory and their application to the solution of specific technological problems. While the four preceding conferences of this series (held at universities and colleges in India) had been devoted mainly to problems of the mathematical theory of elasticity and geology, the program of the Moscow conference was essentially expanded on account of papers on vibration technology, vibrations of engineering structures and, in particular, space vehicles, vibration diagnostics, and vibrations of biological systems and composite materials.

Many new problems of the theory of vibrations that arose lately, originating from applications, were characterized by K.V. Frolov (Moscow, Russia) in his paper "Development of the Theory of Vibrations in Application to Vibration Machines." Vibration processes are the basis for the operation of a wide class of machinery and devices designed for various purposes. These are pile drivers, devices for thickening concrete and casting mixtures, vibrating transporters, etc. As a rule, their operation is described by nonlinear equations. The analysis of these equations leads to the discovery, investigation, and utilization of such physical effects as the transformation of dry friction into viscous friction under the effect of vibration, the alteration of mechanical parameters of materials and media with respect to slowly changing forces, the vibrational separation of multiphase media, and so on. The progress in designing enhanced vibrational machinery depends directly on the results of studies in this area.

Flow laws were studied theoretically and experimentally in the paper "Non-Linear Effects of the Outflow of Granular Materials and Fluids from Vessels" by I.I. Blekhman, L.A. Vaĭsberg, V.B. Vasil'kov, and K.S. Yakimova (St. Petersburg, Russia). In particular, the effect of air suction into a vibrating vessel with a liquid, which was observed apparently for the first time, was described.

The equations of the dynamics of solids in the presence of a microstructure, damage, geometrical and physical nonlinearity, and the interaction of strain and magnetic fields were developed in the paper by V.I. Erofeev (Nizhni Novgorod, Russia), "Non-Linear Waves in Solids with Microstructures." The possibility of utilizing these mathematical models for the description of dynamic processes in polycrystalline and composite materials with allowance for their nonlinear, dispersion, and dissipation properties was substantiated. It was demonstrated that the following phenomena can be observed in media with a microstructure: the resonance interactions of longitudinal waves with waves of longitudinal rotation and shear–rotational waves, the self-modulation of regular and noise shear waves, the formation of nonlinear stationary waves (longitudinal, shear, and shear–rotational) and, in particular, the formation of strain solitons, as well as other effects that do not have analogs in the classical mechanics of continuous media. An opportunity to use these effects for the acoustic testing of solids is indicated.

Vibrations and waves in composite materials and structures were considered in eight papers. In particular, the paper "Vibration and Sound Transmission through Sandwich Composite Plates" by A. Nilsson (Stockholm, Sweden) was devoted to theoretical and experimental studies of light three-layer plates. Losses in these structures were considered in detail. The results of measurements in a railcar made of such composite materials were described and analyzed.

1063-7710/02/4803-0376$22.00 © 2002 MAIK "Nauka/Interperiodica"

Nonlinear oscillations were the subject of many papers. A series of new results were given in the papers by A. Tondl and F. Peterka (Prague, Czech Republic), "Oscillator with Soft Impact Interaction," by D.M. Klimov (Moscow, Russia), "Asymptotic Methods in Non-Linear Mechanics," by V.V. Kozlov (Moscow, Russia), "Diffusion in Non-Linear Vibratory Systems," and other papers.

The problem of the vibrations of composite engineering structures aroused considerable interest at the conference (12 papers). It is especially important for transport, i.e., space vehicles, airplanes, ships, and cars, which are subjected to intense vibrational loads. Designing vehicles from the point of view of noisiness and reliability requires the development of new techniques for the calculation and optimization of composite structures. Experts from the Krylov Central Research Institute (papers by V.I. Popkov *et al.*, S.V. Budrin, A.V. Ionov, and E.N. Afonin), Central Aerohydrodynamics Institute (papers by B.M. Efimtsov *et al.*), RKK Énergiya (papers by S.V. Borzykh *et al.* and S.V. Avdeev *et al.*), Lavochkin NPO (papers by O.P. Klishev *et al.*, A.A. Moisheev and O.P. Marosin, and A.M. Sevost'yanov *et al.*), Central Research Institute of Machine Building (papers by V.L. Levtov *et al.* and A.I. Likhoded *et al.*) and other Russian institutions took an active part in this section of the conference. From the point of view of acoustics, one should note here the paper by T.M. Tomilina (Moscow, Russia) "Coupled Vibration Energy of an Elastic Structure–Fluid System," where an effective numerical apparatus for investigating coupled vibroacoustic fields in acoustoelastic systems was proposed.

It is also necessary to note the increasing interest of experts in problems of the vibrations of biological systems. Four papers devoted to this topic were presented at the conference. In particular, an attempt to theoretically construct the optimal model of fish motion and to compare it with experimental data obtained by filming was made in the paper "Dynamic Optimization of Bending Oscillations of Aquatic Organisms" by V.V. Smolyaninov (Moscow, Russia).

On the whole, the 5th International Conference on Vibration Problems in Moscow was organized at a high scientific level comparable with the level of the best international meetings. It was well equipped technically, streamlined, and attracted the interest of many experts. The abstracts of all papers presented at the conference were published in the digest *5th International Conference on Vibration Problems. October 8–10, 2001, Moscow, Russia: Abstracts* (IMASH, Moscow, 2001). Complete versions of the majority of papers were published in the digest *Proceedings of the 5th International Conference on Vibration Problems, October 8–10, 2001, Moscow, Russia* (IMASH, Moscow, 2002). At the closing session, a decision was made to hold the 6th Conference in 2003 in Prague (Czech Republic).

Yu. I. Bobrovnitskiĭ

Translated by M. Lyamshev

Acoustical Physics, Vol. 48, No. 3, 2002, p. 378. Translated from Akusticheskiĭ Zhurnal, Vol. 48, No. 3, 2002, p. 432.
Original Russian Text Copyright © 2002 by the Editorial Board.

INFORMATION

10th International Congress on Sound and Vibration

The 10th International Congress on Sound and Vibration will be held on July 7–10, 2003, in Stockholm, Sweden.

Information about the scientific program is available through e-mail: icsv10@fkt.kth.se, and from the congress secretariat:

Congrex Sweden AB
Phone: +46 8 459 66 00
Fax: 45 8 661 91 25
e-mail: icsv10@congrex.se
Web-page: www.congrex.com/icsv10

1063-7710/02/4803-0378$22.00 © 2002 MAIK “Nauka/Interperiodica”